DISSERTATION

MICROWAVE EFFECTIVE LINEWIDTH IN POLYCRYSTALLINE FERRITES: PRECISION MEASUREMENTS AND NEW INTERPRETATIONS

Submitted by

Nan Mo

Department of Physics

In partial fulfillment of the requirements

For the Degree of Doctor of Philosophy

Colorado State University

Fort Collins, Colorado

Spring 2006

COLORADO STATE UNIVERSITY

February 24, 2006

WE HEREBY RECOMMEND THAT THE DISSERTATION PREPARED UNDER OUR SUPERVISION BY NAN MO ENTITLED MICROWAVE EFFECTIVE LINEWIDTH IN POLYCRYSTALLINE FERRITES: PRECISION MEASUREMENTS AND NEW INTERPRETATIONS BE ACCEPTED AS FULFILLING IN PART REQUIREMENTS FOR THE DEGREE OF DOCTOR OF PHILOSOPHY.

Committee on Graduate Work

Richard E. Eykholt

John L. Harton

Pavel Kabos

Robert G. Leisure

Carmen S. Menoni

Carl E. Patton
Advisor

Hans D. Hochheimer
Department Head

ABSTRACT OF DISSERTATION

MICROWAVE EFFECTIVE LINEWIDTH IN POLYCRYSTALLINE FERRITES: PRECISION MEASUREMENTS AND NEW INTERPRETATIONS

Experimental investigations have been made to resolve the origins and intrinsic limits of microwave loss in polycrystalline bulk ferrites through the enhanced technology and theory. First, the measurement accuracy has been improved ten-fold relative to previous data through the use of a high quality microwave cavity, a metrological ABA method, and a fine adjustment of gyromagnetic ratio. Second, a full theory of classical spin wave excitation and scattering, including the effects of conductivity, damping, a general anisotropy, and grain boundaries, has been developed based on quaternion analysis and operator algebra.

Effective linewidths have been accurately measured at 10 GHz on ultra dense hot isostatic pressed (hipped) and conventionally sintered (CS) polycrystalline yttrium iron garnet ferrite specimens. (1) The high field data have demonstrated the important and previously unappreciated role of spin wave coupling to degenerate electromagnetic spin wave (EM-SW) modes. The data for fields well above the highly degenerate bulk manifold show field dependence and closely track the computed density of such low wave number (k) EM-SW states and extrapolate to known intrinsic single crystal linewidths in the extreme high field limit. Comparison between spheres and disks confirms the corresponding three-dimensional and two-dimensional EM-SW scattering.

(2) Below a field point shifted up from the high field manifold edge by two-thirds of the saturation magnetization, the moderately porous CS material shows a microstructure -related increase in the loss related to the conventional moderate k dipole-exchange spin waves. This confirms the pseudo manifold effect due to pore-demagnetizing fields. (3) The low field data show an elbow at 0.23 T, the same field for which the density of degenerate EM-SW modes shows an abrupt change. The data at low field is generally larger than at high field. Such discrepancy has been attributed to the high k scattering due to random grain boundaries, in addition to the pseudo manifold effect. (4) The in-manifold effective linewidth for the hipped material shows a pure anisotropy scattering as expected.

Nan Mo

Department of Physics

Colorado State University

Fort Collins, CO 80523

Spring 2006

ACKNOWLEDGEMENT

Carl E. Patton is one of the best advisors. He always gave me hard time that pushes me to work hard. His philosophy, "The truth is in the data", was and will be the beacon lighting my advances. He is very patient even when he had to say to me "You don't know physics!" and I fought back to say he doesn't know mathematics. His "obstinateness" is also admiring. He does not accept any result unless he understands everything I talked. This is why I usually take the calculations more than ten times before I get to him. The only thing I do not favor is his strict writing style. This is because we are trying to do physics but not arts.

I would like to thank all of my colleagues in Magnetics group. I am very grateful to Young-Yeal Song, who taught me the basics of the microwave measurement techniques. Jerry J. Green gave me deep insights in my results, especially the frequency corrections of cavity Q. Pavel Krivosik helped me a lot in some theoretical calculations. I also learned a lot from the helpful discussions with Michael Wittenauer who has wide knowledge of magnetism. Kevin Smith spent lot's time on polishing my English.

Finally, I would like to thank my wife for the moral support.

This work was supported in part by the Office of Naval Research, Grant No. N00014-03-1-0070, the National Science Foundation, Grant DMR-0108797, and the U. S. Army Research Office, Grant No. W911NF-04-1-0247.

TABLE OF CONTENTS

1. INTRODUCTION

The microwave effective linewidth has been used to characterize the magnetic field dependence of the microwave losses for over four decades. For the goal of this thesis, the field dependent effective linewidth in polycrystalline ferrites is studied at high precision level. This chapter gives an introduction to this study.

Section 1.1 briefly introduces the basic concepts with regard to the microwave damping or relaxation in magnetic materials. Section 1.2 presents an overview of the entire investigations. Section 1.3 provides a quick reference for the coordinate systems, the acronyms, and the symbols.

1.1. Basic Concepts

In normal materials, electrons are paired with opposite spins and no net magnetic moment exists. However, this is not the case of ferro- or ferri- magnetic materials. Such a material is a spin system that contains magnetic ions with some unpaired electrons and net magnetic moments. Typical magnetic ions contain iron, cobalt, and nickel. The difference between ferro- and ferri- magnetic materials is that the spins in the former align parallel to each other, while the latter have some spins aligned anti-parallel but still

a large non-zero magnetic moment.

Ferro- and ferri- magnetic materials are characterized by the magnetic moments per unit volume, known as the *spontaneous magnetization*. The quasi-static response of the static magnetization against static magnetic field is characterized by the magnetic hysteresis loop. For a large applied field, magnetization will be saturated since all the microscopic spins may line up to the same direction. The magnetization will begin to "oscillate" or undergo a precession when it is slightly off the equilibrium direction.

The precessing magnetization generally varies with time and space. The corresponding Fourier expansion gives a series of waves as a function of precessional frequency and wave vector. Such kind of wave is microscopically related to the motion of spins and hereby called *spin wave*. The corresponding frequency and wave vector are named spin wave frequency and spin wave vector, respectively. In quantum theory, the magnetization motion is described as *magnon* instead of spin wave based on the particle-wave duality.

Spin waves can be excited by dynamic magnetic fields. The spin wave excitations are categorized two types, namely, linear and nonlinear. The focus of this thesis is on the linear response of magnetization. Specifically, two assumptions are made. First, the magnetization in the concerning magnetic sample is saturated and herby has a constant length. Second, the excited spin waves have small amplitude compared with the saturation magnetization. This assumption is called *small signal limit*. In the small signal limit, the nonlinear phenomena are neglected.

Spin wave dispersion is the relation between the spin wave frequency and wave vector. The spin wave frequency is typically plotted as a function of the spin wave number. This plot also depends on the spin wave propagation directions. The consideration of the propagation directions results in one or several spin wave bands in the format of spin wave frequency versus wave number. The band with moderate or large wave numbers is known as *spin wave manifold.*

The spin wave dispersion is also a function of static external magnetic field. At a fixed frequency, the spin wave band is projected to the format of the spin wave number versus the static external magnetic field. The field region of the spin wave band in the low wave number limit is the *bulk manifold* region. The field regions above and below the bulk manifold region refer to the *high field region* and the *low field region*, respectively. It will be shown in the following chapters that the bulk manifold concept is useful for the understanding of magnetic excitations.

The uniform mode spin wave (or precession) corresponds to a zero wave number. When the microwave drive field has the same frequency as the uniform mode spin wave, the excited uniform mode spin wave reaches a maximum in amplitude and shows a resonance. This resonance is the well-known *ferromagnetic resonance* (FMR). Griffiths reported the first observations of FMR in 1946.

At a fixed static magnetic field, the FMR response can be expressed in terms of the power of uniform mode precession as a function of microwave frequency. A Lorentzian fit of this frequency function gives an experimental resonance frequency and a resonance

width, which are FMR frequency and FMR half power linewidth in frequency units, respectively. The FMR response can also be as a function of static magnetic field at a fixed microwave frequency. The corresponding Lorentzian fit gives a FMR field and a FMR half power linewidth in field units. Typically, only the FMR linewidth in field units is used.

In an ideally lossless material, the FMR linewidth is zero. However, the microwave energy stored in the uniform mode precession generally shows a decay due to microwave damping or relaxation. This decay rate is called *uniform mode relaxation rate*, which is measured by the FMR linewidth.

It was realized in 1960's that the relaxation rate is generally magnetic field dependent. The FMR field linewidth only involves a fixed field for a given operating frequency and cannot provide a good measure of the off resonance relaxation rate. The *effective linewidth* concept was then introduced to characterize the relaxation rate at any field for an operating frequency. The effective linewidth at FMR field is generally equal to the FMR linewidth.

In the bulk manifold region, the driven FMR uniform mode is degenerate with moderate wave number spin waves with micron wavelengths. In polycrystalline ferrites, the coupling to these spin-wave modes, termed *two-magnon scattering*, usually dominates the microwave relaxation. Following the early work of Schlömann (1969), Sparks *et al* (1961), and others, the in-manifold two-magnon processes are reasonably well understood. The scattering defects can be surface pits, pores, randomly orientated

magnetocrystalline anisotropy, grain boundaries, etc.

The two-magnon contribution to the microwave losses in these magnetic systems can be field and frequency dependent. The field dependence is generally related to the situations of density of degenerate states (DOS). FMR typically happens in the bulk manifold. The FMR linewidth is generally large because of the large value of the low wave number DOS. On the other hand, the off resonance effective linewidth could be substantially lower than those indicated by a single FMR linewidth parameter.

Magnetic materials have wide applications, for example, isolators, phase shifters, circulators, filters, delay lines, magnetic recording devices, radar, communications, and some other magnetic systems. There is recently an increasing need of low loss magnetic materials operating at high frequency and high speed. This drives the recent resurgence of interest in the fundamental understanding of precessional dynamics and microwave relaxation processes in the magnetic system.

This also strongly motivates a new examination of the effective linewidth and the related off-resonance losses in ferrites because many microwave magnetic devices operate over a wide range of magnetic fields. For example, microwave filters and isolators may operate in the manifold region while circulators, phase shifter, and some isolators do in the high field and low field region.

1.2. Overview of This Thesis

The basic results of the microwave ferrite effective linewidth have been well

understood based on the effective linewidth work in 1960's and 1970's. The work after 1980's kept unchallenged. The previous effective linewidth measurements will be briefly reviewed in Chapter 4.

The old work confirmed four expected effects. First, the effective linewidth is generally field dependent. Second, the previous data show the considerable structure in the manifold region of degenerate low wave number spin waves when plotted versus field at constant frequency or frequency at constant field. This in-manifold effective linewidth has been well understood based on the work of the anisotropy and porosity scatterings (e.g., Sparks, 1964; Schlömann, 1969; Patton, 1969; and Vrehen, 1970). Third, the off resonance effective linewidth, especially at very high fields, is generally much lower than the FMR linewidth. Finally, the low field effective (LFE) linewidth, at fields well below FMR but still sufficient to achieve the magnetization saturation, is typically a little higher than the average high field effective (HFE) linewidth.

The old data, however, showed two key contradictions. First, it was found that the HFE linewidth was generally higher than the corresponding FMR linewidths in single crystals. This is problematic because at high field, the spin wave band is generally shifted to frequencies that are much higher than the uniform mode FMR frequency, and there should be no two magnon scattering contribution to the linewidth whatsoever. This means that the HFE linewidth should be identical to the intrinsic single crystal linewidth. This was not the experimental case. Second, the HFE linewidth was also found to be strongly dependent on microstructure (Patton, 1970; Vrehen, 1969). There

are substantial increases in this loss parameter with both increasing porosity and decreasing grain size. Both responses are inconsistent with the idea of a high field "intrinsic" loss parameter in the absence of two-magnon scattering.

The above two problems have remained unresolved for the past four decades. The goal of this thesis is to resolve these long-standing problems and to understand the fine structures of full field effective linewidth. Three measures are taken in the new investigations. First, the ultra dense polycrystalline yttrium iron garnet (YIG) materials are used. The modern hot isostatic pressing (hipping) technique allows manufacturing the ultra dense bulk ferrites, in which nearly all the pores are eliminated. The typically dominant two-magnon relaxation due to porosity can be neglected. One then readily investigates the other effects that were previously buried in the dominant porosity contributions. Moreover, YIG has the outstanding attributes of cubic structure and being an excellent insulator. The single crystal YIG linewidth is well understood and attributed to the four-magnon scattering processes (Picus *et al*, 1961), around 0.05 mT at X-band frequencies. This helps avoiding any ambiguity due to the known dominant loss mechanisms.

Second, the effective linewidth measurement accuracy is substantially improved more than ten fold of the previous ultra sensitive technique (Patton, 1970). The effective linewidth is generally solved from the magnetic susceptibility. At high or low fields, far from FMR, the magnetic susceptibility has extremely weak dependence on magnetic field for materials with nearly intrinsic losses. Note that the important details of the specific

physical processes that contribute to loss mechanisms in microwave ferrites are typically extracted from the magnetic field dependence of the effective linewidth. The measurement accuracy becomes critically important for resolving the fine structures of the off resonance effective linewidth.

Third, full spin wave bands, unlike just one band in magnetostatic theory, are used for the understanding of the experimental results. These bands are derived from Maxwell's full equations and the magnetic torque equation. Corresponding modifications are made in the data analyses of effective linewidth.

Based on these three measures, the high field and low field problems are successfully resolved in this thesis. A part of work has been published (Mo et al, 2005). This thesis is organized as follows:

Chapter 2 presents a conceptual description about the linear excitations of spin waves based on the classical theory. Only the classical theory is used in the entire thesis. The quantitative and qualitative approaches are used for the FMR uniform mode response and the non-uniform mode excitations (or coupling), respectively. The magnetic susceptibility governs the quantitative excitations and couplings of the degenerate spin waves. The spin wave dispersion relations that are derived from the magnetic susceptibility provide a qualitative picture of the excitations and couplings of spin waves.

Chapter 3 provides an overview of the classical theory of two-magnon scattering, most of which is developed in this thesis (see Chapter 8). Two-magnon scattering is an extrinsic and typically dominant loss mechanism in polycrystalline ferrites. A classical

theory of the porosity scattering is derived to introduce the concepts of the coupling factor and density of degenerate states. Emphasis is specifically on the magnetic field dependence of the two-magnon relaxation.

Chapter 4 introduces the concept of the field dependent effective linewidth. First, the field dependence of effective linewidth is discussed based on the spin wave dispersion and two-magnon scattering. Second, the popular techniques for effective linewidth measurements are described. Third, the previous effective linewidth work is briefly reviewed.

Chapter 5 describes a high precision effective linewidth technique developed in this thesis. This development is for the accurate effective linewidth measurements on the ultra-low loss materials. Three measures have been taken to achieve high precision. First, the effective linewidth spectrometer system is optimized to improve the measurement stability and substantially reduce the systematic distortions due to the imperfection and mismatching of the system components. Second, the repeated ABA method and the modified ABA method are introduced to eliminate the dominant time drifts and minimize the random errors in the cavity measurements. Third, the data analyses are modified in order to extract the accurate and meaningful effective linewidth from the raw data of the cavity measurements.

Chapter 6 presents the new representative measurement results using the high precision effective linewidth techniques. These results are mainly for resolving the long-standing problems in the off resonance loss origins. First, the HFE linewidth data

for spheres and disks reasonably match up with the intrinsic single crystal linewidth. This represents the first demonstration of the intrinsic linewidth in the long pursuit of the intrinsic limit of the HFE linewidth. Second, the HFE linewidth data actually show field dependence, which was previously unrealized. The field dependence has been found to correlate with the density of states for the electromagnetic spin waves (EM-SW). This is also confirmed by the discrepancies between the three-dimensional scattering for spheres and the two-dimensional scattering for disks. Third, the LHE linewidth shows elbow effects due to the emergence of the electromagnetic Larmor (EML) spin waves. This strongly supports the important role of the EM-SW modes in the LHE and HFE linewidth. Finally, the in-manifold effective linewidth is measured based on the new approach to overcome the cavity-overloading problem by microwave decoupling. The results of the hipped YIG material show the pure contributions due to the anisotropy two-magnon scattering. This also proves that the hipping process can completely eliminate the pores in polycrystalline ferrites.

Based on quaternion analysis, the exact solutions for the full spin wave dispersion in a general anisotropic magnetic material are derived in Chapter 7. The anisotropy and conductivity are included for the future investigations on metallic thin films. The full spin wave bands were never used before for the understanding of the microwave off resonance losses. The low wave number bands are used for the quasi-qualitative interpretations of the field dependence of the HFE and LHE linewidths in Chapter 6.

An operator theory of quantitative effective linewidth is formulated in Chapter 8.

The objective is to derive the classical theory of two-magnon scattering due to porosity, anisotropy, grain boundaries, and non-uniform static magnetization. The operator form is specifically for the future investigations on thin films. This theory is further used to evaluate the previously unexplored two-magnon scattering due to grain boundaries and provide the quantitative explanation of the pronounced tail of the LFE linewidth.

Chapter 9 summarizes the main results of this thesis. The high accuracy effective linewidth technique and the operator effective linewidth theory are also proposed for the future investigations on metallic thin films.

1.3. Quick Reference

1.3.1. Units

The international system (SI) of base and derived units is used in this thesis. One problem with the use of SI units is that most of the literature on the effective linewidth in ferrites uses the Gaussian cgs (centimeter-gram-second) units with the magnetic field H, FMR linewidth ΔH, and effective linewidth ΔH_{eff} expressed in Oe, the magnetization $\mathbf{M}$ in emu/cm^3, and the magnetic induction $4\pi M$ expressed in G (Gauss). In SI units, the standard unit of field, linewidths, and magnetization is A/m, while the standard unit for the magnetic induction is T (Tesla).

In this thesis, the choice has been made to express all such field quantities in Tesla. This is done to facilitate the conversion to Gaussian quantities, insofar as 1 T is

equivalent to a magnetic induction of 10000 G or a magnetic field of 10000 Oe. As a conversion to popular usage, the term "field" will be retained, even though the Tesla unit exactly applies to magnetic induction.

There is a considerable amount of text and figure material that involves fields and linewidths. In cases where a mathematical symbol for these quantities is included, the symbol will be preceeded by a μ_0, and the units will be given in Tesla. Examples from this thesis: "Static external field $\mu_0 H_{\text{ext}}$ (T)" in figures, "The order of measurement fields is 0.75, 0.55, ..., and 0.51 T ...", etc. For simplicity, the specific field in the field coordinate are indicated without μ_0, for example, manifold limit fields H_{00} and H_{90} instead of $\mu_0 H_{00}$ and $\mu_0 H_{90}$.

1.3.2. Acronyms

For convenience of reading, the definitions of the acronyms are given in each chapter and each figure where it appears first. The acronyms in the entire thesis are listed as follows,

CODATA	Committee on Data for Science and Technology DEA Dipole exchange anti-Larmor
DEL	Dipole exchange Larmor
DE-SW	Dipole-exchange spin wave

DOS	Density of degenerate states
EML	Electromagnetic Larmor
EMA	Electromagnetic anti-Larmor
EM-SW	Electromagnetic spin wave
FMR	Ferromagnetic resonance
GBS	Grain boundary scattering
HFE	High field effective (linewidth)
KS	Kohane and Schlömann
LFE	Low field effective (linewidth)
MS-SW	Magnetostatic spin wave
LCS	Local equilibrium coordinate system
OIML	International Organization of Legal Metrology
SCS	Sample equilibrium coordinate system
SLK	Sparks, Loudon, and Kittel
YIG	Yttrium iron garnet

1.3.3. Coordinate Systems

Two main coordinate systems, namely the local equilibrium coordinate system (LCS) and the sample equilibrium coordinate system (SCS), are used in this thesis. The z direction is chosen to be parallel to the equilibrium direction of magnetization for both systems.

In LCS, the notations for the spatial Euclid coordinate are (x, y, z) and the time coordinate is t. The unit vectors along the directions of x, y, and z are denoted by $\hat{x}$, $\hat{y}$, and $\hat{z}$, respectively. The vector form is $(\mathbf{r},t)$ where $\mathbf{r} = x\hat{\mathbf{x}} + y\hat{\mathbf{y}} + z\hat{\mathbf{z}}$. The spherical coordinates of $\mathbf{r}$ are (r, θ, ϕ). $\mathbf{r} = r(\sin\theta\cos\phi\hat{\mathbf{x}} + \sin\theta\sin\phi\hat{\mathbf{y}} + \cos\theta\hat{\mathbf{z}})$. Any vector ψ is typically denoted by (ψ_x, ψ_y, ψ_z) in Euclid coordinate system or (ψ, θ_ψ, ϕ_ψ) in the spherical coordinate system.

In SCS, a subscript $_s$ is added to the above symbols. For example, (r,θ, ϕ) in LCS becomes (r_s, θ_s, ϕ_s) in SCS.

1.3.4. Universal Constants

For simplicity, the following universal constants are not defined in the text. The listed values for the fundamental constants are taken from the current (2002) set of self-consistent values of the basic constants and conversion factors of physics and chemistry recommended by the Committee on Data for Science and Technology (CODATA) for international use. The uncertainties listed in the concise form are the standard uncertainty.

c Light speed *in vacuum*, 299792458 m/s

e Electron charge, $-1.60217653(14)\times10^{-19}$ C

g_e Spectroscopic splitting Landé factor of electron, 2.002 319 304 3718(75)

$\hbar$ Planck's constant over 2π, $1.05457168(17)\times10^{-34}$ J·s

i Imaginary number $\sqrt{-1}$

m_e Electron mass, $0.91093826(16)\times10^{-30}$ kg

$\gamma_e/2\pi$ Gyromagnetic ratio of electron over 2π, -28.0249532(24) GHz/T

ε_0 Permittivity of free space, $8.854187817...\times10^{-12}$ F/m

μ_0 Magnetic permeability of free space, $4\pi\times10^{-7}$ H/m

π 3.1415926...

Pauli matrices defined with real numbers:

$$\boldsymbol{\sigma}_x=\begin{pmatrix}0 & 1\\ 1 & 0\end{pmatrix},\ \boldsymbol{\sigma}_y=\begin{pmatrix}0 & -1\\ 1 & 0\end{pmatrix},\text{ and }\ \boldsymbol{\sigma}_z=\begin{pmatrix}1 & 0\\ 0 & -1\end{pmatrix}.$$

1.3.5. Symbols

The symbols are defined uniquely in this thesis. Best efforts are made to provide the definition of any symbol when it is first used in a given chapter. This is to allow a reader to be able to make use of the individual chapters independently. The symbol definitions follow two conventions:

(1) If a parameter ψ is a function of the other parameters, for example, wave number k and magnetic field H, then ψ means the same thing as $\psi(k)$, $\psi(H)$, and $\psi(k,H)$. The physical meanings of k and H decide the exact form, for example, $\psi(k)\equiv\psi(k,H)$ but not $\psi(k)\equiv\psi(H,k)$, so as to keep units consistent.

(2) The symbol for Fourier transformation is the same as that in the real spacetime.

The explicit form can be defined by its function. For example, $\mathbf{m}(\mathbf{r},t)$ is in the real spacetime $(\mathbf{r},t)$ and $\mathbf{m}(\mathbf{k},\omega)$ is in the phase space $(\mathbf{k},\omega)$.

The symbols are listed as follows according to the order in the international recommendations of OIML (International Organization of Legal Metrology), for example, R111-1 (2004).

$\ddot{\mathbf{A}}$	Tensor of static anisotropy field
a	Void size
a_0, a_x, a_z	Factors of dynamic anisotropy tensor
b	Grain size
b_0, b_x, b_y, b_z	Temporary parameters (see Chapter 7)
C	Two-magnon coupling factor
C_{pk}	Function to characterize the $k-$ dependence of coupling factor in the porosity scattering.
C_{Ak}	Function to characterize the $k-$ dependence of coupling factor in the anisotropy scattering.
$C_{p\theta}$	Function to characterize the dependence on the spin wave propagation directions of coupling factor in the porosity scattering.
$C_{A\theta}$	Function to characterize the dependence on the spin wave propagation directions of

C_T	Linear temperature coefficient.
D	Exchange stiffness
D_0	Normalized exchange stiffness parameter
$d_{l,m}$	A factor relevant to spherical harmonic waves (see Chapter 7)
$\mathbf{e}_d$	Dipolar electric field
$\mathbf{e}_i$	Dynamic internal electric field
$\ddot{\mathbf{G}}$	A factor tensor in magnetic susceptibility (see Chapter 3)
g	Total density of degenerate states
$\mathbf{H}$	General magnetic field
H_0	Effective (total) static field
H_{00}	Top field of bulk manifold
H_{00}^*	Top field of pseudo-manifold
H_{90}	Bottom field of bulk manifold
H_{90}^*	Bottom field of pseudo-manifold
$\mathbf{H}_A$	Effective anisotropy field (static and dynamic)
H_{A0}	Effective static anisotropy field
H_c	Cubic anisotropy field
$\mathbf{H}_D$	Demagnetizing (static) field
$\mathbf{H}_{\text{ext}}$	Static external magnetic field
H_{FMR}	FMR field expressed in static external field

$\mathbf{H}_i$	Static internal field
H_{ref}	Reference field
$\mathbf{H}_s$	Effective surface anisotropy field
H_u	Uniaxial anisotropy field
H_X	Field where the electromagnetic Larmor spin waves show up in the low field region
$\mathbf{h}_A$	Dynamic anisotropic field
$\mathbf{h}_d$	Dipolar field
$\mathbf{h}_{ex}$	Effective exchange field
$\mathbf{h}_i$	Dynamic internal field
$\mathbf{h}_p$	Microwave drive (magnetic) field
K_c	Geometry factor of cavity
$\mathbf{k}$	Spin wave vector, $(k,\ \theta_k,\ \phi_k)$
k_0	Pure electromagnetic wave number
k_{DEA}	Wave number for dipole exchange Anti-Larmor spin waves
k_{DEL}	Wave number for dipole exchange Larmor spin waves
k_{EMA}	Wave number for electromagnetic Larmor spin waves
k_{EML}	Wave number for electromagnetic Larmor spin waves
k_{mnp}	Characteristic wave number of cavity for a normal mode with the indices (m,n,p)
$\tilde{L}$	General linear operator

$\mathbf{M}$	Vector magnetization, (M, θ_m, ϕ_m) in spherical coordinates of SCS.
$\mathbf{M}_0$	Static (saturated) magnetization.
$\mathbf{m}$	Dynamic magnetization
$\mathbf{m}_1$, $\mathbf{m}_2$	Dynamic magnetizations under coordinate transformations (see Chapter 7)
$\ddot{\mathbf{N}}$	Operator for dipolar field
$N_{//}$	In plane dipole field factor for disks
$N_{\perp}$	Perpendicular dipole field factor for disks
n	A general number or index
n_c	Number of ABA cycles
$\hat{\mathbf{n}}_s$	Unit vector normal to grain (or sample) surfaces
P	Distribution of demagnetizing field of a void
P_{abs}	Absorbed microwave power
P_{in}	Microwave input power
p	Porosity
Q_{∞}	Infinite field extrapolated cavity quality factor
Q_c	Cavity quality factor
q	Unit function for grains
q_s	Unit function for sample
R	The distance along the spin wave propagation direction
r_0	Radius of a spherical sample

$\mathbf{S}_n$	Scattering operators, $n \equiv 0,\ 1,\ 2,$ or 3 (see Chapter 8)
$\mathbf{s}$	Spin momentum.
$\mathbf{T}$	Tensor for transformation from LCS to SCS
T_c	Cavity temperature
ΔT_c	Cavity temperature difference
$\mathbf{T}_D$	Damping torque
U	Expanded uncertainty
U_a	Anisotropy energy density
U_r	Relative expanded uncertainty
U_s	Surface anisotropy energy density
U_{zm}	Zeeman energy density
u	Standard uncertainty
u_{10}, u_{12}	Temporal symbols for integrals (see Chapter 8)
V_c	Cavity volume
V_s	Sample volume
w	Temporary quaternion (see Chapter 7)
X_ω	Frequency parameter
X_Q	Quality factor parameter
Y	Temporal parameter, $Y = D_0(k^2 - k_0^2)$
α	Gilbert damping constant

$\beta_{x'}, \beta_{y'}, \beta_{z'}$	Angle for the equilibrium magnetization against the crystalline anisotropy axes
γ	Gyromagnetic ratio of material
$\mathbf{\Gamma}, \mathbf{\Gamma}_1, \mathbf{\Gamma}_2$	Relaxation operators
ΔH_∞	High field limit effective linewidth
ΔH_{eff}	Effective linewidth
ΔQ_c	Cavity quality factor difference between the measurement field and reference field
$\Delta \omega_c$	Cavity center frequency difference between the measurement field and reference field
$\delta n(\omega)$	Number of modes for a given slice of frequency space from ω to $\omega + \delta\omega$.
δ_{eff}	Normalized effective linewidth
ε	Small value
ε_r	Relative dielectric constant
η	Relaxation rate
η_{2m}	Two-magnon relaxation rate
θ_u	Uniform mode limit angle
θ_m	Angle between magnetization and static magnetic field.
λ	Spin wave wavelength
$\boldsymbol{\mu}$	Magnetic moment
ρ	Partial density of degenerate states in a unit one-dimension $\mathbf{k}$ volume,

σ_c Conductivity

$\sigma_{\Delta Q_c}$, $\sigma_{\overline{\Delta Q_c}}$ Standard deviations of ΔQ_c and $\overline{\Delta Q_c}$

$\sigma_{\Delta \omega_c}$, $\sigma_{\overline{\Delta \omega_c}}$ Standard deviations of $\Delta \omega_c$ and $\overline{\Delta \omega_c}$

ξ_0 Parameter for spin pinning on the surface

ϕ_0 Initial value of ϕ_m

ϕ_a An angle for temporary use (see Chapter 7)

ϕ_m Azimuthal angle of the magnetization

$\chi = \chi' - i\chi''$ Complex form of scalar magnetic susceptibility

$\tilde{\chi}$ Susceptibility operator corresponding to $\ddot{\chi}^{-1}$

$\ddot{\chi}_{2m}$ Uniform mode susceptibility tensor with two-magnon scattering considered

$\ddot{\chi}_e$ External magnetic susceptibility tensor, $\ddot{\chi}_e = \begin{pmatrix} \chi_{xx} & i\kappa_{xy} \\ -i\kappa_{yx} & \chi_{yy} \end{pmatrix}$ in a general form. $\ddot{\chi}_e = \begin{pmatrix} \chi & i\kappa \\ -i\kappa & \chi \end{pmatrix}$ for uniform mode for spheres

ψ (or $\boldsymbol{\psi}$) General scalar (or vector) function

$\Omega, \Omega_0, \Omega_1, \Omega_H$ Dimensionless frequency parameters (see chapter 7)

ω Operating angular frequency.

ω_0 Precession frequency of magnetization

ω_∞ Infinite field extrapolated cavity center frequency

ω_A Anisotropy field in frequency unit

ω_B Top frequency of spin wave manifold.

ω_c	Cavity center frequency
ω_{em}	Pure electromagnetic wave frequency
ω_H	Static internal field in frequency unit
ω_k	Spin wave angular frequency.
ω_M	Magnetization in frequency unit
ω_X	The frequency where the electromagnetic spin waves show up in the high frequency region
$\bar{}$	Special notation: average
*	Special notation: complex conjugation except for H_{00}^* and H_{90}^*
$\langle\ \rangle$	Special notation: statistical average

2. MAGNETIC EXCITATION OVERVIEW

This chapter presents a conceptual description of the classical theory of magnetic excitations in ferro- and ferri- magnetic bulk materials. In this theory, the magnetic susceptibility (tensor) governs the quantitative excitations of the degenerate spin waves and their couplings to and from the other spin waves. The spin wave dispersion relations are further derived from the magnetic susceptibility and provide a qualitative picture of the excitations and couplings of spin waves. The ferromagnetic resonance originates from the uniform mode excitation. In this chapter, the magnetic susceptibility approach is hereby used for the uniform mode analyses while the spin wave dispersion approach is used to discuss the non-uniform mode excitations and couplings.

For simplicity, the following discussions are based on an *isotropic magnetic sphere*. This does not affect the basic concepts. This chapter is organized as follows. Section 2.1 describes the ferromagnetic resonance (FMR) concept based on the uniform mode precession and the linear response of microwave power absorbed by the magnetic sample. In Section 2.2, the magnetostatic approximation is used to derive the excitations of the moderate and high wave number spin waves. Section 2.3 briefly describes the full spin wave bands obtained from Maxwell equations and the linearized magnetic torque equation. Finally, it is emphasized in Section 2.4 that the degenerate spin waves are not only frequency dependent but also field dependent.

2.1. Ferromagnetic Resonance

Section 2.1.1 starts with the magnetic toque equation and introduces the concept of uniform mode precession. In Section 2.1.2, a microwave drive field is added into the torque equation, the magnetic susceptibility for uniform mode is derived, and the connection between the magnetic susceptibility and the power absorption or the FMR response is made. Section 2.1.3 introduces the concept of FMR linewidth to characterize the microwave loss.

2.1.1. Uniform Mode Precession

Ferro- and ferri- magnetic materials have a large body of free electron spins. The magnetic properties come from these free spins. Consider a single electron spin with spin momentum $\mathbf{s}$ in a magnetic field $\mathbf{H}$. $\mathbf{s}$ has a length of $|\mathbf{s}| = \hbar/2$. Note that the electron carries a negative charge, $-e$. The classical theory for this electron gives a magnetic moment $\boldsymbol{\mu}$,

$$\boldsymbol{\mu} = -g_e \frac{e}{2m_e}\mathbf{s}. \tag{2.1}$$

The electron in the field $\mathbf{H}$ is acted on by a toque, $\boldsymbol{\mu} \times \mu_0 \mathbf{H}$. The spin will precess around $\mathbf{H}$. The time dependence of $\boldsymbol{\mu}$ can be described by the so-called torque equation,

$$\frac{d\boldsymbol{\mu}}{dt} = -|\gamma_e|\boldsymbol{\mu} \times \mu_0 \mathbf{H}. \tag{2.2}$$

Explicitly,

$$\gamma_e = -g_e \frac{e}{2m_e}. \tag{2.3}$$

Suppose that there are n spins with moment $\boldsymbol{\mu}_i$ (i=1, 2, ... , n) in a small volume ΔV. The magnetization $\mathbf{M}$ is defined by

$$\mathbf{M} = \sum_{i=1}^{n} \frac{\boldsymbol{\mu}_i}{\Delta V}. \tag{2.4}$$

The motion of $\mathbf{M}$ is described by an equation similar to Eq. (2.2) of magnetic moment, but may have a different value of the gyromagnetic ratio, γ. The main reason for a different γ is that the spin momentum of an electron is coupled with its orbital momentum and the material has a different Landé factor from a free electron. The equation for the motion of magnetization is,

$$\frac{d\mathbf{M}}{dt} = -|\gamma|\mathbf{M} \times \mu_0 \mathbf{H}. \tag{2.5}$$

In comparison with Eq. (2.2), $\mathbf{H}$ should be interpreted as the total magnetic field that applies to $\mathbf{M}$.

The total field $\mathbf{H}$ may have many components. These components will be added step by step. As a starting point, only consider the static external field $\mathbf{H}_{\text{ext}}$ applied along the z direction. This corresponds to an infinite isotropic medium. Equation (2.5) can be solved in the time domain for this simple case. Figure 2.1 shows a solution of the motion of $\mathbf{M}$ in an element volume. $\mathbf{M}$ moves along the circular trace. The arrow shows the direction of motion. This motion about the magnetic field is called "precession". The precessional frequency is indicated by ω_0. The spherical coordinate parameters θ_m and ϕ_m of $\mathbf{M}$ are also indicated for further discussions.

In Fig. 2.1, θ_m is constant and ϕ_m is time dependent,

$$\frac{d\phi_m}{dt} = \omega_0 = |\gamma| \mu_0 H_{\text{ext}} . \tag{2.6}$$

Note that the Zeeman (potential) energy density is

$$U_{zm} = -\mu_0 \mathbf{M} \cdot \mathbf{H}_{\text{ext}} = -\mu_0 M H_{\text{ext}} \cos\theta_m . \tag{2.7}$$

The Zeeman energy is only related to the direction of $\mathbf{M}$, but not to the rotation of ϕ_m. θ_m is constant because the energy is conserved.

One can also write $\mathbf{M}$ as a function of time,

$$\mathbf{M} = \begin{pmatrix} M_x \\ M_y \\ M_z \end{pmatrix} = \begin{pmatrix} m \cdot \cos\phi_m \\ m \cdot \sin\phi_m \\ M\cos\theta_m \end{pmatrix} = \begin{pmatrix} m \cdot \cos(\phi_0 + \omega_0 t) \\ m \cdot \sin(\phi_0 + \omega_0 t) \\ M\cos\theta_m \end{pmatrix}, \tag{2.8}$$

where ϕ_0 is the initial value of ϕ_m and $m = M\sin\theta_m$. The x and y components show an oscillation with phase of ϕ_m and frequency of ω_0. The form in Eq. (2.8) represents the circular precession of magnetization.

This solution is applicable to the whole volume of material since only $\mathbf{H}_{\text{ext}}$ is considered. ϕ_0 and θ_m are generally dependent on the position $\mathbf{r}$ of $\mathbf{M}$. Fourier transformation of $\mathbf{M}(\mathbf{r},t)$ gives a series of plane waves with wave vector $\mathbf{k}$ and frequency ω. $\omega = \omega_0$ for the special case of infinite medium. These waves are called "spin wave". One special case is the uniform mode spin wave with $\mathbf{k}$ equal to zero. For the uniform mode, $\mathbf{M}$ is spatially independent and precesses with the same phase ϕ_m and amplitude m. This in-phase precession is also called "uniform mode precession".

2.1.2. Ferromagnetic Resonance Response

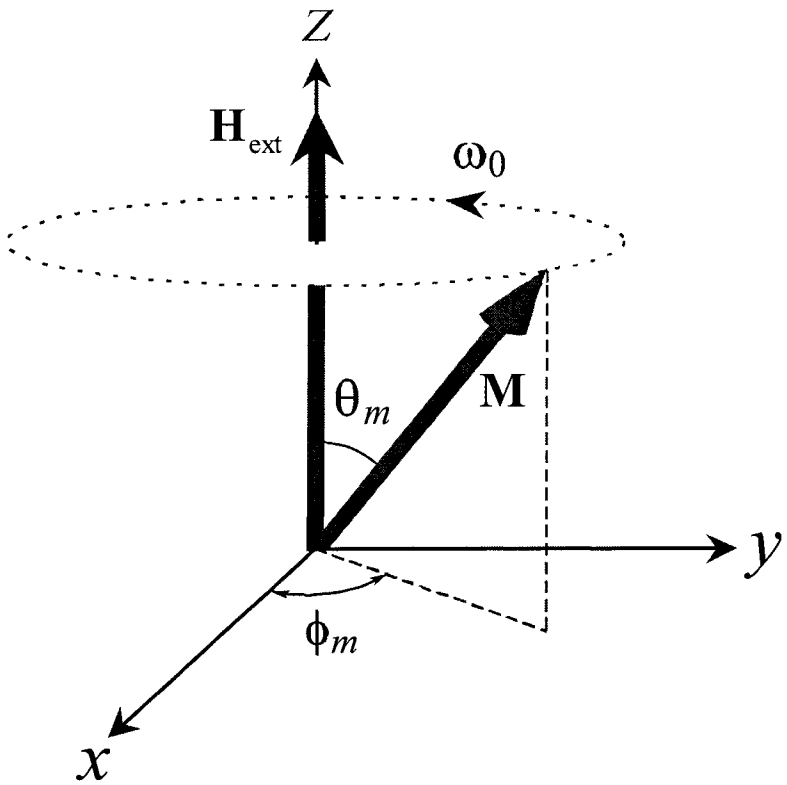

FIG. 2.1. Precession of magnetization. The bold arrows show the magnetization **M** and the external static field $\mathbf{H}_{ext}$. θ_m is the angle between the magnetization and z-axis, and ϕ_M is the angle between the x-y plane projection of magnetization and x-axis, as indicated by the dashed lines. The magnetization precesses around the external static field as shown in the dashed circle. ω_0 indicates the precessional frequency.

This section shows how the uniform mode spin wave can be excited by a microwave drive. The following discussions are based on the two assumptions that (a) the magnetization is saturated, namely, $M = M_0$, where M_0 is the saturation magnetization, and (b) θ_m or m is so small that the nonlinear terms in the torque equation can be neglected, which is the so-called small signal limit.

The magnetization **M** is written as a sum of the static part, $\mathbf{M}_0 = M_0\hat{\mathbf{z}}$, and the dynamic transverse part $\mathbf{m}(t) = m_x\hat{\mathbf{x}} + m_y\hat{\mathbf{y}}$. The static part represents the equilibrium

magnetization and only has a $z-$ component while the dynamic part only has $x-$ and $y-$ components. Note that in the small signal limit $M_0 \gg m$.

A small uniform microwave drive field, $\mathbf{h}_p$, perpendicular to z direction is now added. The demagnetizing field $\mathbf{H}_D$ and dipolar field $\mathbf{h}_d$ are also considered here. Equivalently, the field $\mathbf{H}$ in Eq. (2.5) is modified by

$$\mathbf{H} \to \mathbf{H}_i + \mathbf{h}_i \equiv \mathbf{H}_{\text{ext}} + \mathbf{H}_{\text{D}} + \mathbf{h}_p + \mathbf{h}_d, \tag{2.9}$$

where $\mathbf{H}_i$ is the static internal field and $\mathbf{h}_i$ is the dynamic internal field and $h_i \ll H_i$. For a sphere, $\mathbf{H}_D = -\mathbf{M}_0 / 3$. Insert these fields into Eq. (2.5), neglect the higher order terms of $\mathbf{m}$, $\mathbf{h}_d$, and $\mathbf{h}_p$, and one obtains the linearized torque equations for transverse components of magnetization,

$$-\frac{dm_y}{dt} + \omega_H m_x - \omega_M h_{\text{dx}} = \omega_M h_{\text{px}} \tag{2.10a}$$

and

$$\frac{dm_x}{dt} + \omega_H m_y - \omega_M h_{\text{dy}} = \omega_M h_{\text{py}}. \tag{2.10b}$$

Here, the parameters $\omega_M = |\gamma| \mu_0 M_0$ and $\omega_H = |\gamma| \mu_0 H_i$. These equations show $\mathbf{m}$ has a linear response to $\mathbf{h}_p$.

It is convenient to solve the Eqs (2.10a) and (2.10b) in the frequency domain based on Fourier transformations,

$$\mathbf{m}(t) = \frac{1}{2\pi} \int_{-\infty}^{\infty} \mathbf{m}(\omega) e^{i\omega t} d\omega \tag{2.11}$$

and

$$\mathbf{h}_n(t) = \frac{1}{2\pi}\int_{-\infty}^{\infty} \mathbf{h}_n(\omega) e^{i\omega t} d\omega . \tag{2.12}$$

where $n = p$, i, or d. Equations (2.10a) and (2.10b) become

$$-i\omega m_y + \omega_H m_x - \omega_M h_{dx} = \omega_M h_{px} \tag{2.13a}$$

and

$$i\omega m_x + \omega_H m_y - \omega_M h_{dy} = \omega_M h_{py} \tag{2.13b}$$

The relation between $\mathbf{m}_0$ and $\mathbf{h}_p$ is characterized by the external magnetic susceptibility tensor $\ddot{\chi}_e$ defined by

$$\mathbf{m}(\omega) = \ddot{\chi}_e(\omega) \cdot \mathbf{h}_p(\omega) . \tag{2.14}$$

This susceptibility tensor is generally $\mathbf{k}$ dependent. The tensors $\ddot{\chi}_e$ here should be in the form of $\ddot{\chi}_e(\omega, \mathbf{k} = 0)$. In this section, only the uniform mode is discussed. For simplicity, the argument $\mathbf{k} = 0$ is omitted in this chapter.

With $\mathbf{h}_d = -\mathbf{m}/3$ approximately for uniform mode, equations (2.13a) and (2.13b) give

$$\chi_e(\omega) = \begin{pmatrix} \chi & i\kappa \\ -i\kappa & \chi \end{pmatrix} . \tag{2.15}$$

The parameters χ and κ are

$$\chi = \frac{\omega_M \omega_0}{\omega_0^2 - \omega^2} \tag{2.16}$$

and

$$\kappa = \frac{\omega_m \omega}{\omega_0^2 - \omega^2} . \tag{2.17}$$

Equations (2.16) and (2.17) are not valid at $\omega = \omega_0$ where the denominator is zero. One cannot simply take the limit $\omega \to \omega_0$ because ω is generally complex while ω_0 is real. It will be shown shortly that this $\omega \to \omega_0$ limit is not consistent with the case in the limit of small loss. In order to include the case of $\omega = \omega_0$, one way is

$$\chi = \lim_{\varepsilon \to 0^+} \frac{\omega_M \omega_0}{\omega_0^2 - \omega^2 + i\varepsilon} \tag{2.18}$$

and

$$\kappa = \lim_{\varepsilon \to 0^+} \frac{\omega_M \omega}{\omega_0^2 - \omega^2 + i\varepsilon}. \tag{2.19}$$

The magnetic susceptibility tensor is a 2×2 matrix. The two eigen vectors give the spin wave polarizations. These vectors are typically complex. This means that the oscillations in the x and y directions have a different phase. The vector **m** hereby rotates around the z axis. From the top view in the coordinate system of Fig. 2.1, the anti-clockwise rotation is called Larmor precession and the clockwise rotation is anti-Larmor precession. The condition that the corresponding eigen values equals to zero gives the resonance condition of these eigen modes.

The susceptibility, χ, is generally complex. It is convenient to write it as a sum of the real part χ' and imaginary part χ'' in the form

$$\chi = \chi' - i\chi''. \tag{2.20}$$

The FMR response, which is the power absorption as a function of frequency or field, can be expressed by these components of susceptibility.

For a given drive frequency ω, the absorbed power P_{abs} is (refer to Hurben, 1996)

$$P_{\text{abs}}(\omega) = P_{in}(\omega) \cdot \chi''(\omega) \tag{2.21}$$

where P_{in} is the microwave input power,

$$P_{in} = \frac{1}{2}\mu_0 \omega \, \mathbf{h}_p(\omega) \cdot \mathbf{h}_p^*(\omega) V_s, \tag{2.22}$$

and V_s is the sample volume. The power absorption is defined as the ratio of absorbed power to input power and hereby equal to $\chi''(\omega)$.

$\chi''(\omega)$ is given by

$$\chi''(\omega) = \pi \omega_M \delta(\omega_0 - \omega). \tag{2.23}$$

This means that the power absorption shows a resonance at $\omega = \omega_0$. This resonance is called ferromagnetic resonance. $\omega = \omega_0$ or $H_{\text{ext}} = \omega / |\gamma| \mu_0$ is the Kittel (1948) resonance condition for isotropic spheres. This resonance condition can be obtained from a zero determinant of the inverse of magnetic susceptibility tensor. Furthermore, the delta function indicates a zero width of this resonance because the decay of the dynamic magnetization, $\mathbf{m}$, has not been account for in this section.

2.1.3. Microwave Loss and Ferromagnetic Resonance Linewidth

Microwave loss is considered in this section. There are several different phenomenological damping models, such as complex frequency (CF) damping model (refer to Mckinstry, 1991), Landau-Lifshitz (1935) damping, Gilbert (1956) damping, Codrington-Olds-Torrey (1954) model, Block-Bloombergen (1956) damping, Modified Block-Bloombergen damping (refer to Patton, 1975), tensor-form damping (Safanov, 2002), etc. Most of these models are equivalent for spherical geometry.

The CF model is used to show how the microwave loss changes the FMR response. For uniform mode excitation, the time dependence of **m** is given by $e^{i\omega_0 t}$ at a given FMR frequency ω_0. This indicates that the uniform mode precession amplitude is time-independent. However, this is not the case for real materials where the precession always has a non-zero decay rate and finally vanishes if without an external drive. Suppose the relaxation rate is η and **m** is then proportional to $e^{-\eta t}\cdot e^{i\omega_0 t}$. It is equivalent to replacing ω_0 with a complex frequency $\omega_0 + i\eta$. This replacement applies to the susceptibility tensor in Eq. (2.15).

The expressions for χ and κ, with a nonzero uniform mode relaxation rate η, become

$$\chi(\omega) = \lim_{\varepsilon\to 0^+} \frac{\omega_M(\omega_0 + i\eta)}{(\omega_0 + i\eta)^2 - \omega^2 + i\varepsilon} = \frac{\omega_M(\omega_0 + i\eta)}{(\omega_0 + i\eta)^2 - \omega^2} \tag{2.24}$$

and

$$\kappa(\omega) = \lim_{\varepsilon\to 0^+} \frac{\omega_M\omega}{(\omega_0 + i\eta)^2 - \omega^2 + i\varepsilon} = \frac{\omega_M\omega}{(\omega_0 + i\eta)^2 - \omega^2}. \tag{2.25}$$

The real part and imaginary part of χ are

$$\chi'(\omega) = \frac{\omega_M\omega_0\left(\omega_0{}^2 - \omega^2 + \eta^2\right)}{\left(\omega_0{}^2 - \eta^2 - \omega^2\right)^2 + 4\left(\omega_0\eta\right)^2}. \tag{2.26}$$

and

$$\chi''(\omega) = \frac{\omega_M\left(\omega^2{}_0 + \eta^2 + \omega^2\right)\eta}{\left(\omega_0{}^2 - \eta^2 - \omega^2\right)^2 + 4\left(\omega_0\eta\right)^2}. \tag{2.27}$$

The above damped equations are consistent with the un-damped case shown in Section

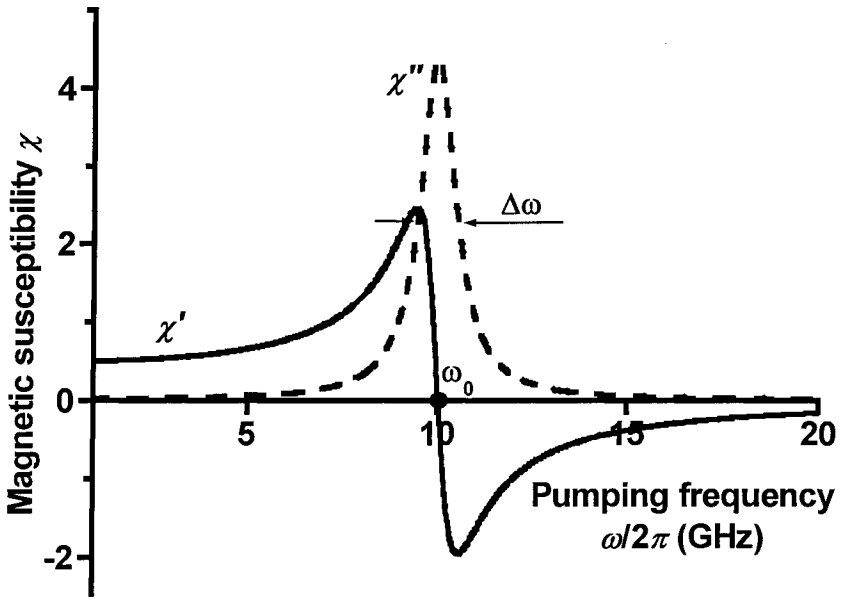

FIG 2.2. Magnetic susceptibility χ as a function of pumping frequency ω at a fixed static external field $\mu_0 H_{\text{ext}} = 0.3571$ T. The solid and dashed curves are the real part χ' and imaginary part χ'' of χ, respectively. The ferromagnetic resonance (FMR) frequency is indicated by ω_0 and the half-maximum width in the resonance curve χ'' by $\Delta\omega$. These curves are calculated using gyromagnetic ratio $|\gamma|/2\pi = 28$ GHz/T, relaxation rate $\eta/2\pi = 560$ MHz, and magnetization $\mu_0 M_0 = 0.175$ T.

2.1.2. For example, if the limit $\eta \to 0^+$ in Eq. (2.27) is taken, the same result as in (2.23) is obtained.

Figure 2.2 shows an example plot of χ versus ω at $\mu_0 H_{\text{ext}} = 0.3571$ T. Physically, ω is real and positive and corresponds to the microwave pumping frequency. The solid and dashed lines are χ' and χ'', which are calculated with the gyromagnetic ratio $|\gamma|/2\pi = 28$ GHz/T, the relaxation rate $\eta/2\pi = 560$ MHz, and $\mu_0 M_0 = 0.175$ T. The FMR frequency is indicated by ω_0. $\Delta\omega$ shows the half-maximum width of the χ'' curve.

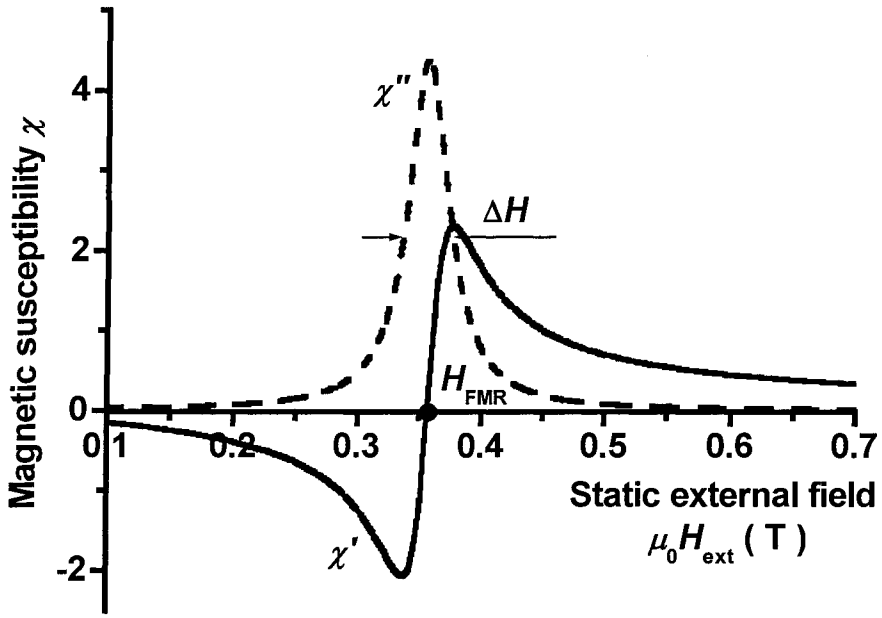

FIG 2.3. Magnetic susceptibility χ as a function of static external field H_{ext} at a fixed pumping frequency $\omega/2\pi = 10$ GHz. The solid and dashed curves are the real part χ' and imaginary part χ'' of χ, respectively. The ferromagnetic resonance (FMR) field is indicated by H_{FMR} and the half-maximum width in the resonance curve χ'' by ΔH. These curves are calculated using with the same gyromagnetic ratio, relaxation rate, and magnetization as in Fig. 2.2.

Note that the imaginary part χ'' represents the power absorption by the sample or the FMR response. For a small relaxation rate, $\eta << \omega_0$, equation (2.27) can be used to obtain an approximate expression near ω_0,

$$\chi'' \approx \frac{\omega_M \eta}{(\omega_0 - \omega)^2 + \eta^2} \tag{2.28}$$

This is a Lorentzian function of ω. A proper Lorentzian fit gives the FMR resonance ω_0 and the linewidth $\Delta\omega$,

$$\Delta\omega = 2\eta. \tag{2.29}$$

Therefore, the linewidth $\Delta\omega$ is just two times the relaxation rate and called frequency-

swept FMR linewidth.

The real part χ' is the dispersion effect discussed in Chapter 4. For a small relaxation rate, χ' is approximately

$$\chi'(\omega) \approx \frac{\omega_M \omega_0 \left(\omega_0{}^2 - \omega^2\right)}{\left(\omega_0{}^2 - \omega^2\right)^2 + 4\left(\omega_0 \eta\right)^2} \tag{2.30}$$

From low frequency to high frequency, χ' changes from positive, to zero, to negative. $\chi' = 0$ corresponds to the FMR frequency $\omega = \omega_0$, as shown in Fig. 2.2. Unlike χ'', χ' is only affected by the relaxation in a very narrow frequency range near FMR frequency ω_0. Off resonance,

$$\chi'(\omega) \approx \frac{\omega_M \omega_0}{\omega_0{}^2 - \omega^2}, \tag{2.31}$$

and is independent on the relaxation.

In typical FMR experiments, the field is swept instead of frequency. In this case, the magnetic susceptibility should be expressed as a function of field H_{ext} at a fixed frequency. Figure 2.3 shows such picture at 10 GHz with the same values of γ, η, and M_0, as in Fig. 2.2. The real part and imaginary parts of χ are indicated by the solid and dashed curves, respectively. These curves have the same features as in the frequency swept picture, but the FMR frequency ω_0 and FMR linewidth $\Delta\omega$ should be replaced by the FMR field H_{FMR} and FMR linewidth ΔH in field units, as indicated. They are proportional to each other, namely,

$$H_{\text{FMR}} = \frac{\omega_0}{|\gamma|\mu_0} \tag{2.32}$$

and

$$\Delta H = \frac{\Delta\omega}{|\gamma|\mu_0} = \frac{2\eta}{|\gamma|\mu_0} \tag{2.33}$$

for spheres. Note that the FMR linewidth ΔH is just the relaxation rate in field units.

2.2. Magnetostatic Excitation Theory

Section 2.1 has shown the excitation of uniform mode spin wave and the FMR response. Non-uniform mode excitations are also important to the FMR response, especially the FMR broadening (see Chapter 3). The non-uniform modes can be excited by a non-uniform microwave drive and coupled from the FMR uniform mode. Note that any spin wave is characterized by wave vector $\mathbf{k}$, frequency ω_k, amplitude m, and polarization $\mathbf{m}(\mathbf{k},\omega)$ (or ellipticity factor). The details of $\mathbf{m}(\mathbf{k},\omega)$ are not discussed here. The relation between $\mathbf{k}$ and ω_k is the so-called the spin wave dispersion relation. The dispersion governs which modes can be excited at a pumping frequency $\omega = \omega_k$ while m determines the intensity of excitation. The magnetic susceptibility (tensor) gives the intensity of spin wave excitation. This section outlines the spin wave dispersion derived from the magnetostatic theory.

2.2.1. Magnetostatic Approximation

The spin wave dispersion relation can be solved from Maxwell's equations and the magnetic torque equation. In magnetostatic theory, it is assumed that the electric and magnetic fields induced by the dynamic magnetization propagate instantaneously over the concerning sample. To understand the magnetostatic approximation, Maxwell's

equations for dynamic fields in an insulator such as yttrium iron garnet (YIG) are used,

$$\begin{aligned} \nabla \times \mathbf{h}_i &= \varepsilon_0 \varepsilon_r \frac{\partial \mathbf{e}_i}{\partial t} \\ \nabla \times \mathbf{e}_i + \mu_0 \frac{\partial (\mathbf{h}_i + \mathbf{m})}{\partial t} &= 0 \end{aligned}, \tag{2.34}$$

where ε_r is the relative dielectric constant, and $\mathbf{e}_i$ is the internal dynamic electric field. The other two equations for AC responses can be derived from Eq. (2.34),

$$\begin{aligned} \nabla \cdot \mathbf{e}_i &= 0 \\ \nabla \cdot (\mathbf{h}_i + \mathbf{m}) &= 0 \end{aligned} \tag{2.35}$$

The time derivative terms in Eq. (2.34) are responsible for the propagation of the dynamic fields and neglected in the magnetostatic limit. Two independent equations for $\mathbf{h}_i$ in the magnetostatic approximation are

$$\begin{aligned} \nabla \times \mathbf{h}_i &\approx 0 \\ \nabla \cdot (\mathbf{h}_i + \mathbf{m}) &= 0 \end{aligned} \tag{2.36}$$

The magnetostatic approximation is equivalent to the case that the induced electric field is negligible. The external fields follow the same equations so that the internal fields $\mathbf{e}_i$ and $\mathbf{h}_i$ can be replaced by the dipolar electric field $\mathbf{e}_d$ and dipolar magnetic field $\mathbf{h}_d$, respectively.

An alternative way for the understanding of the magnetostatic approximation is in the Fourier ($\mathbf{k}$, ω) space. Simply eliminate $\mathbf{e}_d$ in Eq. (2.34) and one can infer that the induced dipolar magnetic field $\mathbf{h}_d$ follows

$$\nabla^2 \mathbf{h}_d - \frac{\varepsilon_r}{c^2} \frac{\partial^2}{\partial t^2} \mathbf{h}_d = -\nabla(\nabla \cdot \mathbf{m}) + \frac{\varepsilon_r}{c^2} \frac{\partial^2}{\partial t^2} \mathbf{m} . \tag{2.37}$$

As mentioned above, the time derivative terms are responsible for the propagation of the dynamic fields and hence neglected in the magnetostatic limit. It becomes

$$\nabla^2 \mathbf{h}_d \approx -\nabla(\nabla \cdot \mathbf{m}). \tag{2.38}$$

Note that

$$\begin{aligned} &\nabla^2 \to -k^2 \\ &\frac{\varepsilon_r}{c^2}\frac{\partial^2}{\partial t^2} \to -k_0^2 \end{aligned}, \tag{2.39}$$

where $k_0 = \sqrt{\varepsilon_r}\omega / c$ is the pure electromagnetic wave number for insulator. Therefore, the approximation from Eq. (2.37) to Eq. (2.38) is equivalent to $k >> k_0$. This condition may also be written as

$$\omega_k << \omega_{em} \equiv ck / \sqrt{\varepsilon_r}\ . \tag{2.40}$$

The spin wave frequency $\omega_k(k, \theta_k, \phi_k)$ is far from the light line defined by the above equation.

Succinctly, the magnetostatic approximation is only related to the dynamic dipolar fields whose propagation is neglected and equivalent to the approximation that the dipolar electric field is neglected. The justification of such approximation is that the spin wave number is much larger than that of pure electromagnetic wave in a material for a given frequency.

2.2.2. Magnetostatic Spin Waves

Section 2.1 shows the uniform mode excitation and FMR response. For non-uniform modes, equations (2.13a) and (2.13b) are still valid but the dipole fields should be

modified by Eq.(2.38). In the Fourier phase space ($\mathbf{k}$, ω), equation (2.38) for transverse components becomes

$$\mathbf{h}_d(\mathbf{k}) = -\frac{1}{2}\begin{pmatrix} 2\sin^2\theta_k\cos^2\phi_k & \sin^2\theta_k\sin 2\phi_k \\ \sin^2\theta_k\sin 2\phi_k & 2\sin^2\theta_k\sin^2\phi_k \end{pmatrix}\cdot\mathbf{m}(\mathbf{k}). \tag{2.41}$$

Here (k, θ_k, ϕ_k) is the wave vector $\mathbf{k}$ in the spherical coordinate system.

By combining Eqs. (2.13a), (2.13b) and (2.41), one obtains

$$\ddot{\chi}_e^{-1}(\mathbf{k})\cdot\mathbf{m} = \mathbf{h}_p. \tag{2.42}$$

The tensor $\ddot{\chi}(\mathbf{k})$ is the $\mathbf{k}-$ dependent magnetic susceptibility tensor,

$$\ddot{\chi}_e(\mathbf{k}) = \begin{pmatrix} \chi_{xx} & i\kappa_{xy} \\ -i\kappa_{yx} & \chi_{yy} \end{pmatrix}. \tag{2.43}$$

The parameters used in the above equation are given by

$$\chi_{xx} = \frac{\omega_M\left(\omega_H + i\eta + \omega_M\sin^2\theta_k\sin^2\phi_k\right)}{\left(\omega_H + i\eta\right)\left(\omega_H + \omega_M\sin^2\theta_k + i\eta_k\right) - \omega^2}, \tag{2.44}$$

$$\chi_{yy} = \frac{\omega_M\left(\omega_H + i\eta + \omega_M\sin^2\theta_k\cos^2\phi_k\right)}{\left(\omega_H + i\eta\right)\left(\omega_H + \omega_M\sin^2\theta_k + i\eta\right) - \omega^2}, \tag{2.45}$$

$$\kappa_{xy} = \frac{\omega_M\left(\omega + \dfrac{i\omega_M\sin^2\theta_k\sin 2\phi_k}{2}\right)}{\left(\omega_H + i\eta\right)\left(\omega_H + \omega_M\sin^2\theta_k + i\eta\right) - \omega^2}, \tag{2.46}$$

and

$$\kappa_{yx} = \frac{\omega_M\left(\omega - \dfrac{i\omega_M\sin^2\theta_k\sin 2\phi_k}{2}\right)}{\left(\omega_H + i\eta\right)\left(\omega_H + \omega_M\sin^2\theta_k + i\eta\right) - \omega^2}. \tag{2.47}$$

The relaxation rate η is assumed to be $\mathbf{k}-$ dependent.

The $\mathbf{k}-$ dependent magnetic susceptibility tensor $\ddot{\chi}_e(\mathbf{k})$ is generalized to include the uniform mode susceptibility tensor denoted by $\ddot{\chi}_e(\mathbf{k}=0)$ here. It should be noted that the generalized susceptibility tensor may discontinue at $\mathbf{k}=0$, namely,

$$\lim_{\mathbf{k}\to 0} \ddot{\chi}_e(\mathbf{k}) \neq \ddot{\chi}_e(\mathbf{k}=0). \tag{2.48}$$

This problem comes from the magnetostatic approximation.

Similar to FMR theory, the susceptibility tensor also shows a spin wave resonance when the denominator is equal to zero. This gives

$$\omega_k(k,\theta_k) = \sqrt{(\omega_H + i\eta)(\omega_H + i\eta + \omega_M \sin^2\theta_k)}, \tag{2.49}$$

where θ_k is the angle between the wave vector $\mathbf{k}$ and the static internal field $\mathbf{H}_i$. ω_k is a complex frequency. The real part of ω_k is the spin wave excitation frequency while the imaginary part is the decay rate of this excited spin wave in propagation. The spin waves defined by Eq. (2.49) are called magnetostatic spin waves (MS-SW). Due to the θ_k dependence, it generates a band in the format of ω_k versus k. This band is called the MS-SW band.

Figure 2.4 shows the MS-SW band for zero relaxation. The plot shows the spin wave frequency, $\omega_k/2\pi$, in units of GHz, as a function of k, in rad/cm. The band limits are for the θ_k values of 0° and 90°, as indicated. The contours indicate the continuum nature of the band for bulk samples. The specific diagram shown here was computed for $|\gamma|/2\pi = 28$ GHz/T, $\mu_0 H_{\text{ext}} = 0.45$ T (or internal field of $\mu_0 H_i = 0.39$ T), and $\mu_0 M_0 = 0.175$ T. The light line at ω_{em}, obtained for $\varepsilon_r = 10$, is drawn as reference.

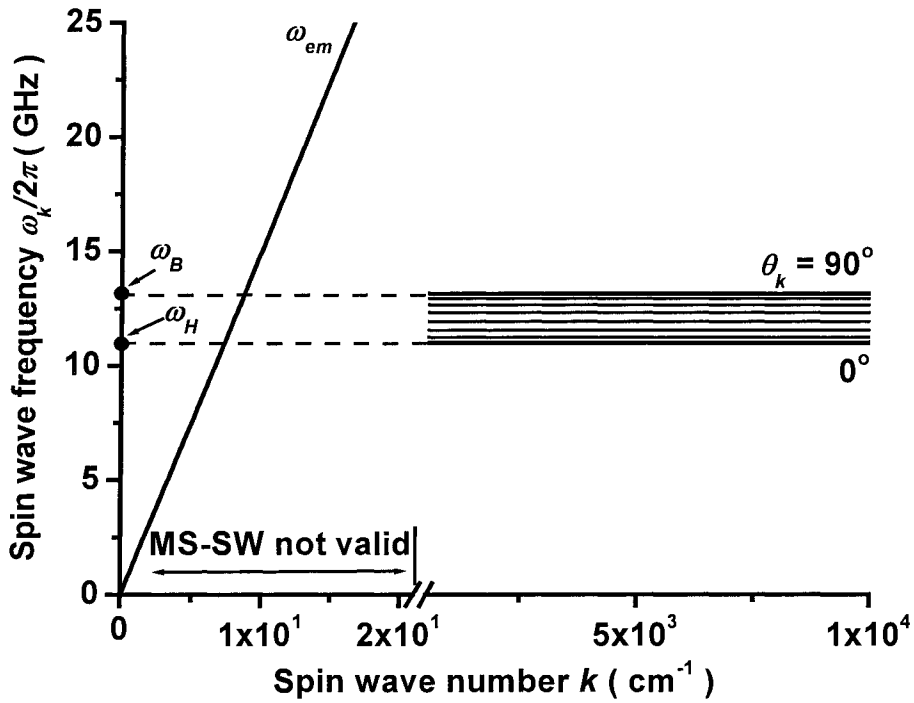

FIG. 2.4. The magnetostatic spin wave (MS-SW) band. The graph shows the spin wave frequency ω_k as a function of the spin wave number k for saturation magnetization $\mu_0 M_0$ =0.175 T, gyromagnetic ratio $|\gamma|/2\pi = 28\,\text{GHz/T}$, external field $\mu_0 H_{\text{ext}}$ =0.45 T, the relaxation rate $\eta = 0$, and spherical demagnetizing factors. The band of contours corresponds to propagation angles (θ_k), relative to the static internal field, that range from 0° to 90°, as indicated. The band was evaluated from Eq. (2.49). The graph also shows the electromagnetic wave dispersion given by ω_{em} with the relative dielectric constant equal to 10. The frequency limits of the MS-SW band, ω_H and ω_B, are indicated on the vertical axis. The horizontal dashed lines extended from the band to these frequency points are intended to emphasize that the MS-SW dispersion is not applicable in this low k regime.

The MS-SW band is formed because of the dipole-dipole energy associated with wave vectors that are not parallel to the vector field $\mathbf{H}_{\text{ext}}$. The band is horizontal because the MS-SW frequency in Eq. (2.49) is only dependent on the spin wave propagation directions, but not on the spin wave number k. The band can be projected to a frequency range indicated by ω_H and ω_B on the vertical axis in Fig. 2.4. This frequency region is

the bulk manifold region. The minimum frequency point at $\omega_k(0,0^o) = \omega_H = |\gamma| \mu_0 H_i$ is due to the Zeeman energy. The top band limit frequency is given by

$$\omega_k(0,90°) = \omega_B = |\gamma| \mu_0 \sqrt{H_i(H_i + M_0)}. \quad (2.50)$$

The MS-SW dispersion is valid under three conditions. First, the spin wave wavelength $\lambda = 2\pi / k$ must be much smaller than dimensions of the sample so that surface dipole fields can be neglected. Second, λ must be much larger than exchange length, typically on the order of 10 nm. The exchange interaction is a quantum mechanical effect and is relevant to the interaction between the adjacent spins on the order of the exchange length. Third, the magnetostatic limit requires that k must be much larger than the corresponding pure electromagnetic wave number k_0. The $k >> k_0$ condition ensures that displacement currents and electromagnetic propagation effects can be neglected. Generally, this dispersion relation is only valid for moderate k spin waves approximately from $10k_0$ to 10^4 rad/cm.

2.2.3. Dipole Exchange Spin Waves

In this section, the exchange interaction is considered. The exchange energy results in an effective exchange field $\mathbf{h}_{ex}$,

$$\mathbf{h}_{ex} = D_0 \nabla^2 \mathbf{m}. \quad (2.51)$$

Here, $D_0 = D / \mu_0 M_0$ where D is the exchange stiffness parameter. The addition of this field to the total field $\mathbf{H}$ modifies all of the equations in Section 2.2.2 by $H_i \rightarrow H_i + \omega_M D_0 k^2$;

$$\omega_k(k,\theta_k)=\sqrt{\left(\omega_H+i\eta+\omega_M D_0 k^2\right)\left(\omega_H+i\eta+\omega_M D_0 k^2+\omega_M \sin^2\theta_k\right)}. \qquad (2.52)$$

This is the well-known dipole exchange spin wave (DE-SW) dispersion relation in the magnetostatic limit. Due to the θ_k dependence, it generates a band in the format of ω_k versus k, which is the DE-SW band.

Figure 2.5 shows this DE-SW band. The plot shows the spin wave frequency, $\omega_k/2\pi$, in GHz, as a function of k in rad/cm. The band limits are for limit θ_k values of $0°$ and $90°$, as indicated. The contours indicate the continuum nature of the band for large samples. The horizontal part of this band is the MS-SW band, as indicated. The parameters for evaluation are the same as in Fig. 2.4. There are two points of reference in the diagram, the light line at ω_{em}, obtained for $\varepsilon_r=10$, and a dashed horizontal line at the nominal operating frequency of 10 GHz.

The curvature of the band contour is due to the exchange interactions. The minimum frequency point at $\omega_{\mathbf{k}}(0,0°)=\omega_H$ is due to the Zeeman energy. The band is formed because of the dipole-dipole energy associated with wave vectors that are not parallel to the vector field $\mathbf{H}$. The top band limit frequency for $k=0$ is given by $\omega_k(0,90°)=\omega_B=|\gamma|\mu_0\sqrt{H_i(H_i+M_0)}$. Both points are indicated on the vertical axis in Fig. 2.5. These frequency limits are the same as in the MS-SW case.

It is important to note the position of the band in Fig. 2.5 relative to the 10 GHz operating point, and observe that there are no spin wave modes that are degenerate with this signal frequency. Note further that the band shifts with field. If H_i is increased, the band will shift to even higher frequencies and the band of DE-SW excitations will move even farther away from the signal frequency.

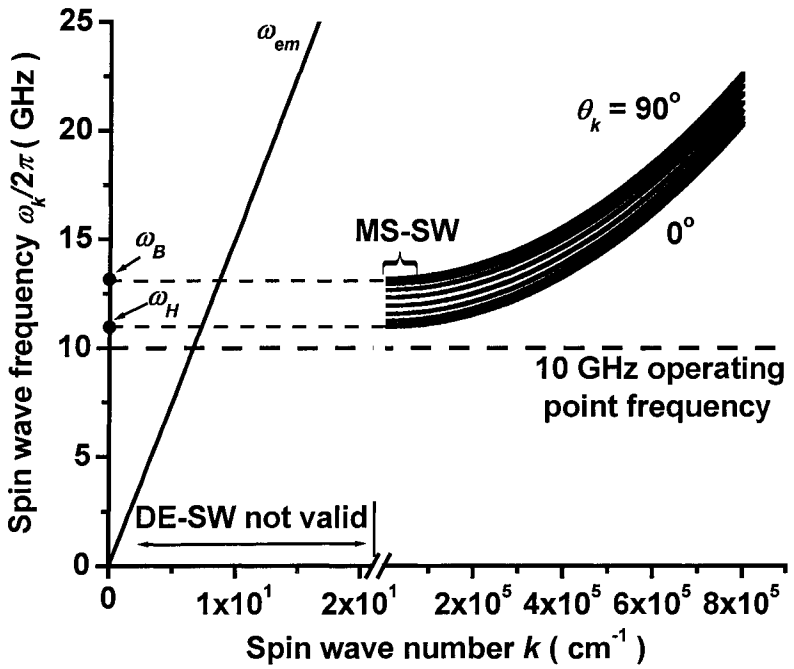

FIG. 2.5. The dipole-exchange spin wave (DE-SW) band in the magnetostatic limit. The graph shows the spin wave frequency $\omega_k / 2\pi$ as a function of the positive real wave number k sphere demagnetizing factors. The band of contours corresponds to propagation angles (θ_k), relative to the static internal field, that ranges from 0° to 90°, as indicated. The band was evaluated from Eq. (2.52) with parameters same as in Fig. 2.4. The graph also shows the electromagnetic wave dispersion given by ω_{em} with the relative dielectric constant equal to 10, and a reference line at the signal frequency of 10 GHz. The low k limit frequencies of the DE-SW spin wave band, ω_H and ω_B, are indicated on the vertical axis. The horizontal dashed lines extended from the band to these frequency points are intended to emphasize that the DE-SW dispersion is not applicable in this low k regime.

Figure 2.5 shows that there are three distinct regions. First, there is no DE-SW excitation below ω_H. Second, in the frequency region between ω_B and ω_H, there are a large number of available modes from low wave number to high wave number. Finally, above ω_B, the curvatures due to the exchange interaction show that only the modes with high wave number are available for excitations.

2.3. Full Spin Wave Bands

This section extends the spin wave dispersion to the low wave number region. The magnetostatic approximation is only valid for spin waves with fairly large wave numbers. For low wave numbers, the magnetostatic approximation is not applicable.

To explore low k spin waves, Maxwell's full equations must be applied. In this case, equation (2.37) can be used to determine the dipolar field. The dispersion relation is still solvable but the derivation is very complicated. Chapter 7 shows a compact derivation using Pauli's matrix (or quaternion) algebra. The derived governing equation for all spin wave excitations is, (Mo *et al*, 2005)

$$H_i = M_0\left[\frac{k^2\left(1+\cos^2\theta_k\right)}{2\left(k^2-k_0^2\right)}-1\right]-Dk^2+\frac{i\eta}{|\gamma|\mu_0} \pm\sqrt{\frac{\omega_k^2}{|\gamma|^2\mu_0^2}+\frac{M_0^2k^4\sin^4\theta_k}{4\left(k^2-k_0^2\right)^2}}=H_{\text{ext}}-\frac{M_0}{3}. \tag{2.53}$$

The above equation is completely general while the last $H_{\text{ext}}-M_0/3$ connection is specific to spherical samples.

It is clear from the form of Eq. (2.53) that a rearrangement of terms will lead to a quartic equation in k^2 and four pairs of roots. It turns out that there are three real root pairs and one imaginary root pair if the frequency ω_k is greater than $\omega_X = |\gamma|\mu_0(H_i+M_0)$. There are two real and two imaginary root pairs for $\omega_k < \omega_X$. It will prove convenient to denote the root pairs as $\pm k_{\text{DEL}}$, $\pm k_{\text{EML}}$, $\pm k_{\text{DEA}}$ and $\pm k_{\text{EMA}}$, where DE stands for dipole exchange spin waves, EM stands for electromagnetic spin waves, L stands for Larmor precession, and A stands for anti-Larmor precession. One

can simply drop the ± sign in these solutions because the sign has been included in the propagation directions. As θ_k is scanned from 0° to 90°, each of these solutions will create a band of allowed excitations, just as the dispersion in Eq. (2.49), creates the bands shown in Fig. 2.6.

For the bands calculated from the real positive $k-$roots of Eq. (2.53), figure 2.6 shows the frequency $\omega_k/2\pi$ in GHz as a function of k in cm^{-1}. All the parameters and field conditions are the same as for Fig. 2.5. In Fig. 2.6, however, there are three bands with real wave numbers, which correspond to the labeled dipole exchange Larmor (DEL) spin waves, electromagnetic Larmor (EML), and electromagnetic anti-Larmor (EMA) excitations, as indicated. As before, the band interior contours indicate the continuum nature of the band for large samples. As in Fig. 4.5, a reference line at $\omega_k/2\pi = 10$ GHz is shown as operating frequency. The manifold limit frequencies ω_H and ω_B from Fig. 2.4 and the new frequency parameter ω_X are indicated along the vertical axis.

It is useful to note several connections between Fig. 2.6 and the DE-SW picture in Fig. 2.5. First, for moderate to large $k-$values, the DEL spin waves correspond closely to the DE-SW spin wave band in Fig. 2.5. The nearly horizontal DEL band limit lines for 10^2 $cm^{-1} < k < 10^4$ cm^{-1} or so correspond to the DE-SW low k band edges at ω_B and ω_H. Additionally, the nearly straight and extremely narrow EMA dispersion band corresponds closely to the light line in Fig. 2.4 described by ω_{em}. The only band not shown in Fig. 2.4 in some form is the EML band. This band starts at the ω_X point that is somewhat above ω_B, and then merges with the DEL light line branch at high frequency. It is important to emphasize that these bands are not new. They are discussed by Lax and

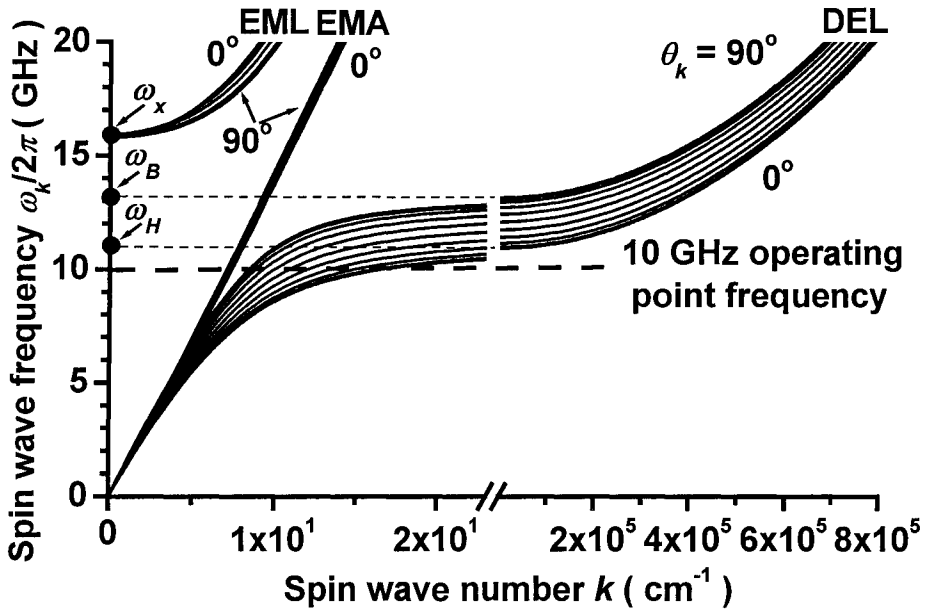

FIG. 2.6. Diagram of the three full spin wave bands for an infinite medium. The graph shows curves for the spin wave frequency $\omega_k / 2\pi$ as a function of the positive real wave number k. The bands of contours correspond to propagation angles (θ_k), relative to the static field, that range from 0° to 90°, as indicated. These curves group into three bands, the dipole exchange Larmor (DEL) band, the electromagnetic Larmor (EML) band, and the electromagnetic anti-Larmor (EMA) band, as indicated. The bands were evaluated from Eq. (2.53) and for the same parameters as used for Fig. 2.5. The graph also shows a reference line at the signal frequency of 10 GHz. The moderate k band limit frequencies ω_H and ω_B from Fig. 2.4 and the new EML limit frequency at $k = 0$, ω_X, are also indicated.

Button (1962). Their detailed characteristics have also been discussed by Patton (1976) for cases in which loss and conductivity effects are included.

2.4. Field Dependence of Spin Wave Manifold

The spin wave dispersion relations are also functions of the static external field H_{ext}. This section shows how the spin wave manifold shifts with H_{ext} and how the

projection of spin wave band into the k versus H_{ext} format gives a full picture of all the degenerate spin waves at a given operating frequency. The following demonstrations of such spin wave manifold shifts and projection are based on the DE-SW band in the magnetostatic limit.

Fig 2.7 shows how the DE-SW band for an isotropic sphere shifts with H_{ext}. The DE-SW band in the ω_k versus k format is plotted in graphs (a) through (e) at five different static external fields. These fields are 0.240, 0.338, 0.357, 0.415, and 0.500 T, as indicated. The situations of these fields are discussed shortly. The line contours are the DE-SW bands generated by a θ_k range from 0° to 90°, relative to $\mathbf{H}_{\text{ext}}$. The typical YIG parameters are used to compute the contours in these graphs based on Eq. (2.52). These material parameters for YIG are (a) $|\gamma|/2\pi = 28$ GHz/T, (b) $\mu_0 M_0 = 0.175$ T, (c) $\mu_0 D = 5.2\times10^{-13}$ T·cm^2, (d) $\varepsilon_r = 10$, (e) zero conductivity, and (f) magnetocrystalline anisotropy field $|\mu_0 \mathbf{H}_A|$=5 mT. The anisotropy field is not used here. As a reference frequency, the dashed line at 10 GHz indicates the operating point frequency.

The fields indicated in Fig. 2.7 are chosen as follows. In graph (a), the field is chosen to make $\omega > \omega_B$ where the frequency ω corresponds to the operating frequency 10 GHz. The field region under the condition $\omega > \omega_B$ is called low field region. The top limit of this region is given by $\omega = \omega_B$. One can solve the corresponding static external field H_{90} from

$$\omega = \omega_B = |\gamma| \mu_0 \sqrt{H_{90}(H_{90} + M_0)}. \qquad (2.54)$$

With the YIG parameters, this field is obtained, namely, $\mu_0 H_{90} = 0.338$ T. The DE-SW

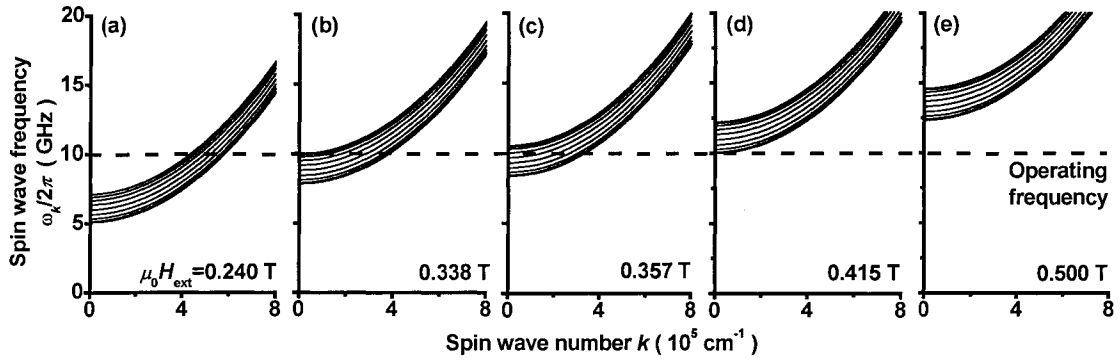

FIG. 2.7. Shifts of dipole exchange spin wave (DE-SW) band for an isotropic sphere with static external field H_{ext}. Graphs (a) through (e) show the spin wave frequency ω_k as a function of spin wave number k at $\mu_0 H_{\text{ext}}$ = 0.240, 0.338, 0.357, 0.415, and 0.500 T, respectively. The line contours are the DE-SW bands generated by a range of the spin wave propagation angle θ_k from 0° to 90°, relative to the static external field. The curves are computed from Eq. (2.52) using the typical polycrystalline yttrium iron garnet parameters listed in the text. The dashed line at 10 GHz indicates the operating frequency.

band at H_{90} is shown in graph (b). The uniform mode limit angle $\theta_u = 90^0$ at $H_{\text{ext}} = H_{90}$ where θ_u is the angle θ_k in the $k \to 0$ limit. When the field H_{ext} increases, the angle θ_u will keep decreasing until H_{ext} reaches the field given by the condition $\omega = \omega_H$. This higher field is denoted by H_{00}. One has $\theta_u = 0°$ at H_{00}. One can obtain, for spheres,

$$H_{00} = \frac{\omega}{|\gamma|\mu_0} + \frac{M_0}{3}. \qquad (2.55)$$

Graph (d) shows the DE-SW band at $\mu_0 H_{00}$=0.415 T for YIG. The field region between H_{90} and H_{00} is known as the bulk manifold in field. Typically, the FMR field is in the bulk manifold region. At 10 GHz, the FMR field is equal to 0.357 T. Graph (c) shows the DE-SW band at FMR. The field region above the bulk manifold is called the high

field region. Graph (e) shows the DE-SW band at a field, 0.5 T, of this region.

The degenerate spin waves in the different field regions can be understood from the graphs in Fig. 2.7. Graph (a) indicates that at low field only the high k spin waves are degenerate with the operating frequency. It has been mentioned that the curvature of spin wave band is due to the exchange interaction. These high k modes have a wavelength on the order of the exchange length. When the field H_{ext} increases, the DE-SW band shifts up in frequency and the wave number k becomes smaller, vice versa. By adjusting H_{ext}, the DE-SW band can be at any position relative to the operating frequency.

The low k degenerate spin waves suddenly emerge when H_{ext} reaches H_{90} as shown in graph (b). The operating frequency is right at the top of the bulk manifold in frequency. Due to the sudden emergence of low k modes, it can be expected that the microwave properties of the magnetic sample should also have abrupt changes below and above H_{90}. One will find in Chapter 3 that the density of relatively low k degenerate spin waves shows a sharp peak at H_{90}.

With a further field increase, the operating frequency moves into the bulk manifold in frequency as in graph (c). The low k and high k spin waves are generally available for excitations and couplings. These degenerate modes are important for the understanding of FMR response since FMR is this case as shown in graph (c). Note that the available k range in DE-SW is narrower at a smaller frequency. The direction of the DE-SW shift with field implies that the available k range and density of states also become smaller when the field H_{ext} keeps increasing and finally vanishes at $H_{\text{ext}} = H_{00}$. The angle θ_u also varies with field. The contours show, in some sense, a uniform

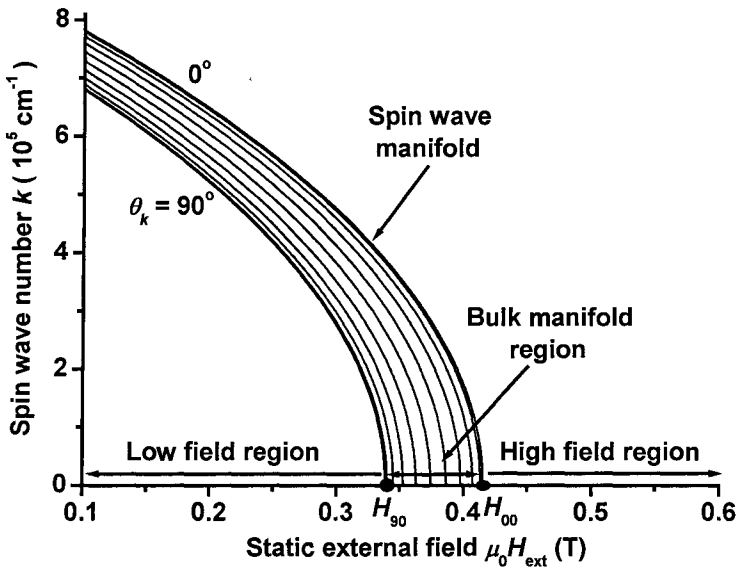

FIG. 2.8. Spin wave number k as a function of static external field H_{ext} at an operating frequency of 10 GHz. The line contour is generated due to variation of the propagation angle θ_k from 0° to 90° is the field projection of the spin wave manifold. H_{90} and H_{00} indicate the bottom and top edges of bulk manifold in field. Three regions, low field region, manifold region, and high field region, are marked. The contour is computed based on Eq. (2.52) using the typical yttrium iron garnet parameters.

distribution of θ_u in the bulk manifold. This means that the angle θ_u is approximately linear with field change.

Above the field H_{00}, both of the low k and high k modes disappear. There are no spin wave states degenerate with the operating frequency. In other word, no DE-SW spin wave can be excited. The operating frequency is fixed in the above frequency shift picture of spin wave manifold.

It proves convenient to project the degenerate spin waves to the (H_{ext} , k) coordinate system for a fixed operating frequency. Figure 2.8 shows such presentation. The available spin wave number is plotted against H_{ext} at the operating frequency of 10

GHz. The frequency manifold edges ω_B and ω_H are converted into the field H_{90} and H_{00}. The three regions in frequency, below ω_H, between ω_B and ω_H, and above ω_B, correspond to the low field region, the bulk manifold region, and the high field region, respectively, as indicated. The spin wave propagation angle θ_k is also indicated at 0° and 90° so that one can directly compare this format with the spin wave manifold in the (k, ω_k) coordinate system. It can be seen that figure 2.8 directly shows the degenerate spin wave modes at all fields from low field to high field.

3. FIELD DEPEDENT LOSS I -- TWO MAGNON SCATTERING

This chapter provides an overview of two-magnon scattering due to inhomogeneities. The microwave loss of ferro- and ferri- magnetic materials primarily depends on the magnetic field. In this chapter and the next chapter, this field dependence is reviewed in details. Two-magnon scattering is an extrinsic, and typically dominant, loss mechanism in bulk ferrites. The field dependence of microwave losses mainly originates from two-magnon scattering. The two-magnon relaxation is hereby outlined in this chapter based on the classical theory.

Section 3.1 presents a brief review of two-magnon scattering and an outline of the inhomogeneities as the scattering sources in polycrystalline ferrites. To show the principles of two-magnon scattering, a classical theory related to scattering due to voids is developed using the simple magnetic susceptibility concept and discussed in Section 3.2. This development serves as a warm-up for Chapter 8, and, in general, for this thesis only a classical formulation is used. The full formulation of classical two-magnon scattering is developed in Chapter 8. Sections 3.3 and 3.4 show the important parameters, namely the inhomogeneity coupling factor and the density of degenerate states, which affect the two-magnon relaxation rate. Finally, Section 3.5 reviews the field dependence of the microwave relaxation due to the porosity scattering and anisotropy scattering.

3.1. Brief Review of Two Magnon Scattering

A magnon is to a spin wave as a photon is to an electromagnetic wave. The classical spin wave parameters (ω , $\mathbf{k}$, $\mathbf{m}(\mathbf{k},\omega)$) and their spin wave dispersion properties can be re-used for the quantum mechanical magnon, but the spin wave energy is continuous and is characterized by spin wave amplitude $|\mathbf{m}(\mathbf{k},\omega)|$. The magnon is a quantum particle with a quantized energy $\hbar\omega_k$ and the total energy is proportional to the number of magnons.

Two-magnon scattering generally refers to the process where one source magnon with (ω, $\mathbf{k}$, $\mathbf{m}(\mathbf{k},\omega)$) transits to another state due to defects, or to an object magnon with a set of different state parameters (ω, $\mathbf{k}'$, $\mathbf{m}(\mathbf{k}',\omega)$). One example of a two-magnon interaction is the FMR relaxation. The FMR relaxation is caused by the transition from a uniform mode magnon (ω, $\mathbf{k}=0$, $\mathbf{m}_{k0}$) to a degenerate non-uniform mode magnon (ω, $\mathbf{k}'\neq 0$, $\mathbf{m}(\mathbf{k}',\omega)$). The source magnon is destroyed and the object magnon is created. The object magnon receives energy from the source magnon and finally decays to a thermal magnon or phonon. The number of the uniform mode magnons decreases because of this scattering process. The two-magnon transition rate simply gives the relaxation rate of the FMR uniform mode due to two-magnon scattering.

Two-magnon scattering from the uniform mode to a degenerate magnon is the well-established relaxation process and is one of the dominant FMR loss mechanisms. Quantitative connections have been made with the FMR linewidth in single crystal and polycrystalline ferrites. It is well established that the scattering sources in these cases consist of various inhomogeneities, such as pores, the randomly oriented

magnetocrystalline anisotropy, grain boundaries, surface pits and roughness.

Theoretical and experimental studies of two-magnon scattering extend as far back as the 1960s. The early studies focus on the scattering in bulk ferrite materials and have been reviewed separately by Sparks (1964) and Patton (1972). It has been found that the most important scattering sources are the porosity and the randomly oriented magnetocrystalline anisotropy. Sparks, Loudon, and Kittel (SLK, 1961) provide a theory to calculate the porosity scattering due to spherical pores. Schlömann (1958, 1969, 1970) has developed an anisotropy scattering theory for large and small magnetocrystalline anisotropy field compared with saturation magnetization in a bulk ferrite. The porosity and anisotropy scattering may result in a fairly large relaxation rate and further modify the spin wave dispersion. In this case, the secondary scattering processes should be accounted for as proposed by Schlömann (1969). The spin wave dispersion bands are also shifted due to the inhomogeneous dipole field generated by pores. This effect on the relaxation rate is proposed by Vrehen (1969) and quantitatively evaluated by Hoeppe (2004).

Most recent two magnon studies focus on two-magnon scattering in thin, especially ultra thin, metallic films. This is due to the renewed interest driven by ultra thin metallic film applications in high density, high speed magnetic recording devices. The boundary conditions significantly change the normal mode dispersion. (Damon and Eshbach, 1961; Harde, 1968; Wolfram and Wames, 1971; Kalinikos *et al*, 1986 and 2004) Two-magnon scattering theory was first applied in thin films by Wigen (1964) to spin wave resonance linewidth data for perpendicularly magnetized permalloy thin films with pinned surface spins. In 1967, Patton and coworkers proposed a two magnon processes to explain FMR

linewidth data as a function of frequency and film thickness for in-plane magnetized films. Sparks (1970), and Hurben and Patton (1998), separately, further applied two magnon concepts to single crystal ferrite films. The key advances that have triggered the modern re-examination of two-magnon scattering in thin films are the often-cited work by Arias and Mills (1999) in which a short wavelength variation in the thickness dependent surface anisotropy field provides a mechanism for scattering. In thin films, and especially in ultra thin films, the spin wave dispersion is severely modified from the bulk relations. There has been further theoretical work by McMichael and Krivosik (2004), and Dobin and Victora (2004), as well as data by Celinski Heinrich (1991), McMichael and co-workers (2003), Heinrich and co-workers (2002), and Woltersdorf and Heinrich (2004).

For ensuing discussions, the following is an examination of scattering sources in polycrystalline YIG as a representative ferrite material. Figure 3.1 shows drawings of microstructures in bulk polycrystalline YIG. In drawings (a) and (b), the gray areas enclosed by dark curves represent the grains while the curves indicate the grain boundaries. Graph (a) specifically shows the voids, indicated by the white areas. Graph (b) shows the random anisotropy field, which varies grain by grain. The arrows indicate the directions of the local anisotropy field. The arrow length does not scale with the intensity of anisotropy field.

Graph (a) shows that voids can have different sizes and irregular shapes. The voids are randomly distributed over the whole sample. The porosity is defined by the ratio of the total void volume to the sample volume. For dense materials, porosity is much smaller than 1. Figure 3.1(a) shows this case and the corresponding porosity may be less

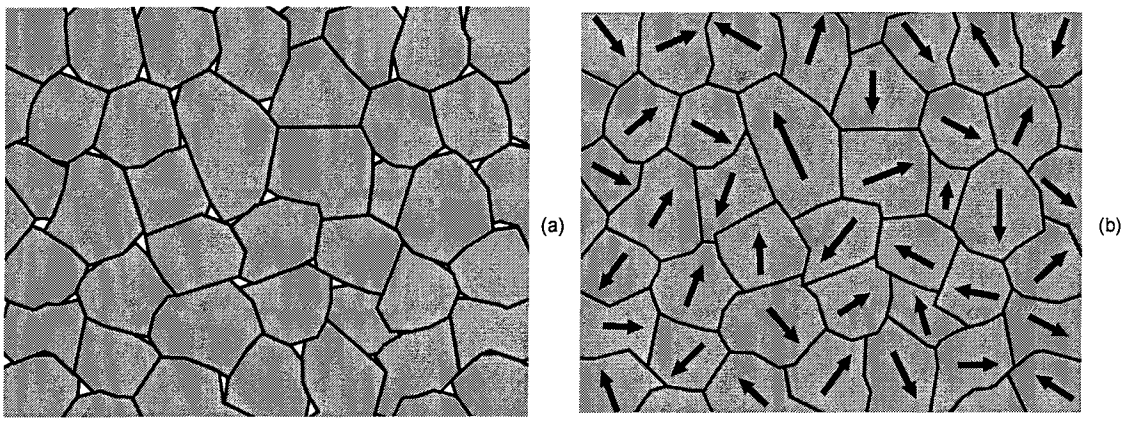

FIG. 3.1. Demonstrations of microstructures in polycrystalline yttrium iron garnet (YIG) bulk. In both graphs (a) and (b), the gray areas enclosed by dark curves represent the grains in materials while the curves indicate the grain boundaries. Graph (a) shows the voids indicated the white areas. Graph (b) shows the anisotropy field varied grain by grains. The dark arrows indicate the directions of these fields. The length does not scale with the intensity of anisotropy field.

than 0.05.

For scattering due to voids, one theory is that the voids effectively generate a non-uniform magnetic field. The other theory states that the void has no magnetization and the net magnetization becomes non-uniform. These two views are equivalent. The total energy is related to this non-uniform field or magnetization and can be expanded as a function of a series of non-uniform mode spin waves or magnon. Once the uniform magnon are excited, this function provides the possibility that some uniform mode magnoms are destroyed and in turn the non-uniform mode spin waves are created or excited. This type of two-magnon scattering is due to porosity and is simply called *porosity scattering.*

Figure 3.1(b) shows the randomly distributed magneto-crystalline anisotropy field. Any single grain is a single crystal of YIG. The anisotropy in YIG is cubic. For different

grains, the anisotropy axes are different and so the anisotropy fields point to different directions, as shown in Fig. 3.1(b). The strength of this field also varies from grain to grain because the anisotropy field also depends on the relative angles between the magnetization and anisotropy axes (see Chapter 7). Graph (b) does not show any porosity. An example of such a material with 0 porosity is hipped YIG. It should be emphasized that the grains in Fig. 3.1(a) also have similar anisotropy fields, but are not sketched.

The anisotropy scattering mechanism is similar to the porosity scattering mechanism. Instead of a dipole field, the anisotropy field directly provides the non-uniform field and contributes to a non-uniform term in the total energy expression. Therefore, the non-uniform mode magnon can be coupled from uniform mode magnon during their propagations and cause a relaxation rate due to random anisotropy. This process is also called *anisotropy scattering*.

In addition to porosity and anisotropy scattering, grain boundaries can also be scattering sources. Qualitatively, the surface of a grain is different from the body. There are two reasons: (1) a single surface spin (or magnetic moment) has fewer neighboring spins and (2) the magnetic ions at the grain boundaries expose to the environment. As a result, the surface of the magnetic material oxidizes more than the body material within the bulk of the sample. This surface significance is only available in a very thin layer called the surface layer. The surface layers produce an extra energy that is absolutely non-uniform. The non-uniform energy induces two-magnon scattering. The related two-magnon process is called *grain boundary scattering*. This process was not quantitatively derived.

In summary, there are three main types of two magnon scattering sources, namely, pores or voids, random orientation of the anisotropy axes within the individual grains, and the grain boundaries themselves. The larger scattering-induced relaxation rates further make the secondary scattering processes (Schlömann, 1969) more important.

3.2. Classical Picture of Porosity Scattering

Nearly all of the two-magnon theories mentioned above, except that by McMichael and Krivosik (2004), are based on quantum theory. However, one usually describes the microwave loss mechanisms with classical physics. Up to now, no special reason has been demanded that quantum mechanics must be used to perform the two-magnon calculations. For this reason, this thesis only uses the classical theory. Additionally, the use of classical theory is consistent with the classical theory discussions in Chapter 2. Chapter 8 provides a general classical theory that uses operators to cover most of the two-magnon calculations. This section demonstrates how to use the classical theory to derive two-magnon relaxation rates due to porosity scattering and shows the general features of two-magnon scattering.

In classical theory, two-magnon scattering from the uniform mode to degenerate magnon states corresponds to the classical scattering from uniform mode spin waves to degenerate spin waves. Although the classical scattering may refer to two waves, it is convenient to call it "two magnon scattering". The uniform mode source spin wave (ω, $\mathbf{k}=0$, $\mathbf{m}(\mathbf{k},\omega)$) scatters into the degenerate object spin wave (ω, $\mathbf{k}\neq 0$, $\mathbf{m}(\mathbf{k},\omega)$) due to the inhomogeneities. The object spin wave takes a part of energy from the source spin wave. The uniform mode energy (or power) can be evaluated by spin wave amplitude.

The energy shows a decay rate due to the lost energy transferred to the object spin waves. This decay rate simply gives the two-magnon relaxation rate for the uniform mode.

The following shows a classical picture of porosity scattering for a simple case as derived with quantum theory by Sparks et al (1961). The relaxation due to surface pits and roughness are similar to the voids (Schlömann and Joseph, 1970). The classical picture of anisotropy scattering is shown in Chapter 8. The following derivation helps introduce the general concepts of two magnon scattering, for example, the coupling factor and the density of degenerate states. It also helps describe how the two-magnon relaxation rate depends on the scattering sources, the spin wave dispersion and the spin wave parameters such as the wave vector and the polarization.

As a starting point, consider only one spherical void at the origin of the coordinate system. This spherical void with a radius of a generates an effective dipole field. The procedure for the consideration of this field has three steps. First, the effective static dipole field modifies the internal static field. Only the z component is modified, however, because the linearized torque equation is only related to the dynamic terms of transverse magnetization components.

$$H_i \to H_i + \frac{M_0 a^3 (3\cos^2\theta - 1)}{3r^3} \tag{3.1}$$

The second term is just the z component of the effective demagnetizing field of the void. This replacement is only applied outside of the void. Second, the void also modifies the dynamic dipole field. The derivation is discussed in Chapter 8. From Eq. (8.48), the dipole field can be considered by the following replacement,

$$\mathbf{h}_d \to \mathbf{h}_d - \frac{a^3 (3\cos^2\theta - 1)}{6r^3}\mathbf{m}. \tag{3.2}$$

Although Equation (8.48) is only for uniform mode, the above replacement has applied to non-uniform modes because the void is very small. Third, the two replacements in Eqs. (3.1) and (3.2) can be made in Eqs. (2.13a) and (2.13b) and are equivalent to one replacement,

$$\omega_H \rightarrow \omega_H + \frac{\omega_M a^3 (3\cos^2\theta - 1)}{2r^3}. \tag{3.3}$$

Equation (3.3) can be written in a Fourier expansion,

$$\omega_H \rightarrow \omega_H + \omega_M \sum_{\mathbf{k}} P(\mathbf{k}) e^{-i\mathbf{k}\cdot\mathbf{r}}, \tag{3.4}$$

where

$$P(\mathbf{k}) = 2\pi V_s^{-1} a^3 (3\cos^2\theta_k - 1)\frac{j_1(ka)}{ka}. \tag{3.5}$$

The following transformation has been made for a finite bulk sample,

$$\frac{V_s}{8\pi^3}\int d\mathbf{k} \rightarrow \sum_{\mathbf{k}} . \tag{3.6}$$

By taking advantage of susceptibility tensor $\ddot{\chi}(\mathbf{k})$ without the two-magnon scattering terms, the equation for spin wave excitations in materials with defects can be separated into a uniform mode excitation $\mathbf{m}(\mathbf{k}=0)$ and non-uniform mode excitations $\mathbf{m}(\mathbf{k}\neq 0)$. For the uniform mode,

$$\ddot{\chi}^{-1}(0)\mathbf{m}(\mathbf{k}=0) + \sum_{\mathbf{k}} P(-\mathbf{k})\mathbf{m}(\mathbf{k}) = \mathbf{h}_p. \tag{3.7}$$

If the pumping field is uniform it has no non-zero $\mathbf{k}$ components, $\mathbf{k}=0$. The uniform mode excitations are from dipole field due to other spin wave modes. Considering only uniform mode excitations,

$$\ddot{\chi}^{-1}(\mathbf{k})\mathbf{m}(\mathbf{k}) + P(\mathbf{k})\mathbf{m}(\mathbf{k}=0) = 0, \text{ if } \mathbf{k} \neq 0. \tag{3.8}$$

The scattering effects are typically treated as a perturbation. This means that the excited non-zero spin waves $\mathbf{m}(\mathbf{k} \neq 0)$ are very small in comparison with the uniform mode spin waves $\mathbf{m}(\mathbf{k} = 0)$.

Several steps are needed to derive the uniform mode spin wave affected by scattering processes. First, the uniform mode is excited without perturbation. Second, a non-zero $\mathbf{m}(\mathbf{k} = 0)$ provides the possibility of scattering from one uniform mode to other non-uniform modes. The scattering process for a specific wave vector according to Eq. (3.8)

$$\mathbf{m}(\mathbf{k}) = -\ddot{\chi}(\mathbf{k})P(\mathbf{k})\mathbf{m}(\mathbf{k}=0). \tag{3.9}$$

Third, as a perturbation, one directly uses this expression for the nonzero $\mathbf{m}(\mathbf{k})$ in Eq. (3.7). This implies that some energy is absorbed by a non-zero $\mathbf{k}$ mode and the absorbed energy comes from the uniform mode spin wave.

$$\left[\ddot{\chi}^{-1}(0) - \sum_{\mathbf{k}} \ddot{\chi}(\mathbf{k})\left|P(\mathbf{k})\right|^2\right]\mathbf{m}(\mathbf{k}=0) = \mathbf{h}_{p0}. \tag{3.10}$$

$P(-\mathbf{k})$ has been replaced by its complex conjugate $P^*(\mathbf{k})$. The above equation implies that two-magnon scattering modifies the uniform mode excitation.

Equation (3.10) is applicable to any kind of spin wave dispersion. In the general form, one can write

$$\ddot{\chi}(\omega_k, \mathbf{k}) = \frac{\omega_M}{\omega_k - \omega_0}\ddot{\mathbf{G}}(\omega_k, \mathbf{k}). \tag{3.11}$$

The tensor $\ddot{\mathbf{G}}(\omega, \mathbf{k})$ depends on which dispersion relation. Note that some dispersion relations, for example, for the magnetostatic cases, do not work for extremely low k.

The tensor function $\ddot{\mathbf{G}}(\omega,\mathbf{k})$ is generally finite. Application of the theorem of residues gives, $(\omega_k-\omega_0)^{-1}\rightarrow 2\pi i\delta(\omega_k-\omega_0)$.

$$\left[\ddot{\chi}^{-1}(0)+\frac{i\eta_{2m}}{\omega_M}\lim_{k\rightarrow 0}\ddot{\mathbf{G}}(\omega_k,\mathbf{k})\right]\mathbf{m}_0=\mathbf{h}_{p0} \tag{3.12}$$

The parameter η_{2m} is

$$\eta_{2m}=\sum_{\mathbf{k}}2\pi\omega_M^2\left|P(\mathbf{k})\right|^2\delta(\omega_k-\omega). \tag{3.13}$$

The physical meaning of η_{2m} is shown as follows.

For consistency with the typical quantum treatment (Sparks, 1964), $\ddot{\mathbf{G}}(\omega,\mathbf{k})$ is used in the low wave number limit. Equation (3.11) should be consistent with the uniform mode magnetic susceptibility, which means the low wave number limit is

$$\lim_{k\rightarrow 0}\ddot{\mathbf{G}}(\omega_k,\mathbf{k})=\frac{1}{\omega_k+\omega_0}\begin{pmatrix}\omega_0 & i\omega_k\\ -i\omega_k & \omega_0\end{pmatrix}. \tag{3.14}$$

This approximation corresponds to the circular polarization approximation made in quantum approach (Sparks, 1961).

One inserts Eq. (3.14) into (3.12) and obtains the uniform mode susceptibility tensor $\ddot{\chi}_{2m}(\mathbf{k})$, which includes two magnon scattering,

$$\ddot{\chi}_{2m}^{-1}=\frac{1}{\omega_M}\begin{bmatrix}\omega_0\left(1+i\dfrac{\eta_{2m}}{\omega_0+\omega}\right) & i\omega\left(1-i\dfrac{\eta_{2m}}{\omega_0+\omega}\right)\\ -i\omega\left(1-i\dfrac{\eta_{2m}}{\omega_0+\omega}\right) & \omega_0\left(1+i\dfrac{\eta_{2m}}{\omega_0+\omega}\right)\end{bmatrix}. \tag{3.15}$$

The FMR condition is given by a zero determinant of $\ddot{\chi}_{2m}^{-1}(\mathbf{k})$, namely,

$$\omega=\omega_0+i\eta_{2m}. \tag{3.16}$$

According to the complex frequency model, the real part is the FMR frequency $\omega = \omega_0$, the same as obtained in Chapter 2. The imaginary part, η_{2m}, is the relaxation rate due to two magnon scattering.

The result of Eq. (3.13) is exactly the same as Sparks' equation (5.14) (Sparks, 1964) if symbol conversions are made. The conclusion can be drawn that the classical porosity and anisotropy scattering theory (see Chapter 8) is equivalent to the quantum scattering theory. The question remains, however, why are these two theories the same? Note that the quantum scattering theory typically starts from Maxwell's equations, which is classical. The quantum theory from the total energy of the magnetization effectively results in the classical torque equation. The spin wave dispersion equations are then derived. This step is the same as that in classical theory. In the quantum approach, the spin waves are further quantized to be magnon. Such a second quantization may only be important for a small number of magnon. In experimental cases, the number of magnon is large. There is hereby no big difference between quantum scattering theory and classical scattering theory. Up to now, the electromagnetic fields have not been quantized in the quantum two-magnon scattering theory. It is an open question whether this quantization makes difference.

One can summarize the validity of Eqs. (3.13) and (3.16). First, these equations are applicable not only to the FMR field, but also to any other static field. The field dependence will be discussed in detail shortly. Second, the validity is based on the low wave number limit of $\ddot{\mathbf{G}}(\omega,\mathbf{k})$. $\ddot{\mathbf{G}}(\omega,\mathbf{k})$ may be different from the uniform mode case because an arbitrary spin wave mode generally has a $\mathbf{k}$-dependent spin wave polarization.

So far, only a single void at the origin has been considered. There are several key

points to be made. First, equation (3.13) is still valid if the void is not at the origin. This is because only the phase in $P(\mathbf{k})$ is changed and vanishes in Eq. (3.13) and the subsequent equations. Second, if there are many voids with different radii, equation (3.13) is applicable for each void with a different value of a and the total relaxation is approximately the sum of all individual void contributions based on the independent scattering model.

The further steps about evaluating η_{2m} from Eq. (3.13) are the same as Sparks' calculations since those are just trivial mathematics. In Eq. (3.13), $\delta(\omega_k - \omega)$ corresponds to the density of degenerate states function shown in Section 3.4. The left part is the coupling factor $C(\mathbf{k})$, which depends on the scattering source. The concept of the coupling factor $C(\mathbf{k})$ is applicable to any other type of two-magnon scattering and depends on the scattering source and scattering mechanisms.

3.3. Coupling Factors

This section provides a description of what affects the intensity of two-magnon scattering. Based on the discussions in the preceding section, the general two-magnon relaxation rate can be written as

$$\eta_{2m}(\omega) = \frac{1}{8\pi^3} \int_{\mathbf{k}\neq 0} C(\mathbf{k}) 2\pi\delta(\omega_k - \omega) d\mathbf{k}. \tag{3.17}$$

For porosity scattering with a spherical void,

$$C(\mathbf{k}) = \frac{4\pi^2 \omega_M^2 a^6}{V_s} (3\cos^2\theta_k - 1)^2 \frac{j_1^2(ka)}{(ka)^2}, \tag{3.18}$$

as shown in Eq. (3.13). The inverse transformation of Eq. (3.5) has been made. Note

that porosity scattering sounds involving the sample volume. This is because the void is within the sample. In most cases, the voids are distributed throughout the sample. The coupling function does not scale with the sample volume, but with the porosity.

For anisotropy scattering (Schlömann, 1969; Chapter 8)

$$C(\mathbf{k}) = \frac{1+19\left(\frac{\omega_H}{\omega_M} + \frac{\gamma\mu_0 Dk^2}{\omega_M} + 0.5\sin^2\theta_k\right)}{155} \cdot \frac{\omega_A^2 16\pi b^3}{\left(1+k^2b^2\right)^2}. \tag{3.19}$$

Here b is the averaged grain size and $\omega_A = |\gamma|\mu_0|\mathbf{H}_A|$. Comparison with Eq. (3.18) shows that the above equation is not related to the sample volume because the anisotropy carriers, namely grains, are randomly distributed over the whole sample.

It is good to take an examination of the $\mathbf{k}-$ dependence of the coupling factors. In porosity scattering, the k dependence can be characterized by a function C_{pk},

$$C_{pk} = \frac{j_1^2(ka)}{(ka)^2} \lim_{ka\to 0}\left[\frac{j_1(ka)}{ka}\right]^{-2} \tag{3.20}$$

The factor of the $k \to 0$ limit is just a $\mathbf{k}-$ independent constant that normalizes this function at $k = 0$. The normalization is convenient for comparison with other coupling factors. It does not, however, affect how the coupling factor depends upon k. This function is basically Fourier transformation of $1/r^3$ in the dipole field generated by the void.

For the case of anisotropy scattering, the k dependence can be determined by the function C_{Ak},

$$C_{Ak} = \left(1+k^2b^2\right)^{-2}. \tag{3.21}$$

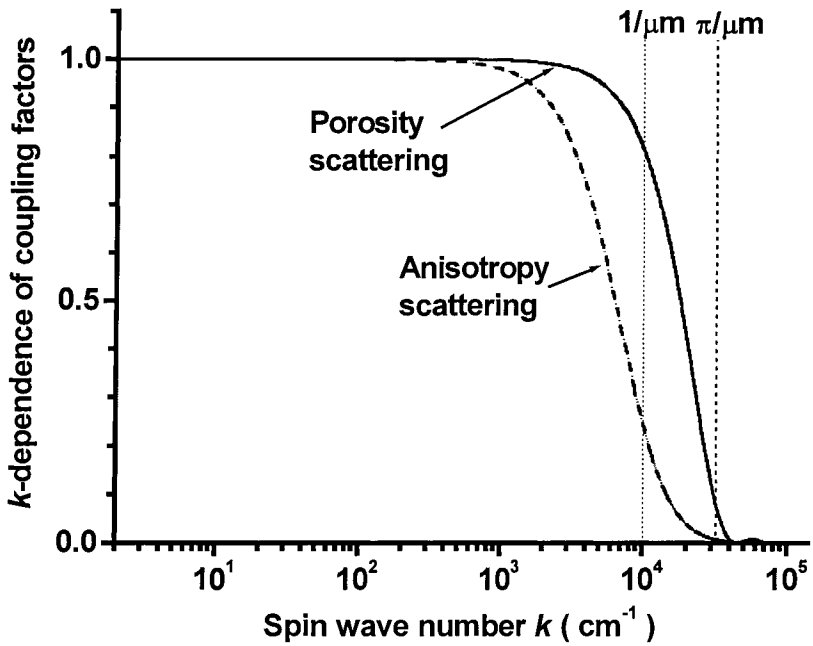

FIG. 3.2. The $k-$dependence of coupling factors as a function of wave number k. The solid curve shows that for porosity scattering and the dashed curve for anisotropy scattering. These two curves are computed using Eqs.(3.20) and (3.21), respectively. Both of pore size and grain size are $1\,\mu m$. The vertical dotted lines show the inverse of and π divided by this size in the horizontal coordinate, as indicated.

The first term in Eq. (3.19) has a fairly weak k dependence. This function comes from the correlation function of the grain distribution.

Figure 3.2 shows these $\mathbf{k}-$ dependence functions as a function of spin wave number k. The solid curve shows C_{pk}, the coupling factor for porosity scattering, and is calculated from Eq. (3.20). The value of the parameter a, the pore size, is 1 μm in this calculation. The dashed curve shows C_{Ak} for the anisotropy scattering and is calculated from Eq. (3.21) with $b = a = 1\,\mu m$. The vertical dotted lines show the positions of $1/a$ and π/a on the horizontal axis.

Both C_{Ak} and C_{pk} are fairly uniform in the low k range, but start to decrease very

fast when k is closer to $1/a$, and become nearly zero when k goes above π/a. The function C_{Ak} decreases at a lower k value than C_{pk} does. Their slopes are similar when they decrease. C_{Ak} also vanishes at a lower k value than C_{pk} does. The k range with non-zero C_{pk} and C_{Ak} values is approximately from 0 to π/a and π/b. There are some very small wiggles in C_{pk} above π/a. These wiggles come from Bessel function.

The coupling factors are one of the important factors that decide the strength of scattering from the uniform mode spin wave to the non-uniform spin waves. What does figure 3.2 mean? There are three important points of interest in Fig. 3.2. First, the uniform mode cannot be scattered to the high k spin waves since the coupling factors vanish very fast near $k = \pi/a$ (or π/b). Second, the spin wave modes with low k values affect somewhat equally the two magnon relaxation rate since the distribution of the coupling factor is fairly uniform in the low k region, for example, at one-tenth of π/a. Third, the spin waves available for scattering have k values in a range that depends the defect size, specifically, the void size for porosity scattering and the grain size for anisotropy scattering. This range is approximately from 0 to π/a (or π/b).

It is now clear why the other factors in Eq. (3.19) are weakly $k-$ dependent. A simple evaluation with typical YIG parameters and at $\mu_0 H_{\text{ext}} = 0.36$ T,

$$\gamma\mu_0 Dk^2/\omega_M \xrightarrow{k=\pi/\mu\text{m}} 0.003 \tag{3.22}$$

and

$$\omega_i/\omega_M = 1.7. \tag{3.23}$$

This means that the Dk^2 term is negligible.

The coupling functions also depend on the propagation directions of spin waves.

For the isotropic spheres discussed here, they are only functions of θ_k, but not of ϕ_k. For porosity scattering, the relation to θ_k can be written as

$$C_{p\theta} = (3\cos^2\theta_k - 1)^2 / 4. \qquad (3.24)$$

This function is Fourier transformation of the angle distribution function, namely, $3\cos^2\theta - 1$, of the dipole field of void. For anisotropy scattering, it is

$$C_{A\theta} \approx \omega_i / \omega_M + 0.5\sin^2\theta_k + 1/19. \qquad (3.25)$$

This function explicitly shows the field dependence of the coupling factor as implied in $\omega_i = |\gamma| \mu_0 (H_{\text{ext}} - M_0 / 3)$ for isotropic spheres.

Figure 3.3 shows these θ_k – dependent functions against θ_k. The solid curve is calculated from Eq. (3.24) and shows the θ_k – dependence $C_{p\theta}$ of the coupling factor for the case of porosity scattering, as indicated. The θ_k value of $C_{p\theta} = 0$ is marked by θ_{dip}. The dashed curve is $C_{A\theta}$ and is for anisotropy scattering calculated from Eq. (3.25) with the parameters $\mu_0 H_{\text{ext}} = 0.36$ T and the typical YIG parameters. These parameters correspond to an FMR frequency of around 10 GHz.

The functions $C_{p\theta}$ and $C_{A\theta}$ represent the θ_k – dependence of the porosity and anisotropy scatterings from the uniform mode to non-uniform degenerate modes with propagation angle of θ_k relative to the external static field. Moving from $\theta_k = 0°$ to $90°$, $C_{p\theta}$ starts from a maximum, gradually decreases down to zero, where $\theta_k = \theta_{\text{dip}}$, and then increases up to one quarter of the maximum. In this view, $C_{A\theta}$ simply increases from minimum to maximum, but never becomes zero.

One can tell from Fig. 3.3 that (1) the porosity scattering shows a dip at

$\theta_k = \theta_{\text{dip}} = \cos^{-1}(1/\sqrt{3})$ and (2) the porosity scattering has a stronger dependence on θ_k than the anisotropy scattering because the change in $C_{p\theta}$ relative to the absolute value is significantly larger than that in $C_{A\theta}$. This means that both of the porosity and anisotropy scatterings are generally anisotropic. The anisotropy feature of porosity scattering comes from the fact that the effective dipole field of a void is anisotropic.

The origin of θ_k dependence of anisotropy scattering is quite complicated. The main origin is the spin wave polarization, which depends on the spin wave propagation. In the porosity scattering calculations, the spin wave polarization is not accounted for, as mentioned in Section 3.2. Schlömann (1969) included the polarization effects, however. Without the considerations of polarization, the anisotropy scattering coupling factor would have no θ_k dependence. This is understandable since the distribution of the magnetocrystalline anisotropy fields is isotropic since the anisotropy axes are randomly distributed, as shown in Fig. 3.1(b). This is why the anisotropy scattering is usually considered to be isotropic.

The spin wave numbers and propagation directions are field dependent, as previously shown in Chapter 2, and pass field dependence to the coupling factors. This occurs because the coupling factors, as shown in the preceding part of this section, are related to k and θ_k. also to ϕ_k generally. It is emphasized here how θ_k is field dependent. Examination of the bulk manifold region under the magnetostatic approximation reveals that one may just use the magnetostatic spin wave band for the non-uniform mode wave numbers for scattering, as shown in Fig. 2.4. This k range is from 0^+ to π over the defect size (void and grain) since the typical defect size is on the

order of a micrometer. Note that the corresponding wavelength for a wave number π / a is relatively small compared with the exchange length that is only important for $k > 10^5$ cm^{-1}. The exchange interaction may be negligible. Second, θ_k is only related to the operating field and frequency. The value of θ_k is generally a function of k. In the MS-SW theory, though, it is simply equal to the $k \to 0$ limit value of $\theta_k(k)$, denoted by θ_u. In the bulk manifold region, however, as obtained from the $\eta \to 0$ case of Eq. (2.47),

$$\cos\theta_u = \sqrt{1 + \frac{H_{\text{ext}} - \frac{M_0}{3}}{M_0} - \frac{\frac{\omega^2}{(|\gamma|\mu_0)^2 M_0}}{H_{\text{ext}} - \frac{M_0}{3}}} \,. \tag{3.26}$$

Equation (3.26) gives the explicit dependence of two-magnon scattering on H_{ext}.

3.4. Density of Degenerate States

The density of degenerate states (DOS) is a basic concept in solid state physics. The DOS is a very useful tool for the contributions due to two magnon scattering, which is a function of and proportional to the DOS. It is usually assumed in the DOS calculations that the allowed plane wave modes are uniformly distributed in $\mathbf{k}$-space. It is then a matter of geometry and the details of the given dispersion relations to obtain the number of modes $\delta n(\omega)$ for a given slice of frequency space from ω to $\omega + \delta\omega$. The relation $\delta n(\omega) = g(\omega)\delta\omega$ then serves as a definition of a DOS function, $g(\omega)$. For bulk, the total DOS function, $g(\omega)$, is defined by the number of the allowed modes in the frequency range of ω to $\omega + \delta\omega$ and the sample volume where $\delta\omega \to 0$, namely,

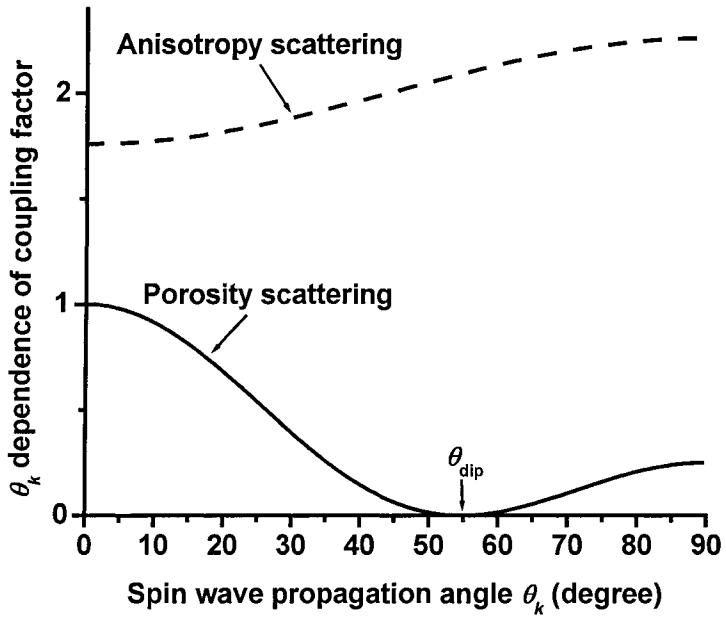

FIG. 3.3. The θ_k – dependence of coupling factors as a function of wave number θ_k. The solid and dashed curves show $C_{p\theta}$ and $C_{A\theta}$ that are defined by and calculated from Eqs. (3.24) and (3.25), respectively. The θ_k value at $C_{p\theta}=0$ is marked by θ_{dip}. The extra parameters for the calculation of the dashed curve are external static field $\mu_0 H_{\text{ext}}=0.36$ T and YIG parameters.

$$g(\omega)=\frac{1}{8\pi^3}\lim_{\delta\omega\to 0}\frac{1}{\delta\omega}\sum_n\left[\int_0^{2\pi}\int_0^{\pi}\int_{k_n(\omega,\theta_k,\varphi_k)}^{k_n(\omega+\delta\omega,\theta_k,\varphi_k)} k^2\sin\theta_k\,dk\,d\theta_k\,d\varphi_k\right]_n. \tag{3.27}$$

The sum parameter n here refers to the index of the available spin wave bands. The function $k_n(\omega,\theta_k,\phi_k)$ is the k solution of the dispersion relations $\omega=\omega_k(k)$ shown in Chapter 2. For isotropic spheres, $k_n(\omega,\theta_k,\phi_k)$ is independent on ϕ_k. The above equation can be simplified to

$$g(\omega)=\frac{1}{6\pi^2}\sum_n\int_0^{\pi/2}\frac{\partial k_n^3(\omega,\theta_k)}{\partial\omega}\sin\theta_k\,d\theta_k. \tag{3.28}$$

It is mentioned that $\delta(\omega_k-\omega)$ is related to the DOS. To understand this, a

comparison is necessary. First, define

$$g'(\omega) = \frac{1}{8\pi^3} \int d\mathbf{k} \delta(\omega_k - \omega) \tag{3.29}$$

The delta function requires $\omega_k = \omega$ with the k solution as $k_n(\omega_k, \theta_k, \phi_k)$,

$$g'(\omega) = \frac{1}{8\pi^3} \sum_n \int d\mathbf{k} \frac{1}{|\partial \omega_k / \partial k|} \delta(k - k_n(\omega, \theta_k, \phi_k)) . \tag{3.30}$$

Use the relation

$$\partial \omega_k / \partial k = \left[\partial k_n(\omega, \theta_k, \phi_k) / \partial \omega \right]^{-1} \tag{3.31}$$

for each branch n and a ϕ_k – independent $k_n(\omega_k, \theta_k)$, and one immediately obtains Eq. (3.28).

These DOS equations are only valid for the wave vectors with a real number. It can, however, also be valid for complex wave vectors if the DOS function is complex if the integral in Eq. (3.28) or (3.29) is over the complex **k**-space. The physical meaning of a complex DOS is quite complicated and depends on how the DOS is used. Simply stated, a complex DOS results in a complex two-magnon relaxation parameter η_{2m}, in which the imaginary part corresponds to an FMR frequency shift and the real part corresponds to the relaxation. The FMR frequency shift is not of interest in this thesis. In most cases, one may somewhat replace ω_k and $\mathbf{k}_n(\omega, \theta_k)$ by its real part as an approximation.

Instead of the total DOS function $g(\omega)$, a density of degenerate states in a unit one-dimension **k** volume, $\rho(k)$ can be used. The relation between them is

$$g(\omega) = \sum_n \int_{\substack{\text{available} \\ k \text{ range}}} \rho(k) dk . \tag{3.32}$$

The integral is over the available k range for the scattering states. This k range depends on the spin wave bands. Based on this, $\rho(k)$ can be derived from Eq. (3.29)

$$\rho(k) = \frac{k^2}{2\pi^2} \int_0^{\pi/2} d\theta_k \sin\theta_k \delta(\omega_k - \omega). \tag{3.33}$$

In this case, $\cos\theta_k$ or θ_k is solved for $\omega_k = \omega$, which gives a solution in terms of $\cos\theta_{kn}$ for the nth spin wave band.

$$\rho(k) = \sum_n \frac{k^2}{2\pi^2} \frac{1}{|\partial\omega_k / \partial\cos\theta_{kn}|}. \tag{3.34}$$

In the magnetostatic limit, $\partial\omega_k / \partial\cos\theta_{kn}$ is approximately proportional to $\cos\theta_{kn}$. Using the partial DOS function $\rho(k)$, the two magnon scattering can be written as

$$\eta_{2m} = \int_{\substack{\text{available} \\ k \text{ range}}} dk \rho(k) C(\mathbf{k})|_{\theta_k = \theta_{kn}}. \tag{3.35}$$

The DOS functions $g(\omega)$ and $\rho(k)$ are related to the spin wave dispersion, which is field dependent. Generally, the DOS functions are also field dependent. One can therefore write them as $g(\omega, H_{\text{ext}})$ and $\rho(k, H_{\text{ext}})$ respectively. Figure 3.4 shows $g(\omega, H_{\text{ext}})$ for low k modes at 10 GHz and $\rho(k, H_{\text{ext}})$ and at 100 cm^{-1} as a function of H_{ext}. In the calculations of $g(H_{\text{ext}})$, only the spin waves with $0 < k < \pi/\mu\text{m}$ are accounted for. The solid curves in graphs (a) and (b) are, respectively, for $g(H_{\text{ext}})$ and $\rho(H_{\text{ext}})$. These curves are computed based on the dipole exchange spin wave (DE-SW) in the magnetostatic limit. The parameters are the typical parameters for polycrystalline YIG. The field limits of the bulk manifold region are indicated by H_{00} at $\theta_u = 0°$ and H_{90} at $\theta_u = 90°$.

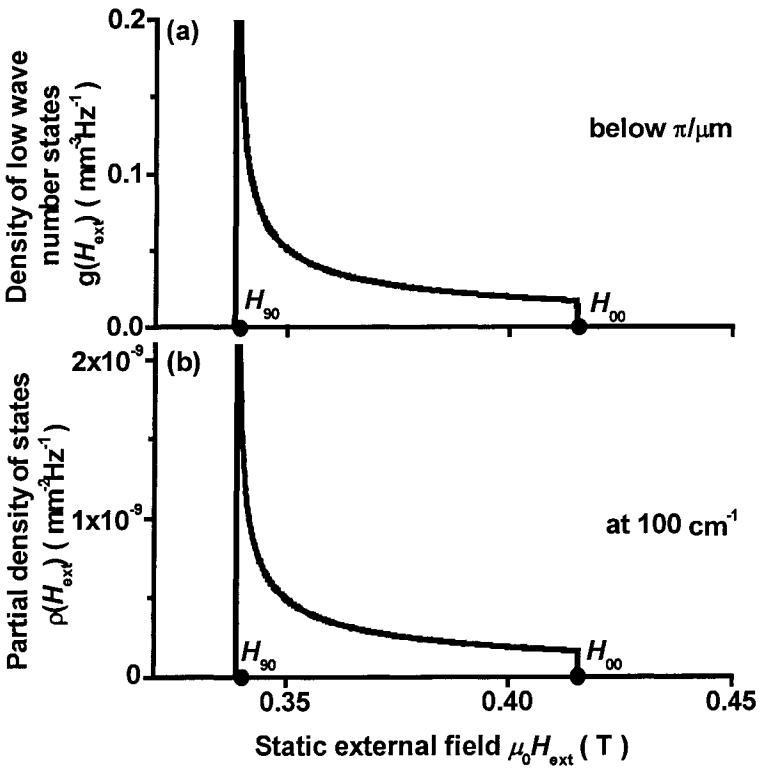

FIG. 3.4. Functions of Density of degenerate states (DOS) against static external fields H_{ext}. The solid curve in graph (a) shows the total DOS function $g(H_{\text{ext}})$ with low wave numbers below $\pi/\mu\text{m}$ as indicated. That in graph (b) shows the partial DOS function $\rho(H_{\text{ext}})$ at 100 cm^{-1}. These functions are defined in the text. The bulk manifold edges are indicated by H_{00} and H_{90}. These DOS curves are calculated using based on the dipole exchange spin wave band in the magnetostatic limit. The parameters for the calculations are the YIG parameters and an X-band operating frequency of 10 GHz.

The reasons for the choice of wave numbers should be emphasized. In Graph (a), $\pi/\mu\text{m}$ is used for the cutoff wave number. This is because Fig. 3.2 shows the cutoff wave number is π divided by the defect size (e.g. void and grain) and the typical defect size is on the order of micrometer. In Graph (b), the specified wave number is chosen to be a small wave number value of 100 cm^{-1}. The particular reasons for this choice is that, (a) the magnetostatic DE-SW band is only valid for a relatively large wave number

compared with electromagnetic wave number and (b), the pure electromagnetic wave number for YIG is around 7 cm^{-1} at 10 GHz.

The DOS functions $g(H_{ext})$ and $\rho(H_{ext})$ have the similar dependence on the static external field. $g(H_{ext})$ somewhat scales with $\rho(H_{ext})$. At fields below H_{90}, the DOS functions are zero in most of this region, nonzero only near H_{90}, and show a sharp increase close to H_{90}. When the field moves into the bulk manifold region, the DOS functions show large values and a relatively gradual decrease up to the top field of the bulk manifold. The DOS functions abruptly go to zero as H_{ext} moves past H_{00}.

How come the total DOS function scale with the partial DOS function? Note that the total DOS function is an integral of the partial DOS function over the available k range for two magnon scattering. The highest value of this range is $\pi/\mu m$. Based on the DE-SW dispersion band (see Chapter 2), the available k range is from 0^+ to $\pi/\mu m$ in nearly all of the bulk manifold. Only in an extreme narrow field regions close to H_{00} and H_{90} are the maximum or minimum available k value different. Therefore, the integral over k makes nearly no difference in the field dependence of the two DOS functions.

Figure 3.4 shows that the DOS functions are field dependent. At high fields, the DOS functions are zero because the DE-SW band shifts up above the operating frequency 10 GHz, and there are no available spin wave modes. In the manifold region, the spin wave propagation angle θ_k changes with field. Since only the relatively low wave number is considered, the exchange interaction does not make big difference and θ_k is approximately equal to a value of θ_u. From H_{90} to H_{00}, θ_u changes from 90° to 0°.

This makes the DOS functions approximately track the inverse of the cosine of θ_u (or H_{ext}), according to Eq. (3.34). At low fields, only the extremely high k modes are available. They are not considered in the above calculations. At low field, the DOS functions are hereby zero, similar to the high field region.

3.5. Field Dependent Relaxation Rate

It has been demonstrated that the coupling factors and the DOS functions depend on k, θ_k, and H_{ext}. The wave vector parameters k and θ_k are also a function of H_{ext} as shown in Fig. 2.8. Therefore, the two-magnon relaxation rate is field dependent. This section discusses the field dependence of the porosity and anisotropy scattering mechanisms.

From Eq. (3.13), the relaxation due to the porosity scattering is approximately,

$$\eta_{2m} \approx p \cdot \frac{\pi\omega_M \left(3\cos^2\theta_u - 1\right)^2}{4\cos\theta_u} \cdot \frac{\omega}{\omega_H}, \tag{3.36}$$

where p is the porosity. Equation (3.36) is from Sparks (1964). There are two main approximations in the derivation of Eq. (3.36). First, θ_k is replaced by θ_u because the difference between θ_k and θ_u is very small for low wave numbers. The parameter θ_u is only meaningful in the bulk manifold region. Outside the manifold, the porosity has no contribution to the relaxation rate. Second, the maximum wave number for the degenerate spin waves is much bigger than π / a. This approximation is valid in the most of bulk manifold region, but not near H_{00}.

Equation (3.36) is only for spherical voids. However, the voids are not generally

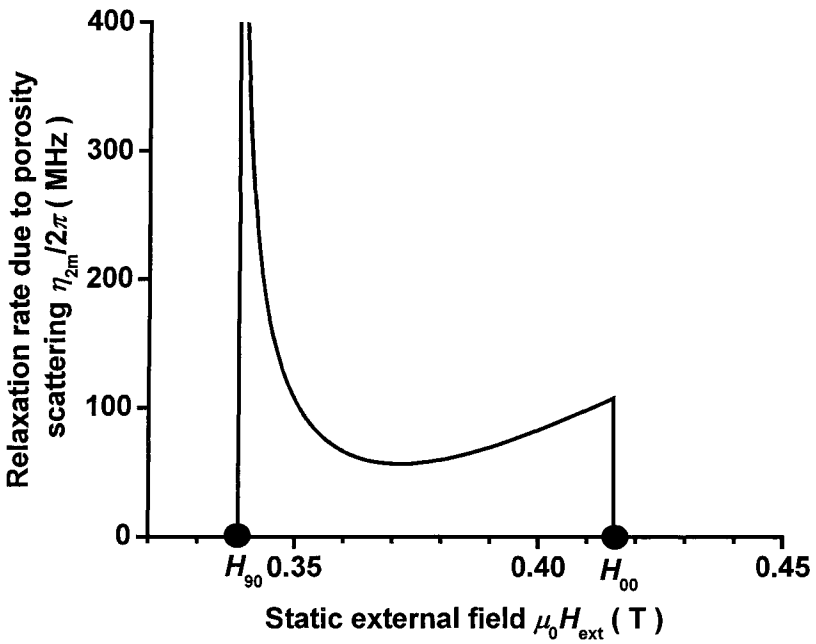

FIG. 3.5. Relaxation rate due to the porosity scattering in an isotropic sphere with a porosity of $p = 0.01$ at 10 GHz. The relaxation rate is plotted as a function of static external field H_{ext}. The solid curve indicates the relaxation rate that is computed from Eq. (3.37) using the yttrium iron garnet (YIG) parameters listed in Section 2.5. The top and bottom of the bulk manifold are indicated by H_{90} and H_{00}.

spherical. The irregularly shaped voids have very complicated dipole fields. Seiden and Sparks (1965) modified Eq. (3.36) by taking into account some of the features of elliptical voids. Equation (3.36) is replaced by

$$\eta_{2m} \approx p \cdot \frac{\pi\omega_M \left[\left(3\cos^2\theta_u - 1 \right)^2 + 1.6 \right]}{16\cos\theta_u} \cdot \frac{\omega}{\omega_H} . \tag{3.37}$$

The number 1.6 is just the average value of $(3\cos^2\theta_u - 1)^2$ over a range from $\cos\theta_u = 0$ to 1.

Equation (3.37) shows that the porosity scattering is only field and frequency dependent, but void size independent. Figure 3.5 shows the calculated two-magnon

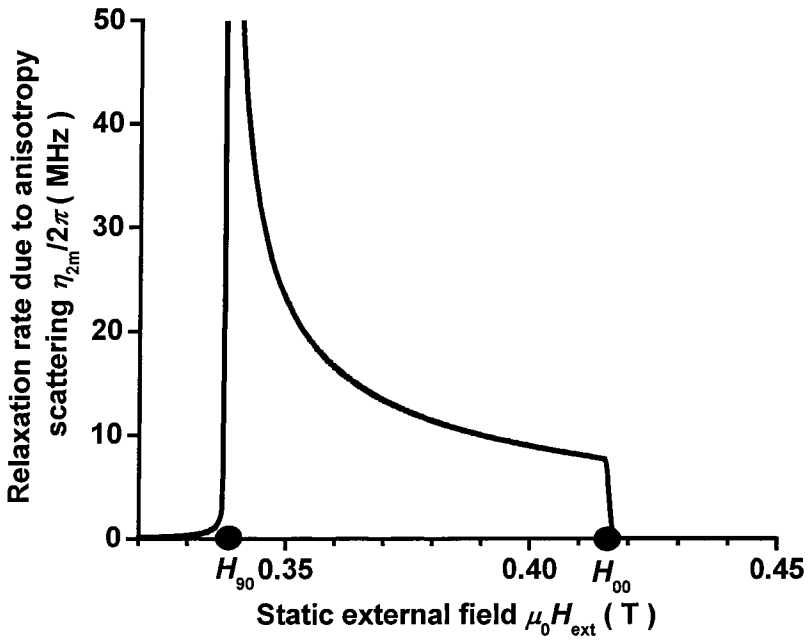

FIG. 3.6. Relaxation rate due to the anisotropy scattering in a polycrystalline yttrium iron garnet (YIG) sphere at 10 GHz. The relaxation rate is plotted as a function of static external field H_{ext}. The solid curve indicates the relaxation rate that is computed from Eqs. (3.17) and (3.19) using the YIG parameters and an averaged grain size of 8 μm. The top and bottom of the bulk manifold are indicated by H_{90} and H_{00}.

relaxation rate η_{2m} as a function of H_{ext} at 10 GHz. The solid curve indicates the relaxation rate η_{2m}. The calculations are based on Eq. (3.37) for an isotropic YIG sphere with a porosity of $p = 0.01$. The top and bottom of the bulk manifold region are indicated by H_{90} and H_{00}, respectively.

Figure 3.5 illustrates four points regarding the field dependence of the relaxation rate due to porosity scattering. First, the porosity scattering does not contribute to the relaxation rate outside the bulk manifold region. Second, the in-manifold relaxation rate shows a sharp peak at H_{90}. This peak originates from the density of states shown in Fig. 3.4. It can also be understood based on Eq. (3.37). At H_{90}, the top of the manifold

region, $\theta_u = 90°$ (see Fig. 2.8) and the denominator in Eq. (3.37) becomes zero. Third, there is a dip in the in-manifold relaxation rate. This dip, known as "porosity dip", comes from the coupling factor near $\cos\theta_u = 1/\sqrt{3}$. This angle corresponds to an effective static external field, H_{dip},

$$H_{\text{dip}} = \sqrt{\left(\frac{\omega}{\gamma\mu_0}\right)^2 + \left(\frac{M_0}{3}\right)^2}\,. \tag{3.38}$$

The field is 0.36 T for YIG at 10 GHz. This field is slightly different from the minimum of the dip in Fig. 3.5. This is because the relaxation rate near H_{dip} is also related to the field dependent DOS function. Finally, the relaxation rate at the FMR position is also shown at 0.357 T in Fig. 3.5. One can obtain $\eta_{2m}/2\pi = 73$ MHz at FMR from Eq. (3.37).

The anisotropy scattering is demonstrated in Fig. 3.6. The computed relaxation rate η_{2m} due to the anisotropy scattering terms is plotted as a function of H_{ext} at 10 GHz, and is indicated by the solid curve. These anisotropy scattering relaxation rates are numerically evaluated using Eqs. (3.17) and (3.19) for a polycrystalline YIG sphere with an average grain size 8 μm. The value 5 mT is used for the magnetocrystalline anisotropy field, $|\mathbf{H}_A|$. The top and bottom of the bulk manifold are indicated by H_{90} and H_{00}.

The relaxation rate due to anisotropy scattering has nearly the same field dependence as the DOS functions. This is because the coupling factor is of weak dependence on the spin wave propagation angle θ_k and then the field H_{ext}. At H_{90}, the relaxation rate is slightly different from the low k DOS functions. The high k states are

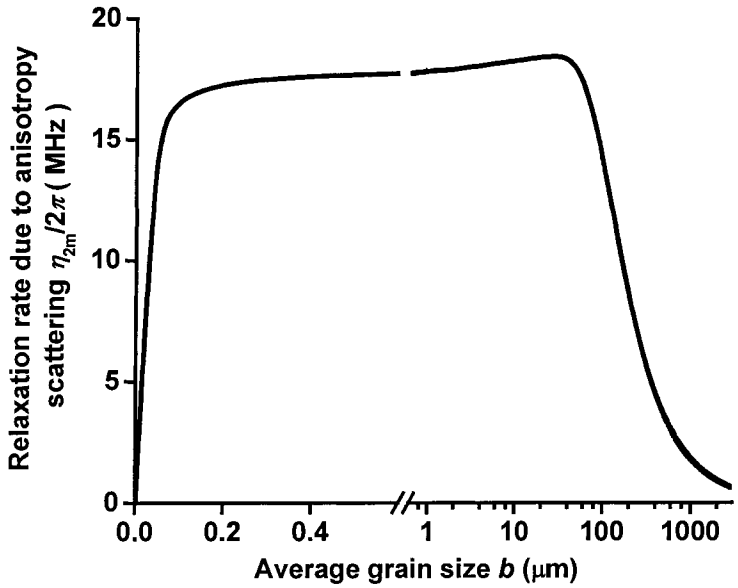

FIG. 3.7. Ferromagnetic resonance relaxation rate due to the anisotropy scattering in a polycrystalline yttrium iron garnet (YIG) sphere at 10 GHz. The relaxation rate is plotted as a function of the average grain size b. The solid curve indicates the relaxation rate that is computed from Eqs. (3.17) and (3.19) using the YIG parameters and an FMR field.

neglected in the DOS calculations in Fig. 2.5. On the other hand, the high k contributions have been accounted for in the numerical evaluation of the anisotropy scattering relaxation. These high k modes contribute to the small tail below H_{90}, as shown in Fig. 3.6.

The anisotropy scattering is also a function of grain size. Figure 3.7 shows the relaxation rate due to the anisotropy scattering terms as a function of the average grain size at the FMR field and 10GHz. The solid curve shows the calculated rates due to the anisotropy scattering terms. The average grain size is varied, but the static external field is fixed at the FMR field 0.357 T. The evaluation procedure and parameters are the same as in Fig. 2.6 where the average grain size is fixed. The region below the break in the horizontal coordinate shows the relaxation rate with a small grain size in a linear scale.

Above the break, it's plotted in the logarithmic scale.

Figure 3.7 illustrates three key points for anisotropy scattering. First, the relaxation rate quickly vanishes with increasing grain size above 40 μm. This is consistent with the results of single crystals that have no anisotropy scattering. A sample with a large grain size can be viewed as a single crystalline sample with a grain size equal to the sample volume. Second, the scattering induced relaxation also vanishes in the small grain size limit. In Fig 3.7, the drop at the small grain size limit starts at around 0.1 μm. This size is on the order of the exchange length. The coupling factor scales with the grain size in small grain size limit (see Eq. (3.19)). The relaxation rate hence decreases for a smaller average grain size. Third, the relaxation rate is nearly constant for grain sizes in the range form 1 μm to 50 μm where the first and the second tendencies are compensated.

4. FIELD DEPEDENT LOSS II – EFFECTIVE LINEWIDTH CONCEPT

Effective linewidth is the field dependent relaxation rate in field units. This chapter provides an overview of the effective linewidth concept, measurement technique, and the previous measurement results. Section 4.1 introduces the effective linewidth concept to characterize the field dependent loss and gives a big picture of effective linewidth. Section 4.2 describes the effective linewidth measurement principles based on the conventional effective linewidth technique. Section 4.3 provides a brief review of the previous effective linewidth measurements and the remaining problems.

4.1. Big Picture of Effective Linewidth

The traditional ferromagnetic resonance (FMR) linewidth ΔH only provides a measure of the loss rate at the FMR field. It has been shown in Chapter 3 that the uniform mode relaxation rate is field dependent especially due to two-magnon scattering. The FMR linewidth is inappropriate to evaluate the field dependent relaxation rate since the FMR field is fixed for a given operating frequency. In the FMR measurements, it is impossible to separate the frequency dependence and field dependence of the FMR linewidth.

The effective linewidth provides a good measure of the field dependent microwave

damping or relaxation of FMR and has been used in a wide range of ferro- and ferri-magnetic materials for over four decades. The effective linewidth parameter ΔH_{eff} simply expresses the uniform mode relaxation rate η of the FMR uniform mode in field units through the connection

$$\Delta H_{\text{eff}}(H_{\text{ext}}) = \frac{2\eta(H_{\text{ext}})}{|\gamma|\mu_0}. \tag{4.1}$$

Equation (4.1) is specifically for isotropic spherical samples. It is the relaxation rate that is field dependent, while ΔH_{eff} just gives this parameter in recognizable units. The gyromagnetic ratio is also treated as field dependent. In the effective linewidth picture, the FMR linewidth is just the effective linewidth at the FMR field H_{FMR},

$$\Delta H = \Delta H_{\text{eff}}(H_{\text{FMR}}). \tag{4.2}$$

As mentioned in Chapter 1, there are a lot of microwave devices which operate in the off resonance region such as isolator, circulator, and phase shifter. The effective linewidth measures the off resonance microwave losses of these devices while the FMR measurements only characterize the loss at FMR field. The physical origins of effective linewidth provide the directions to fabricate the low loss materials for microwave applications.

The origins of effective linewidth are complicated, however. It has been known that two-magnon scattering in addition to the intrinsic loss is an important extrinsic loss mechanism for ferrite materials. Figure 4.1 shows a big picture of the known contributions to the effective linewidth ΔH_{eff} or the uniform mode relaxation rate η. The plots in Fig. 4.1 are not from real measurements or calculations but just sketched to show the basic features of effective linewidth. The solid curve in Graph (a) shows ΔH_{eff}

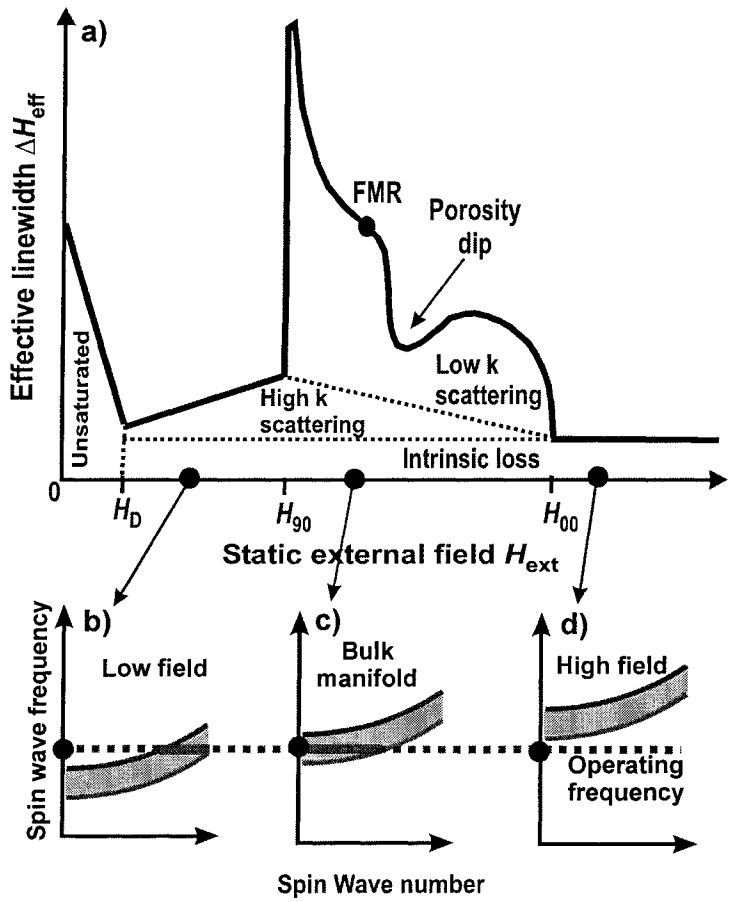

FIG. 4.1. Big picture of effective linewidth ΔH_{eff}. Graph (a) shows ΔH_{eff} as a function of static external field H_{ext}. H_{90} and H_{00} are the edges of bulk manifold. The solid curve stands for the total effective linewidth. The ferromagnetic resonance (FMR) linewidth and the dip due to the porosity scattering are indicated on the effective linewidth curve. The dashed lines separate these contributions as indicated. "Unsaturated" indicates the magnetization is not saturated. Above the demagnetization field H_D, three contributions are indicated, that's, the low wave number (k) scattering, the high k scattering, and the intrinsic loss. As indicated, graphs (b), (c), and (d) show the magnetostatic dipole exchange spin wave band at three representative fields above H_{00}, inside bulk manifold, and below H_{90}, respectively. These graphs are in the format of spin wave frequency versus spin wave number. The shaded areas indicate the spin wave band. The dashed line cross these three graphs shows the operating frequency.

as a function of static external field H_{ext}. The FMR linewidth is just a point in this curve, as indicated. A dip due to the porosity scattering is also indicated. With the dashed lines,

the contributions to effective linewidth are separated. These contributions include the low k scattering, the high k scattering, and the intrinsic loss. For fields below H_D, the magnetization is not saturated as indicated by "Unsaturated". H_{90} and H_{00} are the edges of bulk manifold.

In order to understand the low and high k scatterings, the magnetostatic dipole exchange spin wave (DE-SW) band in the format of ω_k versus k is also plotted at three representative fields in the high field region above H_{00}, inside bulk manifold, and in the low field region below H_{90}, respectively. The shading areas in graphs (b), (c), and (d) indicate these bands. The spin wave manifolds shift with the field H_{ext}. The operating frequency plays a role of a reference frequency indicated by a common dashed line for graphs (b), (c), and (d).

The contributions to effective linewidth vary with the field range:

(1) High Field

In the high field region above H_{00}, only the intrinsic loss contributes. The intrinsic loss is defined as the total magnetic loss in a perfect single crystal material. For yttrium iron garnet (YIG), the intrinsic loss mainly comes from four magnon scattering and magnon-phonon scattering. The intrinsic loss is usually considered to be field independent as indicated by a horizontal line. Only the intrinsic loss should exist in single crystals and the effective linewidth is hereby equal to the single crystal FMR linewidth.

Graph (d) shows the situation of spin wave band in the high field region. At high field, the moderate-k spin wave band is shifted up in frequency, there are typically no

moderate k spin waves degenerate with the pumping frequency, the two magnon scattering contribution to the losses is disallowed, and the relaxation rate for the far-off-resonance driven mode should be field independent, small, and on the order of single crystal linewidths. This is why the high field effective (HFE) linewidth has typically been taken as a measure of the intrinsic losses, even in highly inhomogeneous ferrite materials.

This is not the case found experimentally, however. (Patton, 1970; Vrehen *et al*, 1970) Even though it is usually much smaller than typical FMR linewidths, the HFE linewidth in polycrystalline yttrium iron garnet, for example, is at least several times larger than single crystal linewidths, and it is also found to depend on the microstructure of materials. In addition, HFE linewidth data for polycrystalline ferrites generally show a pronounced tail that extends very far out in field above the manifold region.

(2) Bulk Manifold

In the bulk manifold region, there are three contributions to effective linewidth, namely, the intrinsic loss, the low k scattering, and the high k scattering. When the field gradually decreases from high field and moves into the manifold region, the effective linewidth typically shows an abrupt change at H_{00}. The in-manifold shape is fairly complicated and depends on the microstructure of the sample. Typically, the low k scattering dominates. This is why in Graph (a), most of the in-manifold effective linewidth tracks the density of low k degenerate states as shown in Chapter 3. In the porous materials, a dip may show up due to the porosity scattering since the coupling factor has a dip at $\cos\theta_u = 1/\sqrt{3}$ or at H_{dip}. When the field moves down out of the

manifold, the effective linewidth shows a very sharp drop at H_{90}. This implies that the in-manifold effective linewidth has a different dominant loss origin from the low field region. A straight line is used for the high k scattering that, however, may not be a linear function of field.

The position of the DE-SW band relative to the operating frequency is shown in graph (c). At the bulk manifold fields, the operating frequency crosses over the spin wave manifold. Note that the spin wave band in the low k region has a very small curvature. This means that there is a large number of low k degenerate spin waves and the density of these low k states is fairly large. The cutoff value of low wave number depends on the defect size. For the micrometer defects, the k range of the low k degenerate spin wave is approximately constant in the bulk manifold region.

The available low k degenerate spin waves provide the possibilities of the low k two-magnon scattering. The scattering source can be porosity and random magnetocrystalline anisotropy because the typical voids and grain sizes are on the order of micrometer. The anisotropy scattering is weakly dependent on θ_k and then the contribution to ΔH_{eff} nicely tracks the density of the low k degenerate states. The porosity scattering is different. The coupling factor for the porosity scattering shows the θ_k - dependence of $(3\cos^2\theta_k - 1)^2$. The porosity contribution to ΔH_{eff} results in a dip approximately inside bulk manifold.

From graph (c), it's worth to emphasize that some of high k spin waves degenerate with the uniform mode. The high k two-magnon scattering may also make some contributions to the in-manifold effective linewidth. The high k scattering was not noticed previously. The possible reason is that the contribution of the high k scattering

is fairly small and buried in the typically dominant porosity and anisotropy scattering. When the field decreases, the spin wave manifold shifts down in frequency and the density of high k states also decreases. It can be expected that the high k scattering contributes less at the higher fields.

(3) Low Field

In the low field region but above H_D, only the intrinsic loss and the high k scattering contribute to ΔH_{eff} while the low k scattering is not available in this picture. The low field effective (LFE) linewidth is generally higher than the HFE linewidth because there is an extra high k scattering that is not available in the high field region. As mentioned above, the high k scattering is a small effect. Hence the LFE linewidth is typically much smaller than the in-manifold linewidth. No theoretical calculation of the high k scattering was done previously.

Graph (c) gives more details about the high k scattering. At low fields, the spin wave manifold shifts down in frequency so that all the low wave number modes are below the operating frequency. Only are the high k spin waves degenerate with the uniform modes. The DOS somewhat scales with k^2 and the high k DOS is higher at lower field. One might think that the contribution of the high k scattering would be larger at lower field. This is not the case in the real measurement. The possible reason lies in the coupling factor that has a very fast drop when the wave number is larger than the inverse of the defect size.

(4) Ultra-low Field

Below H_D, the sample is not saturated. In this case, the domain wall and the large non-uniform distribution of magnetization give a fairly large loss. This is out of the scope of this thesis and will not be discussed any more.

4.2. Measurement Principles of Effective Linewidth

In the conventional effective linewidth technique, the sample is mounted in a microwave cavity and the cavity resonance parameters are measured. These parameters for the measurements of magnetic susceptibility are cavity center frequency ω_c and quality factor Q_c. The cavity perturbation theory is used to extract the real part χ' and the imaginary part χ'' from ω_c and Q_c. The effective linewidth is further determined from χ' and χ''.

Section 4.2.1 describes the effective linewidth spectrometer system constructed at Colorado State University (CSU). Section 4.2.2 shows how to measure the cavity parameters for the further determination of effective linewidth. In Section 4.2.3, the cavity perturbation theory is then outlined. This theory connects the magnetic susceptibility with the cavity resonance parameter. Section 4.2.4 describes how to determine the calibration constants and the HFE linewidth based on the high field approximation of susceptibility. Section 4.2.5 shows an analytical solution of the effective linewidth from the magnetic susceptibility.

4.2.1. Effective Linewidth Spectrometer System at Colorado State University

McKinstry (1989 and 1991) had constructed an effective linewidth microwave

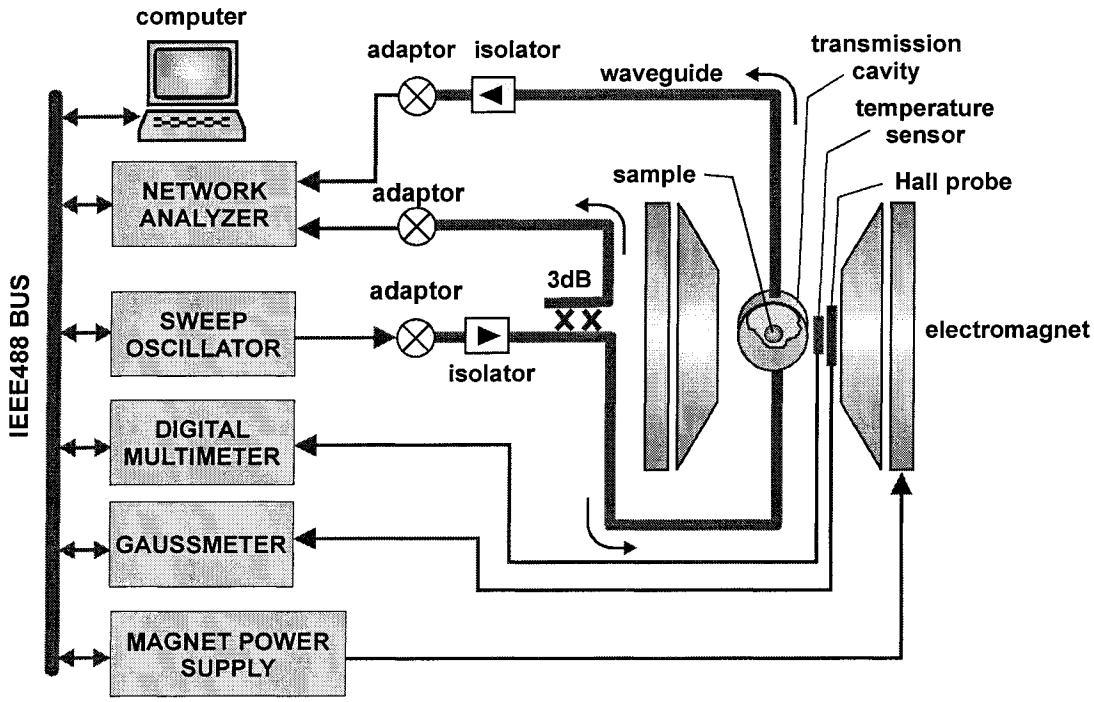

Fig 4.2. Effective linewidth microwave spectrometer system that operates at X-band. The sweep oscillator plays a role of a microwave source and is connected with a transmission cavity through a coaxial cable, a coaxial to waveguide adaptor, a 3dB directional coupler, and x-band waveguides. The cavity is a high-Q cylindrical cavity that operates at the TE_{011} mode. The magnetic sample is mounted at the center of the cavity, as indicated. Another end of this transmission cavity is connected with a channel of the network analyzer through waveguides, an isolator, a coaxial to waveguide adaptor, a coaxial cable, and a microwave power detector not shown in the above figure. Another branch of the 3dB coupler is connected with another channel of the network analyzer through waveguides, a coaxial to waveguide adaptor, and a coaxial cable. The electromagnet provides a uniform static magnetic field for the magnetic sample. The Hall probe and the Gaussmeter are used to measure the magnetic field inside the magnet gap. The temperature sensor attached on the cavity surface and the digital multimeter measure the cavity temperature. The network analyzer, the microwave source, the multimeter, the Gaussmeter, and the magnet power supply are connected with a computer through an IEEE488 (or GPIB) interface. The arrows show the directions of the signal propagations or device controls.

spectrometer system at Colorado Sate University based on the standard scalar network analyzer technique. The spectrometer system used for this thesis' investigation is

basically a clone of this old system that now is modified as a low temperature FMR measurement system.

Figure 4.2 shows a block diagram of the cloned effective linewidth microwave spectrometer system. The system instrumentation includes a synthesized HP8341B sweep oscillator (also called sweeper) as a microwave source, a scalar network HP8575D analyzer to detect the microwave signal of the cavity transmitted signal and the reference signal from the 3dB directional coupler, the GMW magnet power supply, an electromagnet for the uniform static magnetic field generation, a DTM-151 Teslameter (or Gaussmeter) for the measurement of the static magnetic field, and a digital HP3478A multimeter with a resistance-type temperature sensor for the measurement of cavity temperature. The main differences from the previous system are that a 3db directional coupler is added to provide a reference input signal.

The cavity is the heart of the effective linewidth spectrometer system. The cavity shown in Fig. 4.2 is a high-Q TE_{011} cylindrical cavity that operates at a nominal frequency of 10 GHz and a nominal quality factor of 22000. This is a transmission cavity with the height and diameter of 3.81 cm and 1.99 cm, respectively. The perturbation theory geometry factor is 2207 for a 2 mm diameter spherical sample. This cavity is made from oxygen free high-quality copper materials. In the determination of effective linewidth, the field dependence of cavity center frequency and Q-factor are assumed to be due to the dispersion and loss effects of the installed magnetic sample.

This system measures the cavity response that is the power ratio of the cavity output to the input. In a narrow frequency range, i.e., around the cavity frequency linewidth, the microwave frequency power ratio for the system without cavity should be

constant so that there is no deformation in the obtained cavity response. The effective linewidth measurement is fully automatic based on a Labview program installed in the computer. First, the power ratio is directly extracted from the network analyzer through a GPIB card. Second, the curve of cavity response is fitted by a standard Lorentzian function that gives the cavity center frequency and Q-factor at a given field. Third, the program also controls the magnetic field so that a set of (ω_c , Q_c , H_{ext}) and the corresponding cavity temperature can be obtained. The measured temperature is usually used for the temperature corrections.

4.2.2. Cavity Technique

Microwaves can be transmitted through and propagate inside hollow conducting tubes known as waveguide. The dynamic electric and magnetic fields inside the waveguide can be solved from Maxwell's equations with the boundary conditions at the conducting walls of the waveguide. A microwave cavity is a space surrounded by conducting walls. The microwave cavity can be constructed by closing off the ends of a segment of waveguide.

Microwaves inside the cavity are reflected back and forth due to the conducting walls and result in a standing wave or resonance for a specific microwave frequency. The standing wave normal modes can be determined by the boundary conditions. The cavity resonance is characterized by the cavity center frequency and quality factor.

For detection of a cavity resonance, an iris on one of the cavity walls is used to couple the microwave radiation from a waveguide into the microwave cavity. For a reflection cavity, this iris is further used to back couple the microwave radiation from the

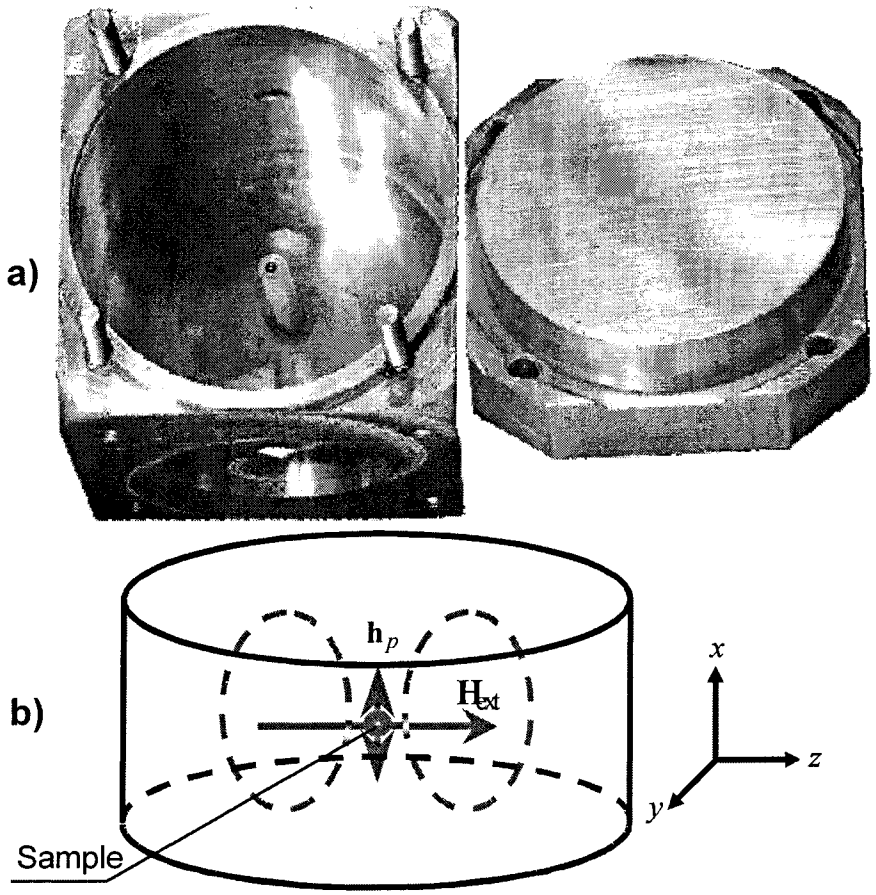

FIG. 4.3. High-Q TE_{011} cylindrical cavity of transmission type with a nominal center frequency of 10 GHz. Graph (a) is a photo for the inside structure (left) and the cover (right). Graph (b) shows the configuration (left) and coordinate system (right) used in this thesis. A spherical ferrite sample is mounted at the center of the cavity. The microwave and static external magnetic fields are indicated by $\mathbf{h}_p$ and $\mathbf{H}_{ext}$. The dashed ellipses that stand inside the cavity represent the distribution of the microwave magnetic field.

microwave cavity. For a transmission cavity, another iris is made to couple the microwave radiation from the cavity to another waveguide. One can use either the reflection cavity or the transmission cavity for effective linewidth measurements. Typically only the transmission cavity is used for the out-of-manifold effective linewidth measurements.

The microwave cavity can be used to measure the microwave properties of magnetic or dielectric materials. For the sake of effective linewidth measurements, a small ferrite sample is mounted inside the microwave cavity so as to determine the dynamic magnetic properties of this sample. At the site of the sample, the microwave magnetic field is assumed to be uniform and the electrical dynamic field is nearly zero.

Figure 4.3 shows a high-Q TE_{011} cylindrical cavity used for the measurements in Chapter 6. Graph (a) shows a photo of the open cavity. Graph (b) shows the cavity configuration of microwave fields relative to the static external magnetic field H_{ext}. The microwave magnetic field $\mathbf{h}_p$ is indicated by the dashed ellipses. This field is invariant under the rotation about the cavity axis (or x axis). At the site of the spherical ferrite sample, this field oscillates along the x direction as indicated. The right of Graph (b) is the coordinate system defined in Chapter 2.

The microwave magnetic field distribution can be calculated based on the electrodynamics' theory. The measured sample is mounted at the position where the microwave magnetic field is the most uniform and has a maximum value. The uniform field is required because the effective linewidth is only relevant to the uniform mode microwave drive and an excitation of uniform mode spin wave. The maximum microwave magnetic field is preferred based on the considerations of the high measurement sensitivity of the sample properties.

The nominal cavity center frequency and Q-factor are 10GHz and 22000, respectively. The cavity resonance linewidth is around 0.5 MHz. The actual cavity center frequency and Q-factor is dependent on the static external field since a ferrite sample is magnetic. The field dependent cavity center frequency is indicative of the

dispersion behavior of $\chi'(\omega)$. The inverse of the Q-factor represents the power absorption and $\chi''(\omega)$. The Lorentzian fit of the inverse of Q-factor near FMR resonance simply gives the FMR linewidth. In the effective linewidth technique, the cavity center frequency ω_c and Q-factor Q_c is used to determine the magnetic susceptibility.

The cavity quality factor is defined as 2π times the ratio of the time-averaged energy stored in the cavity to the energy loss per cycle. This measured quality factor is affected not only by the power absorption of the ferrite sample but also by the energy leakage due to coupling to waveguides and the eddy current losses due to the conducting walls. It is typically assumed that the magnetic field dependence of quality factor only comes from the ferrite sample.

The microwave power is pumped into the cavity through an iris shown in graph (a). The input frequency is swept in a narrow frequency band, for example, 0.75 MHz at 10 GHz. The cavity response shows a resonance. The cavity resonance frequency and Q-factor can be obtained from the cavity response in such narrow frequency range near cavity resonance. The Lorentzian fit can simply give the values of Q_c and ω_c. The ω_c is treated as the operating frequency.

As an example, a typical cavity resonance response is shown in Fig. 4.4. The power transmission is plotted as a function of the microwave swept frequency. Around four hundred sampling points near cavity resonance are collected using a scalar network analyzer, as indicated by the open circles. The solid curve is the corresponding Lorentzian fit. The resonance peak is indicated by $\omega_c / 2\pi$ and the resonance width is $\omega_c / 2\pi Q_c$.

Two things should be emphasized. First, the power transmission is defined as the

ratio of the output power to the input power. The power transmission is assumed only relevant to the cavity. The input power may be affected by imperfections of system components. Second, the Lorentzian fit shown here is nearly perfect and provides high precision determinations of center frequency ω_c and Q-factor Q_c. This curve can be deformed by mismatches in the connections of the cavity with the waveguides.

The cavity frequency varies with H_{ext}. In order to make measurements at constant frequency, this frequency range has to be extremely narrow compared with the absolute operating frequency. Fortunately, the frequency shift is typically small for a small sample. For example, for a nominal operating frequency 10 GHz, this frequency shift can be less than 5 MHz.

The values of $\omega_c(H_{\text{ext}})$ and $Q_c(H_{\text{ext}})$ are obtained at a series of discrete fields and carry the information about the dispersion and power absorption properties of the ferrite sample that is mounted inside the cavity. These series values of $\omega_c(H_{\text{ext}})$ and $Q_c(H_{\text{ext}})$ are further used to extract the susceptibility and subsequently the effective linewidth.

4.2.3. Cavity Perturbation Theory

Cavity perturbation theory is used to determine the magnetic susceptibility from the raw cavity data. A complete formulation of the perturbation method is given by Green (1964) for the magnetic susceptibility measurement. The following is to show the basic ideas of this theory.

A. Empty Cavity

The dynamics of the microwave fields are governed by Maxwell equations and

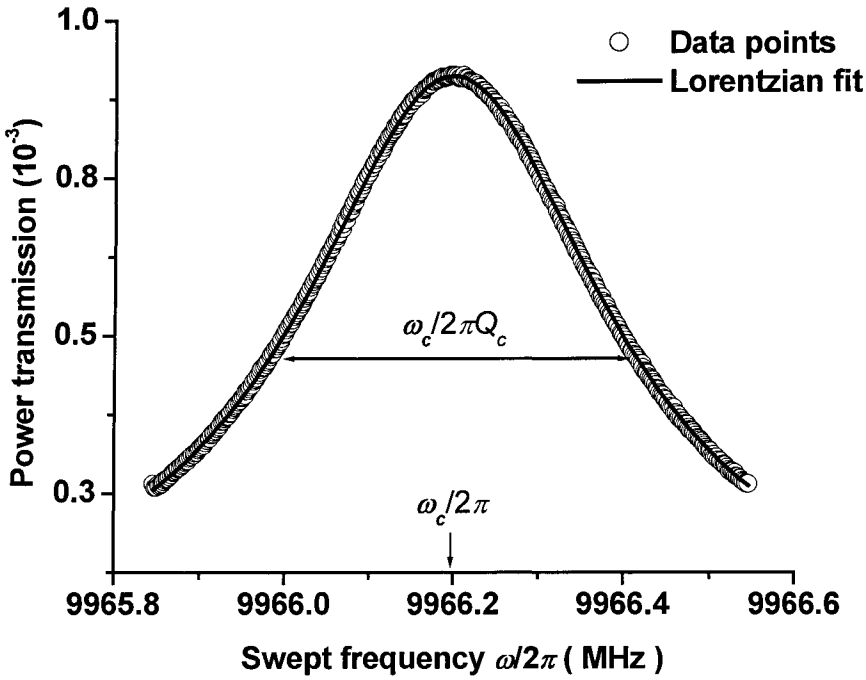

FIG. 4.4. Example of cavity response. The open circles and the solid curve are the data points and Lorentzian fit, as indicated. The data points and the fitting curve are plotted in the format of microwave power transmission versus the swept microwave frequency. The center of resonance peak is indicated by ω_c while the resonance frequency width is $\omega_c / 2\pi Q_c$ where Q_c is the cavity quality factor.

boundary conditions. One can obtain an equation that is only for the microwave magnetic field,

$$c^2\nabla^2\mathbf{h}_p(\omega)+\omega^2\mathbf{h}p(\omega)=0. \tag{4.3}$$

For a particular normal mode, the wave number is fixed,

$$\nabla^2\mathbf{h}_p=-k_{mnp}^2\mathbf{h}_p. \tag{4.4}$$

The subscripts of k_{mnp} are the indices for the nodes of standing waves along three different directions. For a cylindrical cavity, these three directions are corresponding to

the three directions of the cylindrical coordinates. The values of k_{mnp} are typically derived from the boundary conditions. The details of these derivations are not discussed here and most of details are in the textbooks, for example, *Electrodynamics* written by Jackson. Insert Eq. (4.4) into Eq. (4.3), one can immediately obtain the cavity resonance condition for a specified mode.

$$\omega_\infty = ck_{mnp}\,. \tag{4.5}$$

The parameter ω_∞ corresponds to the empty cavity resonance frequency.

More comments on ω_∞ should be made. For simplicity, the dielectric properties are not accounted for. The parameter ω_∞ is generally defined as the cavity resonance frequency with the magnetic effects of the sample frozen. The dielectric properties of the magnetic sample also result in the cavity center frequency shift. Such dielectric frequency shift is magnetic field independent and it's not interesting for the measurements of magnetic properties. In other word, this parameter ω_∞ can be the cavity center frequency in the high field limit where the magnetic susceptibility is zero.

Equation (4.5) is only for an ideal cavity, which doesn't have any power loss. As mentioned in the preceding section, the energy stored in the cavity undergoes decay due to the eddy current losses of the cavity walls and energy leakage due to irises. To include the power loss, a complex resonance frequency is usually introduced,

$$\omega = ck_{mnp} + i\frac{\omega}{2Q_\infty}\,. \tag{4.6}$$

Q_∞ is the empty cavity Q-factor. Similar to ω_∞, the parameter Q_∞ should be generally defined as the cavity quality factor in absence of magnetic loss due to the sample. The parameter Q_∞ can be the cavity quality factor in the high field limit. Equivalently,

equation (4.3) is modified by

$$c^2\nabla^2\mathbf{h}_{p0}+\omega^2\left(1-\frac{i}{2Q_\infty}\right)^2\mathbf{h}_{p0}=0. \tag{4.7}$$

B. Filled Cavity

Consider a small magnetic sample mounted inside the cavity. It's assumed that the sample doesn't change the microwave magnetic field distribution. The response of the dynamic magnetization should be included. Based on Eq. (2.37), this leads to an equation as

$$c^2\nabla^2(\mathbf{h}_p+\mathbf{h}_d)+\omega^2\left(1-\frac{1}{2Q_\infty}\right)^2(\mathbf{h}_p+\mathbf{h}_d)\approx-\omega^2\mathbf{m}. \tag{4.8}$$

The dipolar field of the magnetization is also included while $\mathbf{h}_p$ is only related to the empty cavity. In the derivation of Eq. (4.8), the term $\nabla(\nabla\cdot\mathbf{m})$ is neglected since only the uniform mode in $\mathbf{m}$ is accounted for.

Equation (4.8) is only applicable to inside the magnetic sample. The region outside the sample should be still governed by Eq. (4.7). Just simply introduce a unit function $q_s(\mathbf{r})$ and one obtains,

$$c^2\nabla^2(\mathbf{h}_p+\mathbf{h}_d)+\omega^2\left(1-\frac{1}{2Q_\infty}\right)^2(\mathbf{h}_p+\mathbf{h}_d)\approx-q(\mathbf{r})\omega^2\mathbf{m}. \tag{4.9}$$

Here, $q_s(\mathbf{r})$ is defined to be equal to 1 inside the sample and 0 outside the sample.

As a perturbation, equation (4.4) is used to eliminate ∇^2. The first order solution of Eq. (4.9) can be approximately,

$$\mathbf{h}_p + \mathbf{h}_d \approx -\frac{q_s(\mathbf{r})\omega^2}{\omega^2\left(1-\frac{i}{2Q_\infty}\right)^2 - \omega_\infty^2}\mathbf{m}. \tag{4.10}$$

The total microwave energy in the cavity can be obtained,

$$\begin{aligned}&\frac{\mu_0}{2}\int_{V_c}(\mathbf{h}_p^* + \mathbf{h}_d^*)\cdot(\mathbf{h}_p + \mathbf{h}_d)d\mathbf{r} \\ &\approx -\frac{\mu_0}{2}\frac{\omega^2}{\omega^2\left(1-\frac{i}{2Q_\infty}\right)^2 - \omega_\infty^2}\int_{V_s}(\mathbf{h}_p^* + \mathbf{h}_d^*)\cdot\mathbf{m}d\mathbf{r}\end{aligned}. \tag{4.11}$$

Here, V_c is the cavity volume.

In the energy calculations, the contributions of the dipolar field are neglected because the inserted sample is too small. The dipolar energy is proportional to the energy absorbed by the sample because both of them are proportional to the power of the excited uniform mode spin wave. This approximation requires that the change in the total cavity quality factor due to the magnetic sample should be small. By neglecting the dipole field, equation (4.11) becomes

$$\frac{\omega^2\left(1-\frac{i}{2Q_\infty}\right)^2 - \omega_\infty^2}{\omega^2} \approx -\frac{\int_{V_s}\mathbf{h}_p^*\cdot\mathbf{m}d\mathbf{r}}{\int_{V_c}\mathbf{h}_p^*\cdot\mathbf{h}_p d\mathbf{r}}. \tag{4.12}$$

The frequency ω is generally complex. According to the complex resonance frequency model, ω can be written as,

$$\omega = \omega_c\left(1+\frac{i}{2Q_c}\right). \tag{4.13}$$

As defined before, ω_c and Q_c are the cavity center frequency and the cavity quality

factor.

To obtain a working equation, an extra approximation is applied based on $|\omega_c - \omega_\infty| << \omega_\infty$ and $Q_\infty >> 1$ since the frequency shift is much smaller than the nominal cavity center frequency. This approximation allows neglecting the higher order terms of $\omega_c - \omega_\infty$, $1/Q_c$, and $1/Q_\infty$.

$$\frac{\omega_c - \omega_\infty}{\omega_c} + \frac{i}{2}\left(\frac{1}{Q_c} - \frac{1}{Q_\infty}\right) \approx -\frac{1}{2}\frac{\int_{V_s} \mathbf{h}_p^* \cdot \mathbf{m} d\mathbf{r}}{\int_{V_c} \mathbf{h}_p^* \cdot \mathbf{h}_p d\mathbf{r}}. \tag{4.14}$$

Finally, the right side of Eq. (4.14) is written in terms of the uniform mode magnetic susceptibility χ or tensor $\ddot{\chi}_e$ for spherical samples. Note that the magnetic susceptibility tensor is invariant under the rotation round the z axis. Assume that the z component of $\mathbf{h}_p$ is zero, as shown in Fig. 4.3(b).

$$\frac{\omega_c - \omega_\infty}{\omega_c} + \frac{i}{2}\left(\frac{1}{Q_c} - \frac{1}{Q_\infty}\right) \approx -\frac{\chi}{K_c}, \tag{4.15}$$

where the parameter K_c is defined as

$$K_c = \frac{1}{2}\frac{\int_{V_s} \mathbf{h}_p^*(\omega) \cdot \mathbf{h}_p(\omega) d\mathbf{r}}{\int_{V_c} \mathbf{h}_p^*(\omega) \cdot \mathbf{h}_p(\omega) d\mathbf{r}}. \tag{4.16}$$

This parameter is only related to the distribution of microwave magnetic field in the empty cavity and hereby only dependent on the sample and cavity geometry. The parameter K_c is called the cavity calibration factor.

The real part and imaginary part can be separated. The real part of the susceptibility is given by

$$\chi' = -K_c \frac{\omega_c - \omega_\infty}{\omega_c} \tag{4.17}$$

and the negative imaginary part is

$$\chi'' = \frac{K_c}{2} \cdot \left(\frac{1}{Q_c} - \frac{1}{Q_\infty} \right). \tag{4.18}$$

As commented above, the parameters ω_∞ and Q_∞ should be the infinite field extrapolated values of the measured ω_c and Q_c, respectively.

Equations (4.17)and (4.18) are the working equations that provide a connection between the cavity parameters and the susceptibility. The conditions for the validity of Eqs. (4.17) and (4.18) can be summarized: (a) the sample size is much smaller than the cavity volume, (b) only the uniform mode spin wave susceptibility is considered, (c) the changes in Q_c and ω_c due to the finite static external field are much smaller than Q_c and ω_c, respectively, and (d) $Q_c >> 1$.

Equations (4.17) and (4.18) are not only useful for effective linewidth measurements but also useful for the FMR measurements. The power absorption is linear with the inverse of cavity quality factor. The Lorentzian fitting of $1/Q_c$ versus H_{ext} gives the FMR field and the FMR linewidth. This may be only valid for very small cavity center frequency shifts. Therefore, a good way is to use the exact expression of χ'' so as to take account for the field dependence of ω_c.

4.2.4. High Field Approximation

The high field approximation assumes that the loss is small at high field because the dominant contribution due to two-magnon scattering would be turned off in the

absence of spin wave degeneracy so that the higher order terms of relaxation rate or effective linewidth could be neglected. This approximation is valid when the static external field is far from the FMR field.

The high field approximation is specifically for the determination of the calibration parameters, K_c, ω_∞, and Q_∞ that play an important role in the calculations of the magnetic susceptibility in Eq. (4.17) and (4.18). These calibration parameters are usually evaluated from the high field tail of cavity center frequency and Q-factor and used for any other field.

By neglecting the higher order terms of the HFE linewidth or relaxation rate in the susceptibility expressions, equations (4.17) and (4.18) in the high field region can be written as

$$\omega_c = -\frac{1}{K_c} X_\omega + \omega_\infty \tag{4.19}$$

and

$$\frac{1}{Q} = \frac{\Delta H_{\text{eff}}}{K_c} X_Q + \frac{1}{Q_\infty}, \tag{4.20}$$

where the parameter X_ω and the parameter X_Q are functions of H_{ext} according to

$$X_\omega = \frac{M_0 H_{\text{ext}} \omega_c}{H_{\text{ext}}^2 - \left(\frac{\omega_c}{|\gamma| \mu_0}\right)^2} \tag{4.21}$$

and

$$X_Q = \frac{M_0\left[H_{\text{ext}}^2 + \left(\frac{\omega_c}{|\gamma|\mu_0}\right)^2\right]}{\left[H_{\text{ext}}^2 - \left(\frac{\omega_c}{|\gamma|\mu_0}\right)^2\right]^2}. \tag{4.22}$$

These functions are for isotropic spheres. For Disks, refer to Chapter 6 and Truedson *et al.* (1993,1994)

Equation (4.19) is derived from Eq. (4.17) that basically involves the dispersion properties of the magnetic sample. As discussed in Chapter 2, the real part of magnetic susceptibility is independent on the relaxation rate for the field region far from the FMR field or frequency. The relaxation rate is much smaller than the field difference between the static external field and the FMR field. This makes equation (4.19) is independent on the effective linewidth as in the far field χ'. With a proper value of gyromagnetic ratio, equation (4.19) always shows a nice linear relation between ω_c versus X_ω since the field dependent effective linewidth doesn't affect it.

Equation (4.20) is derived from Eq. (4.18). Unlike Eq. (4.19), equation (4.20) significantly depends on effective linewidth. This is because there is basically an extra factor of effective linewidth in χ'' compared with χ'. The HFE linewidth is very small and χ'' is typically much smaller than χ'. Note that X_Q is a field function. If the effective linewidth is field dependent, the effective linewidth can also be expressed as a function of X_Q. The relation between $1/Q$ and X_Q may be not linear. In other word, $1/Q$ and X_Q are linear only if the effective linewidth is field independent. The details are discussed in Chapters 5 and 6.

A proper linear fitting of ω_c versus X_ω gives the cavity calibration factor K_c and the

infinite field center frequency ω_∞. Typically, the HFE linewidth is assumed to be a field independent constant to represent the intrinsic losses. Equation (4.20) tells that the linear fit of Q_c versus X_Q gives this intrinsic effective linewidth and the infinite field Q-factor Q_∞.

Figure 4.5 shows an example of the measured cavity parameters as a function of static external field H_{ext}. A dense polycrystalline YIG sphere is used to for these measurements. This sphere has been found to have a pronounced impurity. But it's good to be shown here because the HFE linewidth should be nearly constant. Graphs (a) and (b) show ω_c and Q_c versus H_{ext}, respectively. The field range is from $\mu_0 H_{\text{ext}} = 0.49$ T to 0.8 T.

These graphs show that the cavity resonance parameters are field dependent due to the dispersion and loss properties of the inserted magnetic sample. In graph (a), the parameter ω_c shifts down with the field decrease in the high field region. The ω_c shifts are the dispersion effect of the magnetic sample. As shown in Eq. (4.17), the real part χ' of the magnetic susceptibility is linear with $1/\omega_c$ and further ω_c for a small frequency shift. The real part χ' also decreases with field decrease. This is why ω_c is smaller at a lower field than at a higher field in the high field region.

In graph (b), the quality factor Q_c also decreases with field decrease. The inverse of Q_c is the absorption effect of the magnetic sample. The power absorption for spheres can be characterized by the imaginary part χ'' of magnetic susceptibility. In the high field region, χ'' shows a tail. This is consistent with the observed decrease with field increase since χ'' is linear with the inverse of Q_c.

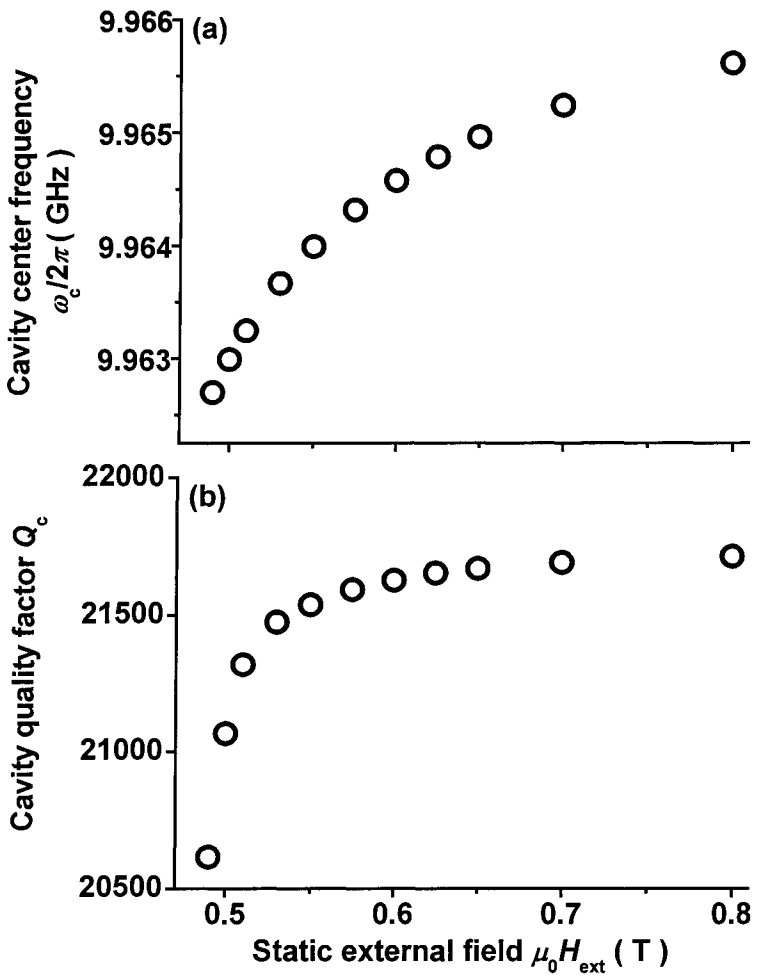

FIG. 4.5 Example of the measured cavity center frequency ω_c in graph (a) and quality factor Q_c in graph (b) as a function of static external field H_{ext}. The data is measured on a dense polycrystalline yttrium iron garnet sphere with some impurity. The open circles are the data points in both graphs. Graphs (a) and (b) shows the cavity center frequency and cavity quality factor for the high field region form $\mu_0 H_{ext}$ =0.49 T to 0.8 T.

Figure 4.5 also shows that the changes in these cavity parameters are fairly small in comparison with their absolute values. The cavity center frequency at 0.8 T may be taken to be a rough value of infinite field center frequency. The frequency shift from graph (a) is less than 3.5 MHz that is extremely smaller than 10 GHz. The same thing can be done for quality factor. Roughly take the quality factor at 0.8 T as the infinite

field quality factor. Graph (a) shows the Q_c changes are less than 1500. The changes are within 10% of 22000. The small changes in ω_c and Q_c indicate that the cavity perturbation theory is valid here.

Figure 4.6 shows how to determine the calibration constants ω_∞, Q_∞, and K_c. The parameters X_ω and X_Q are calculated based on Eqs. (4.21) and (4.22). In these calculations, $|\gamma|/2\pi = 28$ GHz/T, the saturation magnetization $\mu_0 M_0 = 0.175$ T, and the field dependent parameters such as static external field and cavity resonance frequency are based on the data of Fig. 4.5. Graph (a) shows the cavity resonance frequency ω_c as a function of the parameter X_ω. Graph (b) shows the cavity quality factor Q_c as a function of the parameter X_Q. In both graphs, the open circles indicate the data. The solid lines indicate the linear fits that are applied in graph (a) to all of the measured fields shown in Fig. 4.5, namely from 0.49 to 0.8 T, and in graph (b) to the field range from 0.55 to 0.8 T (not including 0.55 T). The intercepts are indicated by ω_∞ and Q_∞.

The linear fits give the empirical values of the calibration constants including ω_∞ and Q_∞. According to Eq. (4.19), the slope of the linear fit in Graph (a) is $-1/K_c$ and used to determine K_c. The nearly perfect fitting gives a high precision K_c value. The intercept at the coordinate of the cavity center frequency is ω_∞ when $X_\omega \to 0$ and hereby $H_{\text{ext}} \to \infty$. The linear fit of Graph (b) is used to determine Q_∞ and a constant effective linewidth. The intercept at vertical coordinate when $X_Q \to 0$ is $1/Q_\infty$ because equation (4.22) implies that $H_{\text{ext}} \to \infty$ when $X_Q \to 0$. The slope is $\Delta H_{\text{eff}} / K_c$ and hence can be used to determine a constant HFE linewidth.

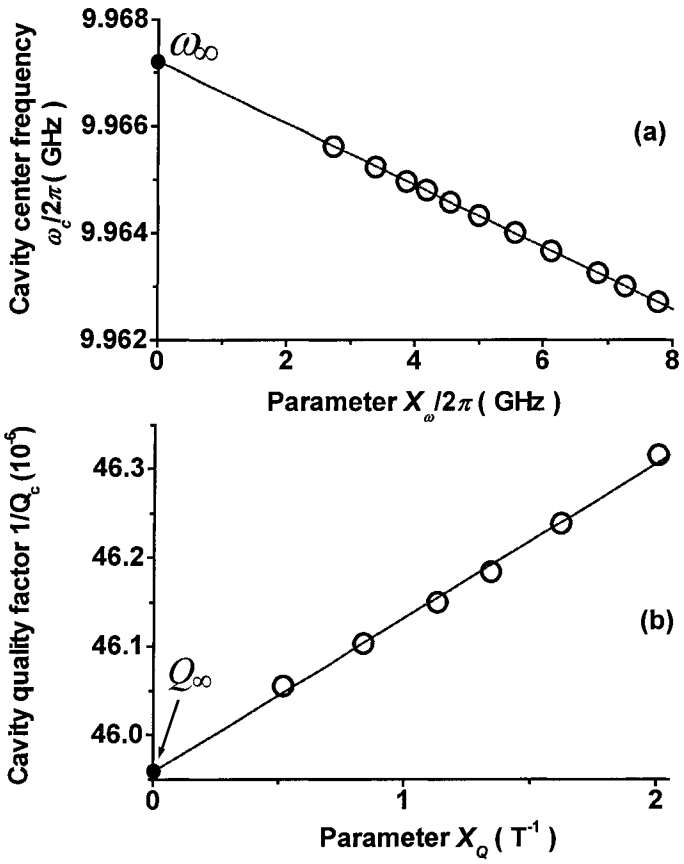

FIG. 4.6. Determination of the calibration constants. Graph (a) shows the cavity resonance frequency ω_c as a function of the parameter X_ω defined by Eq. (4.21). Graph (b) shows the cavity quality factor Q_c as a function of the parameter X_Q defined by Eq. (4.22). In both graphs, the open circles indicate the data that are calculated from the data shown in Fig. 4.4. The solid lines are the linear fittings. The intercepts are indicated by ω_∞ and Q_∞.

These empirical calibration constants are better than the calculated values from perturbation theory. This is because the perturbation does not include the contributions due to the dipole field and the dielectric properties of the inserted magnetic sample. The relative dielectric constant that is around 10 is very different from the empty cavity where the relative dielectric constant is equal to 1. This may significantly change the distribution of microwave fields around the sample. But it doesn't mean that the perturbation theory is invalid because the field at the site of the sample is still very

uniform due to the small volume of the sample.

The linear fit of ω_c versus X_ω is nearly perfect. This implies that the cavity perturbation theory is nicely applicable to the high field region. This also allows comparing the theoretical χ' and K_c with experimental values. X_ω is simply equal to the approximated theoretical value χ' multiplied by ω_c. The perfect linear fitting of ω_c versus X_ω indicates that the theoretical χ' nicely matches up with the experimental χ'. More discussions about the geometry factor can refer to Chapter 5.

One may note that the linear fit of $1/Q_c$ versus X_Q only applies to the extremely high fields from 0.55 T to 0.8 T. At these extreme high fields, the loss due to the impurity is dominant and field independent. Once the field goes to a lower field, the impurity loss is not dominant and the effective linewidth will show field dependent. In this case, the linear fit model is not valid as in Eq. (4.20).

The calibration constants determined in the high field region are further used to calculate the susceptibility components χ' and χ'' also for the other field regions. A constant HFE linewidth can be obtained from the slope of the linear fitting in graph (b). For the HFE linewidth with weak field dependence, one can directly use Eq. (4.20) and obtain the HFE linewidth,

$$\Delta H_{\text{eff}} = \frac{K_c}{X_Q}\left(\frac{1}{Q} - \frac{1}{Q_\infty}\right). \tag{4.23}$$

4.2.5. Analytical Expression of Effective Linewidth as a Function of Magnetic Susceptibility

Unlike the FMR linewidth, the effective linewidth ΔH_{eff} is generally determined from the magnetic susceptibility χ including the real part χ' and imaginary part χ''. The definition of effective linewidth is related to two independent parameters, namely, the uniform mode relaxation rate η and the gyromagnetic ratio γ. Both are field dependent. The effective linewidth cannot be simply determined from the power absorption (χ'') that is typically used for the determination of the FMR linewidth.

The relation between ΔH_{eff} and χ is very complicated. Chapter 2 shows the magnetic susceptibility as a function of the relaxation rate and gyromagnetic ratio. Based on the definition of effective linewidth, one can write the magnetic susceptibility as a function of the effective linewidth and gyromagnetic ratio.

$$\chi' = \frac{M_0 H_{\text{ext}} \left(H_{\text{ext}}^2 - \frac{\omega^2}{\gamma^2 \mu_0^2} + \frac{\Delta H_{\text{eff}}^2}{4} \right)}{\left(H_{\text{ext}}^2 - \frac{\omega^2}{\gamma^2 \mu_0^2} - \frac{\Delta H_{\text{eff}}^2}{4} \right)^2 + H_{\text{ext}}^2 \Delta H_{\text{eff}}^2} \tag{4.24}$$

and

$$\chi'' = \frac{1}{2} \frac{M_0 \Delta H_{\text{eff}} \left(H_{\text{ext}}^2 + \frac{\omega^2}{\gamma^2 \mu_0^2} + \frac{\Delta H_{\text{eff}}^2}{4} \right)}{\left(H_{\text{ext}}^2 - \frac{\omega^2}{\gamma^2 \mu_0^2} - \frac{\Delta H_{\text{eff}}^2}{4} \right)^2 + H_{\text{ext}}^2 \Delta H_{\text{eff}}^2}. \tag{4.25}$$

In the effective linewidth technique, the magnetic susceptibility parameters are first determined. One has to solve the effective linewidth as a function of the magnetic susceptibility parameters. Equations (4.24) and (4.25) indicate that the effective linewidth is nonlinear with the magnetic susceptibility parameters. It was thought that there would be no analytical solution of the effective linewidth. (McKinstry, 1991)

However, this not true because equation (2.24) is just a quadratic equation of complex frequency.

The following provides a way to solve Eqs. (4.24) and (4.25) to obtain a simple expression of effective linewidth. The solving procedure includes three steps. First, express the gyromagnetic ratio as a function of the susceptibility and effective linewidth for the sake of eliminating the gyromagnetic ratio. This can be done from the ratio of Eq. (4.24) to (4.25),

$$\frac{\chi'}{\chi''} = \frac{2H_{ext}\left(H_{ext}^2 - \omega^2/\gamma^2 + \Delta H_{eff}^2/4\right)}{\Delta H_{eff}\left(H_{ext}^2 + \omega^2/\gamma^2 + \Delta H_{eff}^2/4\right)}. \tag{4.26}$$

It's a linear equation of $1/\gamma^2$. One obtains

$$\frac{\omega^2}{\gamma^2\mu_0^2} = \frac{\chi'' - \chi'\delta_{eff}}{\chi'' + \chi'\delta_{eff}}\left(1+\delta_{eff}^2\right)H_{ext}^2, \tag{4.27}$$

The parameter δ_{eff} is the normalized ΔH_{eff} given by

$$\delta_{eff} = \frac{\Delta H_{eff}}{2H_{ext}}. \tag{4.28}$$

Second, insert Eq. (4.27) into Eq. (4.24)

$$\chi' = \frac{M_0}{2H_{ext}\delta_{eff}} \frac{\left(1+\delta_{eff}^2\right)\cdot\chi'\left(\chi'' + \chi'\delta_{eff}\right)}{\left(1+\delta_{eff}^2\right)\left(\chi'^2 + \chi''^2\right)}. \tag{4.29}$$

Note that the expression $1+\delta_{eff}^2$ is nonzero and can be cancelled out in the right side of Eq.(4.29). It is interesting that this gives a linear equation of δ_{eff} or effective linewidth although equations (4.24) and (4.25) are nonlinear.

$$\delta_{\text{eff}} = \frac{M_0}{2H_{\text{ext}}} \frac{\chi'' + \chi'\delta_{\text{eff}}}{\chi'^2 + \chi''^2}. \tag{4.30}$$

One factor χ' is also cancelled out because generally χ' is nonzero. Even if $\chi' = 0$ at FMR, equation (4.30) is still consistent with Eq. (4.25).

Finally, one solves the linear equation (4.30),

$$\Delta H_{\text{eff}} = \frac{\chi''}{\frac{\chi'^2 + \chi''^2}{M_0} - \frac{\chi'}{2H_{\text{ext}}}}. \tag{4.31}$$

Now the gyromagnetic ratio can be solved from the combination of Eq. (4.27) and (4.31),

$$|\gamma| = \frac{\omega}{H_{\text{ext}}\sqrt{1 + \frac{\Delta H_{\text{eff}}^2}{4H_{\text{ext}}^2}}} \sqrt{\frac{\chi'' + \frac{\Delta H_{\text{eff}}}{2H_{\text{ext}}} \cdot \chi'}{\chi'' - \frac{\Delta H_{\text{eff}}}{2H_{\text{ext}}} \cdot \chi'}}. \tag{4.32}$$

With the measured the magnetic susceptibility, the effective linewidth and gyromagnetic ratio can be directly determined using Eqs. (4.31) and (4.32).

4.3. Brief Review of Effective Linewidth

Most of the effective linewidth work is related to the test of two-magnon scattering. The FMR linewidth in single crystal YIG are on the order of 1 Oe, while polycrystalline materials usually have linewidths from tens to hundreds of Oersteds due to two-magnon scattering. The field dependent effective linewidth is a powerful tool for the test of the field dependent two-magnon scattering processes. The effective linewidth test on two-magnon scattering had been investigated in great details during the late of 1960's and the early of 1970's.

A review about the effective linewidth work prior to 1975 was well done by Patton

(1972, 1975). The following summarizes the previous work based on the representative measurements. The loss mechanism due to impurity (Gennes *et al*, 1962; Safanov, 2003) and the radiation damping (Bloembergen, 1954) are not reviewed here.

(1) Effective Linewidth Technique

The effective linewidth work was inspired by the measurement done by Liu and Shaw (see Motizuki, 1965). Instead of absorbed power, the susceptibility of a YIG disk was measured below and above the bulk manifold. The Liu and Shaw's measurement was used to test the two-magnon scattering processes due to nonmagnetic inclusions and voids. Kohane and Schlömann (1968), and Vrehen (1969) extended this measurement technique into the effective linewidth technique as described in the preceding section.

The cavity technique is generally used for these measurements. At the early stage, the low Q cavity was typically used. The off resonance susceptibility measurements require high sensitivity. In 1972, Patton and Kohane developed an ultra-sensitive technique using a high Q cavity and frequency stabilized Klystron (microwave source). The sensitivity is 10^{-4} in χ' and 10^{-5} in χ''. The cavity parameters were obtained using the two points of cavity resonance response at its half maximum. Due to the technological development, the sweep oscillator and network analyzer were introduced to replace the old microwave source and old detectors. These replacements make the cavity measurement much easier. The cavity parameters were determined using a Lorentzian fit of the cavity response. But the accuracy was not significantly enhanced.

(2) Porosity Scattering

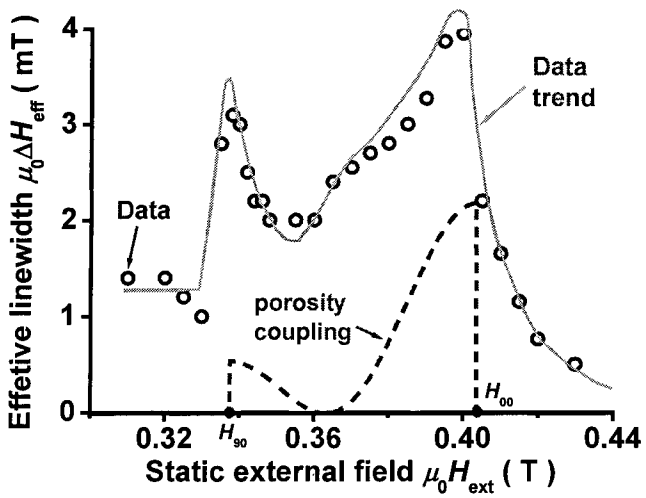

FIG. 4.7. Effective linewidth at 10 GHz as a function of static external field H_{ext}. The data indicated by open circles are for a dense yttrium iron garnet (YIG) sphere with density of 99%, relative to the theoretical YIG density. The solid curve is sketched to show the data trend. The dashed curve is the coupling factor of the porosity scattering. The bulk manifold is indicated by H_{00} and H_{90} The data are from the measurements by Patton in 1969.

The porosity of effective linewidth for the polycrystalline ferrites was measured by Patton (1969), Vrehen (1970), and Scotter (1972). Figure 4.7 shows a representative effective result of a dense polycrystalline YIG sphere measured by Patton in 1969. In the effective linewidth data, the minimum near FMR (around 0.36 T) and the sharp decreases at the edges of the bulk manifold are well understood and predicted by the porosity scattering theory, especially the coupling factor as indicated by the dashed line. The effective linewidth at FMR as a function of porosity was shown to be quantitatively in good agreement with the theory (Sparks *et al*, 1961).

(3) Anisotropy Scattering

The magnetocrystalline anisotropy dependence of effective linewidth for the

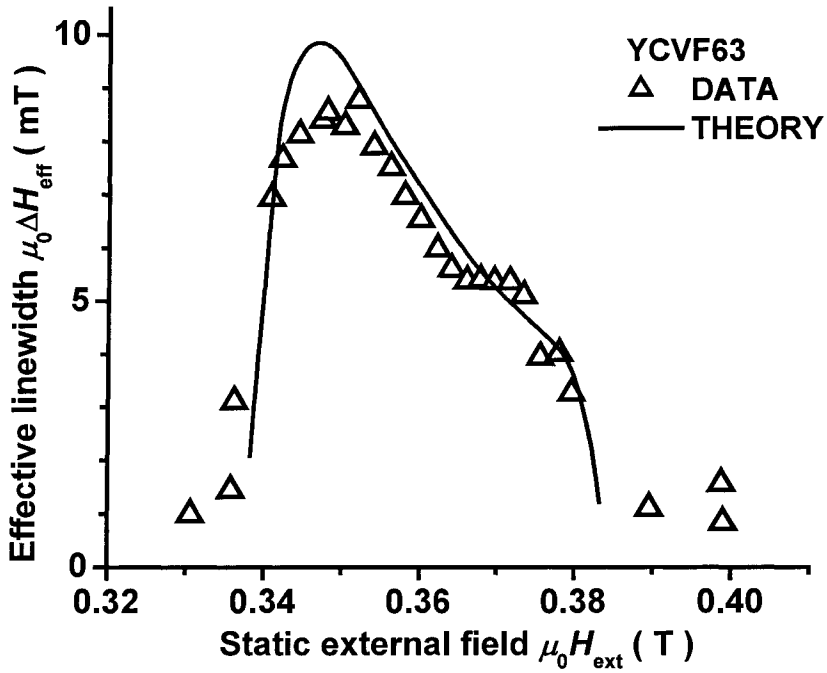

FIG. 4.8. Effective linewidth data ΔH_{eff} and anisotropy scattering theory as a function of static external field H_{ext} for the YCVF material $Y_{1-2x}Ca_{2x}Fe_{5-x}V_xO_{12}$ with x=0.63. The triangles and the solid curve adopted are the data and the theory, respectively. The curve and points are adopted from Patton (1969).

polycrystalline ferrites was measured by Vrehen (1969), Patton (1969), and Van Hook *et al* .(1969) Figure 4.8 shows an example data measured by Patton. The solid curve was calculated using anisotropy scattering theory. (Schlömann, 1958, 1968) The theory is coincidently in excellent agreement with the data. Patton's other data show poor agreement with the theory for other x values in $Y_{1-2x}Ca_{2x}Fe_{5-x}V_xO_{12}$. The higher x values lead to higher anisotropy field. Schlömann's theory is specifically for low anisotropy fields. Patton's results imply that this theory is only applicable to the materials with moderate anisotropy fields. This discrepancy needs further justification.

(4) Secondary Scattering

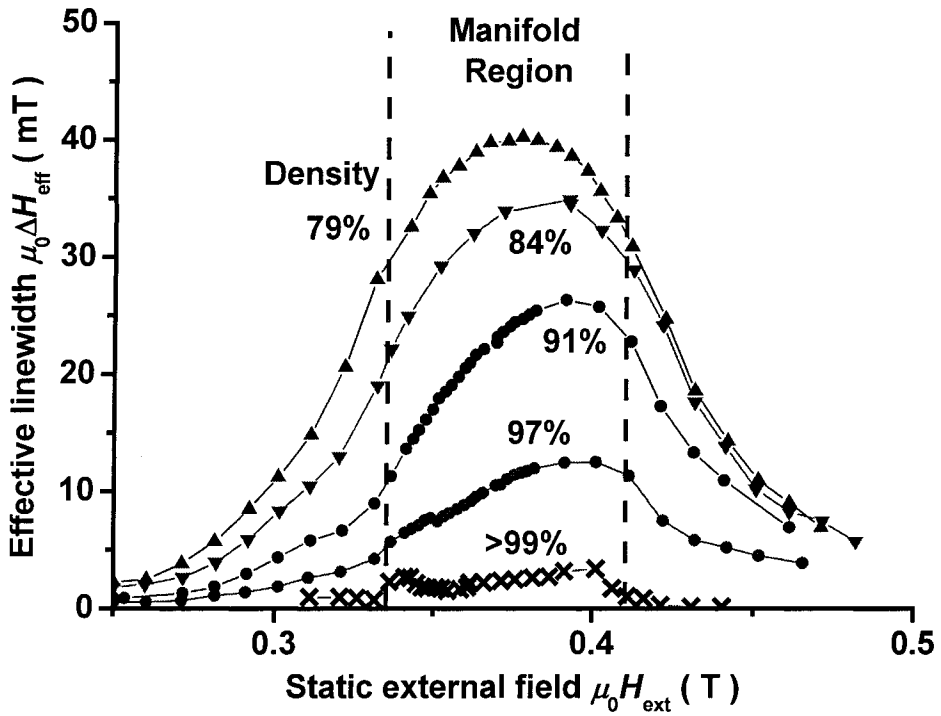

FIG. 4.9. Effective linewidth at 10 GHz as a function of static external magnetic field for polycrystalline yttrium iron garnet (YIG) spheres with different density relative to the theoretical YIG density. The points of cross, diagonal, open circles, open triangle, and solid triangle represent the data points for the density of 99%, 97%, 91%, 84%, and 79%, respectively, as indicated. The lines show the simple neighboring connections. The bulk manifold region is also marked as "degenerate region". The data are from the measurements by Patton in 1969.

According to porosity and anisotropy scattering mechanisms, the effective linewidth outside manifold should be small and nearly field independent. However, this is not the experiment case. The data in Fig. 4.9 show that the large effective linewidth extends out to both the low field and high field. It seems that the in-manifold effective linewidth leaks out and shows two pronounced tails.

This tail effect was explained by the secondary scattering mechanism proposed by Schlömann (1969). The basic ideas of the secondary scattering lie in two major

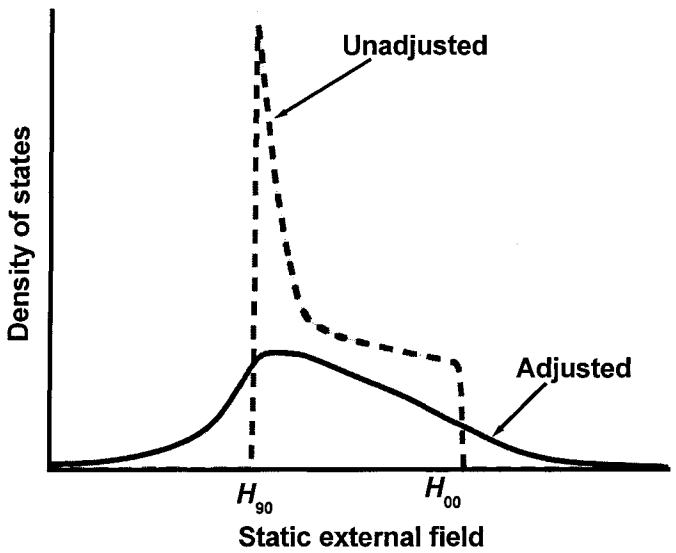

FIG. 4.10. Adjusted density of low wave number states. The dashed curve shows the unadjusted density of low wave number states as in Fig. 3.4(a). The top and bottom of bulk manifold are indicated by H_{00} and H_{90}, respectively. The curves are adopted from Schlömann (1969).

modifications. First, the scattered non-uniform modes with relatively large amplitudes can be also scattered into the non-uniform and uniform modes. Second, the large two-magnon relaxation rate modifies the dispersion relation and the DOS function has a corresponding change. The modified DOS function shows two tails outside the bulk manifold and further requires that for consistence the two-magnon relaxation rate should be modified since it is a function of DOS. Figure 4.10 shows how these two major modifications adjust the DOS function. The DOS tails might qualitatively explain the effective linewidth tails.

However, this explanation is not convincing, in the opinion of the author of this thesis. No matter how large the microwave loss in the bulk manifold is, the first order (two magnon) scattering processes have small effects on the relaxation rate outside the bulk manifold and do not provide any large-amplitude non-uniform mode and any large

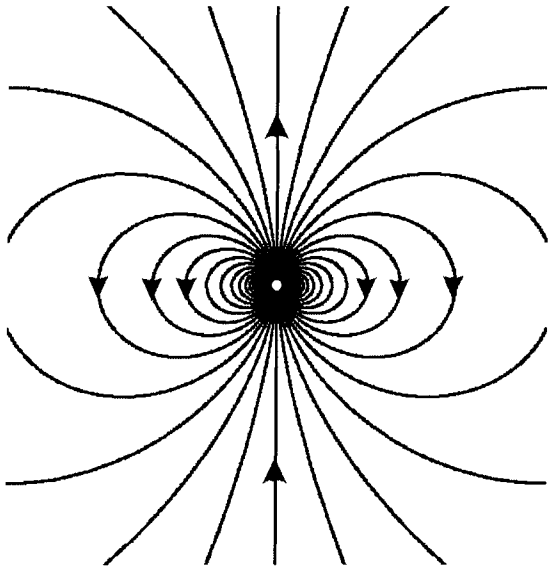

FIG. 4.11. Spatial distribution of the effective dipole field of a spherical pore. The circular whit area at the center is the pore. The slopes of the solid curves show the field directions and density of these curves indicate the field strength. A few arrows are marked how the field directions generally go.

relaxation rate.

(5) Porosity Shift of Bulk Manifold

Instead of the secondary scattering theory, Vrehen proposed the porosity shift of bulk manifold (also spin wave manifold) to explain the effective linewidth tails. The idea is that a void effectively generates a static demagnetizing field and the spin wave manifold is related to the local static field, which becomes non-uniform. Figure 4.11 shows the pattern of the demagnetizing field generated by a small spherical pore. According to Vrehen (1970) and Hoeppe (2004), the static internal field is added by an extra field from $-M_0/3$ to $2M_0/3$. The spin wave manifold is shifted up by $2M_0/3$ and down by $M_0/3$. Vrehen and Hoeppe tested the upper limit of bulk manifold shift.

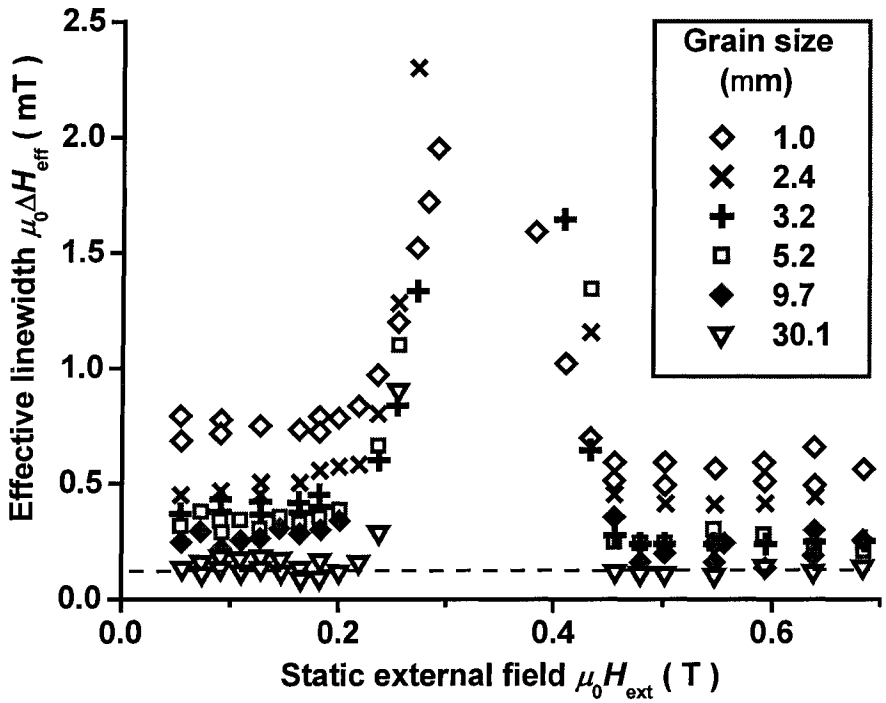

FIG. 4.12. Patton's (1970) measurement data on polycrystalline yttrium iron garnet spheres with different grain sizes. Effective linewidth is plotted as a function of static external magnetic field. The open diagonals, crosses, pluses, open squares, sold diagonals, and open triangles indicate the grain sizes of 1.0 μm, 2.4 μm, 3.2 μm, 5.2 μm, 9.7 μm, and 30.1 μm, respectively. The dashed line shows the smallest high field effective linewidth, 0.18±0.05 mT.

The measurement data by Vrehen and Hoeppe show the sharp drops and discontinuities at the high field manifold limit, which strongly supported such pseudo-manifold effect.

(6) Intrinsic Loss

In line with the test of two magnon processes, the intrinsic loss rate limit has been tested by the measurements of the HFE linewidth. At high fields, two-magnon scattering is disallowed, and the relaxation rate should be field independent, small, and on the order of single crystal linewidths. This is why the HFE linewidth has typically been taken as a

measure of the intrinsic loss even in highly inhomogeneous ferrite materials.

A representative test is the work done by Patton (1970), as shown in Fig. 4.12. The measurements were on the polycrystalline YIG spheres with different grain sizes. The data showed that the HFE linewidth above 0.5 T are grain size dependent and significantly larger than the single crystal YIG linewidth that is known as around 0.05 mT. As expected, the larger the grain size is, the smaller the HFE linewidth. Patton's results also indicated that the LHE linewidth was generally larger than the HFE linewidth.

In the 21st century, the hot isostatic pressing (hipping) technique has been developed. This technique can provide ultra dense polycrystalline ferrite materials in which the porosity could be entirely removed. Unlike the dominance in the regular ferrites, the porosity scattering vanishes. This allows to test whether the porosity scattering is important in the HFE linewidth. The first measurement on the hipped polycrystalline YIG samples was made by Nazarov *et al.* (2003) The obtained HFE linewidth was 0.17±0.05 mT that is consistent with the result of Patton (1970). This implies that the porosity scattering is not the reason why the HFE linewidth is significantly larger than the single crystal linewidth.

(7) Eddy Current Loss

Eddy current loss is well known. Recently, the HFE linewidth in moderate hexagonal ferrite disks has been measured in a white frequency range from 10 GHz to 35 GHz. (Wilber and Silber, 1988; Trudson *et al.*, 1992, 1993) The results give reasonable values of the microwave conductivity, which are consistent with the measured DC conductivity.

(8) Effective Linewidth in Thin Film

It is important to note that there have been only a few attempts to measure off-resonance effective linewidths in thin films. The first work is the measurements on permalloy film by Patton *et al.* (1971). The results showed the direct evidence for two-magnon process in thin films. Kabos and Patton (1985) examined the effective linewidth in single crystal YIG films. It indicated that field dependent dielectric losses due to the substrate can obscure the actual magnetic losses and the effective linewidth. The most recent attempt on the thin metal film is by Moosmüller *et al.* (1990). The main result was the observation of the intrinsic losses for far off resonance loss parameter. The near resonance results were quite strange. More experimental as well as theoretical work on metal films is needed. The effective linewidth on multilayer films has never been tested.

(9) Remaining Problems

There are mainly four remaining problems:

First, the measurement accuracy of effective linewidth need be technically enhanced for the HFE and LFE linewidths of low loss materials. The large data scattering can be seen in Figs. 4.12 and 4.13. The higher accuracy helps to resolve the fine structures of the LHE and HFE linewidths

Second, the HFE linewidth remains unexplained even qualitatively although the in-manifold and near-manifold effective linewidth is well understood based on the two-magnon theory with the porosity shift of bulk manifold. The HFE linewidth show microstructure dependence and fairly large value compared with the single crystal linewidth. This problem has been remained unexplained for over four decades.

Third, the porosity and anisotropy scattering is quantitatively in poor agreement with the in-manifold effective linewidth. The quantitative investigations are quite difficult because both of the porosity and anisotropy contributions are important and make the theoretical calculations complicated.

Four, the effective linewidth investigations on thin metal films are far from done, even in the manifold region.

This dissertation focuses mainly on the first and second problems.

5. HIGH PRECISION EFFECTIVE LINEWIDTH TECHNIQUE

In this chapter, a high precision version of the effective measurement technique is developed to resolve the long-standing problems in the constant pursuit of near intrinsic microwave loss. Such pursuit requires the accurate determinations of the magnetic susceptibility and the effective linewidth. The magnetic susceptibility far from ferromagnetic resonance is very small, on the order of 10^{-5} or less. At such low levels, the measurement accuracy becomes extremely important. The relatively low accuracy in all of the previous effective measurements is the main reason that the near intrinsic high field effective (HFE) linewidth has not been obtained in the past four decades. The importance of the cavity measurement accuracy is emphasized in Section 5.1.

One way to pursue high accuracy is to use high performance equipment. The hardware and installation should always be considered carefully for high accuarcy. It is evident that the higher performance leads to a more expensive budget for the construction of the spectrometer system. An inexpensive but challenging method is to optimize the measurement performance by fine adjustments of the available major equipment. The latter is what is done in this chapter.

Three measures are taken to improve the measurement accuracy of the effective linewidth. First, the effective linewidth spectrometer system is optimized in terms of the

measurement stability and the reduction of the systematic deformation due to imperfections and mismatches of the system components. Second, based on the ABA method, the dominant time and temperature drifts in the cavity measurements are eliminated and the second largest random errors are minimized. Third, the data analyses are modified in order to extract the accurate effective linewidth from the raw data of the cavity measurements. These three enhancements are equally important and discussed in Sections 5.2, 5.3, and 5.4, respectively.

5.1. Importance of Cavity Measurement Accuracy

The effective linewidth measurement technique has been well developed by Patton (1972), McKinstry (1991), and Truedson (1993). The resolution has reached 10^{-5} in the imaginary part, χ'', of the microwave susceptibility. However, the resolution does not account for all of the measurement uncertainty. The conventional technique works very well for $\chi''>10^{-3}$, but not for the χ'' values on the order of 10^{-5}. In the extreme high field region above 0.5 T, an ultra-low loss yttrium iron garnet (YIG) sphere is a good example of the failure of the conventional technique. It will be shown in the following sections that the susceptibility resolution is not the dominant error source. The other uncertainty contributions, especially those due to large systematic errors, may be ten to one hundred times larger than the susceptibility resolution.

The importance of measurement accuracy can be understood based on the cavity perturbation equations (4.19) and (4.20) for the determination of the HFE linewidth. The HFE linewidth can be approximately written as

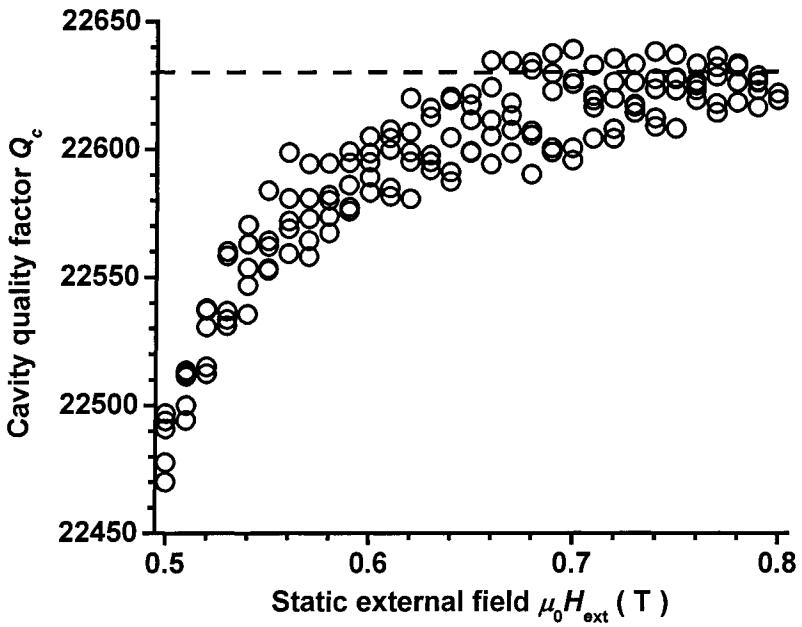

FIG. 5.1. The measured cavity quality factors Q_c as a function of static external field H_{ext}. The open circles show four sets of data points that are measured several times from 0.8 T to 0.45 T and back to 0.8 T. The data are obtained from the high Q cavity shown in Section 4.2.1 with an ultra-dense polycrystalline YIG sphere. The sphere is 2 mm in diameter. Only the data above 0.5 T are shown above. The dashed line indicates the infinite field extrapolated Q-factor Q_∞, which is carefully evaluated in Section 5.3.3.

$$\Delta H_{\text{eff}} = \frac{X_\omega}{X_Q Q Q_\infty} \frac{Q_\infty - Q_c}{\omega_\infty - \omega_c}. \tag{5.1}$$

The errors in $Q_\infty - Q_c$ and $\omega_\infty - \omega_c$ contribute to dominant uncertainties. Both are important at the extreme high fields such as 0.5 T or above for YIG spheres.

The systematic investigations were experimentally made on low Q rectangular cavities. Discussions about the experimental measurements on low Q rectangular cavities may be somewhat misleading in this dissertation since only the high Q cylindrical cavities are discussed in the other chapters. Here take the high Q cavity measurement data as an example.

Figure 5.1 shows four sets of the Q_c data as a function of static external field H_{ext}. The measurements are made several times from 0.8 T to 0.45 T and back to 0.8 T on the high Q TE_{011} cylindrical cavity shown in Section 4.2.1. An ultra dense YIG sphere with a diameter of 2 mm is installed at the center of the cavity. The open circles show the data points. The infinite field extrapolated Q-factor is carefully evaluated based on the method shown in Section 5.3.4 and indicated by the dashed line as a reference Q-factor. The spectrometer system for these measurements is shown in Section 4.2.1. The effects due to the imperfections and mismatches of the system components are minimized.

The data points show the general features of the high field Q_c values as a function of field. The data points at a given field scatter in a range of around ± 25. In other words, the expanded measurement uncertainty of Q_c is around 25 with a coverage factor of 3. The variations of Q_c with H_{ext} H_{ext} at high field are generally very small in comparison with the uncertainty. Q_c is nearly constant at the extreme high fields, approximately above 0.6 T. When the field decreases, Q_c deceases much more rapidly.

One can obtain the uncertainty of χ'' based on the uncertainty propagation law,

$$U(\chi'') = \frac{K_c}{2}\frac{U(Q_c)}{Q_c^2}. \tag{5.2}$$

The above equation is derived from Eq. (4.18). For a simple evaluation, the perturbation theory value 2207 for K_c and the nominal quality factor 2200 for Q_c are used. The total uncertainty of χ'' can be evaluated with $U(Q_c) = 25$,

$$U(\chi'') = 7\times 10^{-5}. \tag{5.3}$$

The absolute measurements with such uncertainties in Q_c and χ'' works well when χ'' is

three times larger than the uncertainty. The effective linewidth measurements have a higher accuracy requirement because ΔH_{eff} also depends on Q_∞ as in $Q_c - Q_\infty$, which is determined from the field dependence of Q_c. Empirically, the ΔH_{eff} measurements requires that χ'' is five to ten times larger than the uncertainty. The approximate requirement is $Q_\infty - Q_c \geq 150$ or $\chi'' \geq 5\times10^{-4}$. This requirement is why the conventional effective linewidth technique only works well below 0.5 T for low loss YIG or when χ'' is larger than or on the order of 10^{-3}.

Note that some of Q_c data above 0.65 T are bigger than Q_∞. If one is forced to use the conventional effective linewidth technique to determine the effective linewidth, one of the consequences is that negative effective linewidths would be obtained at such high fields. For example, see Eq. (5.1). Even the worse case occurs when the Q_∞ value cannot be properly extracted from the field dependence of Q_c. The latter often happens when the spectrometer system is not optimized.

The measurements of $\omega_\infty - \omega_c$ are fairly similar to $Q_\infty - Q_c$. One may argue that the frequency measurement accuracy is very high and the errors in frequency do not affect the effective linewidth too much. It is not always the case, however, that the errors in frequency do not introduce significant errors. First, the field dependent frequency errors will introduce the extra field dependence in X_Q, which is important in the linear fit of $1/Q$ versus X_Q. Second, the term $\omega_\infty - \omega_c$ is in the denominator in Eq. (5.1). Third, ω_∞ may be far off its correct value due to the deformation in the field dependence of ω_c since ω_∞ is the frequency intercept evaluated from the linear fit of ω_c versus X_ω.

5.2. Remarks on Spectrometer Systems

There are mainly four types of errors that affect the effective linewidth measurement accuracy. The first is the resolution that comes with the major equipment. The uncertainty contributions due to limited resolution can be reduced. This will be discussed in Section 5.3. The second type is the random errors that can be minimized by averaging several measurements. The third type is the time and temperature drifts due to the instability of measurement system. This is the main topic of Section 5.3. The last and also most important lies in the systematic distortions in the measurement signal. This type of error is the focus of this section.

The systematic distortions result from the imperfections and mismatches of the system components. Section 5.2.1 shows how the impefection and mismatching affect the cavity response. Section 5.2.2 summarizes how to minimize the dominant systematic deformations for the sake of high accuracy of the cavity measurement.

5.2.1. Systematic Distortions in Cavity Response

The cavity response is the power transmission as a function of the swept microwave frequency. According to Fig. 4.2, the microwave generation and propagation involve the sweep oscillator, cables, isolators, waveguides, network analyzer, detectors, and connections between them. All of these components and connections are not perfect and act as a frequency dependent background. The measured signal is the non-deformed cavity transmission multiplied by the frequency dependent functions, most of which may have fairly weak frequency dependence, which becomes important at the high accuracy level. Therefore, the cavity measurement signal is deformed because of these

components.

The effect of the small distortions on the cavity parameters is investigated using the error simulation. If the deformation is expanded into a Taylor series of the swept microwave frequency, simply stated, the odd terms cause the extra shift in cavity center frequency, but the constant term does not affect anything. The other even terms change the cavity quality factor. These extra frequency and Q shifts are a function of the operating frequency, which varies with static external field. Therefore, the extra shifts are also a function of static external field and play a role of systematic errors in the measurements of the field dependent cavity parameters.

Such systematic distortions are not important in the in-manifold effective linewidth measurements. Inside the bulk manifold, the changes in the cavity parameters due to the sample are large and the systematic deformations are negligible.

The systematic distortions, however, should be carefully treated at extreme high fields or low fields, where the changes in the cavity parameters due to the sample are very small and weakly field dependent. These deformations become very important, especially in a low Q rectangular cavity. The frequency width of cavity resonance is much larger in a low Q cavity than in a high Q cavity. As a result, the cavity measurement must be taken in a wide swept frequency range where the deformations also become larger.

To demonstrate these errors, the distortions in a low Q TE_{102} rectangular cavity is measured. A 0.7 mm single crystal YIG sphere is mounted at the center of the cavity. Figure 5.2 shows the obtained quality factor Q_c as a function of static external field H_{ext}. The open circles are the data points while the solid curve is formed by the connections

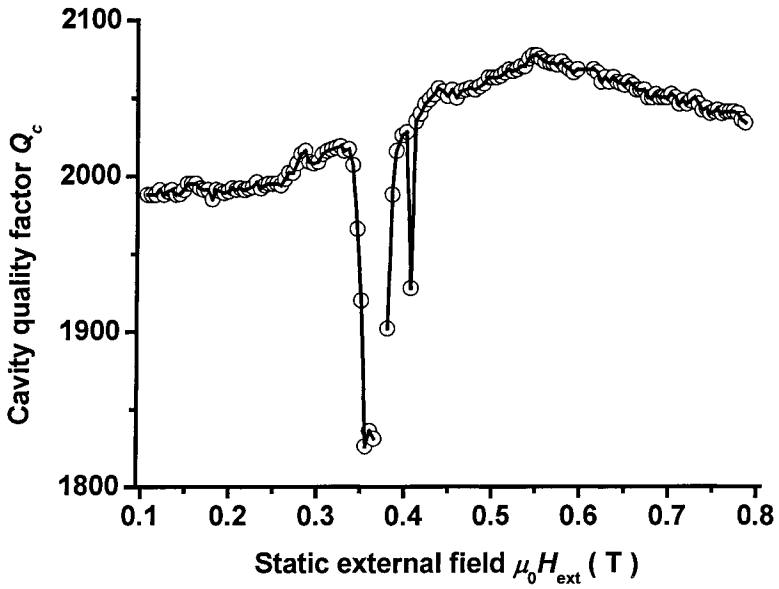

FIG. 5.2. Effect of background deformations on cavity quality factor Q_c. The open circles show Q_c as a function of static external field H_{ext}. The solid curve is the direct connections among the neighboring points. The measurements are on a low Q TE_{102} rectangular cavity with a 0.7 mm single crystal yttrium iron garnet sphere installed at the center of cavity.

between the neighboring points. The measurements were taken using the effective linewidth spectrometer system constructed by McKinstry (1991). A small single crystal YIG sphere is used because the high field Q_c change should theoretically be smaller than 10. Any larger change is due to other effects.

In the high field region above 0.45 T, the quality factor shows strange variations with field. From 0.5 to 0.8 T, Q_c first increases and then decreases. The Q_c drop is around 50. The low field Q_c slowly decreases when the field is far from FMR field. The FMR field is around 0.36 T, as shown by the deep dip near this field. The data also show a one-point dip at 0.42 T. Careful measurements near 0.42 T are also made and it is found that this small dip is repeatable and behaves as a resonance that may be due to

surface modes.

The main point lies in that the field response of Q_c is largely deformed for fields far from FMR. The change at high field is anomalous and much larger than what can be expected for single crystal YIG. Further measurements show that the shape changes with the selection of waveguides, isolators, etc. Therefore, this response comes from the background deformations that can be fairly big.

The following demonstrates why a 3 dB direction coupler is useful. The test is made on the effective linewidth spectrometer system as shown in Section 4.2.1 but without a cavity. The other components are not changed. The measured signal, "A", at the end of the original branch of the cavity is supposed to be the frequency dependent background. The other branch is measured as the reference signal "R". Figure 5.3 shows the measured two signals, "A" and "R" of the two branches of the 3 dB directional coupler, the ratio of A to R, and the input signal. Graphs (a) and (b) show these signals with different cable lengths, around 0.5 m and 1 m, respectively. The frequency range is within 200 MHz of the cavity operating frequency 9.968 GHz. In these graphs, the input signal is measured by the direct connection of the sweep oscillator and the network analyzer without coaxial cables.

The frequency oscillation functions correlate with the cable length. The longer the cable is, the shorter the period in frequency units. This is consistent with the principles of standing waves. Both of signals "A" and "R" are highly dependent on the status of the cable. Even if the cable moves a little bit, these signals will be significantly shifted and twisted. The ratio of "A" to "R" is fairly stable since the rigid waveguide and direction coupler are insensitive to a weak mechanical disturbance. Note that the A/R signal,

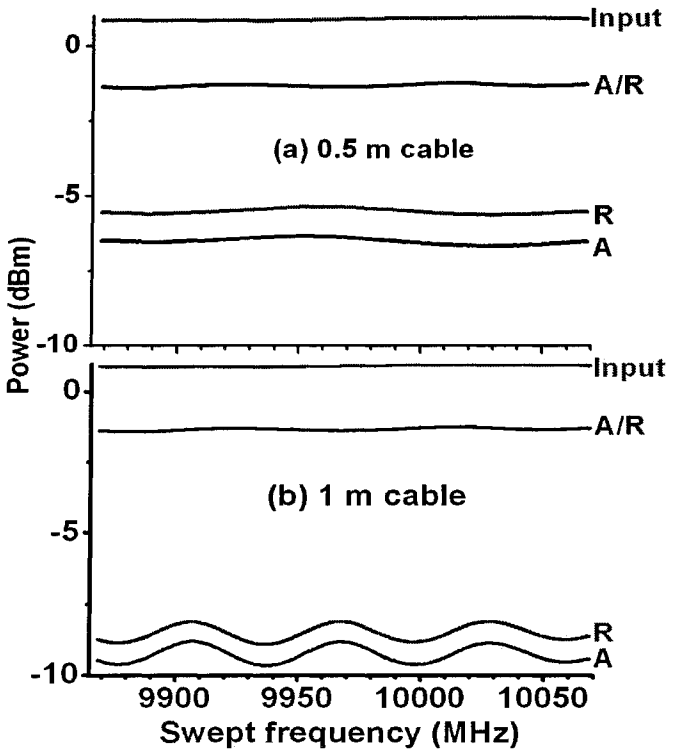

FIG. 5.3. Frequency dependent background as a function of the swept frequency. Graphs (a) and (b) are for a 0.5 m cable and 1 m cable, respectively. The signals of A, R, and A/R, and the input signal are shown, as indicated. For the input, A and R, the vertical coordinate is real powers in the unit of dBm while the A/R curve is a power ratio in a unit of dB. All these signal obtained by a scalar network analyzer and a sweeper with a power output 1 dBm.

unlike the oscillating signals "A" and "R", is nearly flat over the frequency range. These properties of the power ratio provide a possible approach to eliminate most deformations.

In the conventional effective linewidth measurement technique, the signal A is directly used as the cavity input instead of the power ratio A/R. There are two disadvantages to this method. First, the deformation introduces systematic errors into the determination of cavity center frequency and Q-factor. One might think that they are constant shifts in ω_c and Q_c for all measurements so that they would be actually cancelled out in the final determination of the susceptibility and the effective linewidth.

The fact is, however, that these shifts are frequency dependent since for different fields the working cavity frequency is different and the deformations at these different frequencies are different. Second, the operating frequency and the background signal have time and temperature drifts because the properties of the cables, the isolators, the waveguides, and even the sweeper are changing with time or the environmental temperature. The stability of the waveguide system is similar to that of the cables. Even if one slightly touches the system, the cavity center frequency and Q-factor have an abrupt and large change and are never repeatable. These disadvantages are overcome in the measurement of the ratio A/R.

5.2.2. Optimization of Spectrometer System

In order to minimize the effect due to the deformation, four things should be paid attention to, as shown below.

A. Cavity

For the HFE and LHE linewidth measurements of low loss samples, *a high-Q cavity is critical* for two reasons. First, it can be understood from Eq. (5.2) that the higher the Q, the higher the accuracy. Generally, the accuracy is improved at least ten fold by increasing the Q factor in ten fold. Second, the systematic deformations become small and even negligible when the measures mentioned in Sub-section B are taken. Using a high-Q cavity, the frequency range could be very narrow, for example, around 0.5 MHz for $Q_c = 22000$ instead of 5MHz for a low-Q cavity such as $Q_c = 2000$.

The sample should be very stably mounted. The static field is not perfectly uniform.

The non-uniform field generates magnetic force that acts on the magnetic sample. When the field changes, this force also changes. As a result, the sample deviates from its initial position. Even a slight deviation of the sample position results in a substantial change in cavity Q-factor, which plays a role of a systematic error.

B. Background

In the case of no correction, one should measure the background curve in the working frequency range and make sure that *the variation of the background curve is below the level of 0.01 dB,* which is the minimum screen resolution of the HP8757D network analyzer. For a YIG sphere, the working frequency range can be the cavity center frequency range for fields from 0.45 to 0.8 T. The system shown in Fig. 4.2 corresponds to 9962 to 9967 MHz. It is found that the background actually varies below 0.01 dB in the range of 9967 ± 10 MHz. This step is extremely important for the measurements at extremely high fields!!! The reduction of the background requires choosing the suitable system components.

The above adjustments may be quite difficult. The alternative way may be to make corrections for the background curve. Such corrections have been made on the FMR measurement but never on the effective linewidth measurement. The idea is first take the accurate measurement of the background curve and then make corrections in the raw data of cavity response.

If this adjustment is not done, one would obtain a negative effective linewidth or wrong field dependence of Q_c and effective linewidth. Such problems frequently happened at the early stage of this thesis' investigations, when the background problem

was not realized.

C. Directional Coupler

One should carefully choose a 3 dB directional coupler and make sure that the back reflection is negligible (below –40 dB) to the reference branch R. The frequency response of the power ratio should be nearly flat in the frequency range of interest.

D. Measurement Settings

The adjustable settings can be the swept frequency width, the sweep time, and the average factor. The swept frequency width gives the frequency fit range for the determination of the cavity center frequency and Q-factor. The sweep time is the time duration of scanning such a frequency range. For the average factor, the network analyzer obtains several data sets of the cavity response and only saves the average data set, where the number of the data sets for averaging is "average factor".

D.1. Swept Frequency Width

The swept frequency width should be in the range of 1 to 2 times of the cavity resonance width. It was previously thought that the wider swept frequency width might give a higher measurement accuracy or resolution. This is not true. The Lorentzian shape is a nice approximation to the power versus frequency response of a narrow frequency range near cavity resonance, but not for that of a wide frequency range. Simply stated, the cavity response is the multiple microwave interference. The number of these interfering waves is limited by the Q factor. Actually, the interference does not

give a Lorentzian shape. For example, a two-wave interference gives a sine or cosine function. An increase of the number of waves just makes the peaks narrower and sharper.

D.2. Sweep Time

The sweep time should be set as small as possible, for example, 75 milliseconds. The cavity center frequency may changes very fast with rapid temperature fluctuations. For a long time setting, the different parts of the cavity response correspond to different center frequencies. The average of several Lorentzian curves is not Lorentzian. This leads to some unexpected errors of not only the cavity center frequency but also the Q-factor.

D.3. Average Factor

The average factor should be 1, but it is frequently set to be 4. In comparison with an average factor of 1, the random errors in the cavity response as well as those in ω_c and Q_c are significantly reduced. One might therefore favor a large average factor such as 4 (a number higher than 4 makes the network analyzer work unbearably slow) to obtain a relatively high accuracy. Unfortunately, it is found that the actual random errors in a set of cavity measurements have been found to be larger than that without average. The reason lies mainly in that the average of several Lorentzian curves is not Lorentzian. The Lorentzian cavity response is a nonlinear curve. The average over several curves with different center frequencies or Q-factors does not give an averaged center frequency or an averaged Q-factor. The center frequencies and Q-factors in these curves are random and subsequently the introduced errors appear as random-like errors in a number of cavity measurements. The results might be much better if the average were over the inverse of

the transmission cavity response.

5.3. Improved Cavity Measurement

This section shows how the cavity measurement accuracy is improved more than 10 fold of the previous ultra-sensitive measurements (Patton, 1972). Section 5.3.1 provides the evidences of the significant time and temperature drifts, which play a role as the dominant uncertainty source in the high precision cavity measurements. In Section 5.3.2, a well-known metrological method – the repeated ABA method is introduced to eliminate the time and temperature drifts and minimize the random errors that are the second largest uncertainty source. Section 5.3.3 gives the example measurement on an empty cavity using the repeated ABA method. Section 5.3.4 provides a brief description of the modified ABA method, which was used at the early stage of this dissertation' investigation.

5.3.1. Significant Time and Temperature Drifts

Due to the instability in measurement systems, the measured cavity center frequency ω_c and quality factor Q_c vary with time and temperature as in any other measurement system. These variations may come from the warm-up process, ambient temperature changes and time drifts characteristics of electronic and mechanical components. The predictable variations such as temperature dependence are typically corrected, otherwise treated as the type B uncertainties that are not or cannot be evaluated by statistical methods. The unpredictable variations with time and temperature are called the time drift and the temperature drift, respectively. These two drifts correlate with each

other because the temperature drift always behaves like the time drift.

In legal metrology, all the uncertainty sources are treated as random. However, a drift is quite different from a regular random fluctuation in data. The random fluctuation can be significantly reduced by averaging over as few as ten measurements. The drift may not be reduced even by averaging over several hundred measurements. This is because drifts typically do not show a random distribution and the average of the drifts is still a drift.

Figure 5.4 shows a set of representative data of long time cavity measurements. In these measurements, a high-Q cylindrical cavity shown in Section 4.2.1 is operating at a TE_{011} mode with a nominal cavity center frequency 10 GHz. An ultra-dense polycrystalline YIG disk with a 3 mm diameter and a 1mm thickness is mounted at the center of cavity. The cavity is aligned to make the static external field perpendicular to the microwave magnetic field at the site of the sample. A temperature sensor is tightly attached on the outside of the cavity wall to measure the temperature at the attached point. The cavity is exposed to the air and no measure is taken to stabilize the cavity temperature. Before taking data, the spectrometer system warms up for half an hour after the sample installation.

Two static external fields well above the bulk manifold, 0.63 and 0.59 T, are measured in an iterant way so that a direct comparison of the changes due to the field shift and due to the drifts can be made. The field 0.63 T is called "A" field as a reference field and 0.59 T called "B" field as a measurement field. In all the graphs of Fig. 5.4, the corresponding data points at A and B fields are marked by the open circles and the open triangles, respectively. The measurement order of the field is A-B-A-B-A···, as shown by

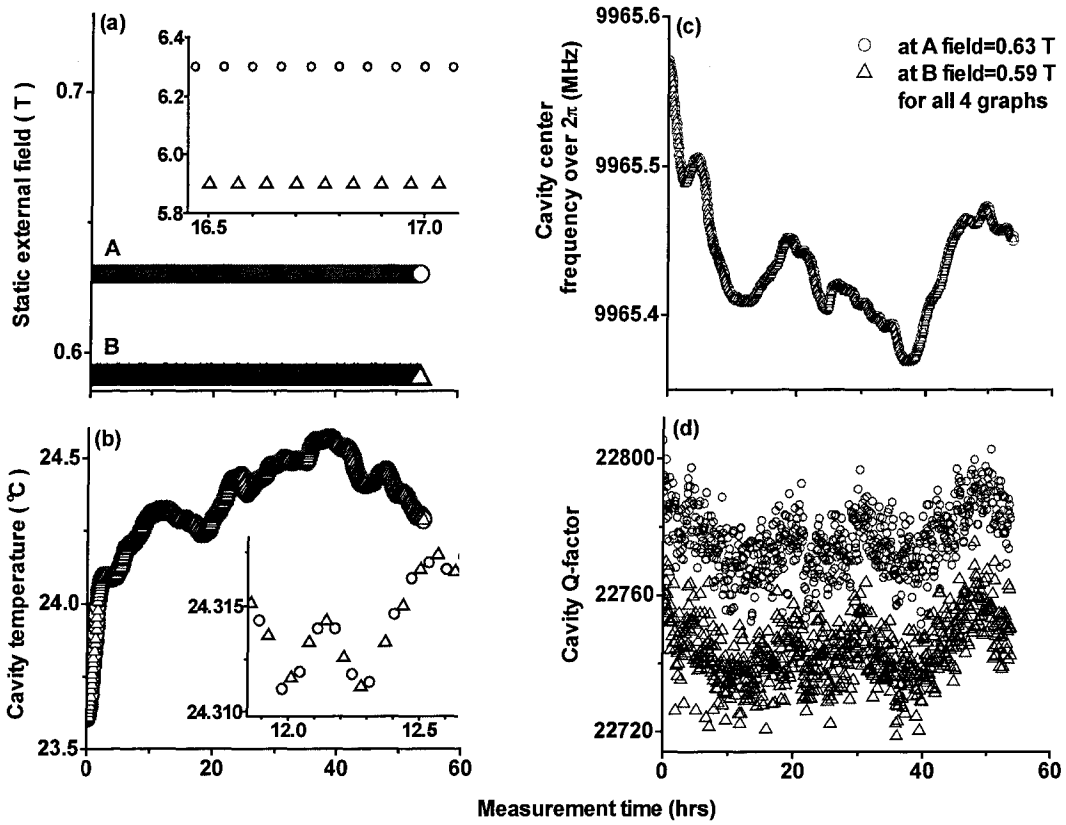

FIG 5.4. Representative plots of long time measurement results of a high-Q cylindrical TE_{011} transmission cavity with a dense yttrium iron garnet sphere at the center of the cavity. Graph (a) shows the measurement field order in the time scale. Two fields are involved, the A field=0.63 T and the B field=0.59T. The inset zooms in the order A-B-A-B-A··· in a short time interval. Graph (b) plots the cavity temperature versus the time and the associate inset zooms in a part of this graph. Graphs (c) and (d) show the cavity center frequency and Q-factor versus the measurement time, respectively. In all these graphs and the insets, the open circles indicate the data points at the A field while the open triangles indicate the data points at the B field.

the measured field versus the time in Graph (a) and its inset. Each point takes almost the same time interval, about 2 minutes. The data of the cavity temperature, center frequency, and quality factor against the measurement time are plotted in graphs (b), (c), and (d), respectively.

There are four points shown in Fig. 5.4. First, the static magnetic field is well stabilized by the GMW magnet power supply. Graph (a) indicates that all the A and B fields are highly repeatable, within a range of ±0.003 mT. With such small field variations, the field dependence of the cavity parameters is negligible at very high fields. This stability allows separate of the variations due to the field changes and the time drift.

Second, there is no abrupt change in the cavity temperature in switching from the A field to the B field. This means that the field switching does not significantly affect the environmental temperature near the cavity, although the current in the electromagnetic coils changes with field. Therefore, the cavity temperature is mainly affected by the environmental temperature. It is necessary to point out that the cavity temperature drifts slowly and smoothly within a typical range of 1 °C a day.

Third, graphs (c) and (d) show that the cavity center frequency and quality factor have pronounced changes with time, or time drifts. The frequency shifts correlate somewhat in a large temperature scale with temperature drifts. The systematic variations with time and temperature are much larger than the random counterpart and the changes due to the field switching. Correlation is hard to identify between the quality factor and the cavity temperature. It is evident that the changes in quality factor are not only from the random errors but also from some other unknown systematic effects. These unknown effects result in a time drift on the order of the random error and the change due to field switching.

The time drifts shown in cavity center frequency and quality factor may introduce some important measurement uncertainties if no steps are taken to remove the time drifts. Especially in the off resonance regions, the cavity parameters Q_c and ω_c have weak field

dependences. The distortion due to the time drifts versus H_{ext} may be so large that it is impossible to determine the parameters Q_∞ and ω_∞.

Finally, the most interesting affect is that the systematic drifts have the same trend for both of the A and B fields. It can be expected that the differences between A and B fields should be nearly time independent except for some random errors. This provides possibility to eliminate these systematic time drifts.

One more examination can be taken about the temperature dependence of the measured cavity parameters. Figure 5.5 re-plots the data in Fig. 5.4. Graphs (a) and (b) show the cavity center frequency and Q-factor as a function of cavity temperature, respectively. The open circles and the triangles represent the data points at the A and B fields, as indicated in graph (a). The lines are the connections between the adjacent points.

Both the cavity center frequency and quality factor shows a linear response with the cavity temperature below 24 ° C. This also corresponds with the first 2 hours of measurement. In graph (a), ω_c may still have some linear temperature dependence in the macroscopic scale after the first two hours. In the moderate frequency scale of ±50 kHz, there is no obvious relation between them. This scale is much larger than the random fluctuations. Due to the relatively large random errors, the parameter Q_c looks like a constant after the first two hours.

As mentioned above, the time drifts in cavity center frequency show some correlation with the temperature changes. One might conclude that these drifts could be corrected using a linear fit with the cavity temperature. Theoretically, that may be right. It is understandable that the size of the cavity varies with the temperature changes due to

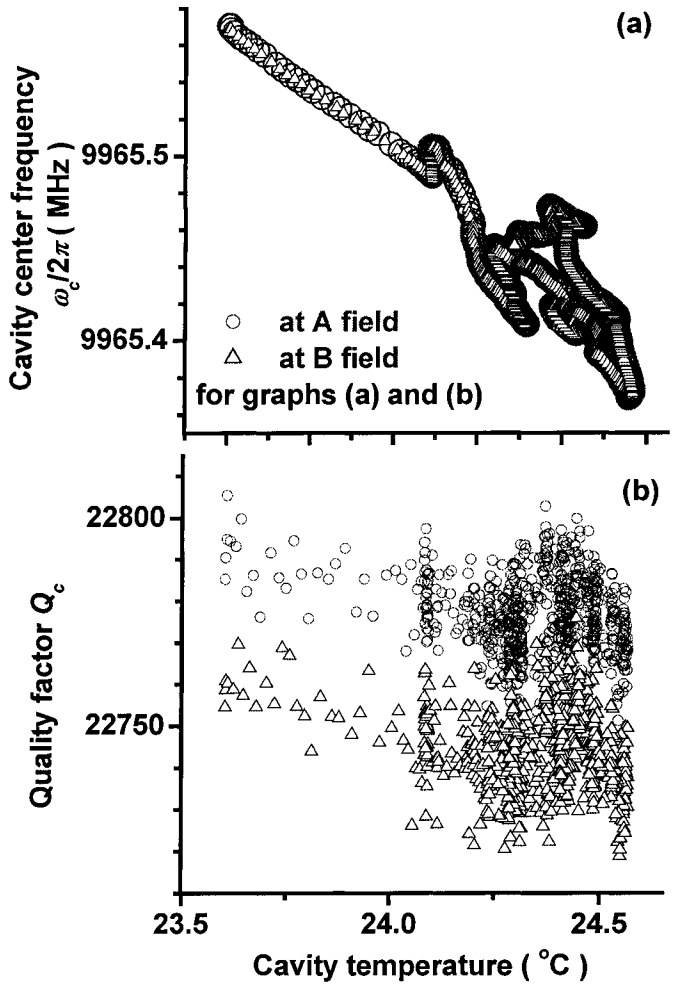

FIG 5.5. Plots of cavity center frequency and Q-factor against cavity temperature. Graphs (a) and (b) shows the cavity center frequency and Q-factor, respectively. The data are from Fig. 5.4. In both graphs, the open circles and the triangles represent the data points at A field and B field, as indicated in graph (a). The lines are the connections between the adjacent points.

the thermal expansion. The cavity center frequency has a fixed relation with the cavity size and so can be connected with the cavity temperature and thermal expansion coefficient.

Practically, the temperature correction is not applicable. First, there are at least 50 kHz that cannot be corrected. This 50 kHz error is much larger than the difference between the A and B fields. In other words, the signal to noise ratio is much smaller than

1 and therefore the high field measurements are not able to be trusted. Second, the slope of cavity center frequency versus temperature is in question. In the previous effective linewidth measurements, one just measured the cavity center frequency against the temperature for 1 hour and obtained the slope. The slopes obtained from the data segments within 1 hour or less are sometimes negative, sometimes positive, and even zero according to graph (a). It turns out that the temperature corrections are practically impossible. This problem often happens when the conventional effective linewidth technique is applied to the high field region. The case in Q_c is worse. The random errors are somehow dominant and any linear fitting is useless.

What causes this temperature problem? Most likely, it comes from the non-uniform distributions of the cavity temperature. Only the temperature at one point of the cavity wall has been measured. Initially, the cavity temperature is largely off the environmental temperature and any small temperature fluctuation is not so important. Both the average cavity temperature and the measured point temperature approximately have a large linear decrease or increase as the time goes. The temperature expansion effect hence causes a nearly linear cavity frequency shift. The cavity center frequency mainly follows the average temperature while the average cavity temperature is generally different from any local point. The slope should not be repeatable. The measured point temperature changes sometimes fast and sometimes slow. After several hours, every part of the cavity independently changes its temperature within a relatively smaller temperature range.

If the average temperature of the whole cavity could be measured, this curve in graph (a) would be much more linear. But the cavity center frequency also drifts with the

instability of the other components. One bit of evidence is that the cavity frequency sometimes changes abruptly due to sudden changes in the connections. The Q-factor in graph (b) behaves similarly. Now it can be concluded that these drifts cannot be properly corrected by using the cavity temperature.

5.3.2. Repeated ABA method

The fact that the drifts at the A and B fields follow the same time dependence provides the feasibility of the elimination of these drifts. A standard metrological method – ABA can be used to eliminate the pronounced drifts described in Section 5.3.1. The ABA method involves the measurement of the difference of any measured quantity at two point fields. It is only applicable in the case where (a) the drifts are linear with time in a short time scale, e.g., in an ABA cycle; (b) the time interval between any two neighboring measurements is constant. This is true for the cavity measurements as in Fig. 5.4. An ABA cycle takes around 6 minutes since the time interval between two neighboring point in Fig. 5.4 is about 2 minutes.

Figure 5.6 shows an ABA cycle for a quantity ψ. First, the value of ψ at the A field is measured, namely ψ_{A1}. Then the field is switched to the B field, and the value of ψ, that is ψ_B, is measured. Finally, the field is switched back to the A field, where the measured value of ψ is ψ_{A2}. Each measurement takes a time interval dt. The measurement times of ψ_{A1}, ψ_B, and ψ_{A2} are 0, dt, and $2 \cdot dt$, respectively, as shown in the figure. The averaged value at the A field can be obtained by $\psi_A = (\psi_{A1} + \psi_{A2})/2$. Its equivalent measurement time should be dt, the same as the B field measurement time, since it is assumed that only linear time drifts exist within a reasonably short time range.

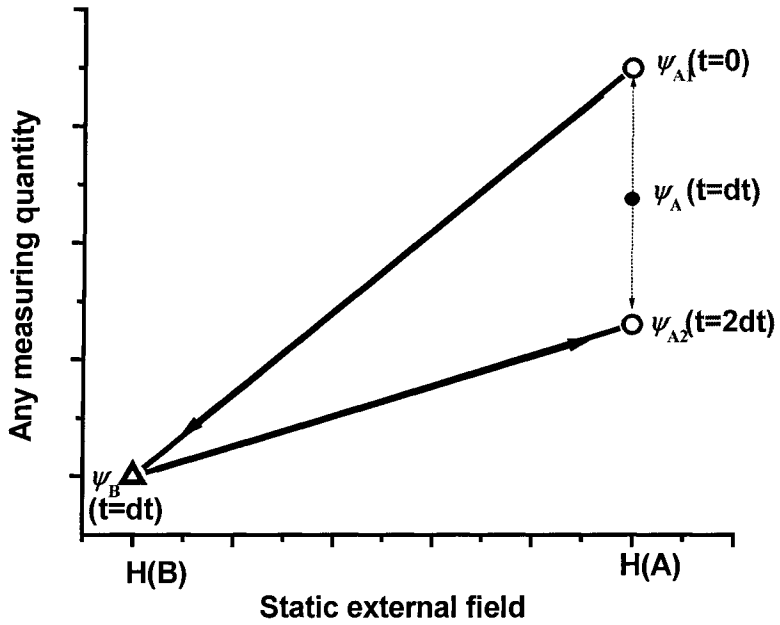

Fig 5.6. An ABA cycle for a quantity ψ at two different static external fields. The open circles show the values of ψ_{A1} and ψ_{A2} that stand for the values of ψ at the A field at the time $t = 0$ and $t = 2dt$, respectively, where dt is the time interval between two neighboring measurements. The dashed line with both ends arrowed indicates the difference between ψ_{A1} and ψ_{A2}. A solid dot at the center of this line represents the average of these two measurements at the A field. The equivalent measurement time of the average is $t = dt$, as indicated. The open triangle shows the measured value of ψ at the B field at the time $t = dt$. The arrowed lines show the time order of these three measurements.

In some sense, the ABA method means simultaneous measurements at two fields. In the last step, the difference between A and B field is evaluated,

$$\Delta\psi = \psi_B - \psi_A . \tag{5.4}$$

In the ABA method, the linear time and temperature drifts are wholly compensated. Application of the ABA method to the cavity measurement compensates the systematic errors in the differences of Q_c and ω_c between any two fields. The random errors,

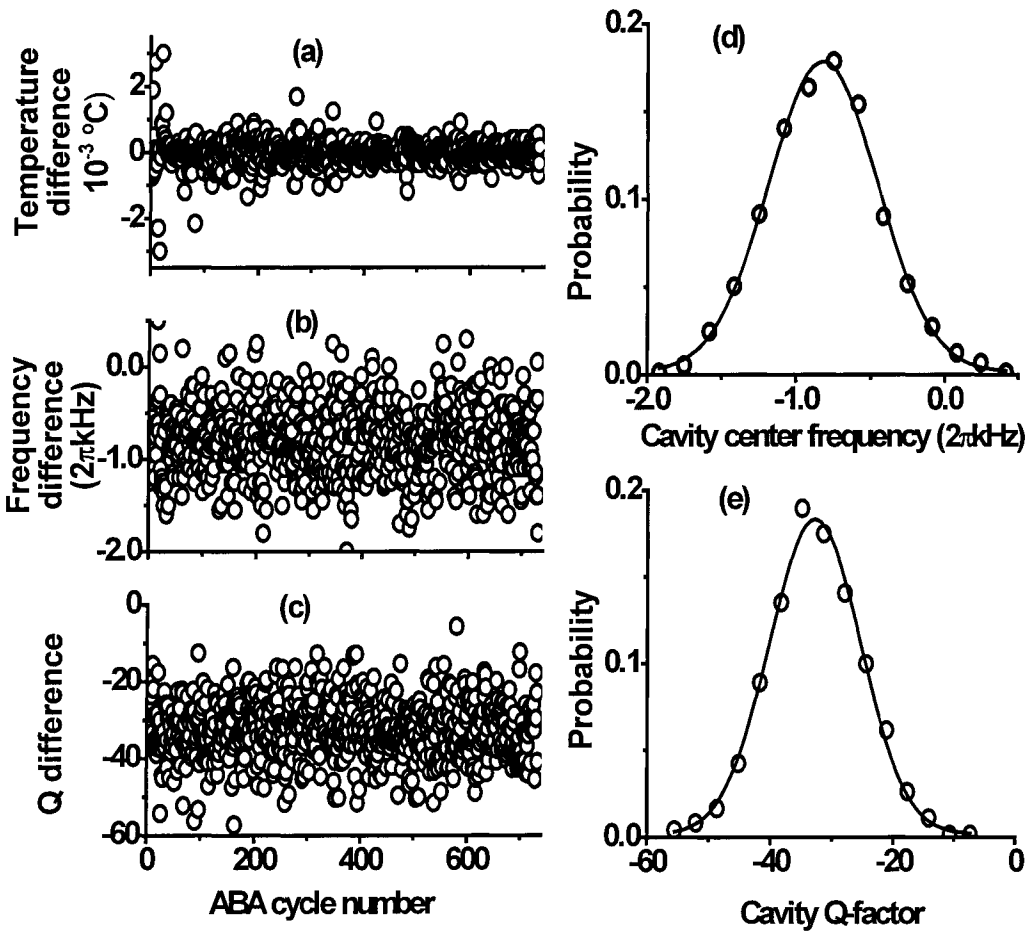

FIG. 5.7. ABA analyses of the cavity temperature, center frequency and Q factor difference between A and B fields. Graphs (a), (b), and (c) show the cavity temperature difference, the cavity center frequency difference, and the Q-factor difference versus the ABA cycle number. Graphs (d) and (e) plot the data distributions of the cavity center frequency difference and the Q-factor difference. The open circles represent the real calculated probability and the sold curves are Gaussian fittings.

especially those in Q_c, can be largely reduced by increasing the number of cycles and averaging all of the cycles.

Based on such effectively simultaneous measurements, another promising advantage of the ABA cavity technique is that the cavity temperature need no longer be stabilized at a high precision level. A water circulator with accuracy ±0.01°C was

previously used. One would be embarrassed by the heat leakage, the waiting time for temperature stabilization, and the sample installation in the magnet gap with a limited size. One is then anxious to give up the temperature stabilization approach if possible. The ABA method provides this possibility. On the other hand, even with a water circulator the cavity temperature still fluctuates very fast and non-uniformly in a narrow range, i.e., ±0.01 °C. This makes the temperature correction impossible and the high accuracy cannot be obtained.

Figure 5.7 shows the ABA analyses of the cavity measurement data shown in Fig. 5.4. The differences of cavity temperature, center frequency, and Q-factor between the A and B fields are determined simply using Eq. (5.4) by replacing ψ with cavity temperature, center frequency, and Q-factor, respectively. Graph (a) shows the temperature differences versus the cycle number. The temperature differences are found to be small, on the order of 10^{-3} °C, which even for a single ABA cycle is much less than the typical temperature stabilization accuracy 0.01°C using a water circulator. This means that the cavity measurements with the ABA method are actually much better than that with a water circulator. Such small temperature differences are based on the slow and smooth change of the cavity temperature. For this reason, the cavity is usually shielded by layers of cloth or cotton, but the shielding is found unnecessary. The averaged temperature difference is -2×10^{-5} °C so that there is no necessity for temperature correction. Graph (a) also shows large temperature fluctuations in the first 1-2 hours. Subsequently the warm up time of 1-2 hours in the conventional measurement technique is necessary for the stability of the whole system.

Graphs (b) and (c) show the cavity center frequency and Q-factor differences

between the A and B fields versus the cycle number. The data distributions indicate that the irregular drifts in the ω_c and Q_c curves completely disappear. Only the random errors in the individual ABA cycles exist. These long time (more than two days) measurements, or many ABA cycles, also indicate that the measurements are highly reproducible. This provides the possibility of the measurements of many of other B fields at each of which many ABA cycles can be performed. The full field range cavity measurements can hereby be done in practically any long time range until the accuracy is met using as large a number of cycles as one wants. The data distributions are also calculated and shown in graphs (d) and (e). The open circles indicate the calculated probability while the sold curves are a Gaussian fit. The nice fittings imply that both of the data distributions follow the normal distribution and further, that only the random errors are important for a single ABA cycle.

The repeated ABA method can give the necessary high precision determination of cavity the center frequency and Q-factor differences. The type A expanded uncertainties of the averaged ω_c and Q_c differences, $U(\overline{\Delta Q})$ and $U(\overline{\Delta\omega_c})$ are the standard deviations multiplied by the coverage factor (equal to 3 here). The type A uncertainties are actually equal to the total uncertainties since the systematic drifts have been eliminated.

$$\begin{aligned} U(\overline{\Delta Q_c}) &= 0.56 \\ U(\overline{\Delta\omega_c})/2\pi &= 0.028 \text{ kHz} \end{aligned} \tag{5.5}$$

As mentioned above, the uncertainties in the conventional technique are around 25 in Q_c and 50 kHz in $\omega_c/2\pi$. In comparison, the uncertainties in Eq. (5.5) are extremely small.

The uncertainty of single absolute measurements of ω_c and Q_c due to random errors can also calculated from the standard deviations,

$$U(Q_c) = 12$$
$$U(\omega_c)/2\pi = 0.61 \text{ kHz} \tag{5.6}$$

Even despite of the large systematic drifts, the accuracy can be improved more than 20 times in comparison with the conventional effective linewidth technique.

The use of the repeated ABA method into the cavity technique is a revolutionary enhancement for the off resonance effective linewidth measurements in which the accuracy is extremely important.

5.3.3. Empty Cavity Test

This section gives example cavity measurements with the repeated ABA method. The empty cavity measurements that are impossible with the conventional technique due to accuracy problem are made on the cavity center frequency and quality factor. Figure 5.8 shows the measured center frequency in graph (a) and quality factor in graph (b) as a function of static external field. The measurement is based on the repeated ABA technique that is discussed in Section 5.3.2. The open circles show the data points with uncertainty bars (type A) for a coverage factor of 3. The solid line in graph (b) is a linear fit, which gives a slope of –0.046/T.

It takes around 6 days (24 hours a day) to perform this test with a few interruptions to set new fields. The order of the measurement fields is 0.75, 0.55, 0.5, 0.4, 0.2, 0.1, 0.85, 0.9, 0.95, and 0.51 T in time. The final field point of 0.51 T is to check the measurement repeatability by the comparison with the 0.5 T field. The reference field (A field) is 0.8 T.

A high field is taken as the reference field, H_{ref} = 0.8 T, as mentioned above. The

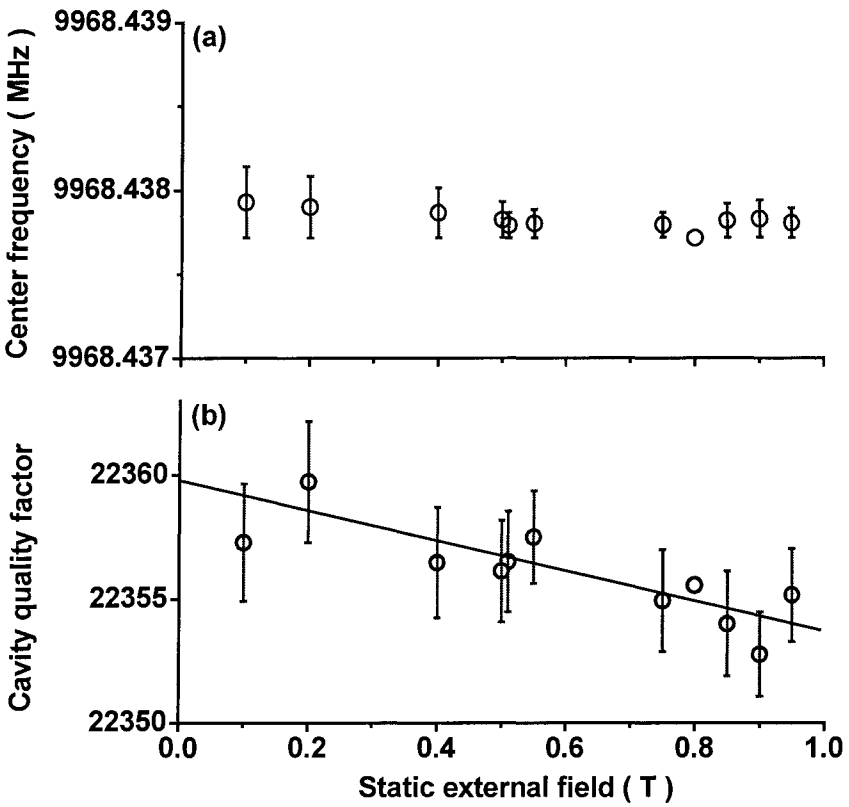

FIG. 5.8. Empty cavity parameters as a function of static external field. Graphs (a) and (b) plot the empty cavity center frequency and Q-factor against the external static field, respectively. The open circles show the data points and the capped vertical lines do the expanded uncertainty bars with a coverage factor of 3. The data points without uncertainty bars correspond to the reference field. The line in graph (b) is a linear fit which gives a slope of –4.6 /T.

cavity parameters in other fields are measured with about 100 ABA cycles against this reference field. For a given static external field, H_{ext}, each ABA cycle is used to determine a $Q_c(H_{\text{ext}})$ difference, namely $\Delta Q_c(H_{\text{ext}})$, and a $\omega_c(H_{\text{ext}})$ difference, namely $\Delta\omega_c(H_{\text{ext}})$, between H_{ext} and H_{ref}. The average differences, $\overline{\Delta Q_c}(H_{\text{ext}})$ and $\overline{\Delta\omega_c}(H_{\text{ext}})$, are calculated for the further determination of the absolute cavity center frequency $\omega_c(H_{\text{ext}})$ and Q-factor $Q_c(H_{\text{ext}})$. These absolute parameters at H_{ext} are obtained by,

$$\omega_c(H_{\text{ext}}) = \omega_c(H_{\text{ref}}) + \overline{\Delta\omega_c}(H_{\text{ext}}). \tag{5.7}$$

and

$$Q_c(H_{ext}) = Q_c(H_{ref}) + \overline{\Delta Q_c}(H_{ext}). \quad (5.8)$$

Here, $\omega_c(H_{ref})$ and Q-factor $Q_c(H_{ref})$ are the average values of all the absolute cavity center frequencies and Q-factors at the reference field, respectively.

The data in Fig. 5.8 prove that the repeated ABA method is very useful for the high precision cavity measurements. First, the measurement accuracy with a reasonable number of ABA cycles is very high. Note that the conventional cavity measurement gives an uncertainty of 25 in Q_c and about 50 kHz in ω_c. The uncertainties shown in graph (a) and (b) are less than 2.5 in the quality factor and 0.2 kHz in the center frequency, respectively. Second, based on the comparison of the measurement results at 0.51 T and 0.5 T, the measurements are also very stable.

No important field dependence of the empty cavity parameters is found in graphs (a) and (b). It is evident that the empty cavity center frequency does not vary with the static magnetic field. For the empty cavity quality factor, the linear fit in graph (b) shows a slight dependence. This may be due to the field dependence of the finite conductivity, just as in the Faraday effect. The slope can be either neglected or corrected in the effective linewidth measurements.

5.3.4. Modified ABA method

In the early investigations of this dissertation, a modified ABA method is used instead of the repeated ABA method. In metrology, the ABA and ABBA methods are typically used in international comparisons of the calibrations (or verifications) of high precision national standards. The ABBA method is not discussed here. The modified

ABA method is a "lazy" method and typically used to perform the calibrations of the low level metrological standards. Using the modified method, the time and labor for calibrations can be largely reduced, but the measurement accuracy is lower than the ABA and ABBA methods. The details of the other methods refer to Bich *et al.* (1993/4)

The difference between these two methods is in the measurement sequence. The modified ABA method is specifically for several standards calibrated at the same time. The measurement order is listed below,

(a) One calibration standard B: A, B, and A.

(b) Two calibration standards (B_1, B_2): A, B_1, B_2, B_1, and A

(c) n calibration standards (B_1, B_2, ..., B_n): A, B_1, B_2, ..., B_n, B_{n-1}, ..., B_1, and A.

The cases (b) and (c) are the so-called modified ABA method.

In these cavity measurements, the above A and B standards are replaced by the static external fields. Namely, the cavity parameters are measured at the fields that are according to the sequence H_{ref}, H_1, H_2, ..., H_{n-1}, H_n, H_{n-1}, ..., H_2, H_1, and H_{ref}. The measured parameters at the same field are then averaged.

Using the modified ABA method, the time or temperature drifts are only compensated in part. The cycle takes a relatively longer time than the ABA method. In this relatively long time, the time and temperature drifts are not linear with time. The longer the time is, the larger the residual drifts. The residue drifts can be further reduced by running the cycle many times and averaging.

The other disadvantage lies in that the temperature corrections are generally necessary. This is because the average temperature at a field is different from that at the other fields and the reference field. Conventionally, the temperature coefficients are

obtained from the linear fits based on a set of data that are measured at a fixed field. According to Fig. 5.5, this conventional approach cannot give the accurate determinations of the temperature coefficients. Therefore, a better approach is developed here.

It is assumed that the temperature coefficients only depend on the system components, especially on the cavity, but do not depend on the static magnetic field. This assumption is fairly reasonable because figure 5.5 shows that the temperature dependence of the cavity parameters are exactly the same at the A and B fields. Based on this assumption, one can model the linear temperature dependence as,

$$\psi(H_{\text{ext}}, T_c) = \psi(H_{\text{ext}}, \overline{T_c}) + C_T \cdot (T_c - \overline{T_c}). \tag{5.9}$$

Here, the quantity ψ represents either the cavity center frequency and quality factor, $\overline{T_c}$ is the average of the cavity temperature T_c at H_{ext}, and C_T is the linear temperature coefficient. This temperature coefficient is the same at any field.

At each field, one can obtain a set of data, ($\Delta\psi$, ΔT_c), from the measurements using the repeated modified ABA method, where

$$\Delta\psi = \psi(H_{\text{ext}}, T_c) - \psi(H_{\text{ext}}, \overline{T_c}) \tag{5.10}$$

and

$$\Delta T_c = T_c - \overline{T_c}. \tag{5.11}$$

The model of Eq. (5.9) gives the fitting equation,

$$\Delta\psi = C_T \Delta T_c. \tag{5.12}$$

This fitting equation is in a general form that is independent of field. This means that such a linear fit is applicable to all fields. Suppose that each field is measured $2n_c$

times where n_c is the number of cycles. For one field, one has $2n_c$ points of $(\Delta\psi\ ,\ \Delta T_c)$. The extension to other fields leads to $2n_c \cdot n$ points of $(\Delta\psi\ ,\ \Delta T_c)$ where n is the number of measured fields. The total number is slightly different from the number of real measurements. This is because fewer measurements at the last field are performed than the other fields. One then obtains a large number of these points $(\Delta\psi\ ,\ \Delta T_c)$. This provides an accurate fit of C_T based on Eq. (5.12). This is equivalent to the conventional way that one first figures out the temperature coefficient at each field and then takes an average over these coefficients.

5.4. Improved Data Analyses

The analyses of the cavity measurement data are modified so as to remove nonphysical contributions to the effective linewidth. Section 5.4.1 shows how to make the corrections in cavity quality factors due to the field dependent shift of the cavity center frequency. The gyromagnetic ratio is finely adjusted in Section 5.4.2. The field dependence of the HFE linewidth is taken account for in Section 5.4.3. Section 5.3.4 provides a simplified uncertainty evaluation of the effective linewidth.

5.4.1 Frequency Correction in Cavity Q-factor

The cavity center frequency shifts with the magnetic susceptibility of the inserted sample due to the change of the static external field. This frequency shift also leads to a shift in the cavity wall losses as well as the total cavity Q-factor. Dr. Jerry J. Green proposed that the Q-factor due to cavity wall eddy current losses is frequency dependent and should be subject to the corresponding frequency corrections when he visited

Colorado State University in the summer of 2003. The wall losses are assumed to dominate in the total losses for the off resonance effective linewidth measurements so that such frequency dependence is used to make corrections in cavity Q-factor.

Based on Green's idea, prior to the susceptibility analysis to obtain $\Delta H_{\text{eff}}(H_{\text{ext}})$ from the frequency and Q_c data, an additional correction was applied to the measured Q_c values to account for the small but possibly significant frequency dependence of the non-magnetic part of the quality factor. In the effective linewidth analysis, it is assumed that the Q_c change with field comes only from the magnetic losses and the χ'' term in Eq. (4.18). However, the change in the cavity frequency due to the χ' term in Eq. (4.17) can also affect the cavity Q through the frequency dependence of the conductivity losses in the cavity walls. The nonmagnetic factor Q_c of a microwave cavity generally scales with the inverse of the electromagnetic skin depth of the metal that makes up the cavity, and this skin depth, in turn, scales with $1/\sqrt{\omega_c}$. If the frequency changes are small, the frequency shift Q_c correction is given as

$$\delta Q_c = Q_\infty \cdot (\omega_c - \omega_\infty)/2\omega_c . \tag{5.13}$$

With this final correction, the operational equation to replace Eq. (4.18) is

$$\chi'' = \frac{K_c}{2}\left(\frac{1}{Q_c - \delta Q_c} - \frac{1}{Q_\infty}\right). \tag{5.14}$$

One needs $-\delta Q_c$ in order to back correct from the measured Q_c and ω_c at a given field back to the value one would have without the eddy current shift of the nonmagnetic part of Q_c from Q_∞. For low loss samples of the sort discussed in this thesis, this frequency correction, as well as the changes in the ΔH_{eff} calculation procedure from that

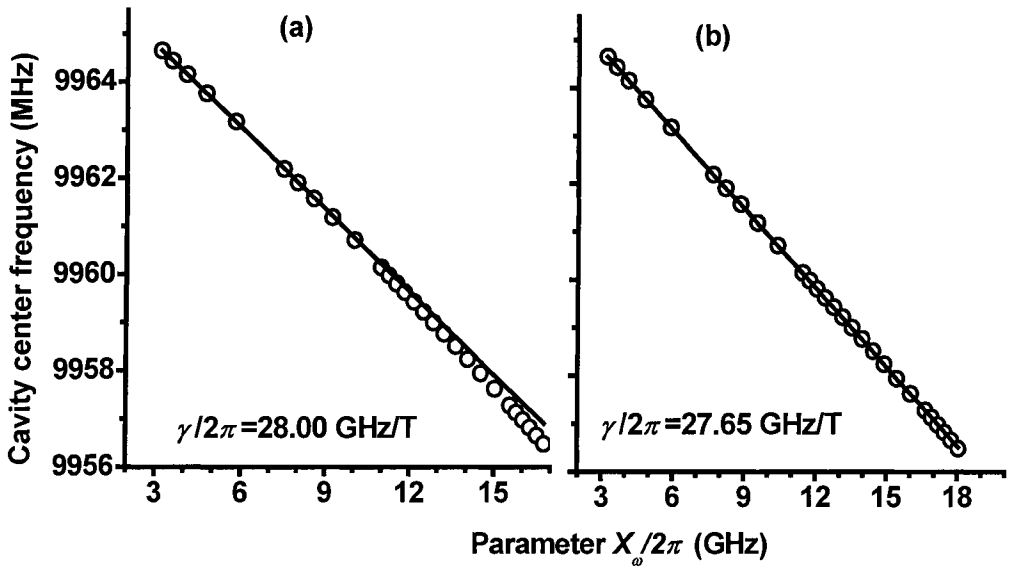

FIG. 5.10. The adjustment of the gyromagnetic ratio γ in the linear fit of the cavity center frequency ω_c versus the parameter X_ω on an ultra dense polycrystalline yttrium iron garnet 2 mm sphere. The field range here is 0.415 to 0.8 T. The data points indicated by the open circles are calculated using $|\gamma|/2\pi = 28$ GHz/T and $|\gamma|/2\pi = 27.65$ GHz/T in graphs (a) and (b), respectively. The solid straight lines are the linear fits of the first 8 points from the lower value of X_ω.

used in Chapter 4 amount to a change within the effective linewidth of 10% or less.

5.4.2. Adjustment of Gyromagnetic Ratio

In the off resonance measurements, a nominal value of the gyromagnetic ratio γ is typically used to determine ω_∞. For the pure YIG crystals, $|\gamma|/2\pi = 28$ GHz/T, which usually applies to the polycrystalline YIG samples. The gyromagnetic ratio depends on the microstructure of the sample, such as the porosity, the random orientation of the magnetic crystalline anisotropy, etc. To take account of such effects, the best way is to directly measure the gyromagnetic ratio. The problem lies in the assumption that the

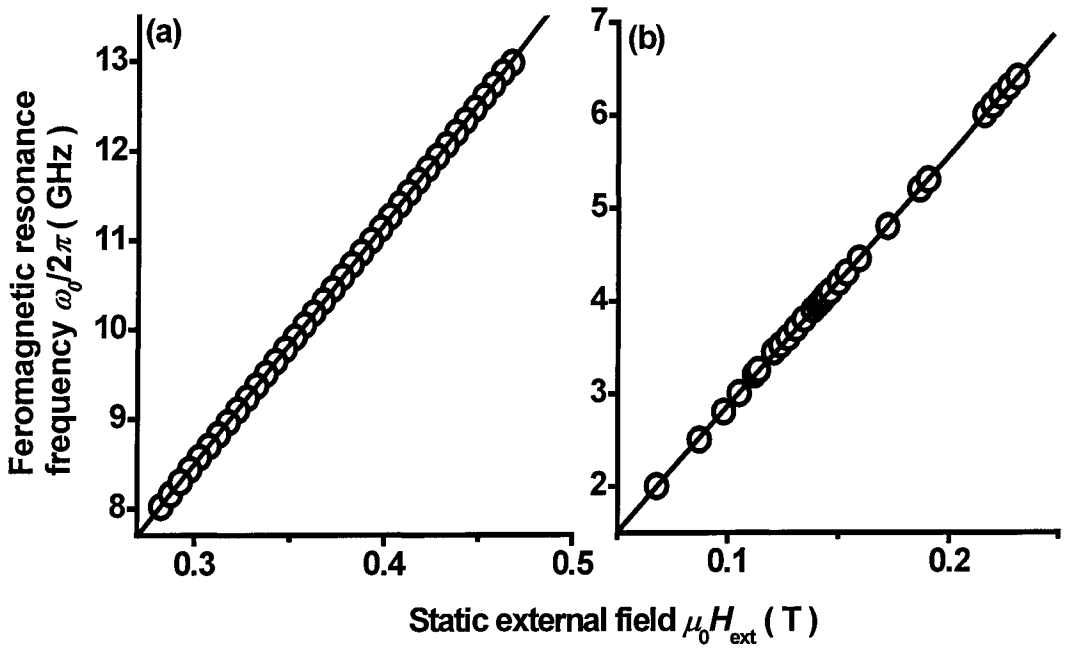

FIG. 5.9. Ferromagnetic resonance (FMR) frequency as a function of the static external field for an ultra-dense polycrystalline yttrium iron garnet sphere with a diameter of 2mm. The open circles indicate the measured data points while the solid straight lines are the linear fit in both graphs. The data in graph (b) were measured by S. Kalarical (unpublished).

gyromagnetic ratio is field dependent. It is impossible to measure the gyromagnetic ratio at high fields using a standard FMR technique since the FMR field cannot be above bulk manifold in field.

The assumption of the field dependent gyromagnetic ratio may be unnecessary. The FMR measurements in a large field range have been done on an ultra-dense polycrystalline YIG 2mm sphere. Figure 5.9 shows the FMR frequency as a function of the external static field. The field range is divided two parts, 0.28-0.48 T in Graph (a) and 0.06-0.24 T in Graph (b). The data in Graph (a) are obtained from a frequency swept response of a shorted waveguide with the sample attached on the bottom. Those in Graph (b) were measured by S. Kalarical (unpublished) and obtained from a field swept

response of a stripline with the sample inside. Both graphs show the nearly perfect linear fit indicated by the solid straight lines.

The Kittel condition tells that the slopes of the linear fits give the gyromagnetic ratio. The nice fits and the same slope imply that the gyromagnetic ratio remains constant in these two large field ranges, or 0.06-0.48 T, that cover not only most of the bulk manifold but also the off resonance (low field) region. One can conclude that the magnetic gyromagnetic ratio with a different value from single crystals is approximately field independent for the full field range including the in-manifold region and the off resonance region.

Instead of direct measurements, the gyromagnetic ratio can be adjusted in a linear fit of ω_c versus X_ω in the effective linewidth calculations. A correct value of the gyromagnetic ratio gives a perfect linear fit, otherwise a poor fit is obtained. Figure 5.10 shows example plots for the adjustment of the gyromagnetic ratio. The original data are obtained for the cavity measurements on a 2 mm ultra-dense polycrystalline YIG sphere. The parameter X_ω is a function of γ. This parameter is calculated using $|\gamma|/2\pi = 28.00$ GHz/T in Graph (a) and $|\gamma|/2\pi = 27.65$ GHz/T in Graph (b). The linear fits indicated by the solid lines are based on the first 8 points which correspond to the high field range of 0.48-0.8 T. The slopes of the linear fits are the negative inverse of the cavity calibration factor K_c.

The fit in Graph (a) deviates from the data points while graph (b) has a nice linear fit. This means that the value of the gyromagnetic ratio for single YIG crystals, $|\gamma|/2\pi = 28$ GHz/T, is improper for even this ultra-dense YIG sample and the real value

should be $|\gamma|/2\pi = 27.65$ GHz/T, which nicely matches up with the direct measurement value 17.6 GHz/T of this sample (Nazarov, 2003). Therefore, the gyromagnetic ratio is finely adjusted to make a nearly perfect linear fit of ω_c versus X_ω for the determination of K_c and ω_∞. This adjustment technique can be applicable not only to the off resonance region but also to the in-manifold region, including the resonance field.

One might favor $|\gamma|/2\pi = 28.00$ GHz/T and a frequency dependent cavity calibration factor from the deviation in Graph (a). There is no firm reason for such a frequency dependence since the frequency has only a tiny change of ±5 MHz in comparison with the absolute frequency of around 10 GHz. Moreover, the gyromagnetic ratio of the polycrystalline YIG materials was previously assumed to be that of single crystals in the determination of the calibration factor and the infinite field extrapolated cavity center frequency, which was used to calculate the susceptibility. The effective linewidth as well as the gyromagnetic ratio is calculated from the real and imaginary part of the susceptibility. The gyromagnetic ratio was found to have a non-physics field dependence, contrary to the known fact that the gyromagnetic ratio has weak field dependence. (McKinstry, 1991) Using the adjustment of the gyromagnetic ratio introduced above, the final calculated gyromagnetic ratio only shows weak field dependence as expected.

5.4.3. Considerations of Field Dependence of High Field Effective Linewidth

The infinite field extrapolated Q value Q_∞ has to be determined for the calculations

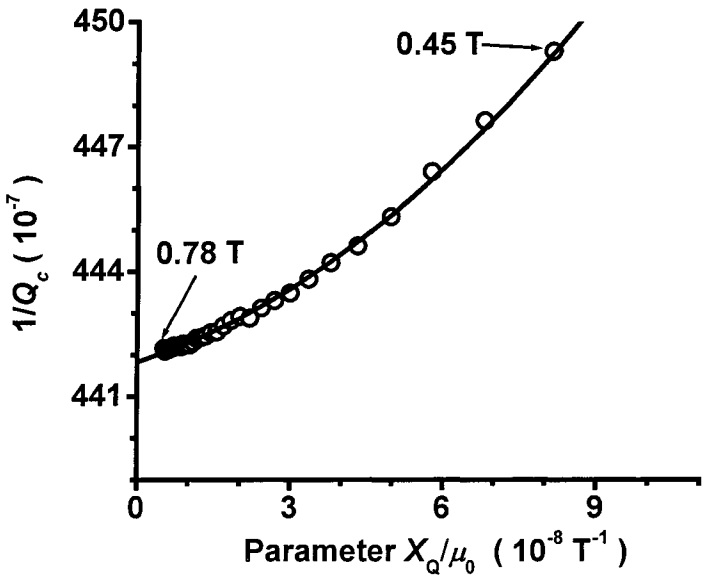

FIG. 5.11. A representative plot of the inverse Q-factor $1/Q_c$ versus the parameter X_Q. The open circles show the data points obtained from the cavity measurements on an ultra-dense yttrium iron garnet 2 mm sphere from 0.45 to 0.78 T as indicated. The solid curve is a quadratic fit. The intercept at the vertical coordinate is the inverse of the infinite field extrapolate cavity-Q, namely, $1/Q_\infty$.

of the imaginary part of the susceptibility. The empirical value of Q_∞ is usually obtained from a linear fit of $1/Q_c$ and X_Q based on the assumption that the HFE linewidth represents the intrinsic field independent linewidth. The corresponding slope is the ratio of the intrinsic effective linewidth to the cavity calibration factor.

Is the high field effective linewidth really intrinsic or constant? "The truth is in the data", Patton said. Actually, the high accuracy curve of $1/Q_c$ versus X_Q typically shows a curvature even in the high field region. The early work was blind to this bent curvature and insists on the linear assumption.

Figure 5.11 shows a representative plot of $1/Q_c$ versus X_Q in the field range of 0.45 to 0.78 T on the 2mm ultra-dense YIG sphere. As reference, the high field edge of

the spin wave manifold is at 0.415 T. The solid curve is a quadratic fit of the data points indicated by the open circles. The extrapolated intercept at the coordinate of $1/Q_c$ gives $1/Q_\infty$.

It is evident that the linear function cannot give a nice fit for all of the data points. The linear fit of a segment of data points near different fields (or X_Q) gives different intercepts and different values of $1/Q_\infty$. The field dependent curvature implies that the effective linewidth in the high field region is also field dependent. The nice quadratic fit implies that the effective linewidth approximately depends linearly on X_Q. What the field dependence actually is subject to the loss origins. For example, the eddy current losses dominate in the HFE linewidth of hexagonal barium ferrites, and subsequently the specific field dependence due to eddy current losses is used to determine Q_∞, as in the work of Truedson (1993). For pure YIG materials, the effective linewidth in the extremely high field region, for example, above 0.5 T for dense YIG, could be assumed to be linearly dependent on X_Q or be a near Lorentzian tail function of H_{ext}.

If Q_∞ was obtained by the linear fit of $1/Q_c$ versus X_Q, two problems might arise. First, the effective linewidth results would be larger than expected. This is why the previous high field effective linewidth, even for large grain sizes, is always significantly larger than that of a single crystal (Patton, 1970). Second, the calculated effective linewidth might have a larger value at a higher field. This increase with the field is nonphysical and artificial since it is well known that the higher the field is, the smaller the HFE linewidth.

A good way is to make a direct measurement of Q_∞. The magnetic energy losses

are "turned off" if the internal static field is parallel to the microwave magnetic field right at the site of the sample. The cavity Q is equal to Q_∞ in this case. Q_∞ can also be obtained from the measurements of the cavity Q against the angle between the internal static field and the microwave magnetic field. Unfortunately, the magnet used for the investigation of this dissertation cannot be rotated. Although a smart design makes the cavity rotatable, this rotation also changes the status of the system so that the cavity Q also changes.

The above discussions are for the off resonance measurements in which the change in the cavity Q is usually small and so the careful determination of Q_∞ is required. For the in-manifold measurement, however, the cavity Q is large off Q_∞ and the imaginary part of the susceptibility can be calculated using the cavity Q, at a very high field, as Q_∞.

5.4.4. Simplified Uncertainty Analysis of Effective Linewidth

Note that the results without uncertainty expressions are incomplete. The uncertainty analysis of the effective linewidth is discussed in this section.

The effective linewidth is extracted from the magnetic susceptibility which is a function of the cavity center frequency and the Q-factor. The uncertainties of cavity measurements should be first evaluated and then propagated to the susceptibility and the effective linewidth. The basics for uncertainty evaluations refer to Taylor and Kuyatt (1994). The uncertainty is categorized into two types based on the evaluation methods. Type A uncertainties are evaluated by statistical methods and Type B uncertainties by other methods.

In the repeated ABA method, a set of ΔQ_c and $\Delta\omega_c$ as single measurements are

obtained and the corresponding standard deviations $\sigma_{\Delta Q_c}$ and $\sigma_{\Delta\omega_c}$ simply give the type A standard uncertainties for such single measurements. Other error sources, for example, field dependence of the empty cavity, deformations in frequency shifts, etc., can be neglected according to the 1/3 rule. The 1/3 rule is that an uncertainty component can be neglected if it is smaller than the dominant uncertainty. The type A uncertainties of these Q and frequency differences subsequently stand for the total uncertainties. This is because the effective linewidth is basically related to the measured $\overline{\Delta Q_c}$ and $\overline{\Delta\omega_c}$, and hereby the type B uncertainties in the absolute values of ω_c and Q_c are negligible. The standard uncertainties of the average values are evaluated by,

$$u(\overline{\Delta Q_c}) = \frac{\sigma_{\Delta Q_c}}{\sqrt{n_c}}$$
$$u(\overline{\Delta\omega_c}) = \frac{\sigma_{\Delta\omega_c}}{\sqrt{n_c}} \quad . \tag{5.15}$$

Equation (5.15) is only valid for the cases in which n_c is more than 10. Otherwise, the uncertainties above should be multiplied by a factor larger than 1 (refer to international recommendations, for example, OIML 111-1 for mass standards).

The uncertainties of K_c, ω_∞, and Q_∞ can be obtained from the corresponding fits. The nearly perfect fit of K_c and ω_∞ indicates that the corresponding uncertainties are negligible, as indicated by the 1/3 rule. The uncertainty of Q_∞ is also assumed to be negligible, although it may be carefully fitted using just a few points but carefully. Based on these simplifications and the law of uncertainty propagation, the standard uncertainties of the susceptibility can be evaluated by

$$u(\chi') \approx K_c \frac{u(\overline{\Delta\omega_c})}{\omega_c}. \tag{5.16}$$

and

$$u(\chi'') \approx K_c \frac{u(\overline{\Delta Q_c})}{2Q_c Q_\infty}. \tag{5.17}$$

The standard combined uncertainty $u(\Delta H_{\text{eff}})$ of the effective linewidth can be evaluated based on Eq. (4.31) and the following equation,

$$u(\Delta H_{\text{eff}}) = \sqrt{\left[\frac{\partial \Delta H_{\text{eff}}}{\partial \chi'} u(\chi')\right]^2 + \left[\frac{\partial \Delta H_{\text{eff}}}{\partial \chi''} u(\chi'')\right]^2}. \tag{5.18}$$

Here the uncertainties of $\overline{\Delta Q_c}$ and $\overline{\Delta\omega_c}$ are assumed to be uncorrelated although the correlation coefficient can be evaluated based on the relation between the measured data of ΔQ_c and $\Delta\omega_c$ in Fig. 5.7. The derivatives can be found from Eq. (4.31). Finally, the expanded uncertainty $U(\Delta H_{\text{eff}})$ is the standard uncertainty multiplied by the coverage factor. The coverage factor is typically set to be 2 in USA. In this dissertation, the coverage factor is 3 based on the convention of primary standards. The corresponding level of confidence is 99.73 % for a normal distribution, as shown in Fig. 5.7.

6. EXPERIMENTAL RESULTS AND INTERPRETATIONS

This chapter presents the representative experimental results of the effective linewidth and the associated physical interpretations. The objective is to resolve the long-standing problems in the high field effective (HFE) linewidth and understand the main features of full field effective linewidth. Section 6.1 describes the materials and the general microwave properties. Section 6.2 shows the HFE linewidth results that are used to solve the high field problems. Section 6.3 presents the HFE linewidth measurement on a disk for comparison with spheres. Sections 6.4 and 6.5 show the representative measurements of the low field and in-manifold effective linewidth, respectively.

6.1. Materials

The effective linewidth measurements shown in the following sections focus on two types of polycrystalline yttrium iron garnet (YIG) materials. One is the conventionally sintered (CS) commercial G113 material produced by Trans Tech. The other is the hot isostatic pressed (hipped) YIG material produced by Pacific Ceramics, Inc.

The CS material is a commercial material manufactured with the standard hot pressed process and has a density greater than 99.0%, relative to the theoretical single crystalline YIG density. This material represents the densest YIG material of which the

effective linewidth was measured in 1960's and 1970's. The 9.5 GHz half power FMR linewidths for the spheres of this material are around 3 mT. This FMR linewidth corresponds to a residual porosity of about 0.5%. The nominal saturation magnetization is taken as $\mu_0 M_0$ =0.175 T.

The hipped YIG material represents the high density and low loss polycrystalline YIG material manufactured with the modern techniques. This material is formed with three steps. First, start with conventionally sintered polycrystalline YIG powders. This starting material is of nearly pure YIG with a rare earth impurity content below 0.01%. The residual porosity was at the level of 1% as in the CS material. Second, these powder materials were subjected to a hipping process in an argon atmosphere. The starting argon pressure was 470 bars. The temperature and pressure were gradually increased from room temperature to 1400 °C and from 470 bars to 1000 bars, respectively, over 10 hours and then held for 3 hours. Third, the system was then cooled and vented back to room temperature and pressure over about 20 h.

The measured density of the hipped YIG material is 5.172 g/cm^3. The density relative to the theoretical single crystalline YIG density is greater than 99.99%. Nearly all the porosity is completely eliminated. The average grain size is 8 μm. Disks and spheres in the millimeter size range are further fabricated and polished from the interior regions of the hipped blocks in order to avoid possible problems with oxygen deficient surface regions.

The saturation magnetization of the hipped YIG material was measured by Nazarov et al (2003) using a commercial vibrating sample magnetometer system. The response of magnetic moment versus field gives a saturation magnetization of $\mu_0 M_0$ =0.1825(20) T

for the hipped YIG spheres and disks. The saturation fields are 0.061 T for sphere and 0.017 T for in-plane magnetized disks.

The microwave properties are evaluated by the standard FMR technique. The nearly complete elimination of porosity for these hipped samples is further confirmed from frequency dependence and temperature dependence of FMR linewidth measurements by Nazarov et al (2003), Kalarical (not published) and Wittenauer (not published). The 9.5 GHz half power FMR linewidths for the hipped spheres are 1.35 mT, according to Wittenauer's precise measurements on a finely polished sphere. The gyromagnetic ratio, 27.6 GHz/T, is obtained from the frequency dependence of the FMR field.

Based on the goal of resolving the problems in the high field effective (HFE) linewidth, three samples are chosen to perform the high precision effective linewidth measurements.

(a) A 1.99 mm diameter hipped YIG sphere with a shining surface. This sample is the 2.04 mm diameter sphere measured by Nazarov et al (2003). The original surface shows some surface pits under a microscope and hence finely polished by Wittenauer. No surface pit on the polished surface is viewable under the microscope and the surface pits are assumed to negligible.

(b) A 2.05 mm diameter CS YIG sphere with a shining polished sphere.

(c) A hipped YIG thin disk with diameter of 1.50 mm and thickness of 0.50 mm. This disk is one of the disks measured by Nazarov et al (2003). The surface is roughly polished by Pacific Ceramics, Inc.

The investigations mainly focus on the hipped YIG sphere. The HFE linewidth on

this sample has been measured by David Menard (Nazarov et al, 2003) and found to be 0.2 mT, which is inconsistent with the single crystal YIG linewidth. One of the main objectives of this thesis' investigations is to solve such problem in the HFE problem that has been long-standing for over four decades. It's interesting that Nazarov's spin wave linewidth measurement on this sample in the zero wave number limit gave a linewidth on the order of single crystal YIG linewidth. This implies that the high field problem is possible to resolve. This is why the high precision effective linewidth technique is developed.

These three samples are the fairly dense YIG sample. The main reason for this choice is to avoid the secondary scattering process, which, for dense materials, would not exist in the extremely high field. For porous materials, the secondary scattering effect and the pseudo manifold effect due to the pore-demagnetizing fields are large and may cause the unknown higher order scattering processes that extend to the extremely high field region. Hence, too high fields are needed to measure so as to avoid the possible unknown processes. These fields may exceed the measurement capability of the spectrometer system. The dense materials can be chosen to avoid the ambiguity and the capability problem.

The CS YIG sample has a residual porosity. The comparisons between the CS YIG sphere and the hipped YIG sphere can provide a test for the known secondary scattering processes and the bulk manifold shifting. This is why these spheres have nearly the same diameter. Moreover, the hipped YIG disk is used to provide the comparison of the HFE linewidth among different sample geometries. The comparison can be made between the hipped YIG disk and sphere.

6.2. High Field Effective Linewidth for Spheres

This section first presents high accuracy data and analyses for the HFE linewidth in polycrystalline YIG materials. Based upon these data, it's then shown that the high field tail for the linewidth data in dense YIG spheres correlates with the density of states for previous ignored low wave number electromagnetic spin wave (EM-SW) modes. It is found, moreover, that a proper extrapolation of the HFE linewidth to the infinite field limit gives the ΔH_{eff} values that match intrinsic linewidths for single crystal YIG.

Section 6.2.1 describes the detailed measurement procedure that is enhanced by the high precision technique in Chapter 5. Section 6.2.2 presents the HFE linewidth results of the hipped YIG and CS YIG spheres. Sections 6.2.3 and 6.2.4 provide the quasi-quantitative interpretations of these new results based on the full spin wave bands and the two-magnon theory.

6.2.1. Measurement Procedure

The $\Delta H_{\text{eff}}(H_{\text{ext}})$ determinations are made through high precision measurements of the cavity center frequency ω_c and quality factor Q_c as a function of H_{ext}. As shown in Section 4.2, the measurements utilize a high Q cavity with a ferrite sample installed inside and standard scalar network analyzer microwave techniques. The change in ω_c and Q_c with field can be related to ΔH_{eff} through cavity perturbation theory and the dynamic magnetization response equations with loss terms included. The details of general effective linewidth measurement are presented in Section 4.2. The descriptions here are the specifics for the HFE linewidth measurement.

The details about the determination of high field $\Delta H_{\text{eff}}(H_{\text{ext}})$ will be discussed in the next section and basically include two steps. One first measures ω_c as a function of H_{ext}, plots ω_c as a function of the X_ω parameter, and obtains the calibration factor K_c from fits of the data to Eqs. (4.19) and (4.21). The values of $|\gamma|/2\pi$ are finely tuned to optimize this linear fit, as described in Section 5.4.2. The fitted $|\gamma|/2\pi$ values for the hipped and CS samples were obtained as 27.65 and 2.74 GHz/T, respectively

In the high field regime, such plots are generally quite linear, and the K_c – values are reasonably close to values from standard cavity perturbation theory. In the second step, one takes the $Q_c(H_{\text{ext}})$ data, applies Eqs. (4.20) and (4.22), and obtains $\Delta H_{\text{eff}}(H_{\text{ext}})$. In practice, $\omega_c(H_{\text{ext}})$ and $Q_c(H_{\text{ext}})$ are measured simultaneously. Previously, the HFE linewidth was taken to be constant and determined from the linear fit to the Eq. (4.20).

It is to be emphasized that the measurement accuracy is paramount for a meaningful HFE linewidth measurement. The experiment is performed on the extremely high field tail of the FMR absorption line, at fields that are 0.1 T or more above the FMR field. With actual FMR linewidths in the 1.5-3.0 mT range, this means that one is measuring the loss component of the susceptibility at fields from several 10 to several 100 of linewidths away from the FMR peak. Under these conditions, the HFE linewidths are derived from extremely small changes in the cavity frequency ω_c and Q_c with field.

For YIG spheres at 10 GHz, the manifold region of degenerate moderate k spin waves extends over a range of about 0.338 to 0.415 T. The HFE linewidth measurements were made from 0.45 to 0.78 T or so. The lower limit is well above the manifold upper

limit field. The separation from the upper manifold limit of 0.03-0.04 T was chosen to avoid secondary two magnon scattering effects. The upper limit is still low enough to allow for a reasonable accuracy for the Q_c measurements. The high field limit is somewhat lower than the 1 – 1.2 T values used in some previous HFE linewidth studies. For such very high fields, the accuracy was extremely low in the previous measurements. As the new data show below, such high fields are not needed to obtain good linewidth extrapolations to intrinsic values in the high field limit.

The optimization for the cavity measurement accuracy is discussed in the chapter 5, using the systematic ABA measurement procedure to minimize the effect of random errors and drifts. The measurements of the HFE linewidth for spheres were made at the early stage of this thesis' investigations using the modified ABA method instead of the repeated ABA method. The modified ABA method is described in Section 5.3.4. In order to obtain the accuracy comparable to the repeated ABA method, the modified ABA cycles are also repeated for 5 to 10 times. The average factor of the network analyzer was set to 4 so that the effective cycles are 20 to 40 and most of the drifts and random errors can be eliminated. For a given set of $\omega_c(H)$ and $Q_c(H)$ measurements, data were obtained by cycling the field from the measurement field H_{ext} – point to some high field reference point and back again many times. From the average of the ω_c and Q_c values data for a given field, and the change from the high field reference, random errors and drift effects are largely eliminated. Through simultaneous measurements of the cavity temperature through this sequence, one also obtains a determination of the average change in ω_c and Q_c with temperature, so that these thermal changes can be compensated as well.

This method gives a relatively low accuracy in comparison with the repeated ABA method because some residual drifts are not eliminated. The residues are mainly in the cavity center frequency. The worst uncertainties in a number of tests are 4.0 in Q_c and 7.3 kHz in $\omega_c / 2\pi$. It's found that these uncertainty levels are still very good in comparison with the conventional technique, 25 in Q_c and 50 kHz. These reasonable uncertainties in cavity measurements give an uncertainty of below 0.02 mT for the HFE linewidth.

6.2.2. Measurement Results

This section first provides the signature for the field dependence of the HFE linewidth based on the data analyses of the hipped YIG measurements, and then shows the high precision effective linewidth results for both of the hipped YIG and CS YIG spheres.

Figure 6.1 provides a view of the step-by-step analysis of the ω_c and Q_c data that yield $\Delta H_{\text{eff}}(H_{\text{ext}})$. The open circle data in both graphs are for the hipped YIG sphere. Graph (a) shows data on the frequency versus field response displayed in a $\omega(X_\omega)$ format. This format shows the linear dependence discussed in Section 5.4.2. As already noted, the $\gamma-$values for the samples were adjusted to optimize the linearity of the ω_c versus X_ω response. The accuracy of the ω_c-data in graph (a) is about ± 0.5 kHz. The solid line shows the linear fit. Graph (b) shows the companion plot of the Q_c versus field data shown in a $Q_c^{-1}(X_Q)$ format. The accuracy of the Q_c-data in (b) is about ± 2.5. The solid curve in graph (b) is a quadratic fit to the data.

Graph (a) shows that the cavity frequency is indeed a linear function of the X_ω inverse field parameter, as expected from perturbation theory and the dispersion component of the microwave susceptibility response analysis that leads to the $X_\omega(H_{\text{ext}})$ functional form in Eq. (4.21). The calibration parameter K_c, as obtained from the slope of the response in graph (a), is also in accord with microwave perturbation theory. The numerical value of K_c from the linear fit in graph (a) is 1746. The perturbation theory value for K_c is 2207. This change is due to the small distortions in the empty cavity mode that result from the nonzero sample volume. Truedson *et al.*(1993) show that in the limit of a vanishingly small sample volume, the empirical K_c – value approaches the perturbation theory prediction. One of the important advantages of the empirical calibration is the more accurate K_c – value and the corresponding improved value for $\Delta H_{\text{eff}}(H_{\text{ext}})$.

Graph (a) and the numerical slope value obtained therefrom show that perturbation theory is applicable in form and that the empirical calibration parameter K_c can be trusted. This is supported by the previous work by Truedson and co-workers (1993) on the effect of sample size on K_c and the convergence to the perturbation theory value in the limit of very small samples.

Graph (b) shows the rather astounding field dependence of the HFE linewidth, relative to previous data. At first glance, equation (4.20) and the intrinsic loss assumption of the HFE linewidth suggest that $1/Q_c$ versus X_Q should show a linear response with a slope of $\Delta H_{\text{eff}} / K_c$. Graph (b), however, shows that $1/Q_c$ versus X_Q *is actually quadratic*. From Eq. (4.20), it is evident that the effective linewidth is related to

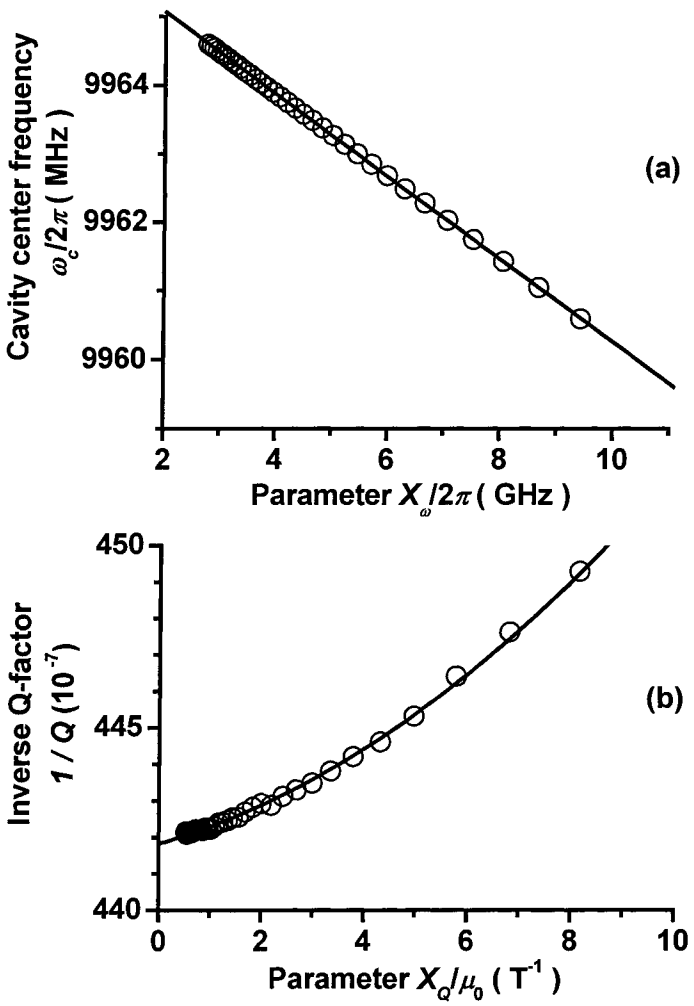

FIG. 6.1. Demonstration of field dependence of the high field effective linewidth. The open circle data points in graphs (a) and (b) show the cavity frequency ω_c and the inverse of quality factor Q_c as a function of the parameters X_ω and X_Q, respectively, for the hipped YIG sphere. The solid line in graph (a) shows the linear fit to the open circle points. The solid curve in graph (b) shows a quadratic fit to the data points.

the slope of the response at the local fields. The slope multiplied by the calibration factor K_c corresponds to ΔH_{eff}. According to the nice quadratic fitting in this graph, the effective linewidth actually *decreases* as the field is increased.

Such field dependence was not observed previously due to the relatively low

accuracy, and buried in the noises of the curve of $1/Q_c$ versus X_Q. The high precision technique developed in Chapter 5 provides possibilities to resolve such fine structures of the HFE linewidth. This means that the previous linear assumption of $1/Q_c$ versus X_Q must be modified, as discussed in Section 5.4.3. Recall from Eq. (4.22) that lower values of X_Q mean higher values of the field H_{ext}. The static external field goes to infinite in the $X_Q \to 0$ limit and hereby the $1/Q_c$ value in this limit or the $1/Q_c$ intercept of the quadratic fitting curve at $X_Q = 0$ gives $1/Q_\infty$.

Figure 6.2 shows values of the HFE linewidth as a function of X_Q, as obtained from Fig. 6.2. The open circles and the open squares stand for the hipped and CS YIG spheres, respectively. This figure also shows a solid linear line fit to the hipped YIG effective linewidth data and a dashed line fit to the CS sample data for values below about 4.5 T^{-1}. The intercepts of these linear fittings are 0.056 ±0.021 mT for hipped YIG and 0.046±0.027 mT for CS YIG. The accuracy of the ΔH_{eff} points depends on the field and the uncertainty is in the range from 0.002 to 0.02 mT. The details will be shown in the next section. Note that the data below $X_Q / \mu_0 = 3$ T^{-1} or in the extreme high field region show some small deformations. These deformations in the uncertainty range come from the residual drifts that are not compensated in the modified ABA method.

As mentioned above, the effective linewidth is quite different from the previous high field ΔH_{eff} results. It can be seen that the hipped YIG material shows a linear ΔH_{eff} versus X_Q, while the CS sample has an HFE linewidth that is linear only for lower X_Q or relatively high fields. For the CS sample, ΔH_{eff} appears to rise rapidly at

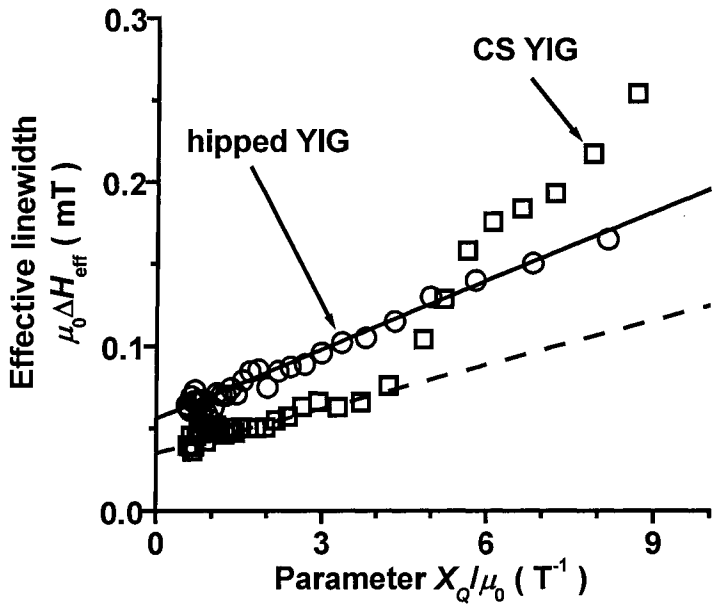

FIG. 6.2. High field effective linewidth ΔH_{eff} as a function of the field parameter X_Q. The open circles and squares show the hipped and CS YIG results, respectively. The solid lines show a linear fit to the open circle points. The dashed line in (c) shows a linear fit to the solid circle points for low X_Q / μ_0 values below about $4.5\ \text{T}^{-1}$.

high X_Q and corresponding low fields. These results run counter to almost all of the previous results on the HFE linewidth in polycrystalline ferrite materials. In many of these works, the high field ΔH_{eff} obtained far outside the manifold region was taken to be constant, based on the idea that there were no degenerate spin waves at the signal frequency for high fields. The accuracy in effective linewidth for the data in those works was about ±0.1 to ±0.2 mT, and it was not possible to discern any clear change in ΔH_{eff} with field in the high field regime.

The new high accuracy results shown here indicate that this old picture is in need of major revision. There are points of note. First, the hipped YIG shows a linear ΔH_{eff} versus X_Q response. As the next section will show, this translates into a decrease in the

HFE linewidth with increasing field that closely matches the density of states for degenerate electromagnetic branch spin waves. This new connection is one of the key results of this thesis. Previously, the role of the electromagnetic spin waves and two-magnon scattering in the HFE linewidth was completely ignored. It is also clear from the different responses for the hipped and G113 samples that the field response is affected by microstructure. These connections will be discussed in the next section.

Second, the data show that the extrapolated ΔH_{eff} in the high field $X_Q \to 0$ limit is very close to the known intrinsic linewidths in single crystal YIG. At 10 GHz, such linewidths lie typically in a small range of 0.05 mT. The present data represent the first measurement of a near intrinsic high field effective linewidth in a polycrystalline ferrite. The combination of a previously unrealized field dependence and the experimental demonstration of an intrinsic linewidth in the high field limit also shows, for the first time, that the HFE linewidth concept proposed by Kohane and Schlömann (KS, 1968) is correct. The high field limit does indeed give ΔH_{eff} values that are close to single crystal intrinsic values and not affected by microstructure. The only caveat to the KS concept is in the previously unrealized role of high field two-magnon scattering that involves the EM-SW branches of the dispersion. This connection is developed below.

Third, the clear differences in the high field $\Delta H_{\text{eff}}(X_Q)$ responses for the hipped and CS samples mark the effect of porosity on the effective linewidth for fields close to the manifold region. It was noted above that the CS data show a linear response with a near intrinsic $X_Q \to 0$ extrapolation only below about 4.5 T^{-1}, which corresponds to a field of around 0.53 T. There is an apparent break at $X_Q / \mu_0 \approx 4.5\ \text{T}^{-1}$, with a more

rapid rise in ΔH_{eff} as X_Q is further increased.

Hoeppe (2004) has recently shown a detailed analysis of the effective linewidth in porous ferrites. Vrehen (1969) and Hoeppe (2004) proposed that the dipole field around the pores can cause an artificial shift in the upper field limit for the manifold region to higher values of the static field. Their data and analyses support this proposal. The results indicate that for YIG materials, this shifted manifold limit field is just at the corresponding X_Q break point apparent in Fig. 6.2. The high accuracy data here corroborate and extend this model. Not only do the data show the break point and the pseudo-manifold two magnon scattering to low wave number spin wave modes for lower fields and high X_Q. The results also show that for low X_Q, there is a clear transition to a different mode of scattering that yields a near intrinsic linewidth in the high field $X_Q \to 0$ limit.

6.2.3. Spin Wave Band Considerations

To understand the results shown above, the full spin wave bands must be accounted for. It is convenient to cast the $\omega_k(k,\theta_k)$ band picture for a constant static field into a band picture in which the spin wave number k is given as a function of the external field H_{ext} and the angle θ_k for a fixed ω_k – value equal to the operating frequency ω. Figure 6.3 shows such a presentation for the full spin wave bands at $\omega_k / 2\pi = 10\,\text{GHz}$. No curves or bands are shown for $H_{\text{ext}} < M_0 / 3$ because this would correspond to negative internal fields or unsaturated magnetization.

In this k versus H_{ext} format, the bulk manifold region now corresponds to the

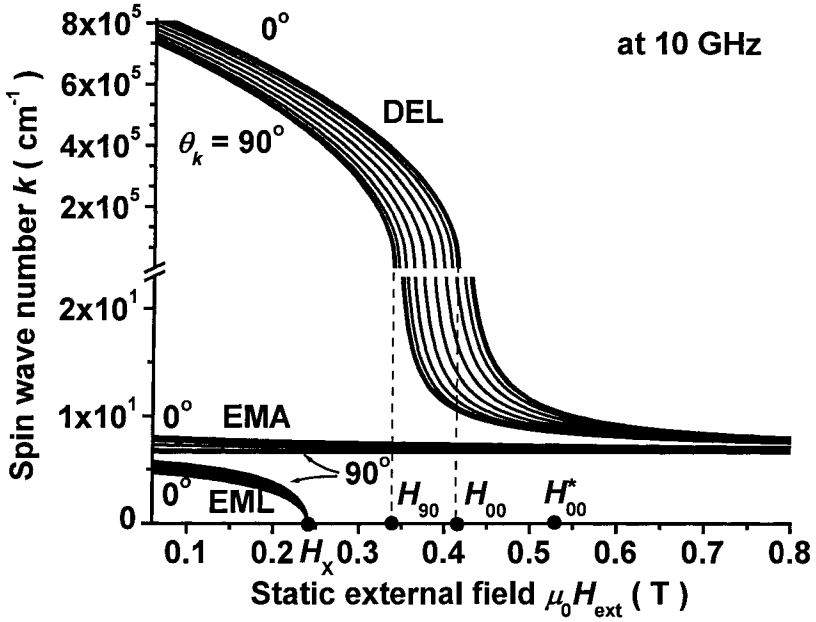

FIG. 6.3. Diagram of the three spin wave bands in a wave number versus field format for a fixed frequency. The graph shows curves the spin wave number k as a function of the static external field H_{ext} at a fixed frequency 10 GHz for the full range of propagation angle θ_k from $0°$ to $90°$, as indicated. As in Fig.2.6, the curves group into three bands, the dipole exchange Larmor (DEL) band, the electromagnetic Larmor (EML) band, and the electromagnetic anti-Larmor (EMA) band, as indicated. The bands were evaluated from Eq. (2.53) and for the YIG parameters as used for Fig. 2.6. The graph shows four important field points along the H_{ext} – axis, an H_X field that corresponds to the ω_X frequency point in Fig. 2.6, the moderate k band limits in field at $H_{\text{ext}} = H_{90}$ and $H_{\text{ext}} = H_{00}$ that correspond to the frequency limits ω_B and ω_H in Fig. 2.6, and an additional field point shifted up from H_{00} by $2M_0/3$, and denoted as H^*_{00}.

vertical section of the DEL band for $\mu_0 H_{90} = 0.338\ \text{T} < \mu_0 H_{\text{ext}} < \mu_0 H_{00} = 0.415\ \text{T}$. The k versus H format in Fig. 6.3 is particularly useful here because one can see immediately the range of modes that are degenerate with the signal frequency. If one were considering DE-SW excitations only, there would be *only one band*, the DEL band, and *even this band would truncate below* $k = 300\ \text{cm}^{-1}$ or so. In that case, there would be

no DE-SW excitations available at the signal frequency for fields above the upper limit manifold band edge at H_{00}. If the dipole fields from spherical pores are taken into account, this cut-off band edge is shifted up in field by $M_0/3$ to H_{00}^*.

However, when the full band picture in Fig. 6.3 is considered, one can see that there are always *some* spin wave modes that are degenerate with the signal frequency. These modes were found important for microwave application of ferrites (Rupke, 1970). The high frequency transition frequency ω_X (see Fig. 2.6) is now converted to a transition field H_X, as indicated. For any field $H_{\text{ext}} > H_X$, there will always be two real and positive root solutions to Eq. (2.53) for a given θ_k. For $H_{\text{ext}} < H_X$, there will be three roots. The corresponding root solutions for the full range of θ_k from 0° to 90° give rise to the indicated bands.

One can also see from Fig. 6.3 that the two surviving bands for $H_{\text{ext}} > H_X$ become extremely narrow in the limit of very high fields. Two-magnon scattering processes that involve excitations in these two tail bands are proposed as the source of the experimental effective linewidth responses presented above. The field dependence of ΔH_{eff} is attributed to the shrinkage in the field width of these bands at $\omega_k = \omega$ with increasing field. The near intrinsic effective linewidth in the high field limit is attributed to this shrinkage to zero width and band convergence to the light line.

Two-magnon scattering from the uniform mode to degenerate spin waves is a well-established relaxation process for ferromagnetic resonance. Quantitative connections have been made to the FMR linewidth in single crystal and polycrystalline ferrites as well as the near FMR effective linewidth for fields within the manifold region. It is well

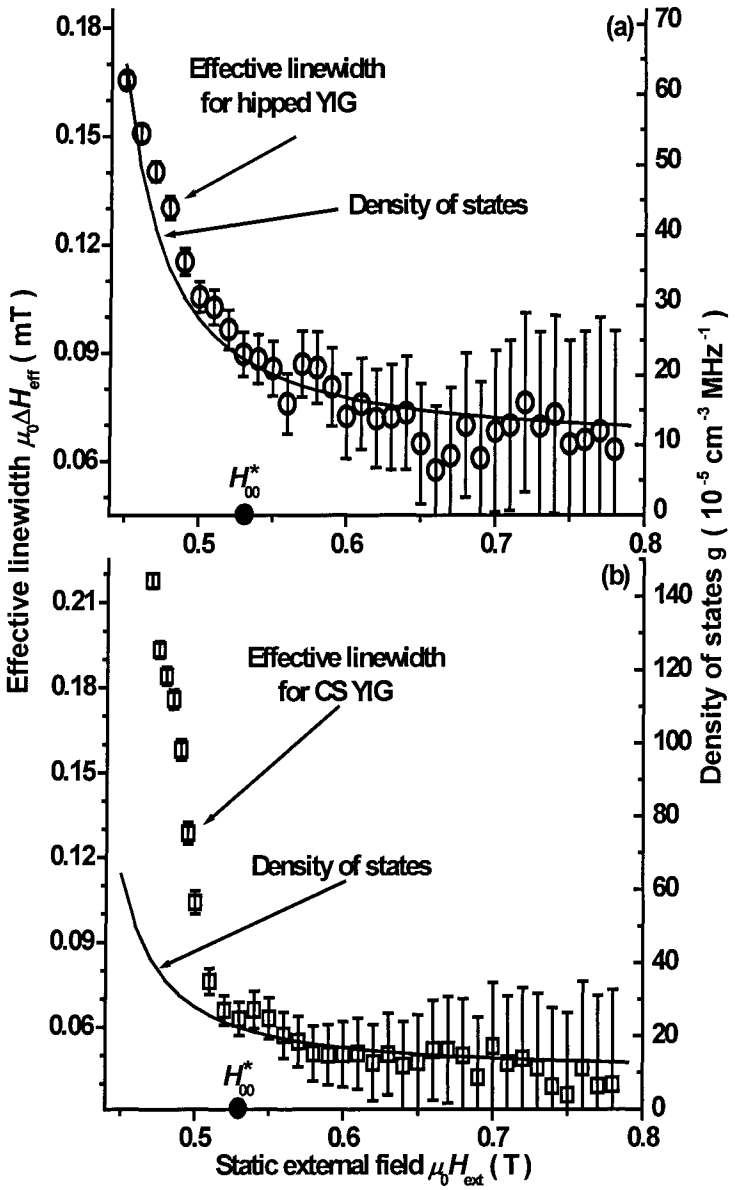

FIG. 6.4. Graphs of the high field effective linewidth ΔH_{eff} and the total electromagnetic spin wave two band density of states g as a function of the static external field H_{ext}. The open circles in graphs (a) and (b) and the corresponding error bars show the measured effective linewidth data for the hipped and CS YIG samples, respectively. The solid curves show the calculated density of states for degenerate electromagnetic spin wave modes at the signal frequency, as a function of the field. The H_{00}^* point indicates the effective band edge field when the dipole field of spherical pores is accounted for.

established that the source of the scattering in these cases consists of various

inhomogeneities such as surface pits, porosity, and the magnetocrystalline anisotropy in the randomly oriented grains in polycrystals.

Two-magnon relaxation in the context of FMR in ferrite materials is reviewed by Sparks (1964). Simply stated, inhomogeneities related to pores, grains, or pits of some size a in the micron range couple the uniform mode to degenerate spin waves with wave numbers in the range from zero to about π / a. For typical polycrystalline ferrite with $a-$ values in the range of $1-10$ μm, this means that only degenerate modes with $k-$ values below about $10^3 - 10^4$ rad/cm can contribute to the scattering. From the traditional spin wave band picture in Fig. 2.5 or 2.8, such modes would be only available for scattering for fields below the upper field manifold region cutoff point H_{00} shown in Fig. 6.3.

The new data presented above, and the situation depicted in Fig. 6.3, provide a strong motivation to re-examine these old assumptions. It is important to note that at any high field two-magnon process must involve extremely low k modes. From Fig. 6.3, one can see that the degenerate modes for fields above 0.4 – 0.5 T or so have $k-$ values below 100-150 cm^{-1} and drop even lower at higher fields. One important question concerns the efficiency with which micrometer and sub-micrometer size inhomogeneities can produce scattering to such low k modes with wavelengths of a few tenths of a millimeter or larger.

6.2.4. Two Magnon Scattering Considerations

An important test of a possible two magnon term in the HFE linewidth would be to make a quantitative comparison between the field dependence of the density of states

(DOS) for the $\omega_k = \omega$ spin waves in the degenerate modes in the DEL and EMA bands in Fig. 6.3 with the field dependence of the HFE linewidth. In the high field region, only the EM-SW modes are available and these modes have extremely low wave numbers. The two-magnon scattering contributions of these modes may be viewed as wave number independent since these modes are in a very small range. Therefore, the relaxation rate due to two-magnon scattering can be expected to be linear with the density of states.

Figure 6.4 shows plots of the combined two-band density of states (DOS) at the signal frequency ω as a function of the static external field H_{ext} in the high field regime, along with suitably scaled plots of the measured high field ΔH_{eff} versus H_{ext}. In the DOS calculations, the experimental high field limit frequency $\omega_\infty / 2\pi = 9.967$ GHz is used for the operating frequency so as to be able to compare with the HFE data. The DOS calculations are based on Section 3.4. Graphs (a) and (b) show separate comparisons for the hipped and CS YIG samples, respectively. Note that the common leftmost field limit for the graphs is well above the upper manifold band edge field H_{00} value of 0.415 T. The theoretical up shifted H_{00}^* point at $H_{00} + 2M_0/3$ from Fig. 6.3 is indicated on the field axes for both graphs. The vertical axes have been scaled and shifted in both cases to yield approximate qualitative matches with the DOS curves for $H_{\text{ext}} > H_{00}^*$. Error bars on the data points indicate the uncertainty of the ΔH_{eff} values from the modified ABA measurements. For use in the discussion below, the label H_{00}^* indicate the highest field point to which the local upper manifold band edge would be shifted due to dipole fields around a pore in a YIG sphere.

The results in Fig. 6.4 show three things. First, both graphs show that the HFE

linewidth tracks the DOS response reasonably well for fields above the H_{00}^{*} point. Second, the data indicate high field limit values for $\mu_0 \Delta H_{\text{eff}}$ in the 0.05-0.06 mT intrinsic linewidth range. This is in line with the results from the ΔH_{eff} versus X_Q extrapolations in Fig. 6.2. Third, for fields below H_{00}^{*}, the ΔH_{eff} data for the CS sample in Fig. 6.5(b) show a distinct departure from the DOS curve. One can see that (1) the departure in the HFE linewidth values from the DOS response is rather abrupt and (2) this jump occurs very close to the $H_{\text{ext}} = H_{00}^{*}$ marker. These linewidth departures from the DOS line are relatively large, in the 0.05 – 0.2 mT range.

These results indicate that there are *two distinct two magnon scattering contributions to the HFE linewidth.* Both of them are turned off in the extreme high field limit because of the shrinking spin wave bands and their convergence with the light line. In this limit, one obtains an extremely low linewidth that matches closely to known intrinsic single crystal linewidths. This conclusion applies to both the hipped YIG and the CS samples. This long sought after and previously unrealized result is extremely satisfying.

As the field is first reduced, one sees the growing contribution of low k electromagnetic spin wave scattering to the ΔH_{eff}. This is evidenced by the gradual rise in the HFE linewidth for fields down to the H_{00}^{*} field point. This rise, moreover, scales nicely with the computed density of states for these modes. There are no adjustable parameters in the DOS calculation. In Fig. 6.2, the slope of the ΔH_{eff} versus X_Q response is slightly larger for the CS than for the hipped YIG. This implies that the scattering to the low-k EM-SW modes is stronger for the less dense microstructure. The more details of this scattering process will be discussed in Section 6.4 about low field

effective linewidth measurements and interpretations.

Finally, for fields below H_{00}^{*}, the abrupt rise in ΔH_{eff} above the DOS response for the CS sample signals the onset of manifold scattering to moderate k spin wave modes within the conventional DE-SW band. Following the arguments of Hoeppe (2004), this onset point is shifted up from the expected onset field point at H_{00} because of the dipole fields around residual pores and other possible inclusions. Here too, the value of the onset field H_{00}^{*} is based solely on the working equations for the spin wave band and known dipole field considerations. There are no adjustable parameters. The hipped YIG samples don't have such response of manifold up shift due to the complete elimination of porosity.

6.3. High Field Effective Linewidth for Disks

The high field effective linewidth for in plane-magnetized hipped YIG disks is also measured. The motivation for this measurement is two-fold, (a) to determine the high field limit effective linewidth for disks and to compare with that in sphere, and (b) to explore possibility to apply the high accuracy technique developed in Chapter 5 to the samples with other shapes as well as sphere.

6.3.1. Measurement Method

The cavity measurement technique is similar to what described in Section 6.2.1 for spheres. The field dependent cavity parameters for disks, namely ω_c and Q_c, are measured based on the repeated ABA method instead of the modified ABA method. 100 cycles are made for all the high fields from 0.45 to 0.65 T against a reference field of 0.7

T.

The data analyses are slightly different from that for spheres since the different shape has different demagnetizing factors. For disk, it's usually assumed that the thickness is small comparing with the disk diameter, the edges could be approximately rounded, and then the equivalent shape is elliptical. The demagnetizing factors for the elliptical shapes are known. (Osborn, 1945) One applies Osborn's formulae to the disk shape and obtain,

$$N_{//} = \frac{1}{2(r_d^2 - 1)}\left(\frac{r_d^2}{\sqrt{r_d^2 - 1}} \operatorname{asin} \frac{\sqrt{r_d^2 - 1}}{r_d} - 1 \right) \tag{6.1}$$

and

$$N_{\perp} = \frac{r_d^2}{r_d^2 - 1}\left[1 - \left(r_d^2 - 1\right)^{-\frac{1}{2}} \operatorname{asin} \frac{\sqrt{r_d^2 - 1}}{r_d} \right], \tag{6.2}$$

where r_d is the ratio of the disk diameter to the thickness and $N_{//}$ and $N_{\perp}$ are the demagnetizing factors along the in plane directions and the perpendicular direction, respectively.

In order to apply the high field effective linewidth technique described in Section 4.2.4 to the disk-shaped samples, the only modification is simply to redefine the parameter X_Q and X_ω in Eqs. (4.19) to (4.22) for disks,

$$X_\omega = \frac{M_0\left[H_{\text{ext}} + M_0 \cdot (N_{\perp} - N_{//})\right]\omega}{H_{\text{ext}}\left[H_{\text{ext}} + M_0 \cdot (N_{\perp} - N_{//})\right] - \left(\frac{\omega}{|\gamma|\mu_0}\right)^2} \tag{6.3}$$

and

$$X_Q = \frac{M_0\left\{\left[H_{\text{ext}} + M_0\cdot(N_\perp - N_{//})\right]^2 + \left(\frac{\omega}{|\gamma|\mu_0}\right)^2\right\}}{\left\{H_{\text{ext}}\cdot\left[H_{\text{ext}} + M_0\cdot(N_\perp - N_{//})\right] - \left(\frac{\omega}{|\gamma|\mu_0}\right)^2\right\}^2}. \qquad (6.4)$$

Based on these re-defined X_Q and X_ω parameters, the other HFE linewidth data analyses are the same as that for spheres. Refer to Truedson *et al* (1993, 1994) for more details.

6.3.2. Measurement Results

Figure 6.5 shows the measured representative HFE linewidth results for a polished hipped YIG disk with 3mm diameter and 1 mm thickness using the high Q TE_{011} cylindrical cavity. The static external field and the microwave magnetic field are in the plane of the disk and they are perpendicular to each other. The demagnetizing factors were $N_{//} = 0.11$ and $N_\perp = 0.78$. The open circle points are the data. The measurement configuration and a Lorentzian tail fit to the HFE linewidth data are also shown. The solid curve shows the Lorentzian tail fit. The Lorentzian fit is comparable to the linear fit with X_Q that is approximately a Lorentzian tail in the high field region.

The top of the bulk manifold in field for this disk is 0.38 T for the nominal frequency 10 GHz. The field range shown in this graph is well above the field manifold. Similar to the HFE linewidth for sphere, the data also show a tail extension the field dependent HFE linewidth. From the Lorentzian tail fit indicated by the solid curve, the high field extrapolated linewidth goes to a value of $\mu_0\Delta H_\infty = 0.019 \pm 0.07$ mT for this hipped YIG disk.

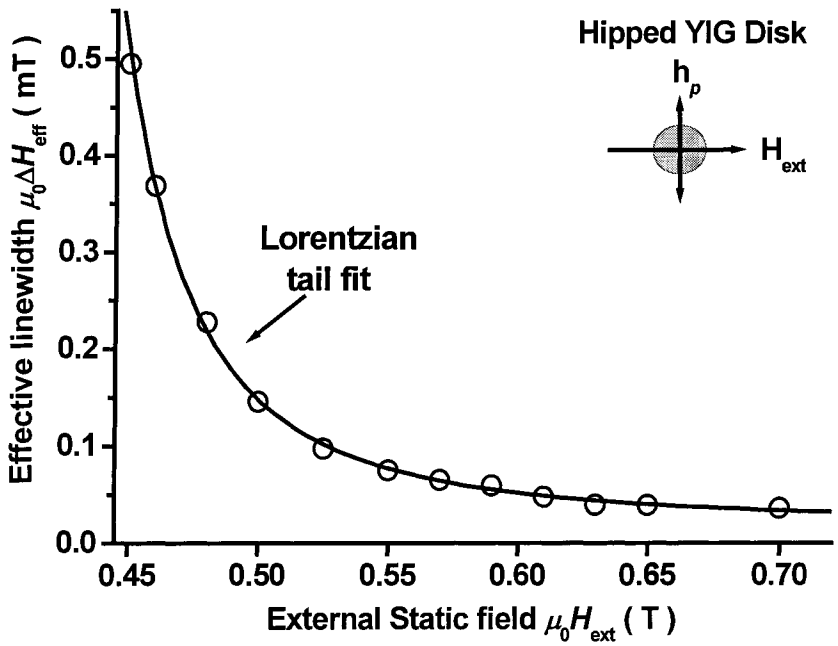

FIG. 6.5. High field effective linewidth data in a hipped yttrium iron garnet (YIG) disk with 3 mm diameter and 0.5 mm thickness. The open circles shows the effective linewidth data points. The solid curve is a fit by a Lorentzian tail, as indicated. The right corner shows the measurement configuration. The microwave pumping field h_p and the static external field H_{ext} are in plane and perpendicular to each other.

The meaningful data for disk indicate that the high accuracy effective linewidth technique is also applicable to the disk shape and most possibly other shapes, especially thin film that is very similar to the disk when the disk thickness goes to be very thin. Due to the recently increasing interest in thin film materials, the high precision effective linewidth technique developed in this thesis would be of great interest for the applications in the thin film effective linewidth. This will be very helpful to understand the relaxation mechanisms in thin film.

6.3.3. Comparison with Spheres

The interesting comparison between spheres and disks is on the high field limit linewidth ΔH_∞. For the same hipped YIG material, the HFE linewidth in the high field limit is $\mu_0 \Delta H_\infty = 0.056 \pm 0.021$ mT for spheres as shown in Section 6.3.2 and $\mu_0 \Delta H_\infty = 0.019 \pm 0.012$ mT for disks. The difference between disks and spheres can be obtained to be 0.037 ± 0.024 mT. Note that the listed expanded uncertainty corresponds to a coverage factor of 3 and a confidence probability is 99.73% based on the normal distribution. It's clear that about 30% of the deviation is not covered by the uncertainty range. In other words, *the intrinsic linewidth for sphere is different from and, precisely stated, slightly bigger than that for disks.*

Such experimental results are surprising. The terminology "intrinsic losses" implies that the intrinsic linewidth should be independent of the exterior geometry. On can expect from the theoretical model for "intrinsic loss" that the high field limit linewidth would be identical for spheres and disks.

Typically, magnon-phonon scattering process has been taken to be the main contribution to the intrinsic losses. Theoretical linewidth for single crystal sphere is 0.03 mT at X-band frequencies due to magnon-phonon process, as reviewed by Sparks (1964). This value is approximately within both of uncertainty ranges of 0.056 ± 0.021 mT for spheres and 0.019 ± 0.012 mT for disks. From this point of view, both the measurement results of spheres and disks are approximately consistent with magnon-phonon scattering theory.

However, the experimental value for a single crystal YIG sphere is 0.05 mT. This indicates that the discrepancy between spheres and disks is true and there are some other relaxation mechanisms, which is not considered in the current theories. How can this

discrepancy be explained? Figures 6.3 and 6.4 show that the density of spin wave states doesn't vanish in the high field limit. Conceptually, the residual degenerate spin waves should make contributions to effective linewidth based on the standard two-magnon theory. This can also be understood according to the discussions in Section 6.2.3. Figure 6.4a shows that the fitted DOS and effective curves give a non-zero value in the high field limit and hereby the high field limit spin wave modes contribute in part to the total effective linewidth.

For the scattering among these modes, the situation of disks is different from spheres. A thin disk is approximately two-dimensional while a sphere is three-dimensional. The scattered modes in disks have in plane wave vectors. It turns out that all the modes contribute to the scattering in spheres and only the modes with in plane wave vector contribute to the scattering in disks. Therefore, the high field limit linewidth for disks is qualitatively smaller than that for spheres. This also confirms the importance of the EM-SW scattering in the HFE linewidth.

6.4. Low Field Effective Linewidth

The HFE linewidth results resolve the long-standing problems about the loss origins of the field dependent HFE linewidth. This leads to new realizations about the low field effective (LFE) linewidth response. The focus in the preceding sections is on the electromagnetic branch spin wave or EM-SW modes that are slightly below the $\omega_{em} = ck_0 / \sqrt{\varepsilon_r}$ light line dispersion. It is these *low* k below-the-light-line EM-SW modes that give rise to the HFE linewidth response. The important point for this section is that in the low field region there are also low k EM-SW modes that lie above the light

line. Based on the HFE linewidth results, it is expected that *both* sets of EM-SW modes, as well as the usual high k dipole exchange spin wave modes, can have a significant effect on the LFE linewidth.

The purpose of the LFE linewidth measurements is to make new connections between measurements of the LFE linewidth, the HFE linewidth, and all three classes of spin wave modes enumerated in the full spin wave band picture. More specifically, this section presents high precision measurements on the LFE linewidth for the hipped and CS polycrystalline YIG materials. The so-obtained data show a kink or elbow at a field of around 0.23 T, the same field for which the density of degenerate states (DOS) for the EM-SW modes show an abrupt change that derives from the nature of the EM-SW branch spin waves. This connection has never been made before. The present LFE linewidth results extend and amplify the results on the HFE linewidth discussed in Sections 6.2 and 6.3.

6.4.1. Measurement Method

The measured samples are nominal 2 mm diameter hipped and CS YIG spheres. The main reason for the choice of these samples lies in that they have very high densities, as mentioned in Section 6.1. Another important consideration for the LFE linewidth in these samples will relate to grain size. The hipped sample has a nominal grain size of about 8 microns, while the CS samples has a grain size on the order of 20 microns.

The cavity measurement method is exactly the same as in Section 6.2.1. The only difference lies in the concerning field range. Based on the modified ABA method, the cavity center frequency and quality factor Q_c are measured as a function of static

external field H_{ext} from a high field limit value of 0.70 T down to a low field limit of 0.1 T. Fields in the so-called manifold region of degenerate moderate k spin waves from 0.28 to 0.45 T were excluded. This is the interval that includes the usual FMR peak and where there is an especially large two magnon scattering contribution to the FMR losses and to the effective linewidth. For spheres, the nominal FMR field is about 0.35 T. The high losses in the manifold region generally cause a severe degradation in the Q_c of the cavity and precision Q_c measurements are not possible. The low field limit of 0.1 T is set by the onset of sample demagnetization effects that come in for external fields below about 0.07 – 0.08 T for YIG spheres. The high field limit of 0.7 T was adequate to obtain the high field limit cavity frequency and Q_c values needed for the effective linewidth analysis.

For effective linewidth measurements in the low field regime, it is necessary to go beyond the approximate treatment for the high field ΔH_{eff} analysis. This is necessary for two reasons. First, at low field, one cannot assume *a priori* that the condition $\Delta H_{eff} << H_{ext}$ is valid. Second, one cannot take the operational gyromagnetic ratio parameter that appears in the susceptibility expressions equal to the intrinsic gyromagnetic ratio γ as defined above. For these reasons, it is necessary to seek a somewhat more rigorous form of analysis. The equations below summarize a new approach that gives exact expressions for ΔH_{eff} that can be used in manifold as well as out of manifold.

Based upon Eqs. (4.17) and (4.18), the χ' and χ'' susceptibility components for a given field can be obtained from measurements of the cavity center frequency ω_c and

quality factor Q_c. The calibration parameters are generally obtained from high field measurements with the sample in place, and an extrapolation procedure, as shown in Section 6.2.2. These calibration parameters are then taken to be applicable over the full out-of-manifold high and low field regimes. That is, the changes in the cavity frequency and Q, relative to ω_∞ and Q_∞, are not too large.

Apart from the determination of K, ω_∞, and Q_∞, the one remaining connection is between the measured cavity parameters and $\Delta H_{\text{eff}}(H_{\text{ext}})$. In past effective linewidth work, various ways have been presented to extract $\Delta H_{\text{eff}}(H_{\text{ext}})$ from measurements of $\chi'(H_{\text{ext}})$ and $\chi''(H_{\text{ext}})$. Section 4.2.5 gives a new and previously undocumented algebraic solution for ΔH_{eff} directly in terms of the known field H_{ext}, the magnetization M_0, and the susceptibility components χ' and χ''. For convenience of discussions, the result is reproduced here,

$$\Delta H_{\text{eff}} = \frac{2M_0 H_{\text{ext}} \chi''}{2H_{\text{ext}}\left(\chi'^2 + \chi''^2\right) - M_0 \chi'}. \tag{6.5}$$

This equation constitutes an entirely rigorous expression for the effective linewidth at any field for which accurate data on χ' and χ'' are provided. The combination of Eqs. (4.17), (4.18), and (6.5), in turn, allow one to obtain $\Delta H_{\text{eff}}(H_{\text{ext}})$ from measurements of $\omega_c(H_{\text{ext}})$ and $Q_c(H_{\text{ext}})$. It is noteworthy that the working equation for ΔH_{eff} given in Eq. (6.6) does not involve knowledge of the gyromagnetic ratio γ. In the present approach, a numerical value of γ is needed only for the high field analysis used to get K_c, ω_∞, and Q_∞. Apart from this operation, therefore, an accurate value of γ does not play a crucial role in the data analysis of effective linewidth.

Prior to the susceptibility analysis to obtain $\Delta H_{\text{eff}}(H_{\text{ext}})$ from the ω_c and Q_c data, an additional correction was applied to the measured Q_c values to account for the small but possibly significant frequency dependence of the non-magnetic part of the quality factor. Corrections are made for the frequency dependence of the conductivity losses in the cavity walls. The details refer to Section 5.4.1. For low loss samples of the sort used here, this frequency correction amount to a change in the LFE linewidth by 10% or less and that in the HFE linewidth by 2% or less.

6.4.2. Measurement Results

Figure 1 shows representative measurement results on the nominal 10 GHz out-of-manifold effective linewidth. The open circles and squares show the data for the hipped and the CS YIG samples, as indicated. The graph shows HFE linewidth data for fields from about 0.45 to 0.7 T and LFE linewidth data for fields from about 0.1 T to 0.3 T. No data are shown in the high loss manifold region indicated by the vertical dotted lines at $\mu_0 H_{\text{ext}}$ = 0.338 T ($\mu_0 H_{90}$) and $\mu_0 H_{\text{ext}}$ = 0.415 T ($\mu_0 H_{00}$), or below 0.1 T in the region where sphere samples start to demagnetize. The vertical dashed reference lines labeled H_{00}^* and H_{90}^* mark shifted H_{00} and H_{90} field point to account for local pore demagnetizing fields. The dashed H_X reference line marks a transition field for EM-SW dispersion properties. Elaborations on the significance of these reference fields and curves are given below. These marked field values are calculated based on the standard YIG material parameter except for the saturation magnetization that is the measured value 0.1825 T for hipped YIG (Nazarov, 2003). This is because H_X is very sensitive to the saturation magnetization. The field designations will be of particular significance for

the discussion of 6.4.3.

What do these data show? Consider the high field region first. The HFE linewidth data for both samples show a gradual decrease as the field is increased. For fields above the H_{00}^{*} point, both sets of data follow closely to the scaled DOS curve, as expected from Section 6.2.4. For fields approximately below the H_{00}^{*} point, however, the HFE linewidth data points for the CS sample break from the hipped YIG data. This break is related to pore demagnetizing field and pseudo-in-manifold two magnon scattering effects. Such pseudo-in-manifold two-magnon scattering will also be a consideration for the LFE linewidth results.

For the low field effective linewidth results, there are two general observations and four specific points related to the structure of the responses. The first general observation is that the LFE linewidths in Fig. 6.6 are larger than the HFE linewidth values. The second general observation is that the relative hipped and CS ΔH_{eff} values are now reversed, as compared to the high field response. Now, the hipped sample LFE linewidths are generally *larger* than those for the CS samples.

With regard to structure, the most obvious point is in the change in the ΔH_{eff} vs. H_{ext} responses for both samples close to the H_X point. (1) Above $H_{\text{ext}} = H_X$ but below $H_{\text{ext}} = H_{90}^{*}$, both linewidths increase rapidly with field but the change for the CS sample is more rapid than for the hipped sample. (2) The CS linewidths start out smaller but increase more rapidly than the hipped linewidths as one moves from the H_X point to larger fields. (3) There is also an apparent crossover of the data for the two samples at a field close to $H_{\text{ext}} = H_{90}^{*}$. (4) As one moves below $H_{\text{ext}} = H_X$, the ΔH_{eff} for the

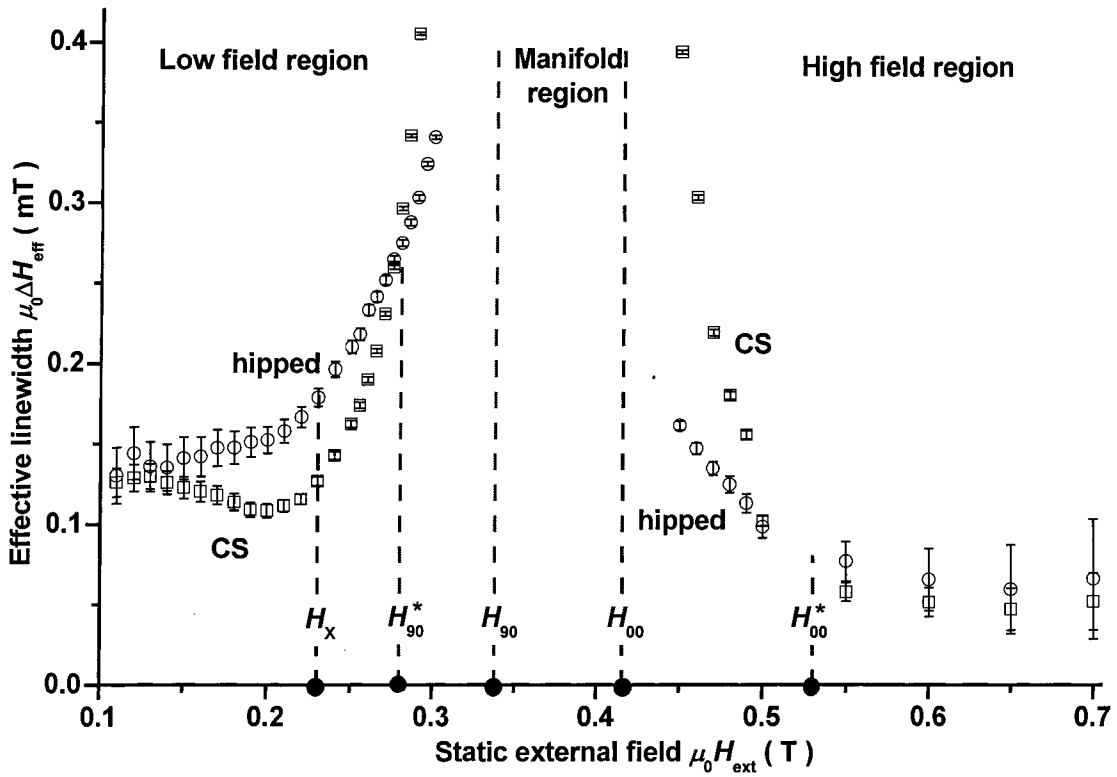

FIG. 6.6. Measured out-of-manifold effective linewidth ΔH_{eff} as a function of static external field $\mu_0 H_{\text{ext}}$ from 0.1 to 0.3 T and from 0.45 T to 0.7 T for the nominal 2 mm diameter hipped and conventionally sintered (CS) YIG spheres at a nominal signal drive frequency of 10 GHz. The open circles and the open squares show the hipped and the CS data, respectively. The uncertainty bars are also indicated with a coverage factor equal to 3. The low field, manifold, and high field regions are indicated. Vertical dashed lines indicate five important field reference points related to the spin wave band, at $\mu_0 H_X = 0.23$ T, $\mu_0 H_{90}^* = 0.28$ T, $\mu_0 H_{90} = 0.338$ T, $\mu_0 H_{00} = 0.415$ T, and $\mu_0 H_{00}^* = 0.53$ T.

hipped sample continues to decreases, albeit with a weaker response, while the CS data show an increase.

6.4.3. Qualitative Spin Wave Band Connections

What do these data mean? Detailed two magnon scattering connections based on the actual spin wave band evolution with field will be given in the next section. As

groundwork for this discussion, this section is intended to make some qualitative connections between the data and such processes.

For the HFE linewidth data, the decrease in ΔH_{eff} with increasing field corroborates the main result according to Section 6.2. There, it was shown that this tail response for fields above the H_{00}^{*} point in field correlates nicely with the decrease in the density of states for low wave number electromagnetic spin waves. In the high field regime, there are no other spin wave modes degenerate with the signal frequency.

The participant modes in this case are the EM-SW modes that lie *below* the light line, as shown in Fig. 2.6. These data may also be extrapolated to the high field limit to give a limit linewidth in the 0.05 mT range, very close to the intrinsic 10 GHz linewidth for YIG materials. The more rapid rise in the ΔH_{eff} for the CS sample as the field drops below H_{00}^{*} is due to differences in microstructure and, in particular, the effect of pores. The maximum pore-demagnetizing field in the direction *opposite* to the static external field is about $2M_0/3$, and this is precisely the separation of the H_{00}^{*} point from the H_{00} (no asterisk) point at the high field edge of the manifold region. As H_{ext} drops below H_{00}^{*}, there are regions in the CS sample that correspond to a local in-manifold bias and there is a corresponding increase in the effective linewidth.

For the LFE linewidth data, the generally larger values than found at high field may be attributed to the different spin wave density of states situations between high and low fields. In the early effective linewidth work by Patton (1969,1970), it was pointed out that one has high wave number dipole exchange spin waves degenerate with the drive frequency at low field, and these modes are not present at high field. One may argue,

qualitatively, that this difference accounts for the somewhat larger LFE linewidths relative to the HFE linewidth values. The high k will be discussed in Chapter 8.

The interchange of the relative CS and hipped effective linewidth values in going from high to low field is also related to the scattering to very high k short wavelength modes that are not available at high field. Scattering to high k and extremely short wavelength modes means that the predominant low field effective linewidth scattering source is in the grain boundaries rather than the grains themselves. For the low field ΔH_{eff}, the smaller grain size for the hipped samples means a larger net grain boundary area. Hence, high k grain boundary scattering will be larger for the hipped samples than for the CS samples. Simple geometric arguments give a grain boundary area that scales with the grain size a as $1/a$. This means that the hipped sample, with $a \approx 8$ μm, will have a little more than double the grain boundary area of the CS sample with $a \approx 20$ μm. One can see, therefore, that in the low field regime, it is reasonable to see a higher ΔH_{eff} for the hipped sample.

The structure in the LFE linewidth vs. field response is all related to the field dependent spin wave bands and changes in the two magnon scattering processes that depend on the degenerate modes associated with these bands. The basic connections are made here and detailed spin wave band explanations are considered shortly. The clear change in the ΔH_{eff} vs. H_{ext} response at fields close to $H_{\text{ext}} = H_X$ for both the CS and the hipped samples is due to the appearance of above-the-light-line EM-SW modes at the signal frequency for $H_{\text{ext}} < H_X$ that are not present at higher fields, as shown in Fig. 2.6. Below-the-light-line EM-SW modes are available for two-magnon scattering at all fields, but above-the-light-line modes come in *only* for $H_{\text{ext}} < H_X$.

For $H_{ext} > H_X$, there is interplay of different two magnon scattering effects that must be considered. In the interval $H_X < H_{ext} < H_{90}^*$, one is limited essentially to the high k scattering processes indicated above. The details of the corresponding ΔH_{eff} response involve interplay between the change in the density of states for these modes with field and the change in the coupling. With increasing field, the wave numbers for this band of modes will generally decrease and the density of states will also decrease. The drop in k, however, will also result in an increase in the coupling and a shift from the grain boundaries to the random grains and the pores as the dominant scattering source. The data in Fig. 6.6 indicate an increase in ΔH_{eff} with field in this region for both the hipped and the CS samples, and this suggests that the increase in the coupling as k decreases is the dominant effect. The more rapid increase in ΔH_{eff} for the CS samples is consistent with this conclusion, insofar as the somewhat larger grains and the porosity give a stronger low k scattering component.

There is a change in the degenerate mode situation as H_{ext} moves above the H_{90}^* field marker. Recall that in the high field regime, a drop in field below H_{00}^* results in a rapid increase in the effective linewidth for the CS sample because the demagnetizing fields around the residual pores produce regions that are effectively biased inside the manifold region and a corresponding very large two magnon scattering effect. This increase kicks in just at H_{00}^*, which is shifted up from H_{00} by $2M_0/3$. This shift is the same size as the maximum value of the demagnetizing field around a spherical pore directed *opposite* to the static field. This means that as soon as the external field H_{ext} drops below H_{00}^*, there are some regions of the sample that have a local internal field

that is actually below H_{00} and are inside the manifold region.

This same pseudo-in-manifold argument can also be applied to the low field region. Here, however, one must consider the maximum value of the pore-demagnetizing field that is *parallel* to the static field. For a spherical pore, this maximum demagnetizing field is equal to $M_0/3$. The field point at $H_{\text{ext}} = H_{90}^*$ is shifted down from H_{90} by this amount. A close examination of the low field data in Fig. 6.6 shows, moreover, that the hipped and the CS data points *appear to cross* at precisely this point in field. The rise in ΔH_{eff} for both samples as the field is increased is already quite rapid in this local region, and it is difficult to tell if there is an actual increase in the slope of the response, as one would expect from an onset of pseudo-in-manifold scattering for $H_{\text{ext}} > H_{90}^*$.

Consider the ΔH_{eff} responses for $H_{\text{ext}} < H_X$. The change in the ΔH_{eff} vs. H_{ext} field responses for both samples is clearly connected to the appearance of above-the-light-line EM-SW modes for $H_{\text{ext}} < H_X$. The discussion in the next section will make this clear. But why are these responses different? Recall that, empirically, there is *no* significant difference in the hipped and CS scattering for the below-the-light-line EM-SW modes in the high field regime. The two data sets in Fig. 6.6 fall essentially right on top of each other for $H_{\text{ext}} > H_{00}^*$. What is different in the low field regime? One possible argument concerns the spin wave ellipticity. At high field, the EM-SW modes have a weaker precession ellipticity and $k-$ dependence of the scattering is weaker. At low field, however, the ellipticity of the modes is much higher, and is also strongly field dependent. This could, in turn, lead to a stronger dependence on the microstructure.

The above connections provide the groundwork for more specific explanations

based on spin wave band considerations. More specific spin wave band, degenerate mode, and density of state scenarios to make these arguments somewhat more concrete are provided in the following part of this section.

Figure 6.7 together with Fig. 6.3 shows spin wave band diagrams that elucidate the manner in which these degenerate spin wave mode populations change with field. All diagrams were obtained for YIG parameters. The graphs in Fig. 6.7 show traditional plots of spin wave frequency ω_k vs. wave number k for two specific fields, as indicated. The vertical axes show frequency in GHz as $\omega_k / 2\pi$. The frequency cuts at $\omega_k / 2\pi = 10$ GHz indicate the signal frequency for the effective linewidth experiment. The bands evident in these graphs are formed from dispersion branches that range from wave vectors that are parallel to the static field ($\theta_k = 0$) to wave vectors that are perpendicular to the field ($\theta_k = 90°$), as indicated. The bands are labeled in all graphs as EML-HI, EMA, EML-LO, and DEL. The EML-LO and DEL labels actually correspond to the same band for low and high $k-$ranges, as indicated. The single graph in Fig. 6.3 has shown the corresponding plot of wave number k vs. the external field H_{ext} for a spherical sample with the frequency $\omega_k / 2\pi$ set to 10 GHz.

It is important to take note of the nomenclature for the band labels in Fig. 6.7. This will set the stage for the connections to two-magnon scattering considered below. An important line of reference is the narrow straight line EMA band in the Fig. 6.7 graphs. This narrow band corresponds to the light line at $\omega_{em} = c\,k / \sqrt{\varepsilon_r}$ in the nonmagnetic limit. The EML-HI label identifies the above-the-light-line band just above the EMA light-line band. The EML-LO label identifies the below-the-light-line band just below the EMA

band. This band was defined as the low wave number part of DEL band in Section 6.2. At high k, the EMA-HI band converges with the light line, while the EMA-LO band moves farther and farther away and finally evolves into the DEL band. The DEL band is so labeled to denote the relatively high k dipole-exchange (DE) nature of the high k far-from-the-light-line response.

The notation here follows that used in the preceding sections, except for the additional "HI" and the "LO" designations that are now invoked to designate the above-the-light-line and the below-the-light-line EM-SW bands. For high field effective linewidth, only the EML-LO band was important. For the low field effective linewidth, it is the EML-HI and DEL bands that play important roles.

The advantage of the Fig. 6.7 format is that one can see the full spin wave band scheme in reference to the specific slice of modes that are degenerate with the 10 GHz drive frequency for given field values. The $H_{\text{ext}} = 0.5$ T value for (b) was chosen to show the various positions of the spin wave bands that are relevant to the HFE linewidth. The $H_{\text{ext}} = H_X$ field point for (a) demonstrates the two-magnon scattering connections that are relevant to the low field effective linewidth. This is also the particular value for which the EML-HI band converges to the $\omega_k / 2\pi = 10$ GHz reference line at $k = 0$. These connections will become evident in the following discussion.

The advantage of the Fig. 6.3 format is that one can see directly the manner in which the wave numbers for the modes that are degenerate with the 10 GHz drive frequency change with field. The labels H_X, H_{90}, and H_{00} along the field axis show, respectively, the point in field at which the above-the-light-line EM-SW band limit frequency at $k = 0$ sits at 10 GHz, and the points in field at which the $\theta_k = 90°$ and

$\theta_k = 0$ low k limit frequencies for the DEL band also sit at 10 GHz. From the dispersion bands in Fig. 6.3 and the H_X, H_{90}, and H_{00} labels, one can now see why these points in field are identified in Fig. 6.7. Explicit connections will be developed shortly.

6.4.4. Two Magnon Scattering Connections

How do these spin wave band diagrams elucidate the role of two-magnon scattering in the effective linewidth? As a starting point, consider graph (a) in Fig. 6.7. For this relatively high field of 0.5 T, the main DEL band is shifted well above the $\omega_k / 2\pi = 10$ GHz reference line. One can see that the available degenerate modes all belong to the EML-LO band. It is these modes that dominate the effective linewidth change with field in the high field regime. This is discussed at length in Section 6.2. The decrease in the ΔH_{eff} with field for the hipped and CS materials in the right side high field regime of Fig. 6.6 is due to the decrease in the density of states for the modes in this EML-LO band. As one moves to higher and higher fields, the 10 GHz cut across the EML-LO band becomes smaller and smaller. The match up of the data with the DOS curve in Fig. 6.6 for $H_{\text{ext}} > H_{00}^{*}$ illustrates the process. It is important to emphasize that this scattering to the extremely low k EML-LO band of modes is relatively weak and the measured effective linewidths are only slightly larger than intrinsic linewidths.

Turn now to Fig. 6.7(b) and the low field effective linewidth situation. With the field set at $\mu_0 H_X$ = 0.23 T, the degenerate mode situation is quite different. The main change from (a) is that the entire ensemble of bands has dropped in frequency. There are three specific changes to note: First, the previously degenerate EML-LO modes are all

well below the $\omega_k / 2\pi$ = 10 GHz frequency cut. This means that the EML-LO modes that dominate the two magnon scattering contribution to the high field effective linewidth *are completely out of the picture* for the low field effective linewidth.

Second, note that the high k DEL modes that were previously available only for very high frequencies, now cross the 10 GHz cut. One can see that this high k 10 GHz cut will persist for the entire low field regime. This means that one can have scattering to these high k DEL modes over the entire low field regime. If large enough, one can expect that this scattering will provide the main part of the overall low field effective linewidth response. Keep in mind that the high k nature of these modes means that one must have strong scattering to spin wave modes *with very short wavelengths*, typically in the submicron range. As already noted, such scattering will invoke considerations of grain boundaries and not simply the micron sized grains of the polycrystals.

Third, for this particular choice of field for graph (b) at $H_{\text{ext}} = H_X$, one can see that the EML-HI band is now coming in to touch 10 GHz line just at $k = 0$. One can see that if the field is dropped further, to some value *below* H_X, the EML-HI band will drop even more in frequency and the 10 GHz cut *will then include more modes for this band.* The changes in the low field ΔH_{eff} vs. field response at $H = H_X$ in Fig. 6.6 for both the hipped and the CS samples may be attributed to the vanishing DOS component at 10 GHz for the EML-HI band for $H_{\text{ext}} > H_X$ and the appearance of an EML-HI DOS component for $H_{\text{ext}} < H_X$. Any change in the actual scattering, of course, will involve modes with low wave numbers and extremely large wavelengths. These are the same type of modes that are now known to play an important role in the high field effective linewidth, except that the EML-HI modes now replace the EML-LO modes and there is

now the additional effect of a field cut-off effect for $H_{\text{ext}} > H_X$.

The degenerate mode wave number vs. field display at fixed frequency in Fig. 3 provides an additional perspective to these processes. This format shows, at a glance, the ranges of k values and their associated bands for all modes that are degenerate with the driving frequency of 10 GHz. One sees, for example, the nearly horizontal cut of EMA band modes across the entire field range. Recall that this band goes over to the light line, $\omega_{em} = c\,k/\sqrt{\varepsilon_r}$, in the nonmagnetic limit. In the fixed frequency format of Fig. 6.3, this line is at a constant k value. Arguments will be given below to show that this field independent band of modes does not contribute to ΔH_{eff} in any field regime.

Figure 6.7 also shows that the positions of the EML-LO and EML-HI bands, relative to the EMA band, are now reversed from their positions in the Fig. 6.3 graphs. The EML-HI band is now below the essentially horizontal EMA light-line band and the EML-LO band is above. As far as the low field effective linewidth is concerned, the EML-LO band is now completely out of the picture. In the high field regime, of course, this is the only band of interest. At the same time, the EML-HI band, irrelevant in the high field regime, is now the relevant band for the low field case. One also sees, explicitly, the H_X cutoff point in field for EML-HI band. There are no EML-HI modes for $H_{\text{ext}} < H_X$. Finally, one sees from the DEL band position in Fig. 3 that these modes are only available to participate in two magnon scattering processes at $\omega_k / 2\pi$ = 10 GHz in the low field regime below $H_{\text{ext}} = H_{90}$. In contrast with the EML-HI band, however, there is no cutoff effect associated with this band.

The essentially field independent character of the narrow EMA light-line band of modes in Fig. 6.7 leads to the conclusion that these modes to not contribute to the field

dependence of the effective linewidth for any field in any appreciable way. There are two steps to this argument. First, the fact that the light-line band is flat in field implies that any contribution to ΔH_{eff} from EMA modes would be constant. Second, one notes that in the extreme high field limit, ΔH_{eff} extrapolates to values very close to the known intrinsic linewidths. Considered together, this means that any field independent background EMA band contribution to the effective linewidth can be taken to be near zero. This is certainly reasonable. One can also take note that the precession sense of the modes in the EMA band is anti-Larmor. The coupling between the predominantly Larmor character uniform mode in sphere samples and anti-Larmor modes would be expected to be weak.

Turn now to specific mode connections from Fig. 6.7(b) and Fig. 6.3 to the low field effective linewidth. First consider the two general points from Section 6.4.2. One can now see that the basis for a larger ΔH_{eff} in the low field regime, relative to high field, is that there are more degenerate modes. For $H_{\text{ext}} < H_X$, there are 10 GHz cuts across both the DEL and the EML-HI bands. For $H_{\text{ext}} > H_X$, there are only degenerate DEL modes. The high k nature of these modes generally means a larger density of states. The DEL modes are also the key to the interchange of the relative ΔH_{eff} values, with those for the hipped sample now greater than those for the CS samples. As already noted, scattering to high k and short wavelength modes will be connected more closely to grain boundaries, rather than grains and pores, and this will favor the ultra dense and relatively smaller grain hipped sample. One can see from Fig. 6.3 that the degenerate DEL modes have $k-$values in the 10^5 rad/cm range, with corresponding wavelengths well into the submicron range.

The specific ΔH_{eff} vs. H_{ext} dependences considered in Section 6.4.3 can also be placed into a clear spin wave perspective, based in the diagrams in Figs. 6.7 and 6.3. The role of the H_X field point is clear from both figures. The changes in the ΔH_{eff} vs. H_{ext} responses for both data sets at $H_{\text{ext}} = H_X$ are clearly related to the onset of mode degeneracy for the EML-HI modes at this field. The more rapid rise in the ΔH_{eff} for the CS sample, relative to that for the hipped sample for $H_{\text{ext}} > H_X$ must be related to the different interplay between the coupling and the density of states for these different microstructures. The apparent crossover at $H_{\text{ext}} = H_{90}^{*}$, and the larger CS ΔH_{eff} as one moves into the low field pseudo-manifold region is consistent with the similar effect in the high field regime for $H_{\text{ext}} < H_{00}^{*}$.

Finally, there are the quite different ΔH_{eff} responses for $H_{\text{ext}} < H_X$. This is the region where the EML-HI modes come into play. The fact that the EML-LO modes give rise to the same ΔH_{eff} vs. H_{ext} responses for $H_{\text{ext}} > H_{00}^{*}$ in the high field regime, while the EML-HI modes give rise to different responses for the hipped and the CS samples in the low field regime with $H_{\text{ext}} < H_X$, one can surmise that some different aspects of the scattering must be coming into play. One such possibility, noted in Section 6.4.3, concerns ellipticity. All of the modes tend toward a circular polarization as the field is increased and an elliptical polarization at lower fields. The different ΔH_{eff} vs. H_{ext} responses for the hipped and CS samples in this extreme low field regime may be related to different ellipticity related coupling factors for the different microstructures. It may be noteworthy that the two linewidths are roughly equal for an external field slightly above 0.1 T. This is about the point at which the spherical YIG samples will start to

demagnetize. Demagnetization will tend to average out polarization effects.

6.5. In-manifold Effective Linewidth

The difficulty of the in-manifold effective linewidth lies in the well-know cavity-overloading problem. The perturbation theory requires that the cavity Q change due to the absorption of the inserted sample should be small and usually in a relative range of 10%. When the field moves to the vicinity or the inside of the bulk manifold, the Q change may be larger than 10% and the determined effective linewidth is incorrect. This is called "cavity overloading". The smaller sample or the larger cavity can decrease the drop percentage of cavity Q change. In the previous effective linewidth measurements, a series of samples and cavities with different sizes must be used to overcome the overloading problem. This approach is so cumbersome that only Patton and Vrehen did it 40 years ago. Hoeppe (2004) tried to use it on low loss samples but failed in the near resonance measurements that require a tiny sample.

The cavity Q change can be decreased to any small range by the rotation of the cavity or the magnet poles. The magnetic energy coupling depends on the angle θ_h between the static external field and the microwave magnetic field at the site of the inserted sample. The smaller this angle is, the smaller the cavity Q change due to field. This technique has never been used before. The rotation should cover the range from 0° to 90°. The 90° case corresponds to a maximum coupling and the 0° case to zero coupling.

Although this decoupling approach is quite simple and the principle is well known, the measurements using this approach had never been made practically before. This

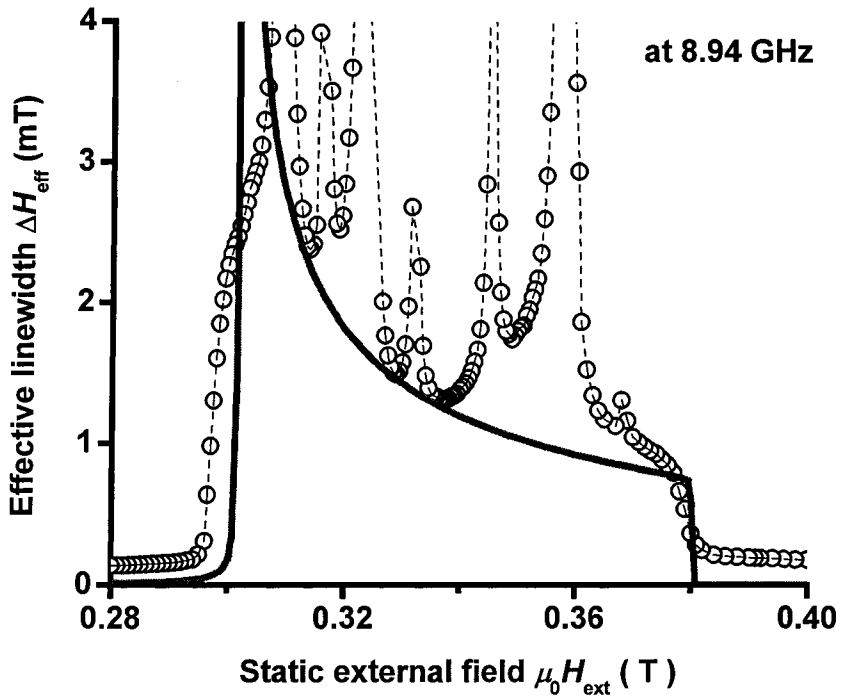

FIG. 6.8. Effective linewidth ΔH_{eff} as a function of static external field H_{ext} for a 2 mm diam hipped yttrium iron garnet (YIG) sphere measured with a reflection High Q TE_{011} cylindrical cavity with nominal center frequency be 9 GHz and nominal Q be 12000. The open circles show the data points and the thin dashed curve shows the adjacent connections. The solid curve shows the theoretical effective linewidth due to the anisotropy scattering using the same YIG parameters as in Fig. 6.3.

section shows such practical measurements on the 2mm diameter hipped YIG spheres. The measurements are obtained using the rotations of the reflection high Q cylindrical cavity. The objective of the reflection cavity measurements is to give a preliminary test for the feasibility of the cavity rotation approach and the problems thereof so as to further apply this approach to the more accurate transmission cavity measurements.

Figure 6.8 shows the effective linewidth ΔH_{eff} data for a 2mm diameter hipped YIG sphere in the static external field range of 0.28 to 0.4 T. The used reflection TE_{011} high Q cylindrical cavity is operating at a nominal frequency 9GHz and a nominal Q of

12000. Due to the inserted sample, the actual cavity center frequency is around 8.94 GHz. At this frequency, the FMR field is around 0.324 T. The open circles show the data points. To show the visual shape of the field dependence of the effective linewidth, the thin dashed curve shows the connections between the adjacent points. The solid curve shows the theoretical effective linewidth due to the anisotropy scattering using the standard YIG parameters (see Section 2.4) and a frequency of 8.94 GHz. The theoretical calculations are from Eqs. (3.16), (3.18), and (4.1). The first two equations are for the calculations of the relaxation rate as done in Fig. 3.6 and 3.7.

The first cavity measurement step is the ranges of 0.4 to 0.6 T and 0.06 to 0.25 T. These field ranges are outside the bulk manifold region. The data above 0.4 T are used to determine the calibration constants, K_c, f_∞, and Q_∞ so that the susceptibility and further the effective linewidth can be determined from the cavity center frequencies and Q factors in both filed ranges. The effective linewidth data above 0.4 T and below 0.28 T are truncated in Fig. 6.8.

Then, the cavity was rotated to make the angle between the microwave field and external field smaller. The rotation will also change the calibration constants, especially the geometry factor K_c while the Q_∞ and ω_∞ just have a slight change. In order to determine these new constants, the next field ranges were chosen to be 0.8 T and from 0.4 to 0.38 T. The re-measured data at 0.8 T give f_∞ and Q_∞. This approximation works well since the cavity data in the range of 0.4 to 0.38 T are far off 0.8 T and the susceptibility calculations are mainly dependent on these deviations. The cavity center frequency at 0.4 T together with that at 0.8 T was used to determine the K_c. As done in the first step, the susceptibility and the effective linewidth were calculated. Following

this rule, the whole manifold region is measured. The repeated ABA method is applied to every step individually. The number of cycles is from 10 to 20 for these in-manifold fields while the high field measurement cycles are more than 50 for the accurate determination of the calibration constants.

The field range shown in this figure covers the bulk manifold region that is H_{90}=0.302 T to H_{00}=0.378 T at 8.94 GHz. Inside the manifold, the effective linewidth has large values and shows the shoulders at around the edges of the bulk manifold while the out-of-manifold effective linewidth decreases as the field is away from the bulk manifold. This large linewidth range nicely matches up with the bulk manifold region where the linewidth values are much larger than the off resonance linewidths. There are several significant peaks in the manifold region.

In the scale of the large in-manifold linewidth, the HFE and LHE linewidths appear fairly field independent and has very small value of around 0.1 – 0.2 mT near the manifold edges, and the HFE linewidth here is larger than the LHE linewidth shown in Section 6.2. Such difference may come from an artifact introduced by the direct reflection of the cavity. This also implies that the reflection cavity is inappropriate for the measurements of the HFE and LFE linewidth that requires high accuracy data and is sensitive to the small deformation in the cavity response. The in-manifold linewidth is different and has large values that dominate over these small deformations.

The large values of the in-manifold linewidth are understandable since the density of degenerate spin wave states is very large and two-magnon scattering makes dominant contributions to the relaxation and further the effective linewidth. One might argue that the density of states in the low field region is larger than in manifold but the LHE

linewidth is very small. The spin wave numbers in these two regions are quite different. In the low field region, wave numbers are much larger than the inverse of the typical micrometer grain size, and the two-magnon scattering contributions are very small and even negligible. On the other hand, the available in-manifold spin wave numbers start from nearly zero. The modes with low wave number below the inverse of grain size lead to important two magnon scattering as discussed in Sections 6.2 and 6.4.

The hipped YIG sample is of no porosity. The available two-magnon scattering is due to the randomly distributed crystalline anisotropy. The anisotropy scattering for the manifold effective linewidth gives the larger contributions at lower field as shown in Fig. 3.6. This is consistent with the tendency in the data except for the peaks. If the peaks could be removed, the in-manifold linewidth has larger value at the lower field end and gradually decreases as the increase of the field. This nicely matches up with the calculated effective linewidth due to the pure anisotropy scattering indicated by the solid curve. The theoretical curve is slightly off the data. This may be because of the secondary scattering proposed by Schlömann (1969).

The peaks originate from the excited Walker (1957) normal modes. In the effective linewidth technique, it's assumed that only the uniform mode can be excited and the non-uniform modes are not accounted for. The microwave field around the sample appears nearly uniform but not exactly uniform especially for the large sample. The hipped YIG sample has very small losses and the non-uniform mode resonance peaks are very high. The data measured by Patton (1969) did show such high peaks with rounded shoulders. One can expect that using a small and high loss sample could largely eliminate the peak effect shown here.

7. QUATERNION-LIKE FORMUALTION OF FULL SPIN WAVE DISPERSION THEORY

As overviewed in Chapter 2, spin wave dispersion bands represent the characteristics of magnetic materials and provide the basis for the understanding of the spin dynamics, non-reciprocal phenomena, and relaxation in the magnetic materials. Typically, ferromagnetic resonance (FMR) analyses are based on the magnetostatic spin wave theory. In this approximation, only the moderate wave number (k) dipole-exchange spin wave band is taken into account while the low k and other bands are ignored. Such a treatment is incomplete, and leads to problems when one analyzes the FMR response in metals (Cochran *et al*, 1977) or attempts to explain off resonance losses (Mo *et al*, 2005). The full spin wave dispersion theory can be done classically through use of the magnetic torque equation and the Maxwell equations (Lax and Button, 1962), but a full treatment that includes conductivity, damping, and a general anisotropy is generally algebraically tedious and laborious (Patton, 1976).

In this chapter, a new approach to the classical theory of electromagnetic spin wave excitations has been developed, based on the use of Pauli matrices $\boldsymbol{\sigma}_x$, $\boldsymbol{\sigma}_y$, and $\boldsymbol{\sigma}_z$ to simplify the dynamic equations. One can analyze the low k propagation region and the high k exchange region, without approximation, and obtain relatively simple working equations in closed form. Based on this Pauli matrix formulation, one can write down

simple expressions for the spin wave dispersion and mode polarizations, and solve the requisite boundary value problems for finite geometry problems in a simple way. Such problems have previously required complicated transcendental analyses and numerical solution.

The three Pauli matrices were used first by William R. Hamilton (1843) to represent the vector basis of three-dimension space. A Quaternion is a 2×2 matrix in which the three coefficients of Pauli matrix components are the values of a vector along the x, y, z directions. Such matrix has four independent coefficients and should be treated to be a four-dimension vector. Quaternions have been found to be extremely useful for the theory in the four-dimensional relativistic spacetime, such as electrodynamics, general relativity, and Dirac theory. Quaternion analysis (Abdel-Khalek, 1996; Needham, 1997) also provides powerful tools for the nonlinear problems, such as fractals and chaos. For the linear dispersion problem of the two-dimension transverse magnetization, the coefficient matrix is automatically quaternionic even without Hamilton's vector conversion and the transverse magnetization can be expressed as a general quaternion multiplied by a regular vector.

Full spin wave bands have not yet been well explored due to the complexity in the calculations of spin wave dispersion relation, spin wave polarization, and boundary conditions. Note that the ferromagnetic resonance is expressed in terms of uniform mode excitation. The considerations of full spin wave bands leads to a big question, "what's the uniform mode?" since spin wave number is generally non-zero. The complexity also lies in the anisotropy fields and the damping parameters such as conductivity and relaxation, which were in part considered in the previous calculations. The field is

"magnetic" except for the explicit declaration of "electric". These parameters can substantially change the spin wave bands. For example, a large relaxation rate should adjust the spin wave dispersion curve due to secondary scattering processes (Schlömann, 1969). All these parameters may result in extra quaternions inserted into the torque equation.

The following derivation is quite general although only polycrystalline yttrium iron garnet (YIG) is of specific interest in this thesis. This is because of future investigations on metallic materials. In Section 7.1, the full Maxwell equations and linearized torque equation are described with effective static and dynamic anisotropic fields included. Section 7.2 describes the quaternion transformations and shows how to solve the dispersion relations for the plane waves. Section 7.3 gives the wave number solutions for spherical waves, which is particularly useful for spherical samples.

7.1. Governing Equations for Linear Responses

The classical theory is used to describe the local properties of ferro- and ferri-magnetic materials. The focus is upon a local small volume. This volume is assumed to be much bigger than the lattice of single crystals but much smaller than the grains. In Section 7.1.1, the anisotropy energy is converted into the effective static and dynamic anisotropy fields. Section 7.1.2 describes the local coordinate system based on the static equilibrium of local magnetization. Section 7.1.3 presents the matrix form of the linearized equations governing the motion of magnetization. Section 7.1.4 summarizes the boundary conditions.

7.1.1. Effective Crystalline Anisotropy Fields

The total free energy of a spin system is dependent on the directions of magnetization relative to the crystalline axes. This energy component is called the crystalline anisotropy energy that originates mainly from the lattice microstructures and spin-orbital interactions. The cubic and uniaxial anisotropies are two typical types of crystalline anisotropy. Here, the crystalline anisotropy energy is expressed as the sum of the cubic anisotropy energy and the uniaxial anisotropy energy so that the following analysis can cover most of magnetic materials with the cubic or uniaxial anisotropy.

For a typical single crystal, either the cubic anisotropy or the uniaxial anisotropy exists while any other kind of anisotropy is negligible. The typical examples can be yttrium iron garnet that has cubic anisotropy and the hexagonal barium ferrite that has uniaxial anisotropy. This allows making the axis for uniaxial anisotropy along one of the cubic crystalline axes for simplicity.

The anisotropy energy density U_a can be written as a function of the magnetization $\mathbf{M}$ and the unit vector of the crystalline axes, $\hat{\mathbf{x}}'$, $\hat{\mathbf{y}}'$, and $\hat{\mathbf{z}}'$.

$$U_a = -\frac{U_u}{M_0^2}\left(\mathbf{M}\cdot\hat{\mathbf{z}}'\right)^2 - \frac{U_c}{2M_0^4}\sum_{j=x',y',z'}\left(\mathbf{M}\cdot\hat{\mathbf{j}}'\right)^4. \tag{7.1}$$

Here, the first term stands for uniaxial anisotropy and the rest for cubic anisotropy. The parameters, U_u and U_c, are the uniaxial and cubic anisotropy energy constants, respectively. In comparison with the conventional expression, a constant term is neglected because the constant term makes no difference in the derivation of the effective anisotropy fields. M_0 is the saturation magnetization. The U_c can be simply set to be zero for uniaxially anisotropic materials while the U_u can be zero for the materials only with cubic anisotropy.

The anisotropy energy leads to a modification of the magnetic torque equation by inserting effective anisotropy field, $\mathbf{H}_A(t)$, into the total effective magnetic field. The anisotropy field is generally time dependent because the magnetization is time dependent. The $\mathbf{H}_A(t)$ is the negative gradient of the anisotropy energy density against the vector magnetization,

$$\mathbf{H}_A(t) = -\nabla_{\mathbf{M}} U_a = -\frac{dU_a}{d\mathbf{M}}. \tag{7.2}$$

Based on Eq. (7.1), one can obtain this field,

$$\mathbf{H}_A(t) = H_u \frac{\mathbf{M}\cdot\hat{\mathbf{z}}'}{M_0}\hat{\mathbf{z}}' + H_c \sum_{j=x',y',z'} \left(\frac{\mathbf{M}\cdot\hat{\mathbf{j}}'}{M_0}\right)^3 \hat{\mathbf{j}}'. \tag{7.3}$$

The magnitudes of the uniaxial and cubic anisotropy fields are denoted, respectively by $H_u = 2U_u / M_0$ and $H_c = 2U_c / M_0$.

The field can be written as a combination of a static component and a dynamic component. The $x'y'z'$ crystalline coordinates and the reference directions are shown in Fig. 3.1. The angles, $\beta_{x'}, \beta_{y'}$, and $\beta_{z'}$, are the angles between the static equilibrium magnetization, $\mathbf{M}_0$, and the crystalline axes, $\hat{\mathbf{x}}'$, $\hat{\mathbf{y}}'$, and $\hat{\mathbf{z}}'$, respectively.

The dynamic magnetization $\mathbf{M}$ is processing around the direction of $\mathbf{M}_0$. For small excitations, the angle between $\mathbf{M}$ and $\mathbf{M}_0$ is small and the static component of $\mathbf{M}$ is approximately equal to the saturation magnetization. The dynamic magnetization, $\mathbf{m}(t)$, is also small and approximately perpendicular to $\mathbf{M}_0$. One can write the magnetization in the following form,

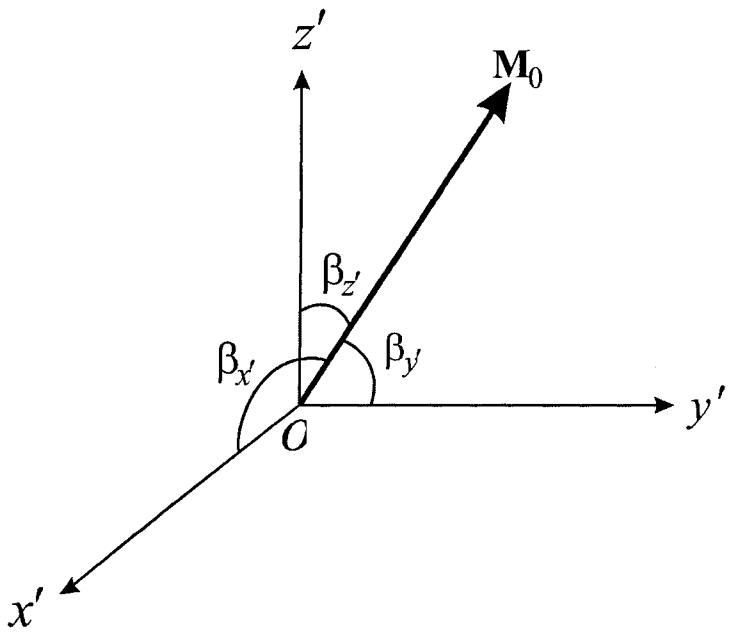

FIG 7.1. Diagram of the $x'y'z'$ crystalline coordinate system and the equilibrium magnetization $\mathbf{M}_0$. The angles between $\mathbf{M}_0$ and the axes, x', y', and z', are indicated by $\beta_{x'}$, $\beta_{y'}$, and $\beta_{z'}$, respectively.

$$\mathbf{M} = \mathbf{M}_0 + \mathbf{m}(t). \tag{7.4}$$

One then inserts Eq. (7.4) into Eq. (7.3) and only leave the linear term of **m** by neglecting the higher order terms in the small signal limit. The static component of the anisotropy field, $\mathbf{H}_{A0}$, is

$$\mathbf{H}_{A0} = H_u \cos\beta_{z'}\hat{\mathbf{z}}' + H_c \sum_{j=x,y,z} \cos^3\beta_{j'}\hat{\mathbf{j}}'. \tag{7.5}$$

The dynamic anisotropic field, $\mathbf{h}_A$, is

$$\mathbf{h}_A \approx H_u \frac{\mathbf{m}\cdot\hat{\mathbf{z}}'}{M_0}\hat{\mathbf{z}}' + 3H_c \sum_{j=x,y,z} \cos^2\beta_{j'} \frac{\mathbf{m}\cdot\hat{\mathbf{j}}'}{M_0}\hat{\mathbf{j}}'. \tag{7.6}$$

In Eqs. (7.5) and (7.6), the first terms and the second terms correspond to the uniaxial

anisotropy and the cubic anisotropy, respectively.

The non-zero dynamic anisotropy fields will be induced by the dynamic magnetization motion as shown in Eq (7.6). For large anisotropy field, the dynamic term must be considered, for example, barium ferrite (Truedson, 1992). The dynamic anisotropy response is not quite well known because the anisotropy in most magnetic materials is relatively weak typically ignored in the FMR response. It can be shown that the dynamic anisotropy is a maximum when the static anisotropy is a minimum. One will see in Section 7.1.3 that the dynamic and static anisotropies are of equal importance. It's improper to generally ignore one and only take account for the other. Otherwise, one may lead to a non-physical rotatable anisotropy (Schneider *et al*, 2005).

7.1.2. Static Equilibrium and Coordinate System

For the linear response of the magnetization, the static equilibrium and the magnetization dynamics can be separately considered. The equilibrium should be first solved since the dynamics of magnetization is related to the equilibrium as implied by Eq. (7.6). The equilibrium is also useful for choosing an appropriate coordinate system. For an inappropriate system, the governing equations for solving the spin wave dispersion relation would be 8^{th} order polynomial. A general 8^{th} order polynomial equation cannot be analytically solved. By choosing the coordinate system, the governing equations can be equivalent to a 4^{th} order polynomial equation.

The static equilibrium can be solved based on

$$\mathbf{M}_0 \times \mathbf{H}_0 = 0. \tag{7.7}$$

The field, $\mathbf{H}_0$, is the total static magnetic field. This field includes the static part of the

external field, $\mathbf{H}_{ext}$, the demagnetizing (or dipolar) field, $\mathbf{H}_D$, and the anisotropy field, $\mathbf{H}_{A0}$. Namely,

$$\mathbf{H}_0 = \mathbf{H}_{ext} - \ddot{\mathbf{N}} \cdot \mathbf{M}_0 + \ddot{\mathbf{A}} \cdot \mathbf{M}_0 . \tag{7.8}$$

Here $\ddot{\mathbf{N}}$ and $\ddot{\mathbf{A}}$ are the 3×3 tensors of demagnetizing factor and anisotropy. The 2nd and 3rd terms stand for the static demagnetizing field and the static anisotropy field, respectively. It's known that $\ddot{\mathbf{N}}$ is dependent on the sample geometry. As example, $\ddot{\mathbf{N}} = \ddot{\mathbf{I}}_{3\times3}/3 = 1/3$ for sphere where $\ddot{\mathbf{I}}_{3\times3}$ is the 3×3 identity matrix. In this thesis, the identity matrix is omitted.

In the $x'y'z'$ coordinate system, the anisotropy tensor $\ddot{\mathbf{A}}$ can be derived from Eq. (7.5).

$$\mathbf{H}_{A0} = \begin{bmatrix} H_c \cos^3 \beta_{x'} \\ H_c \cos^3 \beta_{y'} \\ H_u \cos \beta_{z'} + H_c \cos^3 \beta_{z'} \end{bmatrix} = \ddot{\mathbf{A}} \cdot \mathbf{M}_0 . \tag{7.9}$$

Note that

$$\mathbf{M}_0 = M_0 \begin{bmatrix} \cos \beta_{x'} \\ \cos \beta_{y'} \\ \cos \beta_{z'} \end{bmatrix} . \tag{7.10}$$

One can obtain the form of $\ddot{\mathbf{A}}$,

$$\vec{\vec{\mathbf{A}}} = \begin{bmatrix} \dfrac{H_c \cos^2 \beta_{x'}}{M_0} & 0 & 0 \\ 0 & \dfrac{H_c \cos^2 \beta_{y'}}{M_0} & 0 \\ 0 & 0 & \dfrac{H_u + H_c \cos^2 \beta_{z'}}{M_0} \end{bmatrix}. \qquad (7.11)$$

Equation (7.7) tells that the static magnetization in equilibrium is parallel to the static effective field. Based on this, the direction of the magnetization can be solved. The further calculations are trivial mathematics.

A general coordinate system involves three-dimension vectors. This usually makes the calculations fairly cumbersome. The small signal limit allows using 2-dimensional vectors instead of three-dimensional vectors since the component of $\mathbf{m}(t)$ along the equilibrium direction is neglected. The coordinate system can be chosen to make the equilibrium direction of magnetization as the positive z direction. The magnetization precesses around the z-axis with non-zero transverse components. The choices of x and y axes are not critical. Such system is here called "local coordinate system" (LCS) since the equilibrium direction varies with the position for non-uniform magnetized samples.

7.1.3. Linearized Torque Equation

The dynamic properties of magnetization are basically governed by Maxwell's equations and the torque equation. The effective terms will be added for considerations of anisotropy field, damping (or relaxation), and exchange interaction. In the small signal limit, these equations, especially the torque equation, can be linearized. The torque equation is reproduced here,

$$\frac{\partial \mathbf{M}}{\partial t} = -|\gamma|\mathbf{M} \times \mu_0 \mathbf{H} + \mathbf{T}_D . \tag{7.12}$$

As defined in Chapter 2, γ is the gyromagnetic ratio and $\mathbf{H}$ is the total field including static and dynamic terms. The last term, $\mathbf{T}_D$, is introduced so as to account for the microwave damping or relaxation.

The total field $\mathbf{H}$ can be written as a sum of the static component and the dynamic component.

$$\mathbf{H} = \mathbf{H}_0 + \mathbf{h}(t) = H_0 \hat{\mathbf{z}} + \mathbf{h}(t) . \tag{7.13}$$

The field, $\mathbf{h}$, is the dynamic part of $\mathbf{H}$. This includes the Maxwellian internal field, the anisotropy field, and the effective exchange field. The exchange field is here assumed to be dynamic because typically the static magnetization is of weak spatial dependence. This assumption may not be correct in some special cases; for example, exchange bias field is very big (McMichael, 2000). In the LCS system, $\mathbf{M}_0$ and $\mathbf{H}_0$ point to the positive z direction. One takes the small signal limit and obtains a linear equation for the dynamic transverse magnetization. Equation (7.12) becomes

$$\frac{\partial \mathbf{m}}{\partial t} = -\hat{\mathbf{z}} \times \left(\omega_M \mathbf{h} - \omega_H \mathbf{m} \right) + \mathbf{T}_D . \tag{7.14}$$

As defined in Chapter 2, $\omega_M = |\gamma| \mu_0 M_0$ and $\omega_H = |\gamma| \mu_0 H_0$. The only difference is that more generally the anisotropy field is included in ω_H.

Only the x and y components need be considered because $\mathbf{m}$ only has transverse components. In all the following discussions, the dynamic field and magnetization refer to the transverse components whereas the z dynamic components are ignored, except that the three components are explicitly mentioned. The torque equation is written as a 2×2

matrix equation,

$$\boldsymbol{\sigma}_y \frac{\partial \mathbf{m}}{\partial t} + \omega_H \mathbf{m} - \boldsymbol{\sigma}_y \cdot \mathbf{T}_D = \omega_M \mathbf{h}. \tag{7.15}$$

The definition of Pauli's matrices are reproduced here,

$$\boldsymbol{\sigma}_x = \begin{bmatrix} 0 & 1 \\ 1 & 0 \end{bmatrix}, \boldsymbol{\sigma}_y = \begin{bmatrix} 0 & -1 \\ 1 & 0 \end{bmatrix}, \text{ and } \boldsymbol{\sigma}_z = \begin{bmatrix} 1 & 0 \\ 0 & -1 \end{bmatrix}. \tag{7.16}$$

The only difference from typical Pauli's matrices is just a constant coefficient, $-i$, in $\boldsymbol{\sigma}_y$. The advantage of the re-definition is that the above equation may be solved in the real space where the physical meanings are clear. For these constant tensors, the tensor notation is removed, $\ddot{\boldsymbol{\sigma}}_{x,y,z} \equiv \boldsymbol{\sigma}_{x,y,z}$. The above-defined Pauli matrices follow the left hand rule. One can obtain,

$$\boldsymbol{\sigma}_x \boldsymbol{\sigma}_y = \boldsymbol{\sigma}_z, \boldsymbol{\sigma}_x \boldsymbol{\sigma}_z = \boldsymbol{\sigma}_y, \text{ and } \boldsymbol{\sigma}_y \boldsymbol{\sigma}_z = \boldsymbol{\sigma}_x. \tag{7.17}$$

In Chapter 2, it has been shown that the effective linewidth for sphere can be converted to an effective Gilbert damping constant α, which is generalized to be frequency and field dependent. The damping torque $\mathbf{T}_D$ is replaced by the Gilbert damping term (Gilbert, 1954),

$$\mathbf{T}_D = \frac{\alpha}{M_0} \mathbf{M} \times \frac{\partial \mathbf{M}}{\partial t} \rightarrow \alpha \boldsymbol{\sigma}_y \frac{\partial \mathbf{m}}{\partial t}. \tag{7.18}$$

Equation (7.15) becomes

$$\left(\boldsymbol{\sigma}_y + \alpha\right) \frac{\partial \mathbf{m}}{\partial t} + \omega_H \mathbf{m} = \omega_M \mathbf{h}. \tag{7.19}$$

In order to understand a spin wave in the matrix form, let's look at free precession, $\mathbf{h} \rightarrow 0$. In this simple case, equation (7.19) can be easily solved in the time domain,

$$\mathbf{m}(t) \approx e^{(\boldsymbol{\sigma}_y - \alpha)\omega_H t}\mathbf{m}(t=0). \tag{7.20}$$

Note that this expression is purely in real space. The square of $\boldsymbol{\sigma}_y$ is equal to negative identity and $e^{\boldsymbol{\sigma}_y \omega_H t}$ is a special plane wave since $\boldsymbol{\sigma}_y$ can play the same role as the imaginary number i. This wave corresponds to the uniform mode free precession. The trivial expansion to the x and y components indicates that the phase $\omega_H t$ corresponds to the rotated angle of $\mathbf{m}$ about the z axis. This can be understood in Fig. 2.1. The tensor $\boldsymbol{\sigma}_y$ represents the counterclockwise (Larmor) circular polarization. The waveform $e^{-\boldsymbol{\sigma}_y \omega_H t}$ is the clockwise (anti-Larmor) circular precession and $-\boldsymbol{\sigma}_y$ represents the anti-Larmor circular polarization. This is completely different from $e^{\pm i\omega t}$ where ± means nothing about Larmor and anti-Larmor precessions. With a general normalized quaternion σ, the waveform $e^{\pm\sigma\omega_H t}$ may not stand for circular polarization. This quaternion can be called polarization tensor.

Moreover, it is evident that $\alpha\omega_H$ is the exponential decay rate. This indicates that the phenomenological damping can be obtained based on a replacement of $\boldsymbol{\sigma}_y$ by $\boldsymbol{\sigma}_y - \alpha$. The Gilbert damping $\alpha\omega_H$ is only related to the total static field as in ω_H but not to the relative directions and magnitudes of the field components in $\mathbf{H}_0$. This is not the case of extrinsic losses. Therefore, the Gilbert constant is only good to characterize the intrinsic loss.

Now back to Eq. (7.19), the total dynamic field $\mathbf{h}$, includes microwave drive field $\mathbf{h}_p$, $\mathbf{m}$-induced dipole field $\mathbf{h}_d$, the effective exchange field $\mathbf{h}_{\text{ex}}$, and the dynamic anisotropy field $\mathbf{h}_A$. The first two fields are Maxwellian fields, namely the dynamic

internal field $\mathbf{h}_i = \mathbf{h}_p + \mathbf{h}_d$. The last three fields can be expressed as function of $\mathbf{m}$. The exchange field is

$$\mathbf{h}_{ex} = D_0 \cdot \nabla^2 \mathbf{m}. \tag{7.21}$$

For the dynamic anisotropic field, equation (7.6) gives its expression in the crystalline coordinate system. The expression in the LCS system can be found by trivial coordinate transformations. No matter what the transformations are, it can be found that in the LCS system, the x and y components of the dynamic anisotropy field can be written as a general matrix form as follows,

$$\mathbf{h}_A \approx \left(a_0 + a_x \boldsymbol{\sigma}_x + a_z \boldsymbol{\sigma}_z\right)\mathbf{m}. \tag{7.22}$$

The dimensionless parameters, a_0, a_x, and a_z, depends on the coordinate transformation and the anisotropy fields. This general form is applicable to any kinds of anisotropy fields although only the uniaxial and cubic anisotropy fields are discussed here. It's interesting that the dynamic anisotropy tensor $a_0 + a_x \boldsymbol{\sigma}_x + a_z \boldsymbol{\sigma}_z$ doesn't have a term related to $\boldsymbol{\sigma}_y$. The $\boldsymbol{\sigma}_y$ term means a component perpendicular to $\mathbf{m}$ because $\hat{\mathbf{z}} \times \rightarrow \boldsymbol{\sigma}_y$ and $\mathbf{m}$ is perpendicular to $\hat{\mathbf{z}}$. Equation (7.6) indicates that the dynamic anisotropy field along each anisotropy axis is always parallel to this axis. The motion of such dynamic anisotropy field has a linear polarization. One can choose the appropriate x and y coordinates to make $a_x = 0$. The following discussions in Chapters 7 and 8 are focused on this case.

Insert the exchange field and the anisotropy field into Eq. (7.19) and one obtains

$$\left[\frac{\boldsymbol{\sigma}_y + \alpha}{\omega_M}\frac{\partial}{\partial t} + \Omega_H - D_0\nabla^2 - a_0 - a_z\boldsymbol{\sigma}_z\right]\mathbf{m} = \mathbf{h}_p + \mathbf{h}_d. \tag{7.23}$$

Here, $\Omega_H = \omega_H / \omega_M$. Meanwhile, it has been shown in Chapter 2 that the dipole field for an insulator should follow Eq. (2.37). With the inclusion of conductivity σ_c, it becomes

$$\left[\nabla^2 - \left(\frac{\sigma_c}{\varepsilon_0 c^2} + \frac{\varepsilon_r}{c^2}\frac{\partial}{\partial t}\right)\frac{\partial}{\partial t}\right]\mathbf{h}_d = -\nabla_t(\nabla_t \cdot \mathbf{m}) + \left(\frac{\sigma_c}{\varepsilon_0 c^2} + \frac{\varepsilon_r}{c^2}\frac{\partial}{\partial t}\right)\frac{\partial \mathbf{m}}{\partial t}. \tag{7.24}$$

The parameter ε_r is the relative dielectric constant. Generally, the conductivity is a tensor due to Hall effect. The generalization is not discussed here. Note that

$$\nabla_t = \frac{\partial}{\partial x}\hat{\mathbf{x}} + \frac{\partial}{\partial y}\hat{\mathbf{y}}. \tag{7.25}$$

From Eqs. (7.23) and (7.24), one obtains the final governing equation,

$$\left[\frac{\boldsymbol{\sigma}_y + \alpha}{\omega_M}\frac{\partial}{\partial t} + \Omega_H - D_0\nabla^2 - a_0 - a_z\boldsymbol{\sigma}_z + \tilde{\mathbf{N}}\right]\mathbf{m} = \mathbf{h}_p, \tag{7.26}$$

where $\tilde{\mathbf{N}}$ is an operator for dipole field,

$$\tilde{\mathbf{N}} = \frac{\nabla_t(\nabla_t \cdot) - \left(\frac{\sigma_c}{\varepsilon_0 c^2} + \frac{\varepsilon_r}{c^2}\frac{\partial}{\partial t}\right)\frac{\partial}{\partial t}}{\nabla^2 - \left(\frac{\sigma_c}{\varepsilon_0 c^2} + \frac{\varepsilon_r}{c^2}\frac{\partial}{\partial t}\right)\frac{\partial}{\partial t}}. \tag{7.27}$$

The inverse of derivative operators is discussed in Chapter 8. It's used here for the elegance of equations. This tensor is equivalent to the integral Green function. For bounded $\mathbf{m}$, this operator automatically includes Maxwellian boundary conditions. The damping, conductivity, and exchange parameter are included in Eq. (7.26). This working equation is completely general and can apply to materials ranging from isotropic to anisotropic, insulator to metal, and single crystal to polycrystalline, nano-crystalline, or random media.

The external microwave field $\mathbf{h}_p$ is defined as the microwave magnetic field in the absence of magnetic properties of the concerning sample. Therefore this field follows,

$$\left[\nabla^2 - \left(\frac{\sigma_c}{\varepsilon_0 c^2} + \frac{\varepsilon_r}{c^2}\frac{\partial}{\partial t}\right)\frac{\partial}{\partial t}\right]\mathbf{h}_p = 0. \tag{7.28}$$

One can simply use the above equation to solve the microwave drive field by applying Maxwellian boundary conditions.

7.1.4. Boundary Conditions

When the spin wavelength is comparable to the sample size, especially for the low wave number spin wave excitations and for the small sample dimension such as thin film, the boundary conditions become important. The boundary conditions are well known. This section just summarizes these conditions. There are two types of boundary conditions for the differential equation (7.26). One is the exchange boundary condition due to the spatial derivatives in the exchange field. The other is the Maxwellian boundary condition, which is usually expressed in terms of the electric field and the magnetic field but not the magnetization.

The surface layer of magnetic material has different microstructures from the body, which gives extra surface anisotropy energy. The surface anisotropy energy is also associated with the randomly distributed surface directions. These anisotropy variations may make important contributions to two-magnon scattering (Arias and Mills, 1999). For a given normal direction $\hat{\mathbf{n}}_g$ of the surface, this energy density ε_s can be expressed by

$$\varepsilon_s = -\frac{U_s}{M_0^2}\left(\mathbf{M}\cdot\hat{\mathbf{n}}_g\right)^2, \tag{7.29}$$

where U_s is surface anisotropy energy constant. The corresponding effective surface field $\mathbf{H}_s$ follows the same rule as that in the static uniaxial anisotropy,

$$\mathbf{H}_s = \frac{2U_s}{M_0}\frac{\mathbf{M}\cdot\hat{\mathbf{n}}_g}{M_0}\hat{\mathbf{n}}_g. \tag{7.30}$$

The general exchange boundary condition based on thin films has been derived (Soohoo, 1960; Kalinikos *et al*, 1986).

$$\left(\hat{\mathbf{n}}_g\cdot\nabla\right)\mathbf{m} + \xi_0\left(\hat{\mathbf{z}}\cdot\hat{\mathbf{n}}_g\right)^2\mathbf{m} = 0 \text{ at boundaries.} \tag{7.31}$$

ξ_0 is a parameter of spin pinning on the surface. It can be expressed in terms of surface anisotropy field,

$$\xi_0 = \int_{\substack{\text{surface}\\ \text{layer}}} \frac{2D_0}{M_0}\hat{\mathbf{z}}\cdot\mathbf{H}_s dz. \tag{7.32}$$

This boundary condition can also be applicable for surfaces of the grains. In this case, $\hat{\mathbf{n}}_g$ stands for the normal direction at any local position of the grain surface. The parameter $D_0\xi_0$ has a unit of length and can be interpreted as the effective thickness of the surface layer.

The boundary condition (7.31) is valid under two conditions. First, it was assumed that the surface anisotropy field is large compared with the other fields. Generally, the static effective field may also be big and comparable to the surface anisotropy field. In this case, the parameter ξ_0 should be effectively field dependent. Second, the static equilibrium in the surface layer is assumed to be the same as that in the body of the

materials. This is not true since the surface anisotropy is assumed to be large. Even the directions of the dynamic magnetization that is perpendicular to the static equilibrium direction would be different since the surface anisotropy field is assumed to be very big. These two conditions contradict with each other. It implies that the exchange boundary condition needs major modifications.

For the Maxwellian boundary conditions, it's well known that the tangential components of $\mathbf{E}$ and $\mathbf{H}$ are continuous. These boundaries are applicable to not only the static cases but also the dynamic cases. This leads to

$$\begin{aligned} \hat{\mathbf{n}}_s \times \mathbf{h}_i &= \hat{\mathbf{n}}_s \times \mathbf{h}_i^{out} \\ \hat{\mathbf{n}}_s \times \mathbf{e}_i &= \hat{\mathbf{n}}_s \times \mathbf{e}_i^{out} \end{aligned} \quad \text{at boundaries,} \tag{7.33}$$

where the superscript ^{out} stands for the region outside the material.

The Maxwellian boundary conditions can be expressed in terms of magnetization. The fields in the left side of Eq. (7.33) can be expressed in terms of magnetization inside the material. In the right side, the electric field can be connected with the magnetic field based on Maxwell equations in air or vacuum and the vectors of the right side are also in the plane perpendicular to $\hat{\mathbf{n}}_g$. A rotation about $\hat{\mathbf{n}}_g$ can connect these two fields and finally the electric and magnetic fields of the right side are eliminated. This derivation and the boundary condition problem are not included in this thesis.

7.2. Spin Wave Dispersion for Plane Waves

This section shows the derivation of the spin wave dispersion for ferro- and ferri-magnetic materials based on Eq. (7.26). Spin waves are written as plane waveform. Section 7.2.1 describes the transformations for the simplification of the governing

equation. The approximate and exact solutions for the eight spin wave number solutions are presented in Section 7.2.2 and 7.2.3, respectively. Section 7.2.4 gives the solution of the field against the spin wave parameters. Example calculations for YIG with non-zero damping and anisotropy field are shown in Section 7.2.5.

7.2.1. Transformations

A. Plane Waveform

Equation (7.26) is a linear differential equation. The first transformation is the spatial and time Fourier transformation. This transformation can turn the derivatives into frequency ω and wave vector $\mathbf{k}$. In the spherical coordinate system, $\mathbf{k} = (k, \theta_k, \phi_k)$. One assumes plane spin waves of the form $\mathbf{m}(\mathbf{r},t) \to \mathbf{m}(\mathbf{k},\omega)e^{i(\omega t - \mathbf{k}\cdot\mathbf{r})}$, where ω is the operating spin wave frequency and $\mathbf{k}$ is the spin-wave wave vector. Note that $\mathbf{m}(\mathbf{k},\omega)$ is two component vectors. The $\mathbf{m}(\mathbf{k},\omega)$ gives the spin wave polarization. The right-hand wave is of Larmor and the left-hand is of anti-Larmor.

Based on the partial waveform, the derivatives can be converted into functions of spin wave frequency and wave vector. For example,

$$\nabla(\nabla\cdot) \to -\frac{k^2 \sin^2\theta_k}{2}(1+\boldsymbol{\sigma}_z e^{-\boldsymbol{\sigma}_y 2\phi_k}) \tag{7.34}$$

One hereby obtains a quadratic quaternion equation for k^2 that may be written as

$$\left\{\left[i\Omega(\boldsymbol{\sigma}_y+\alpha)+\Omega_H + D_0 k^2 - (a_0 + a_z\boldsymbol{\sigma}_z)\right](k^2 - k_0^2) + \frac{k^2 \sin^2\theta_k (1+\boldsymbol{\sigma}_z e^{-\boldsymbol{\sigma}_y 2\phi_k})}{2} - k_0^2\right\}\mathbf{m} = 0 \tag{7.35}$$

The parameter k_0 is the pure electromagnetic complex wave number defined by

$$k_0 = \sqrt{\frac{\varepsilon_r \omega^2}{c^2}\left(1 - i\frac{\sigma_c}{\varepsilon_0 \varepsilon_r \omega}\right)}. \tag{7.36}$$

The parameter Ω is the normalized frequency, $\Omega = \omega / \omega_M$. The external field $\mathbf{h}_p$ vanishes based on Eq. (7.28).

The vector equation (7.35) is general for governing the dispersion properties of spin waves and applicable to any kind of magnetic materials. Compared with the previous efforts by Herring and Kittel (1951), Lax and Button (1962), and Patton (1975), the dielectric constant and the anisotropy fields are included here. Apply this equation to the special cases or some approximations and three previous versions can be obtained. Lax and Button (1962) did the more special case of $\sigma_c \to 0$ for the applications in the insulators and the work of Patton (1985) was based on the metal approximation of $k_0^2 \to -i\sigma_c \omega / \varepsilon_0 c^2$. The earliest version by Herring and Kittel (1951) was only for the magnetostatic or long wavelength limit, which is equivalent to $k_0 \to 0$.

B. Quaternion Form

There are three forms of these solutions for Eq. (7.35): (I) the spin wave frequency is expressed in terms of the wave vector and the static field; (II) the spin wave numbers are function of spin wave frequency, wave vector directions, and the static field; (III) the static field as function of the spin wave frequency and wave vector. In the magnetostatic limit, the first one is easy to obtain. The second one is quite useful for applying the boundary conditions and also convenient to solve for the general case. The third one

called field dispersion can provide an overall picture of the degenerate spin wave modes for the sake of two magnon scattering and field dependent effective linewidth.

For convenience of Type II solutions, one can write Eq. (7.35) with quaternion coefficients.

$$\left[Y^2 + \left(\Omega_0 + 2D_0 k_0^2 + i\Omega\boldsymbol{\sigma}_y - a_z\boldsymbol{\sigma}_z + \frac{\sin^2\theta_k}{2}\boldsymbol{\sigma}_z e^{-\boldsymbol{\sigma}_y 2\phi_k} \right) Y \right. \\ \left. - \frac{D_0 k_0^2}{2}\left(1 + \cos^2\theta_k - \boldsymbol{\sigma}_z \sin^2\theta_k e^{-\boldsymbol{\sigma}_y 2\phi_k}\right) \right] \mathbf{m} = 0 \quad , \tag{7.37}$$

where

$$Y = D_0(k^2 - k_0^2), \tag{7.38}$$

and

$$\Omega_0 = \Omega_H + i\alpha\Omega - a_0 - D_0 k_0^2 + \frac{1}{2}\sin^2\theta_k \tag{7.39}$$

Typically, the solution $k(\Omega, \theta_k, \phi_k)$ is related to make the determinant of the matrix coefficient equal to zero and get a quartic equation of k^2 in a general form. The solutions of a general quartic equation involve solving a general cubic equation. Here, let's solve k directly from the quaternion equation (7.37). This way can make not only the solving procedure simpler but also the polarization be in an explicit form.

C. Rotations

The quaternion coefficient is fairly complicated and includes the components of $\boldsymbol{\sigma}_x$, $\boldsymbol{\sigma}_y$, and $\boldsymbol{\sigma}_z$. It's necessary to make some simplifications. First, make a transformation of $e^{-\boldsymbol{\sigma}_y\phi_k}$. The physical meaning is an anti-clockwise rotation around z axis by an angle

ϕ_k. One obtains

$$\left\{Y^2+\left[\Omega_0+i\boldsymbol{\sigma}_y\sqrt{\Omega^2+a_z^2\sin^2 2\varphi_k}\,e^{i\boldsymbol{\sigma}_z\tan^{-1}\frac{a_z\sin 2\phi_k}{\Omega}}\right.\right.$$
$$\left.+2D_0k_0^2-\boldsymbol{\sigma}_z\left(a_z\cos 2\phi_k-\frac{\sin^2\theta_k}{2}\right)\right]Y \qquad . \qquad (7.40)$$
$$\left.-\frac{D_0k_0^2}{2}\left(1+\cos^2\theta_k-\boldsymbol{\sigma}_z\sin^2\theta_k\right)\right\}e^{-\boldsymbol{\sigma}_y\phi_k}\mathbf{m}=0$$

The next transformation is to eliminate the $\boldsymbol{\sigma}_x$ component in the coefficient of Y. It's $\exp(-i\boldsymbol{\sigma}_z/2\cdot\tan^{-1}(a_z\cos 2\phi_k/\Omega)$ that has clearly a nonzero determinant as required for any valid transformation.

$$\left\{Y^2+\left(\Omega_0+2D_0k_0^2+i\boldsymbol{\sigma}_y\Omega_1e^{i\boldsymbol{\sigma}_x\phi_a}\right)Y\right.$$
$$\left.-\frac{D_0k_0^2}{2}\left(1+\cos^2\theta_k-\boldsymbol{\sigma}_z\sin^2\theta_k\right)\right\}\mathbf{m}_1=0 \qquad . \qquad (7.41)$$

Here,

$$\mathbf{m}_1=e^{i\boldsymbol{\sigma}_z\frac{1}{2}\tan^{-1}\frac{a\sin 2\phi_k}{\Omega}}e^{-\boldsymbol{\sigma}_y\phi_k}\mathbf{m},$$

$$\Omega_1=\sqrt{\Omega^2+a_z^2-a_z\sin^2\theta_k\cos 2\phi_k+\frac{\sin^4\theta_k}{4}}$$

and

$$\phi_a=\tan^{-1}\frac{2a\cos 2\phi_k-\sin^2\theta_k}{2\sqrt{\Omega^2+a_z^2\sin^2 2\phi_k}}.$$

The final transformation is used to eliminate the $\boldsymbol{\sigma}_z$ component in the coefficient of Y.

$$\left[\left(D_0k^2+\frac{\Omega_0-i\boldsymbol{\sigma}_y\Omega_1}{2}\right)^2-\left(b_0-i\boldsymbol{\sigma}_yb_y-\boldsymbol{\sigma}_zb_z\right)\right]\mathbf{m}_2=0, \tag{7.42}$$

where

$$\mathbf{m}_2=e^{i\boldsymbol{\sigma}_x\frac{1}{2}\phi_a}e^{i\boldsymbol{\sigma}_z\frac{1}{2}\tan^{-1}\frac{a\sin 2\phi_k}{\Omega}}e^{-\boldsymbol{\sigma}_y\phi_k}\mathbf{m},$$

$$b_0=\frac{1}{4}(\Omega_0^2+\Omega_1^2)+D_0\Omega_0k_0^2+D_0^2k_0^4+\frac{D_0k_0^2\left(1+\cos^2\theta_k\right)}{2},$$

$$b_y=\frac{\Omega_0\Omega_1+D_0k_0^2\sin^2\theta_k\sin\varphi_a+2D_0k_0^2\Omega_1}{2},$$

and

$$b_z=\frac{D_0k_0^2\sin^2\theta_k\cos\phi_a}{2}.$$

7.2.2. Insulator Approximation

This section provides the approximate solutions for insulators. The objective is to help understand the spin wave polarizations.

First, in the magnetostatic limit $k_0^2\to 0$,

$$\left[D_0^2k^4+\left(\Omega_0-i\boldsymbol{\sigma}_y\Omega_1\right)D_0k^2\right]\mathbf{m}_1=0. \tag{7.43}$$

The eigenvalues of $i\boldsymbol{\sigma}_y$ are ±1. It's easy to obtain the magnetostatic k solutions, namely, 0, $\sqrt{(\Omega_1-\Omega_0)/D_0}$, $i\sqrt{(\Omega_1+\Omega_0)/D_0}$. The $\pm$ sign is omitted in these solutions because it comes from the propagation direction that's already considered in θ_k and φ_k. The magnetostatic theory is only related to the 2nd solution and it's hard to understand why

the uniform mode can be excited at all frequencies and all fields. Here, the solution $k = 0$ tells the truth.

Second, let's find a set of approximate solutions for insulators. Equation (7.42) can be written as,

$$\left[\left(D_0 k^2 + \frac{\Omega_0 + i\boldsymbol{\sigma}_y \Omega_1}{2}\right)^2 - \left(u_0 - i\boldsymbol{\sigma}_y u_y - \boldsymbol{\sigma}_z u_z\right)^2\right]\mathbf{m}_1 = 0, \tag{7.44}$$

where

$$u_0 = \frac{\sqrt{b_0 + \sqrt{b_y^2 + b_z^2}} + \sqrt{b_0 - \sqrt{b_y^2 + b_z^2}}}{2},$$

$$u_y = \frac{b_y\sqrt{b_0 + \sqrt{b_y^2 + b_z^2}} - b_y\sqrt{b_0 - \sqrt{b_y^2 + b_z^2}}}{2\sqrt{b_y^2 + b_z^2}},$$

and

$$u_z = \frac{b_z\sqrt{b_0 + \sqrt{b_y^2 + b_z^2}} - b_z\sqrt{b_0 - \sqrt{b_y^2 + b_z^2}}}{2\sqrt{b_y^2 + b_z^2}}.$$

For $k_0 = 0$, one obtains $u_0 = \Omega_0/2$, $u_y = \Omega_1/2$, and $u_z = 0$. This is consistent with the magnetostatic limit. This implies that u_z in Eq. (7.44) is small since b_z is on the order of $D_0 k_0^2$. Based on this approximation, the two terms in Eq. (7.44) approximately commute with each other. One obtains two equations equivalent to Eq. (7.44),

$$\left[D_0 k^2 + \Omega_0/2 \pm u_0 - i\boldsymbol{\sigma}_y\left(\Omega_1/2 \pm u_y\right) \mp u_z\boldsymbol{\sigma}_z\right]\mathbf{m}_1 = 0, \tag{7.45}$$

The quaternion k solutions can be first obtained,

$$k^{\pm}=\sqrt{\frac{i\sigma_y\left(\Omega_1/2\pm u_y\right)\mp u_z\sigma_z-(\Omega_0/2\pm u_0)}{D_0}}. \tag{7.46}$$

The corresponding partial wave expression of $\mathbf{m}$ is

$$\mathbf{m}^{\pm}=e^{\sigma_y\phi_k}e^{-i\sigma_z\frac{1}{2}\tan^{-1}\frac{a\sin 2\phi_k}{\Omega}}e^{-i\sigma_x\frac{1}{2}\phi_a}e^{i(\omega t-\mathbf{k}^{\pm}R)}\boldsymbol{\Psi} \tag{7.47}$$

where $R=x\cos\theta_k\cos\varphi_k+y\cos\theta_k\sin\varphi_k+z\sin\theta_k$ and $\boldsymbol{\Psi}$ is any nonzero vector.

The fact that $\boldsymbol{\Psi}$ is any nonzero vector provides the possibility to replace the quaternion solution by a number using the eigenvectors and the eigenvalues. The eigenvalues of $\mp u_z\sigma_z-i\sigma_y(\Omega_1/2\pm u_y)$ can be easily found, based on quaternion analysis, to be $[(\Omega_1/2\pm u_y)^2+u_z^2]^{1/2}$ and $-[(\Omega_1/2\pm u_y)^2+u_z^2]^{1/2}$. The corresponding eigenvectors can be

$$\mathbf{m}_{k1}^{A\pm}=\begin{pmatrix}\mp u_z-\sqrt{\left(\Omega_1/2\pm u_y\right)^2+u_z^2}\\ -i\left(\Omega_1/2\pm u_y\right)\end{pmatrix} \tag{7.48}$$

and

$$\mathbf{m}_{k1}^{L\pm}=\begin{pmatrix}\mp u_z+\sqrt{\left(\Omega_1/2\pm u_y\right)^2+u_z^2}\\ -i\left(\Omega_1/2\pm u_y\right)\end{pmatrix}. \tag{7.49}$$

The superscripts ^{A} and ^{L} stand for the anti-Larmor precession and the Larmor precession, respectively. This is understandable for $k_0\to 0$. In this limit,

$$\mathbf{m}_1^{A\pm}\propto\begin{pmatrix}1\\ i\end{pmatrix} \tag{7.50}$$

and

$$\mathbf{m}_1^{L\pm} \propto \begin{pmatrix} 1 \\ -i \end{pmatrix}. \tag{7.51}$$

These vectors represent the anti-Larmor and Larmor circular polarizations. The D_0 has very small value on the order of 10^{-12} cm^2 and the imaginary parts of u_z and u_y are hereby small. This makes $\mathbf{m}_{k1}^{A\pm}$ and $\mathbf{m}_{k1}^{L\pm}$ always stand for the anti-Larmor polarization and the Larmor polarization.

The corresponding four k solutions are

$$k_{\mathrm{DEL}} = \sqrt{\frac{\sqrt{\left(\Omega_1/2+u_y\right)^2+u_z^2}-\left(\Omega_0/2+u_0\right)}{D_0}} \quad \text{for } m_1^{L+}, \tag{7.52}$$

$$k_{\mathrm{EML}} = \sqrt{\frac{\sqrt{\left(\Omega_1/2-u_y\right)^2+u_z^2}-\left(\Omega_0/2-u_0\right)}{D_0}} \quad \text{for } m_1^{L-}, \tag{7.53}$$

$$k_{\mathrm{DEA}} = i\sqrt{\frac{\sqrt{\left(\Omega_1/2+u_y\right)^2+u_z^2}+\left(\Omega_0/2+u_0\right)}{D_0}} \quad \text{for } m_1^{A+}. \tag{7.54}$$

and

$$k_{\mathrm{EMA}} = \sqrt{\frac{\sqrt{\left(\Omega_1/2-u_y\right)^2+u_z^2}+\left(\Omega_0/2-u_0\right)}{D_0}} \quad \text{for } m_1^{A-}, \tag{7.55}$$

As in the magnetostatic solutions, the ± sign in these solutions is omitted. The above approximate solutions are the consistent with what Lax and Button obtained in 1962 for un-damped isotropic insulators. The subscripts are named after the spin wave characteristic, dipole-exchange Larmor (DEL), electromagnetic Larmor (EML), dipole-exchange anti-Larmor (DEA), and electromagnetic anti-Larmor (EMA).

7.2.3. Exact Solutions

The above approximate solutions work very well for insulators. The exact solutions of Eq. (7.42) can also be found and important for highly anisotropic and metallic materials. The approach is presented as follows.

Suppose Eq. (7.42) could be written as

$$\left(D_0k^2+\frac{\Omega_0-i\boldsymbol{\sigma}_y\Omega_1}{2}+w\right)\left(D_0k^2+\frac{\Omega_0-i\boldsymbol{\sigma}_y\Omega_1}{2}-w\right)\mathbf{m}_1=0, \tag{7.56}$$

where w is a quaternion to be determined. This requires that

$$-\left[\frac{i\boldsymbol{\sigma}_y\Omega_1}{2},w\right]+w^2=b_0-i\boldsymbol{\sigma}_yb_y-\boldsymbol{\sigma}_zb_z. \tag{7.57}$$

Assume

$$w=w_0+i\boldsymbol{\sigma}_xw_x+i\boldsymbol{\sigma}_yw_y+\boldsymbol{\sigma}_zw_z. \tag{7.58}$$

Equation (7.57) gives

$$\begin{aligned} &w_0w_x-iw_z\Omega_1/2=0\\ &w_0w_y=-b_y/2\\ &iw_x\Omega_1/2+w_0w_z=b_z/2\\ &w_0^2+w_x^2+w_y^2+w_z^2=b_0 \end{aligned} \tag{7.59}$$

By eliminating w_x, w_y and w_z, one obtains a cubic equation of w_0^2,

$$w_0^6-(\frac{\Omega_1^2}{4}+b_0)w_0^4+(b_0+\frac{b_y^2+b_z^2}{4})w_0^2-\frac{b_y^2\Omega_1^2}{16}=0. \tag{7.60}$$

The above equation is analytically solvable but the solutions will not be listed here because their forms are complicated. There are three solutions. But they are dependent.

One only need take any one of them. But one need make sure that this solution is not equal to $\Omega_1/2$. This can be understood in the following equation (7.61). Then two solutions of w_0 are obtained, that's, $\pm w_0$. Once w_0 is known, w_x, w_y, and w_z can be derived from Eq. (7.59).

$$\begin{aligned} w_x &= -\frac{ib_z\Omega_1/4}{w_0^2-\Omega_1^2/2} \\ w_y &= -\frac{b_y}{2w_0} \\ w_z &= -\frac{b_z p_0/2}{w_0^2-\Omega_1^2/4} \end{aligned} \quad . \tag{7.61}$$

w is hereby written as a function of the w_0 solution of Eq. (7.60). Finally, equation (7.56) is equivalent to two equivalent equations,

$$\left(D_0k^2+\frac{\Omega_0-i\boldsymbol{\sigma}_y\Omega_1}{2}-w(\pm w_0)\right)\mathbf{m}_1=0. \tag{7.62}$$

The quaternion solutions are,

$$k^{\pm}=\sqrt{\frac{i\boldsymbol{\sigma}_y\Omega_1-\Omega_0+w(\pm w_0)}{2D_0}}. \tag{7.63}$$

Find the eigenvalues of the matrix in the above equation and the four solutions can be found,

$$k_{1,2}=\sqrt{\frac{\pm w_0-\Omega_0+\sqrt{\frac{b_z^2}{w_0^2-\Omega_1^2/4}+\left(\frac{\Omega_1}{2}\mp\frac{b_y}{2w_0}\right)^2}}{2D_0}} \tag{7.64}$$

and

$$k_{3,4}=\sqrt{\frac{\pm w_0-\Omega_0-\sqrt{\frac{b_z^2}{w_0^2-\Omega_1^2/4}+\left(\frac{\Omega_1}{2}\mp\frac{b_y}{2w_0}\right)^2}}{2D_0}}. \tag{7.65}$$

For the exact solutions, it is not easy to identify the corresponding DEL, EML, DEA, and EMA branches. The identification depends on the value of w_0, which is field dependent. The solutions $k_{1,2}$ and $k_{3,4}$ are respectively the Larmor and anti-Larmor branches.

7.2.4. Solutions for Field Dispersion

Equation (7.35) is a linear function of Ω_H or H_0, quadratic of k^2, and cubic of ω in the quaternion form. It can be expected that the field dispersion expressions would be the simplest. This section presents the exact solutions (type III) for field dispersion.

As mentioned in the section 7.2.1, the field dispersion is the form that the static field H_0 (or the corresponding parameter Ω_H) is expressed as a function of spin wave frequency and wave vector. This allows directly finding the eigenvalues and obtaining scalar solutions. Let's reorganize Eq. (7.35).

$$\begin{aligned}&\left[\Omega_H-a_0+D_0k^2-\frac{k^2\left(1+\cos^2\theta_k\right)}{2(k^2-k_0^2)}+1\right]\mathbf{m}\\&=\left[i\Omega\boldsymbol{\sigma}_y+a_z\boldsymbol{\sigma}_z-\frac{\sin^2\theta_k}{2}\frac{k^2}{k^2-k_0^2}\boldsymbol{\sigma}_z e^{-\boldsymbol{\sigma}_y 2\phi_k}\right]\mathbf{m}\end{aligned}, \tag{7.66}$$

It's easy to solve the solutions of H_0. However, it can be expected that the field solutions would be complex because of nonzero α and σ_c. This seems meaningless since H_0 is physically real and positive. Generally, $\omega(k)$ is complex and the imaginary

frequency is relaxation frequency. If $\omega(k)$ is assumed to be real, the relaxation frequency is converted into the effective linewidth in field units. With such conversion, the field H_0 is generalized to be $H_0 + i\Delta H_{\text{eff}}/2$ where ΔH_{eff} is here assumed to be the $\mathbf{k}$-dependent effective linewidth. Equation (7.66) gives two solutions,

$$H_0 + i\frac{\Delta H_{\text{eff}}}{2} = M_0\left[a_0 + \frac{k^2\left(1+\cos^2\theta_k\right)}{2(k^2-k_0^2)} - 1\right] - Dk^2 + \frac{i\alpha\omega}{|\gamma\mu_0|} \pm \sqrt{\frac{\omega}{\gamma^2\mu_0^2}^2 + M_0^2\left[a_z^2 + \frac{a_z k^2\sin^2\theta_k\cos 2\phi_k}{k^2-k_0^2} + \frac{k^4\sin^4\theta_k}{4\left(k^2-k_0^2\right)^2}\right]}. \tag{7.67}$$

This equation is the resonance condition for the internal spin waves. For emphasis, the resonance depends on the dynamic anisotropy parameters a_0 and a_z. Note that $\Delta H_{\text{eff}} \to 2\alpha\omega/|\gamma|\mu_0$ when $k \to 0$. This is consistent with the intrinsic linewidth limit for insulators with infinite large size. However, ΔH_{eff} in Eq. (7.67) is not a real linewidth for finite sample sizes. ΔH_{eff} is the effective linewidth for a spin wave with a specified wave vector and frequency. In the real experiments, for example, FMR measurements, there are excited many waves with different wave vectors at a given field. These waves have different values of ΔH_{eff}. The total effective linewidth is the properly weighted average of these $\mathbf{k}$-dependent effective linewidths. If it's possible to establish an effective wave vector $\mathbf{k}_{\text{eff}}$, the equation (7.67) could be used to determine the real effective linewidth. It can be expected that $\mathbf{k}_{\text{eff}}$ depends on the boundary conditions and typically has a nonzero magnitude. For nonzero wave number, ΔH_{eff} is also dependent on the conductivity in k_0^2.

From this solutions, it is easy to determine some special fields, H_X, H_{00}, and H_{90}.

The special field H_X requires $k = 0$. Under this condition, the above equation gives

$$H_X = M_0(a_0 - 1) + \sqrt{\left(\frac{\omega}{\gamma\mu_0}\right)^2 + (M_0 a_z)^2}\,. \tag{7.68}$$

This also can be used to determine the corresponding frequency ω_X,

$$\omega_X = |\gamma|\mu_0\sqrt{[H_0 - M_0(a_0 - 1)]^2 - (M_0 a_z)^2}\,. \tag{7.69}$$

The fields H_{00} and H_{90} are the values of H_0 at $\theta_k = 0$ and $\theta_k = \pi/2$, respectively, under the magnetostatic limit ($k_0^2 \to 0$) and the $k \to 0$ limit. By taking these limits, one obtains

$$H_{00} = M_0 a_0 + \sqrt{\frac{\omega^2}{\gamma^2} + (M_0 a_z)^2} \tag{7.70}$$

and

$$H_{90} = M_0\left(a_0 - \frac{1}{2}\right) + \sqrt{\frac{\omega^2}{\gamma^2} + M_0^2\left(a_z + \frac{1}{2}\right)^2}\,. \tag{7.71}$$

Typically, $H_0 > H_{90}$. In the field manifold $H_{90} < H_0 < H_{00}$, there are a number of available spin wave modes especially with low wave numbers. That's why two-magnon scattering typically dominates the contributions to effective linewidth.

From Eqs. (7.70) and (7.71), the frequency manifold edges ω_H and ω_B are modified by the anisotropy fields,

$$\omega_H \to |\gamma|\sqrt{(H_0 - M_0 a_0)^2 - (M_0 a_z)^2} \tag{7.72}$$

and

$$\omega_B \to |\gamma|\sqrt{[H_0 - M_0(a_0 + a_z)][H_0 + M_z(a_z - a_0 + 1)]}\,. \tag{7.73}$$

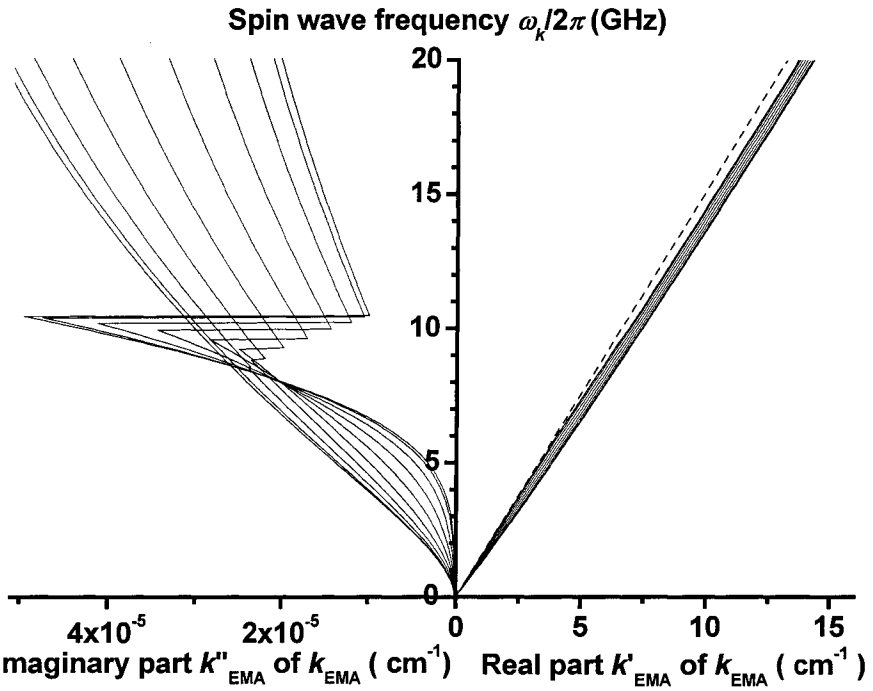

FIG 7.2. Electromagnetic anti-Larmor (EMA) spin wave band. The right and left sides plot, respectively, the real part k'_{EMA} and the imaginary part k''_{EMA} of the EMA spin wave number k_{EMA} as function of the spin wave frequency $\omega/2\pi$. The line contours show the curves in the range of . $0^{\circ} \le \theta_k \le 90^{\circ}$, as indicated. The dashed line indicates the light line defined by $\omega_{em} = ck/\sqrt{\varepsilon_r}$ where ε_r is the dielectric constant.

This implies that the manifold region depends not only on the static anisotropy field in H_0 but also on the dynamic anisotropy parameters a_0 and a_z.

7.2.5. Example Plots

In Chapter 2, the real parts of dispersion relation with α equal to zero are plotted in Fig. 2.6. The α may also change the dispersion. This section presents the example plots of the real parts and the imaginary parts of the four (eight with the ± sign) k roots for nonzero α. The following calculations is on the single crystal YIG with $\mathbf{H}_0$ along

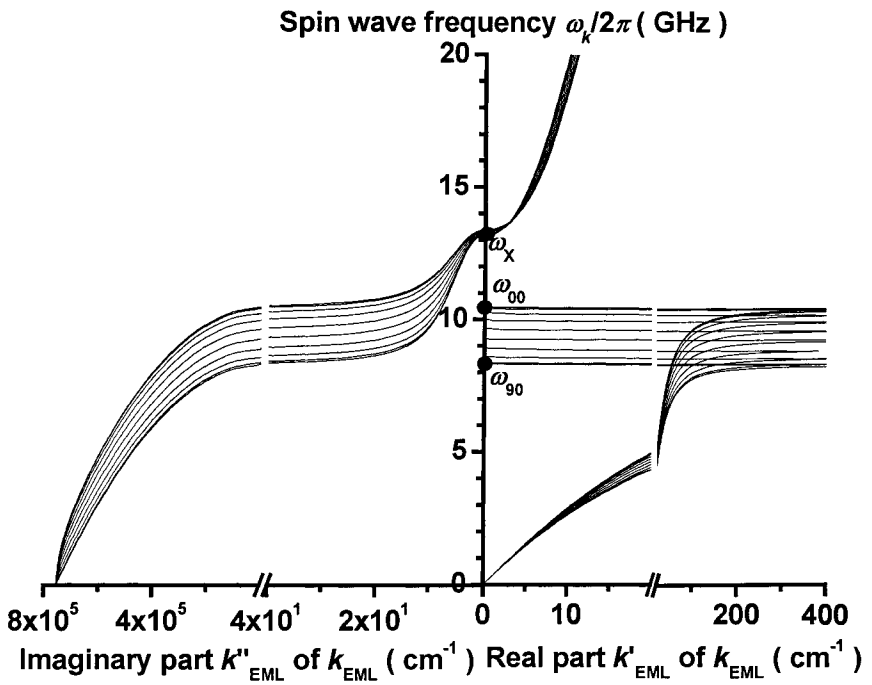

FIG 7.3. Electromagnetic Larmor (EML) spin wave band. The right and left sides plot, respectively, the real part k'_{EML} and the imaginary part k''_{EML} of the spin wave number k_{EML} as function of the spin wave frequency $\omega/2\pi$. The line contours show the curves in the range of . $0^{\circ} \le \theta_k \le 90^{\circ}$, as indicated. The manifold edges ω_{00} and ω_{90} are marked in the vertical coordinate.

one of the anisotropy axis. For this case, $a_0 = 0.03$ and $a_z = 0$. The intrinsic linewidth is around 0.05 mT at 10 GHz and it can be converted into the Gilbert constant $\alpha = 0.00007$. The relative dielectric constant the gyromagnetic ratio is $\varepsilon_r = 10$ and $\gamma/2\pi = -28$ GHz/T. The exchange stiffness is $\mu_0 D = 5.2 \cdot 10^{-13}$ T$\cdot$cm^2. The following figures are based on the calculations of Eqs. (7.64) and (7.65) at $\mu_0 H_0 = 0.3$ T.

Figure 7.2 shows the electromagnetic Anti-Larmor (EMA) spin wave band. The real part k'_{EMA} is plotted in the right graph and the imaginary part k''_{EMA} is plotted in the left graph. Both of k'_{EMA} and k''_{EMA} depend on θ_k. The line contours show such

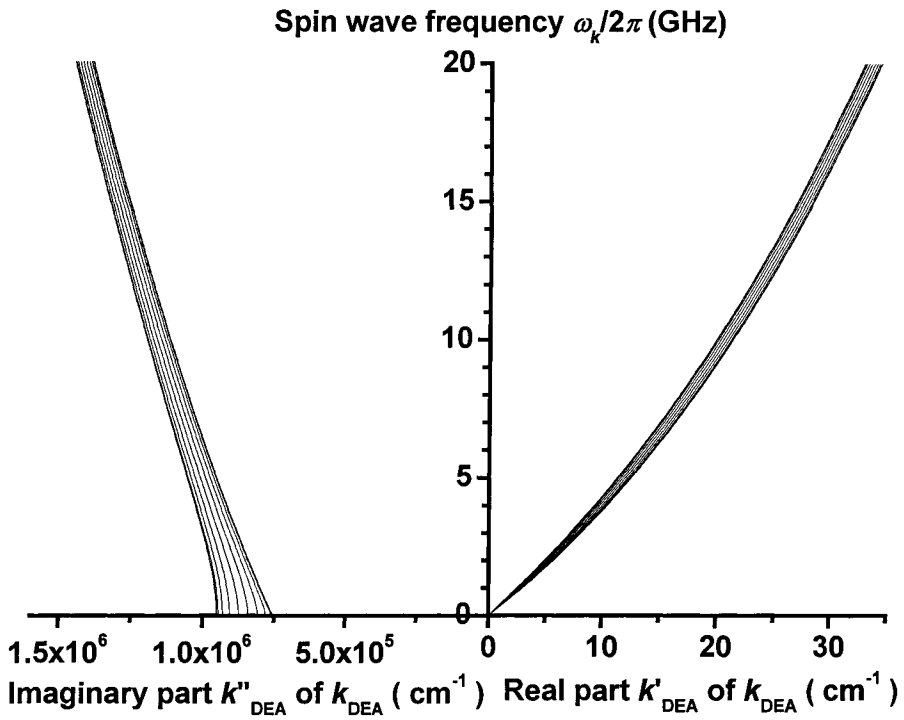

FIG 7.4. Dipole exchange anti-Larmor (DEA) spin wave band. The right and left sides plot, respectively, the real part k'_{DEA} and the imaginary part k''_{DEA} of the spin wave number k_{DEA} as function of the spin wave frequency $\omega/2\pi$. The line contours show the curves in the range of . $0^{\circ} \leq \theta_k \leq 90^{\circ}$, as indicated.

dependence. The electromagnetic spin wave (EMSW) has low wave number or long wavelength comparable to that of electromagnetic wave. For comparison, the light line in the material is also shown according to $\omega_{em} = ck/\sqrt{\varepsilon_r}$. The real part k'_{EMA} of k_{EMA} at any given θ_k is nearly a linear function of frequency and the slope is comparable to the light speed $c/\sqrt{\varepsilon_r}$ in material. The imaginary part k''_{EMA} is quite small and in the order of 10^{-5} cm^{-1}.

Figures 7.3 through 7.5 show in the same way the electromagnetic Larmor (EML) spin wave band, the dipole exchange anti-Larmor (DEL) spin wave band, and the dipole

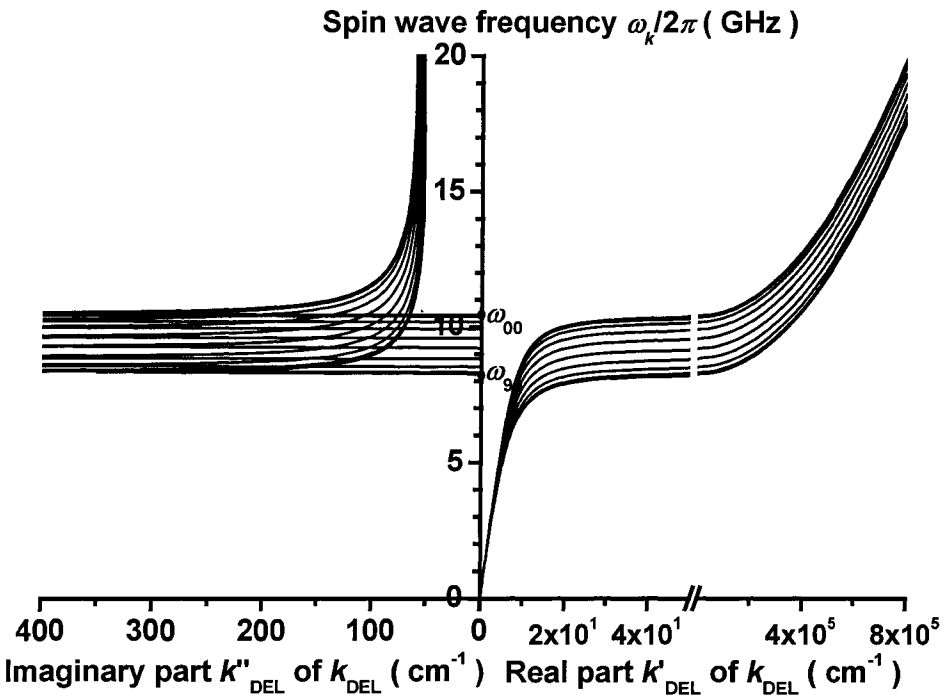

FIG 7.5 Dipole exchange anti-Larmor (DEA) spin wave band. The right and left sides plot, respectively, the real part k'_{DEL} and the imaginary part k''_{DEL} of the spin wave number k_{DEL} as function of the spin wave frequency $\omega/2\pi$. The line contours show the curves in the range of. $0^o \le \theta_k \le 90^o$, as indicated. The manifold edges ω_{00} and ω_{90} are marked in the vertical coordinate.

exchange Larmor (DEL) spin wave band. Three features can be found. (a) Above ω_X, there is nearly real low wave number EML band available according to the real part k'_{EML} of k_{EML} and the EML modes below this frequency have nearly pure imaginary wave number. (b) The imaginary part k''_{DEA} of k_{DEA} is much larger than the real part k'_{DEA} and has a large value in the order of 10^6 rad/cm due to exchange interaction. (c) The DEL modes have low wave number at low frequency and high wave number at high frequency. The right side of the break in the right graph of Fig. 7.5 are the regular dipole exchange spin waves.

The conductivity can also change the dispersion relation significantly. Equations

(7.64) and (7.65) are also applicable to the materials with nonzero conductivity, for example, metallic magnetic materials. The main points of these demonstration figures are (1) to show the complexity of realistic spin wave bands, even for a simple, low loss insulator situation, (2) to make the connection with the relatively simple Pauli matrix approach to the theory summarized in Eq. (7.26). One can readily obtain similar results for metals and highly anisotropic materials.

7.3. Dispersion relationship for spherical harmonic waves

This section provides the derivations of unbounded mode dispersion for spherical harmonic waves, which is particularly useful for the boundary condition problem of spheres. The measurement results shown in Chapter 6 are mainly on spherical polycrystalline YIG samples. The sample is assumed to be isotropic and no conductivity. The analyses here are based on the spherical coordinates $\mathbf{r} \to (r, \theta, \phi)$. Unfortunately, the partial harmonic wave $j_l(kr)Y_{lm}(\theta,\phi)$ is not an eigen solution of Eq. (7.26) even for isotropic materials. Section 7.3.1 shows operator transformations so that the transformed $j_l(kr)Y_{lm}(\theta,\phi)$ can be an eigen function. Section 7.3.2 presents the field dispersion for these spherical harmonic modes.

7.3.1. Operator Transformations

Define scalar derivative operators $\tilde{k}$, $\tilde{\theta}_k$, and $\tilde{\phi}_k$ as

$$\begin{aligned} \tilde{k}e^{-i\mathbf{k}\cdot\mathbf{r}} &= ke^{-i\mathbf{k}\cdot\mathbf{r}} \\ \tilde{\theta}_k e^{-i\mathbf{k}\cdot\mathbf{r}} &= \theta_k e^{-i\mathbf{k}\cdot\mathbf{r}} \\ \tilde{\phi}_k e^{-i\mathbf{k}\cdot\mathbf{r}} &= \phi_k e^{-i\mathbf{k}\cdot\mathbf{r}} \end{aligned} . \qquad (7.74)$$

These three operators commute with each other and the algebra of $\tilde{\theta}_k$ and $\tilde{\phi}_k$ follows that for the regular θ_k and $\tilde{\phi}_k$. Based these operators, ∇^2 and $\nabla_t(\nabla_t\cdot)$ can be written as

$$\nabla^2 = -\tilde{k}^2 \tag{7.75}$$

and

$$\nabla_t(\nabla_t\cdot) = -\tilde{k}^2 \sin^2\tilde{\theta}_k(1+\boldsymbol{\sigma}_z e^{-2\sigma_y\tilde{\phi}_k}). \tag{7.76}$$

The equation (5.31) for an isotropic YIG sample becomes

$$\left[\left(\boldsymbol{\sigma}_y+\alpha\right)i\Omega+\Omega_H+D_0\tilde{k}^2+\frac{\frac{\tilde{k}^2\sin^2\tilde{\theta}_k}{2}(1+\boldsymbol{\sigma}_z e^{-2\sigma_y\tilde{\phi}_k})+k_0^2}{\tilde{k}^2+k_0^2}\right]\mathbf{m}=0\ . \tag{7.77}$$

The following shows how the operator $\sin^2\tilde{\theta}_k$ acts on the partial spherical harmonic wave $\psi_{lm}=j_l(kr)Y_{lm}(\theta,\phi)$. The Fourier transformation of ψ_{lm} can be found

$$\psi_{lm}=\int\frac{d\mathbf{k}}{8\pi^3}4\pi j_l(kr)Y_{lm}^*(\theta_k,\tilde{\phi}_k)e^{-i\mathbf{k}\cdot\mathbf{r}}\ . \tag{7.78}$$

Use the definition of Eq. (7.74),

$$\begin{aligned}\sin^2\tilde{\theta}_k\psi_{lm} &= \int\frac{d\mathbf{k}'}{8\pi^3}4\pi j_l(k'r)Y_{lm}^*(\theta_k',\tilde{\phi}_k')e^{-i\mathbf{k}'\cdot\mathbf{r}}\\ &= j_l(kr)Y_{lm}(\theta,\phi)\int_0^{\pi}d\theta_k'\int_0^{2\pi}d\phi_k'\sin^2\theta_k'Y_{lm}(\theta_k',\tilde{\phi}_k')Y_{lm}^*(\theta_k',\phi_k')\end{aligned} \tag{7.79}$$

The angle integral is solvable based on

$$\cos\theta_k'Y_{l,m}(\theta_k',\phi_k')=d_{l,m}Y_{l+1,m}(\theta_k',\phi_k')+d_{l-1,m}Y_{l-1,m}(\theta_k',\phi_k'), \tag{7.80}$$

where

$$d_{l,m} = \sqrt{\frac{(l+1)^2 - m^2}{(2l+1)(2l+3)}}. \tag{7.81}$$

One obtains

$$\frac{\sin^2\tilde{\theta}_k}{2}\psi_{lm} = \frac{1 - d_{l,m}^2 + d_{l-1,m}^2}{2}\psi_{lm} \equiv d'_{l,m}\psi_{lm}. \tag{7.82}$$

This means that ψ_{lm} is the eigenfunction of the operator $\sin^2\tilde{\theta}_k$.

Similarly, $\exp(\pm i\tilde{\phi}_k)$ can be found to be proportional to $L^{\pm}$ where

$$L^{\pm} = e^{\pm i\phi}(\pm\frac{\partial}{\partial\theta} + i\cot\theta\frac{\partial}{\partial\phi}). \tag{7.83}$$

$\exp(\boldsymbol{\sigma}_y\tilde{\phi}_k)$ can be expressed into a function of the operators $\exp(\pm i\tilde{\phi}_k)$, that's

$$\exp(\boldsymbol{\sigma}_y\tilde{\phi}_k) = \frac{1 - i\boldsymbol{\sigma}_y}{2}e^{\boldsymbol{\sigma}_y\tilde{\phi}_k} + \frac{1 + i\boldsymbol{\sigma}_y}{2}e^{-\boldsymbol{\sigma}_y\tilde{\phi}_k}. \tag{7.84}$$

This means that ψ_{lm} is not the eigenfunction of $\exp(\boldsymbol{\sigma}_y\tilde{\phi}_k)$. Take an operator transformation,

$$\mathbf{m}' = e^{-\boldsymbol{\sigma}_y\tilde{\phi}_k}\mathbf{m}. \tag{7.85}$$

This transformation is not applicable to the $l = 0$ mode because

$$e^{-\boldsymbol{\sigma}_y\tilde{\phi}_k}\psi_{00} = 0. \tag{7.86}$$

For this special case the transformation of Eq. (7.85) is not necessary. Based on this transformation, the equation (7.77) becomes

$$\left[\left(\boldsymbol{\sigma}_y + \alpha\right)i\Omega + \Omega_H + D_0\tilde{k}^2 + \frac{\tilde{k}^2\sin^2\tilde{\theta}_k(1+\boldsymbol{\sigma}_z) + 2k_0^2}{2\tilde{k}^2 + 2\tilde{k}_0^2}\right]\mathbf{m}' = 0. \tag{7.87}$$

7.3.2. Field Dispersion

Note that ψ_{lm} $(l \neq 0)$ is an eigen function of Eq. (7.97). For the partial wave

$$\mathbf{m}'_{lm} = j_l(kr)Y_{lm}(\theta,\varphi)e^{i\omega t}\mathbf{m}'_{0lm}(k). \tag{7.88}$$

In order to include the $l = 0$ mode, the corresponding partial spherical wave in $\mathbf{m}$ for $\mathbf{m}'_{lm}$ is written as

$$\mathbf{m}_{lm} = (\delta_{l0} + e^{\sigma_y \tilde{\phi}_k})\mathbf{m}'_{lm}. \tag{7.89}$$

Insert Eqs. (7.88) and (7.89) into Eq. (7.87), one obtains

$$\begin{aligned}&\left[\left(\sigma_y + \alpha\right)i\Omega + \Omega_H + D_0k^2\right]\mathbf{m}'_{0lm}(k) + \\ &\frac{k^2 d'_{l,m}\left[1 + (1-\delta_{10})\sigma_z\right] - k_0^2}{(k^2 - k_0^2)}\mathbf{m}'_{0lm}(k) = 0\end{aligned}. \tag{7.90}$$

The wave number k as a function of field and frequency can be solved from the above equation using the similar approaches that are shown in Section 7.2. Here, only the field dispersion is solved,

$$\begin{aligned}&H_i + i\frac{\Delta H_{\text{eff}}}{2} = M_0\frac{k_0^2 - k^2 d'_{lm}}{k^2 - k_0^2} - Dk^2 \\ &+\frac{i\alpha\omega}{|\gamma|} \pm \sqrt{\frac{\omega}{\gamma}^2 + \left[\frac{M_0 k^2(1-\delta_{10})d'_{l,m}}{k^2 - k_0^2}\right]^2}\end{aligned}. \tag{7.91}$$

Based on the calculations of Eq. (7.91) at a frequency of 10 GHz, the wave number k as a function of the internal static field H_i is plotted in Fig. 7.6 for the range of l from 0 to 10. The parameters used in these calculations are the same as that of Fig. 7.6. This results in the three bands. These curves or bands are quite similar to that in Fig. 7.6.

It's useful to compare with the known FMR resonance for sphere. The FMR mode is

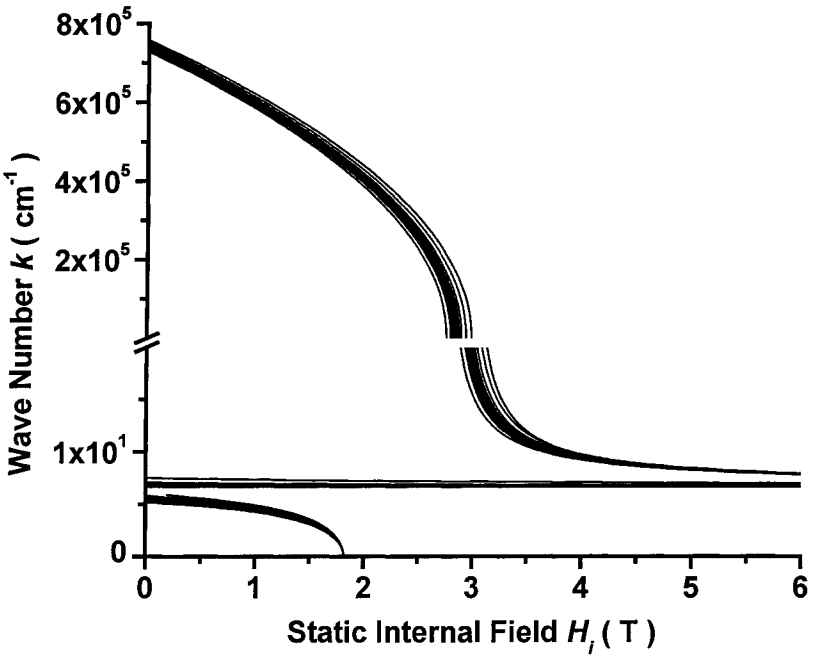

FIG. 7.6. Spectrum of the spherical harmonic modes of $j_l(kr)Y_{lm}(\theta,\phi)$ in a wave number versus field format for fixed frequency 10 GHz. The graph shows curves of the spin wave number k as a function of the static internal field H_i at a fixed frequency f of 10 GHz for the range of l =0 to 10 and all possible indices $_m$. Three bands with real wave numbers are plotted. These bands were evaluated from Eq. (7.91)) and for the same parameters as used for Fig. 7.2.

typically assumed to be uniform and so $l = 0$. The wave number k can be found from the boundary conditions. For magnetostatic theory, $k_0 \to 0$ first and then $k \to 0$

$$H_i + i\frac{\Delta H_{\text{eff}}}{2} = -M_0 d'_{0,0} + \frac{i\alpha\omega}{|\gamma|} \pm \frac{\omega}{|\gamma|}. \tag{7.92}$$

Note that $d'_{0,0} = 1/3$ and physically H_i is positive. Therefore

$$H_i = \frac{\omega}{|\gamma|} - \frac{M_0}{3} \text{ (at FMR)} \tag{7.93}$$

and

$$\Delta H_{\text{eff}} = \frac{2\alpha\omega}{|\gamma|} \text{ (at FMR).} \qquad (7.94)$$

Equation (7.93) indicates the FMR field that is consistent with the magnetostatic theory. Equation (7.94) shows that the effective linewidth at FMR is equal to the FMR linewidth. Therefore, equation (7.91) is consistent with the known magnetostatic theory.

8. OPERATOR THEORY OF CLASSICAL TWO MAGNON SCATTERING

This chapter outlines a newly developed classical two-magnon scattering theory for polycrystalline materials. Based on operator algebra, a general operator form for two-magnon scattering is derived by taking account for the electromagnetic spin waves (EM-SW) as well as the regular dipole exchange spin waves (DE-SW). The scattering sources include voids, a random crystalline anisotropy, and grain boundaries. These sources typically dominate in the microwave relaxation of polycrystalline ferrite materials. It presumes that grains and voids are randomly distributed over the whole body of the sample. The random properties allow treating these sources using statistical methods, such as correlation functions. The equation for the magnetization motion is modified with consideration of the extrinsic two-magnon processes.

This chapter focuses on the conceptual formulation. The concepts are used for discussions in the preceding chapters. Section 8.1 describes a grain model using unit functions. Based on the grain model, the equation for the magnetization motion is expressed in the sample equilibrium coordinate system (SCS). Section 8.2 presents the modifications in the dipole fields and the Gilbert equation due to the existence of anisotropic grains and pores. Scattering operators are used to express the role of the scattering sources in governing equations. In Section 8.3, the random scattering

operators are further converted into the linear operators for two-magnon scattering. The detailed derivations have been applied to the anisotropy scattering and grain boundary scattering (GBS).

The quantitative evaluations of scattering and the boundary condition problems by considering the EM-SW and DE-SW modes are not fully done for polycrystalline bulks. These problems are subject to future work. Applications of the theory in Chapters 7 and 8 will be first explored on thin magnetic films, for which the boundary condition problems are much simpler than bulk materials. Specifically, these theoretical efforts have been applying to the interesting investigations on the effective linewidth of thin metallic films. The interesting topics about metallic films can refer to Platow *et al* (1998), McMichael *et al* (2000), and Mills (2003).

8.1. Grain Model for Polycrystalline Materials

The polycrystalline materials are not isotropic in the microstructure scale. Gilbert equation and Maxwell equations depend on the local properties of the materials, such as crystalline anisotropy, magnetization saturation (equivalently zero for voids), equilibrium magnetizations, and the dielectric constant. In order to consider the statistical properties of these parameters, a grain model is developed here. Section 8.1.1 introduces the unit functions associated with the microscopic grains and the macroscopic materials. Section 8.1.2 discusses the coordinate transformations so as to take account for the non-uniform distributions of static magnetization and anisotropy.

8.1.1. Unit Functions

It's assumed that the polycrystalline materials be made of a huge number of grains with random grain sizes and shapes. The gaps among the grains stand for voids. Based on this model, one can define a unit function $q(\mathbf{r})$ for the grain-void microstructures in infinite media,

$$q(\mathbf{r}) = \begin{cases} 1, & \text{inside the grains} \\ 0, & \text{otherwise} \end{cases}. \tag{8.1}$$

Figure 8.1 shows a demonstration of $q(\mathbf{r})$. The shaded areas represent grains and the white areas represent voids. The function $q(\mathbf{r})$ is 1 inside grains and 0 inside voids. Note that

$$q^n(\mathbf{r}) = q(\mathbf{r}) \ (n = 1, 2, \ldots). \tag{8.2}$$

This is why $q(\mathbf{r})$ is called a unit function.

The grains are randomly distributed over the whole space. The grain distribution can be assumed to be isotropic for any direction. This gives an important property of such unit function, namely, statistical properties of $q(\mathbf{r})$ should be invariant under the coordinate rotation and translation transformations.

The real samples are also of finite sizes. Similarly, the corresponding unit function can be defined,

$$q_s(r) = \begin{cases} 1, & \text{inside the sample} \\ 0, & \text{otherwise} \end{cases}. \tag{8.3}$$

Let's first discuss an operator of $q(\mathbf{r})\tilde{L}q(\mathbf{r})$ for any linear scalar operator $\tilde{L}$ because it will be shown shortly that the two-magnon scattering processes can be expressed in

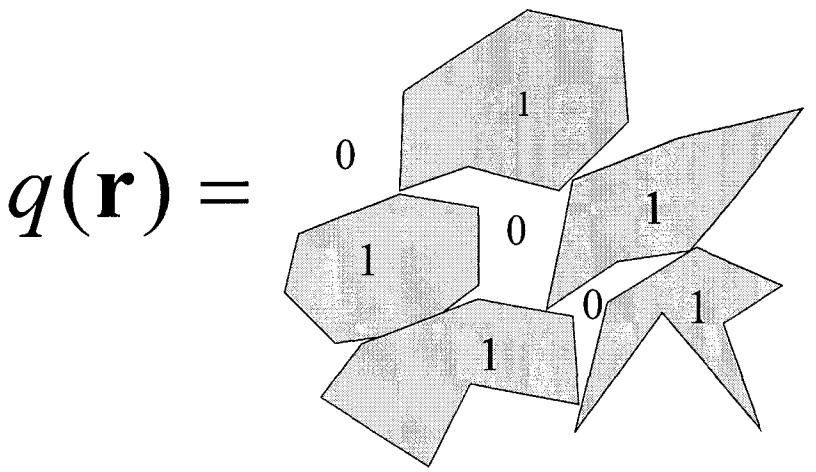

FIG. 8.1. Demonstration of the unit function $q(\mathbf{r})$. The gray areas show the bounded grains and the white areas are the voids. The $q(\mathbf{r})$ is equal to 1 in the gray areas and 0 in the white areas.

such form. The operator $q(\mathbf{r})\tilde{L}q(\mathbf{r})$ acting on any function $\psi(\mathbf{r})$ is $q(\mathbf{r})\tilde{L}q(\mathbf{r})\psi(\mathbf{r})$. Suppose that

$$\tilde{L}e^{-i\mathbf{k}\cdot\mathbf{r}} = L(\mathbf{k})e^{-i\mathbf{k}\cdot\mathbf{r}}. \tag{8.4}$$

One obtains,

$$q(\mathbf{r})\tilde{L}q(\mathbf{r})\psi(\mathbf{r}) = q(\mathbf{r})\int\frac{d\mathbf{k}}{8\pi^3}\left[q(\mathbf{k})\otimes\psi(\mathbf{k})\right]L(\mathbf{k})e^{-i\mathbf{k}\cdot\mathbf{r}}. \tag{8.5}$$

Here, the symbol $\otimes$ means the convolution,

$$q(\mathbf{k})\otimes\psi(\mathbf{k}) = \int d\mathbf{k}'q(\mathbf{k}-\mathbf{k}')\cdot\psi(\mathbf{k}'). \tag{8.6}$$

Further,

$$q(\mathbf{r})\tilde{L}q(\mathbf{r})\psi(\mathbf{r}) = \int\frac{d\mathbf{k}}{8\pi^3}q(\mathbf{k})\otimes\left\{\left[q(\mathbf{k})\otimes\psi(\mathbf{k})\right]L(\mathbf{k})\right\}e^{-i\mathbf{k}\cdot\mathbf{r}}. \tag{8.7}$$

Explicitly,

$$q(\mathbf{k})\otimes\left[q(\mathbf{k})\otimes\psi(\mathbf{k})\right]L(\mathbf{k}) = \int d\mathbf{k}''\int d\mathbf{k}' q^*(\mathbf{k}''-\mathbf{k})q(\mathbf{k}''-\mathbf{k}')\cdot\psi(\mathbf{k}')L(\mathbf{k}'') \tag{8.8}$$

This integral can be simplified if the statistical average $\langle ... \rangle$ applies. Note that the correlation function for the random function $q(\mathbf{k})$ satisfies

$$\left\langle q^*(\mathbf{k})q(\mathbf{k}')\right\rangle = \left\langle q^*(\mathbf{k})q(\mathbf{k})\right\rangle \delta(\mathbf{k}'-\mathbf{k}) \tag{8.9}$$

for any $\mathbf{k}$ and $\mathbf{k}'$. This relationship is applicable for any random function. Based on this relationship, the equation (8.8) becomes

$$\left\langle q(\mathbf{k})\otimes\left[q(\mathbf{k})\otimes\psi(\mathbf{k})\right]L(\mathbf{k})\right\rangle = \int\frac{d\mathbf{k}'}{8\pi^3}\left\langle q^*(\mathbf{k}')q(\mathbf{k}')\right\rangle L(\mathbf{k}'+\mathbf{k})\psi(\mathbf{k}) \tag{8.10}$$

Return back to the operator form

$$q(\mathbf{r})\tilde{L}q(\mathbf{r}) = \int\frac{d\mathbf{k}'}{8\pi^3}\left\langle q^*(\mathbf{k}')q(\mathbf{k}')\right\rangle L(\mathbf{k}'+i\nabla). \tag{8.11}$$

It will be shown later that this operator can be considered as a general form of two-magnon scattering for a general random spatial function $q(\mathbf{r})$ and a general linear operator $\tilde{L}$.

8.1.2. Grain Coordinates

The coordinate system used in Chapter 7 is the local equilibrium coordinate system (LCS) based on the static equilibrium of the saturated magnetization. However, the static equilibrium would be different for anisotropic grains since the equilibrium depends on the static anisotropy field and the static internal field. The static anisotropy field

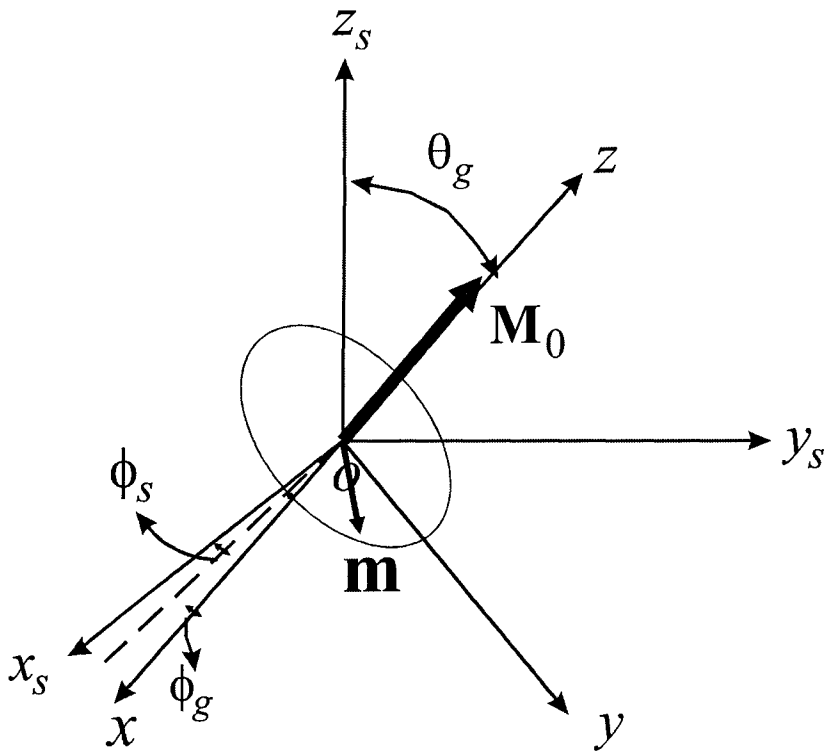

FIG. 8.2. Relation between the sample coordinate system (x_s, y_s, z_s) and the local coordinate system (x, y, z). The static magnetization $\mathbf{M}_0$ is along the z direction from the definition of the equilibrium coordinate system. The dynamic magnetization **m** is precessing around z axis as indicated by the elliptical loop and so perpendicular to the z direction. The dashed line is the intersect line between the x_s - y_s and x, y planes. The parameter ϕ_s is the angle between the x_s direction and this dashed line. The parameter ϕ_g is the angle between the x direction and this dashed line. The angle between the z_s and z directions is marked as θ_g.

varies with the anisotropy axes of grains. The demagnetizing field of a void also varies with the position as shown in Chapter 3. This non-uniform field was discussed by Vrehen (1970) and Hoeppe (2004).

The following discussions are based on a polycrystalline sphere. It's convenient to use the SCS system here. This system $\mathbf{r}_s$=(x_s, y_s, z_s) is defined based on that the z_s direction is parallel to the external static field. Figure 8.2 shows the relation between

SCS and the LCS. When the static equilibrium varies with the position, the LCS in grains is slightly different from SCS. In LCS, the static magnetization $\mathbf{M}_0$ always points to the z direction, as indicated. The dynamic magnetization $\mathbf{m}$ precesses around $\mathbf{M}_0$. The elliptical loop indicates the precession. The vector $\mathbf{m}$ may only have the nonzero x and y components but no z component. This is why the equation for magnetization motion only involves the x and y components. Figure 8.2 only shows the relations about the angles. The SCS or LCS is shifted so that the coordinate origins match up with each other. θ_g is the angle between the z_s and z directions as indicated. The dashed line is the intersect line between the x-y and x_s-y_s planes. The angles ϕ_s and ϕ_g are the angle between this dashed line and the x_s and x directions, respectively. These angles, θ_g, ϕ_s, and ϕ_g may be positive or negative in the range from $-\pi$ to π.

The LCS in Fig. 8.2 is a local system. The angle ϕ_g and θ_g can be written as a function of $\mathbf{r}_s$. The static external field is quite big compared with the static anisotropy field and the porosity is also quite small for dense materials. One can expect that the angle θ_g should be nearly zero. Otherwise, the magnetization would not be saturated. In this case, the equation for the magnetization motion, under some proper transformations, can also be expressed in terms of the x_s, y_s components without the z_s component.

One more comment is about the statistical properties of the angles ϕ_s, ϕ_g, and θ_g. They are also functions of $\mathbf{r}_s$. ϕ_s and ϕ_g can be any of $-\pi$ to π with a uniform probability $1/2\pi$. Their statistical averages equal to zero. θ_g may be only in a small

angle range and the probability for θ_g may vary with θ_g. The probability density can be derived from the static anisotropy and dipole fields. The probability density is symmetrical for θ_g and $-\theta_g$. So the statistical average of θ_g is also equal to zero.

The following shows how to convert Eq. (7.27) into the SCS. Any vector $\psi_{x,y}$ with only the x and y components will have the x_s and y_s components $\psi_{sx,y}$. One can obtain

$$\psi_{sx,y} = e^{\sigma_y \phi_s}\left(\cos^2\frac{\theta_g}{2} + \sigma_z \sin^2\frac{\theta_g}{2}\right)e^{-\sigma_y \phi_g}\psi_{x,y}. \tag{8.12}$$

Under this transformation, the matrices σ_y and σ_z should be replaced as

$$\sigma_y \rightarrow \mathbf{T}\sigma_y\mathbf{T}^{-1} \tag{8.13}$$

and

$$\sigma_z \rightarrow \mathbf{T}\sigma_z\mathbf{T}^{-1}, \tag{8.14}$$

where

$$\mathbf{T} = e^{\sigma_y \phi_s}\left(\cos^2\frac{\theta_g}{2} + \sigma_z \sin^2\frac{\theta_g}{2}\right)e^{-\sigma_y \phi_g}. \tag{8.15}$$

The operators ∇^2 and $\partial/\partial t$ are invariant except for replacing ∇ by $\nabla_s = \partial/\partial x_s \hat{\mathbf{x}}_s + \partial/\partial y_s \hat{\mathbf{y}}_s + \partial/\partial z_s \hat{\mathbf{z}}_s$.

The most complicated part is the dipole field in which the three-dimension operator $\nabla(\nabla\cdot)$ should be involved because $\mathbf{m}(\mathbf{r}_s)$ has a non-zero z_s component. It's known that the form of Maxwell equations doesn't change under the rotation and translation

transformations. The x_s, y_s components of the dipole field can be written as

$$\mathbf{h}_d(\mathbf{r}_s) = \left(\tilde{\mathbf{N}} + \mathbf{S}_1\right)\mathbf{m}(\mathbf{r}_s), \tag{8.16}$$

where $\nabla_{st} = \partial/\partial x_s \hat{\mathbf{x}}_s + \partial/\partial y_s \hat{\mathbf{y}}_s$,

$$\mathbf{S}_1 = \left(\nabla_s^2 - \frac{\varepsilon_r}{c^2}\frac{\partial^2}{\partial t^2}\right)^{-1} \begin{pmatrix} -\dfrac{\partial^2}{\partial x_s \partial z_s}\tan\theta_g \sin\phi_s & \dfrac{\partial^2}{\partial x_s \partial z_s}\tan\theta_g \cos\phi_s \\ -\dfrac{\partial^2}{\partial y_s \partial z_s}\tan\theta_g \sin\phi_s & \dfrac{\partial^2}{\partial y_s \partial z_s}\tan\theta_g \cos\phi_s \end{pmatrix}, \tag{8.17}$$

and

$$\tilde{\mathbf{N}} = \left(\nabla_s^2 - \frac{\varepsilon_r}{c^2}\frac{\partial^2}{\partial t^2}\right)^{-1} \left(\nabla_{st}(\nabla_{st}\cdot) + \frac{\varepsilon_r}{c^2}\frac{\partial^2}{\partial t^2}\right). \tag{8.18}$$

The operator $\tilde{\mathbf{N}}$ will be discussed in Section 8.2. The operator $\mathbf{S}_1$ can be thought to be a scattering operator because it's a random function and its statistical average is equal to zero.

Based on the above transformations, equation (7.26) in SCS is,

$$\left[\frac{\boldsymbol{\sigma}_y + \alpha}{\omega_M}\frac{\partial}{\partial t} + \Omega_H - D_0\nabla_s^2 + \tilde{\mathbf{N}} - \mathbf{S}_1(\mathbf{r}_s) - \mathbf{S}_2(\mathbf{r}_s)\right]\cdot\mathbf{m} = \mathbf{h}_p, \tag{8.19}$$

Note that the external field $\mathbf{h}_p$ only includes the transverse components. A new scattering operator $\mathbf{S}_2(\mathbf{r}_s)$ is introduced,

$$\mathbf{S}_2(\mathbf{r}_s) = \frac{\boldsymbol{\sigma}_y - \mathbf{T}\boldsymbol{\sigma}_y\mathbf{T}^{-1}}{\omega_M} + a_0(\mathbf{r}_s) + a_z(\mathbf{r}_s)\mathbf{T}\boldsymbol{\sigma}_z\mathbf{T}^{-1}, \tag{8.20}$$

These two scattering operators $\mathbf{S}_1(\mathbf{r}_s)$ and $\mathbf{S}_2(\mathbf{r}_s)$ are relevant to the non-uniform

distribution of static magnetization. $\mathbf{S}_1(\mathbf{r}_s)$ is also related to the EM-SW scattering. The last two terms in $\mathbf{S}_2(\mathbf{r}_s)$ correspond to the anisotropy scattering that will be discussed in more details in Section 8.3.

8.2. Modifications Under the Grain Model

The grains may have any kind of shape and size. The boundary conditions presented in Section 7.1.4 are complicated if they are applied to the grains. This section actually presents an alternative way for the boundary conditions, especially for grains. The unit functions $q(\mathbf{r}_s)$ and $q_s(r_s)$ are used to modify the equation for the magnetization motion so that the grain and sample boundary conditions are automatically included. Section 8.2.1 shows the modifications in the dipole field using an operator theory and shows the consistence with the theory using Green function. Section 8.2.2 shows an example of the dipole field using the operator theory. Section 8.2.3 shows the modifications in Gilbert equation especially due to grain boundaries so as to consider the exchange boundary condition in the three-dimensional governing equation.

8.2.1. Modified Dipole Field

First, take a look at infinite polycrystalline media. The microscopic Maxwell equations can be applicable to the porous materials. The treatment of the dielectric properties can use that in the *Electrodynamics* textbook. The dielectric losses are not of interest here. So, the dielectric constant is simply replaced by an effective constant, which is applicable to the whole materials. By taking account for the grains, the

equation (8.16) can be replaced in SCS by

$$\begin{cases} \nabla_s \times \mathbf{h}_d = \varepsilon_0 \dfrac{\partial \varepsilon_r \mathbf{e}_d}{\partial t} \\ \nabla_s \times \mathbf{e}_d + \mu_0 \dfrac{\partial}{\partial t}\left[\mathbf{h}_d + q(\mathbf{r}_s)\mathbf{m}\right] = 0 \end{cases}, \tag{8.21}$$

where the internal fields are replaced by the dipole field $\mathbf{h}_d$ (magnetic) and $\mathbf{e}_d$ (electric).

Equation (8.21) is applicable to grains and pores and further to the whole space. The Maxwellian boundary conditions can be derived from Eq. (8.21) and are equivalently included in it if applying this equation to the whole space. Further, one can include the effects of the finite sample using the defined unit function $q_s(r_s)$.

$$\nabla_s \times \mathbf{h}_d = \varepsilon_0 \frac{\partial}{\partial t}\left[1 + (\varepsilon_r - 1) q_s(r_s)\right] \mathbf{e}_d \tag{8.22}$$

and

$$\nabla_s \times \mathbf{e}_d + \mu_0 \frac{\partial}{\partial t}\left[\mathbf{h}_d + q_s(r_s) q(\mathbf{r}_s)\mathbf{m}\right] = 0 . \tag{8.23}$$

Here, ε_r is replaced by $1 + (\varepsilon_r - 1) q_s(r_s)$ because the dielectric constant outside the sample is 1. It can be solved,

$$\mathbf{h}_d = -\frac{\nabla_s(\nabla_s \cdot) - \dfrac{\varepsilon_r}{c^2}\dfrac{\partial^2}{\partial t^2}}{\nabla_s^2 - \dfrac{\varepsilon_r}{c^2}\dfrac{\partial^2}{\partial t^2}} q_s(r_s) q(\mathbf{r}_s)\mathbf{m}, \text{ inside the sample}, \tag{8.24}$$

and

$$\mathbf{h}_d = -\frac{\nabla_s(\nabla_s \cdot) - \dfrac{1}{c^2}\dfrac{\partial^2}{\partial t^2}}{\nabla_s^2 - \dfrac{1}{c^2}\dfrac{\partial^2}{\partial t^2}} q_s(r_s) q(\mathbf{r}_s)\mathbf{m}, \text{ outside}. \tag{8.25}$$

The solution of Eq. (8.25) represents the radiation outside the sample.

Note that the Gilbert equation only involves the volume of the sample and the motion of the magnetization also happens only inside the sample. The solution for the volume outside the sample doesn't change anything about the motion of magnetization. Due to such reasons, only take the solution of Eq. (8.24). Compare with the materials without the effects of grain and sample finiteness and equivalently $\mathbf{m}$ is replaced by $q_s(r_s)q(\mathbf{r}_s)\mathbf{m}$.

Equations (8.24) and (8.25) introduce the inverse of the derivative operators. In order to make it understandable, the following shows what is the inverse of the linear operators. As an example, for a general equation,

$$\left(\nabla_s^2 - \frac{\varepsilon_r}{c^2}\frac{\partial^2}{\partial t^2}\right)\mathbf{h}(\mathbf{r}_s,t) = \psi(\mathbf{r}_s,t). \tag{8.26}$$

where $\psi(\mathbf{r}_s,t)$ represents any vector function. In the operator theory, one obtains

$$\mathbf{h}(\mathbf{r}_s,t) = \left(\nabla_s^2 - \frac{\varepsilon_r}{c^2}\frac{\partial^2}{\partial t^2}\right)^{-1}\psi(\mathbf{r}_s,t). \tag{8.27}$$

However, this is not exactly true for the general case. When $\psi = 0$, equation (8.27) gives $\mathbf{h} = 0$, which might not be true because a general field $\mathbf{h}$ can have the nonzero normal modes of the operator $\nabla_s^2 - \varepsilon_r\partial^2/c^2\partial t^2$. This means that equation (8.27) is true only under the condition,

$$\mathbf{h} = 0 \text{ if } \psi = 0. \tag{8.28}$$

Fortunately, this condition is always held for the dipole field, $\mathbf{h} \to \mathbf{h}_d$ but not for the external field. It's convenient to work on the partial wave component with frequency

ω,

$$\mathbf{h}_d(\mathbf{r}_s,t) \rightarrow \mathbf{h}_d(\mathbf{r}_s,\omega)e^{i\omega t} \tag{8.29}$$

and

$$\psi(\mathbf{r}_s,t) \rightarrow \psi(\mathbf{r}_s)e^{i\omega t}. \tag{8.30}$$

One insert these two equations into Eq. (8.27) and obtains

$$\mathbf{h}_d(\mathbf{r}_s) = \left(\nabla_s^2 + k_0^2\right)^{-1} \psi(\mathbf{r}_s). \tag{8.31}$$

Expand $\psi(\mathbf{r}_s)$ to

$$\psi(\mathbf{r}_s) = \int d\mathbf{r}' \delta(\mathbf{r}_s - \mathbf{r}')\psi(\mathbf{r}'). \tag{8.32}$$

This allows the operator only acts on $\delta(\mathbf{r}_s - \mathbf{r}')$. Using Fourier transformation,

$$\mathbf{h}_d(\mathbf{r}_s) == -\int d\mathbf{r}' \int_0^\infty \frac{dk}{8\pi^3} \frac{k^2}{k^2 - k_0^2} 4\pi j_0(k|\mathbf{r}_s - \mathbf{r}'|)\psi(\mathbf{r}'). \tag{8.33}$$

The integral over k can be obtained using the residue theorem,

$$\mathbf{h}_d(\mathbf{r}_s) == -\int d\mathbf{r}' \frac{e^{ik_0|\mathbf{r}_s - \mathbf{r}'|}}{4\pi|\mathbf{r}_s - \mathbf{r}'|}\psi(\mathbf{r}'). \tag{8.34}$$

The form of Eq. (8.34) is exactly the same as the theory of Green function. Therefore, the operator theory is consistent with that of Green functions.

8.2.2. Example of Dipole Field Using Operators

This section presents an example of dipole field directly using operators but not Green function. In order to show the comparisons with the known results, this example

is on (1) the constant magnetization $\mathbf{m}$, (2) the spherical sample, and (3) the magnetostatic limit. It's known that the dipole field factor is $-1/3$ inside the sample in the magnetostatic limit. For this simple example, it proves convenient to use the operators introduced in Section 7.3.1. In the magnetostatic limit, the dipole field in the operator form can be

$$\mathbf{h}_d \approx -\frac{\sin^2\tilde{\theta}_k}{2}(1+\boldsymbol{\sigma}_z e^{-2\boldsymbol{\sigma}_y\tilde{\phi}_k})q_s(r)\mathbf{m}\,. \tag{8.35}$$

This is in LCS because the SCS and the LCS can be the same in this example. Moreover, equations (8.24) and (8.25) are the same in the magnetostatic limit and then equation (8.35) is correct for the regions outside and insider the sample. Since $\mathbf{m}$ is a constant vector, the operators can directly act on the unit function $q_s(r)$. $q_s(r)$ for a sphere with a radius of r_0 can be expanded into

$$q(r) = \int\frac{d\mathbf{k}}{8\pi^3}\int_0^{r_0} dr' 4\pi r'^2 j_0(kr')e^{-i\mathbf{k}\cdot\mathbf{r}}\,. \tag{8.36}$$

First, what is $e^{-2\boldsymbol{\sigma}_y\tilde{\phi}_k}$ acting on $q_s(r)$?

$$e^{-2\boldsymbol{\sigma}_y\tilde{\phi}_k}q(r) = \int dk\int_0^{r_0} dr'\int_0^{2\pi} d\phi_k 2k^2r'^2 j_0(kr')j_0(kr)e^{-2\boldsymbol{\sigma}_y\phi_k}\,. \tag{8.37}$$

The ϕ_k integral on the sine and cosine functions results in zero since the sine and cosine functions are half positive and half negative in the range of 0-π. In other word, $e^{-2\boldsymbol{\sigma}_y\tilde{\phi}_k}$ commutes with $q_s(r)$ in this case.

Based on the result of Eq. (8.37), equation (8.35) becomes

$$\mathbf{h}_d = -\frac{\sin^2\tilde{\theta}_k}{2} q_s(r)\mathbf{m} = \left(-\frac{1}{3} + \frac{3\cos^2\tilde{\theta}_k - 1}{6}\right) q_s(r)\mathbf{m}. \tag{8.38}$$

The operator has been written into two terms that are proportional to $Y_{00}(\tilde{\theta}_k, \tilde{\phi}_k)$ and $Y_{20}(\tilde{\theta}_k, \tilde{\phi}_k)$, respectively. Note that

$$e^{-i\mathbf{k}\cdot\mathbf{r}} = \sum_{l=0}^{\infty} \sum_{m=-l}^{l} 4\pi i^l j_l(kr) Y_{lm}^*(\theta_k, \phi_k) Y_{lm}(\theta, \phi). \tag{8.39}$$

Based on Eq. (8.36), the two-term form of Eq. (8.38) tells that only the terms with Y_{00} and Y_{20} survive.

$$\mathbf{h}_d == -\frac{1}{3} u_{10}(r)\mathbf{m}_0 - \frac{3\cos^2\theta - 1}{6} u_{12}(r)\mathbf{m}_0, \tag{8.40}$$

where

$$u_{10}(r) = \int_0^{r_0} dr' \int dk \frac{2}{\pi} k^2 r'^2 j_0(kr') j_0(kr) \tag{8.41}$$

and

$$u_{12}(r) = \int_0^{r_0} dr' \int dk \frac{2}{\pi} k^2 r'^2 j_0(kr') j_2(kr). \tag{8.42}$$

It will be shown shortly that $u_{10}(r)$ will be zero when $r > r_0$ and $u_{12}(r)$ will be zero when $r < r_0$. The two terms in Eq. (8.40) are physically corresponding to the dipole field inside the sample and outside the sample, respectively.

The function $u_{10}(r)$ can be easy to obtain using

$$\int dk \frac{2}{\pi} k^2 r'^2 j_l(kr') j_l(kr) = \delta(r - r') \text{ for } l = 0, 1, ... \tag{8.43}$$

Based on this identity,

$$u_{10}(r) = q_s(r). \tag{8.44}$$

So, the dipole field factor inside the sample is equal to $-1/3$. This is consistent with the known dipole factor for sphere.

The function $u_{12}(r)$ is more complicated. First, use the definition of the spherical Bessel function,

$$u_{12}(r) = -r\frac{d}{dr}\int_0^{r_0} dr' \int dk \frac{2}{\pi} k^2 r'^2 j_0(kr') \frac{j_1(kr)}{kr}. \tag{8.45}$$

Secondly, use

$$\frac{d}{dx} x^2 j_1(x) = x^2 j_0(x), \tag{8.46}$$

and one obtains

$$u_{12}(r) = -r\frac{d}{dr}\frac{1}{r^3}\int_0^{r} dr'' \int_0^{r_0} dr' \delta(r' - r'') r''^2. \tag{8.47}$$

It can be obtained,

$$\mathbf{h}_d = \begin{cases} -\dfrac{1}{3}\mathbf{m}_0, & r < r_0 \\ \dfrac{r_0^3(3\cos^2\theta - 1)}{6r^3}\mathbf{m}_0, & r > r_0 \end{cases}. \tag{8.48}$$

For $r > r_0$, there is an extra factor $1/2$ compared with textbook result for static magnetization in a uniformly magnetized sphere (Jackson, 1998). This is because the form in Eq. (8.35) is the effective dynamic transverse dipole field in linearized torque equation but not the total field. Equation (8.48) was used in the development of the

porosity scattering in Chapter 3.

8.2.3. Modifications in Gilbert Equation

Gilbert equation

$$\frac{\partial}{\partial t}\mathbf{M} = -|\gamma|\mathbf{M}\times\mathbf{H}_{\text{eff}} + \frac{\alpha\mathbf{M}\times(\mathbf{M}\times\mathbf{H}_{\text{eff}})}{M_s} \tag{8.49}$$

is applicable to grains and voids. To include the effects of grains and pores, one can just do a simple replacement

$$\mathbf{M} \to q(\mathbf{r}_s)q_s(r_s)\mathbf{M}\,. \tag{8.50}$$

This replacement includes the static part and dynamic part of the magnetization $\mathbf{M}$. To consider all the effects due to the random grains and the random voids existing in the sample, the operation is simply to apply Eq. (8.50) to Eq. (8.19) and one obtains

$$\begin{aligned} &q_s(r_s)q(\mathbf{r}_s)\left[\frac{\boldsymbol{\sigma}_y+\alpha}{\omega_M}\frac{\partial}{\partial t}+\Omega_H - D_0\nabla_s^2+\tilde{\mathbf{N}}-\right. \\ &\left.\mathbf{S}_1(\mathbf{r}_s)-\mathbf{S}_2(\mathbf{r}_s)\right]q(\mathbf{r}_s)q_s(r_s)\mathbf{m} = q_s(r_s)q(\mathbf{r}_s)\mathbf{h}_p \end{aligned}\,. \tag{8.51}$$

Note that the function $q(\mathbf{r}_s)$ exists in the whole space. Based on the correlation function, $q(\mathbf{r}_s)$ may be treated as invertible because its statistical average is nonzero and equal to $1-p$ where p is the porosity. But $q_s(\mathbf{r}_s)$ is different since $q_s(\mathbf{r}_s)$ only exists in the finite space and its average over the whole space is zero. Moreover, $q(\mathbf{r}_s)$ commutes with $q_s(\mathbf{r}_s)$. This make it possible to delete a $q(\mathbf{r}_s)$ on both sides, namely,

$$q_s(r_s)\left[\frac{\boldsymbol{\sigma}_y+\alpha}{\omega_M}\frac{\partial}{\partial t}+\Omega_H-D_0\nabla_s^2+\tilde{\mathbf{N}}-\mathbf{S}_1(\mathbf{r}_s)-\mathbf{S}_2(\mathbf{r}_s)\right]\cdot \qquad (8.52)$$
$$q(\mathbf{r}_s)q_s(r_s)\mathbf{m}=q_s(r_s)\mathbf{h}_p$$

Unlike Maxwellian boundary conditions, this equation does not include the exchange boundary conditions. This is because the surface layers of the grains are not included in the derivation of Eq.(8.49). Equivalently, the exchange boundary conditions can be considered by introducing a new term, $\mathbf{S}_3(\mathbf{r}_s)$,

$$q_s(r_s)\left(\frac{\boldsymbol{\sigma}_y+\alpha}{\omega_M}\frac{\partial}{\partial t}+\Omega_H-D_0\nabla_s^2+\tilde{\mathbf{N}}-\mathbf{S}_1-\mathbf{S}_2-\mathbf{S}_3\right)\cdot, \qquad (8.53)$$
$$q(\mathbf{r}_s)q_s(r_s)\mathbf{m}=q_s(r_s)\mathbf{h}_p$$

where

$$\begin{aligned}\mathbf{S}_3(\mathbf{r}_s)&=D_0\xi_0(\hat{\mathbf{z}}\cdot\hat{\mathbf{n}}_g)^2\left[\hat{\mathbf{n}}_g\cdot\nabla_s q(\mathbf{r}_s)\right]\\&\approx D_0\xi_0(\hat{\mathbf{z}}_s\cdot\hat{\mathbf{n}}_g)^2\left[\hat{\mathbf{n}}_g\cdot\nabla_s q(\mathbf{r}_s)\right]\end{aligned}. \qquad (8.54)$$

$\hat{\mathbf{z}}$ has been replaced by $\hat{\mathbf{z}}_s$ for fully saturated magnetization. This approximation is not valid for highly anisotropic materials. The inclusion of this operator is equivalent to Eq. (7.31) that is the exchange boundary condition for grains. The exchange is only important for high k spin waves. $\mathbf{S}_3(\mathbf{r}_s)$ is related to grain boundary scattering.

It's convenient for further scattering analyses to separate the random operators. $q(\mathbf{r}_s)$ is a random function but has a non-zero statistical average unlike the scattering operators $\mathbf{S}_1(\mathbf{r}_s)$, $\mathbf{S}_2(\mathbf{r}_s)$, and $\mathbf{S}_3(\mathbf{r}_s)$. Write $q(\mathbf{r}_s)$ into two terms.

$$q(\mathbf{r}_s)=(1-p)\left[1-\left(1-\frac{q(\mathbf{r}_s)}{1-p}\right)\right]. \qquad (8.55)$$

One has

$$\left\langle 1-\frac{q(\mathbf{r}_s)}{1-p}\right\rangle = 0. \tag{8.56}$$

Based on Eqs. (8.55) and (8.56), one more scattering operator $\mathbf{S}_0(\mathbf{r}_s)$ is introduced. Equation (8.51) is written as

$$q_s(r_s)\left\{\frac{\boldsymbol{\sigma}_y+\alpha}{\omega_M}\frac{\partial}{\partial t}+\Omega_H-D_0\nabla_s^2+\tilde{\mathbf{N}}-\mathbf{S}_0(\mathbf{r}_s)-\frac{[\mathbf{S}_1(\mathbf{r}_s)+\mathbf{S}_2(\mathbf{r}_s)+\mathbf{S}_3(\mathbf{r}_s]q_s(r_s)}{1-p}\right\}q(\mathbf{r}_s)\mathbf{m}=\frac{q_s(r_s)}{1-p}\mathbf{h}_p, \tag{8.57}$$

where

$$\mathbf{S}_0(\mathbf{r}_s)=\left(\frac{\boldsymbol{\sigma}_y+\alpha}{\omega_M}\frac{\partial}{\partial t}+\Omega_H+\tilde{\mathbf{N}}-D_0\nabla_s^2\right)\left(1-\frac{q(r_s)}{1-p}\right). \tag{8.58}$$

This operator is related to in part the porosity scattering and the EM-SW scattering. $\mathbf{S}_0(\mathbf{r}_s)$ also contributes in part to grain boundary scattering.

One can simplify Eq. (8.57) based on the assumption of dense materials,

$$q_s(r_s)[\tilde{\chi}-\mathbf{S}(\mathbf{r}_s)]q_s(\mathbf{r}_s)\mathbf{m}\approx q_s(r_s)\mathbf{h}_p. \tag{8.59}$$

Here, $\mathbf{S}(\mathbf{r}_s)$ is the total scattering operator, namely,

$$\mathbf{S}(\mathbf{r}_s)\approx\mathbf{S}_0(\mathbf{r}_s)+\mathbf{S}_1(\mathbf{r}_s)+\mathbf{S}_2(\mathbf{r}_s)+\mathbf{S}_3(\mathbf{r}_s). \tag{8.60}$$

The operator $\tilde{\chi}$ corresponds to the *inverse* of the unbounded internal susceptibility. One of the important properties of $\mathbf{S}(\mathbf{r}_s)$ is $\langle\mathbf{S}(\mathbf{r}_s)\rangle=0$. This relation is useful for the derivation of two-magnon scattering.

8.3. Extrinsic Losses

In polycrystalline ferrites, two-magnon scattering typically dominates over the other extrinsic losses. This section shows how to convert the scattering operators into the two-magnon scattering terms using the correlation functions. Section 8.3.1 presents the operator form of two-magnon scattering and the discussions such as the perturbed manifold, secondary scattering. Section 8.3.2 is a simple example of the calculations of two-magnon scattering using the operator theory to show the consistence with the previous results on the anisotropy scattering. Section 8.3.3 shows a preliminary GBS calculation.

8.3.1. Operator Theory of Two Magnon Scattering

The contributions of two-magnon scattering can be obtained from Eq. (8.59). For a given spin wave in $q_s(\mathbf{r}_s)\mathbf{m}_{x,y}$ with wave vector $\mathbf{k}$, the $\mathbf{k}'$ component of the operator $\mathbf{S}(\mathbf{r}_s)$ acting on it gives another spin wave with wave vector $\mathbf{k}+\mathbf{k}'$. Such picture is provided in Chapter 3 and found to be two-magnon scattering. This is why the operator $\mathbf{S}(\mathbf{r}_s)$ is called a scattering operator. However, $\mathbf{S}(\mathbf{r}_s)$ cannot be directly used for the evaluation of two-magnon scattering. There are two main reasons. One is that the statistical average of $\mathbf{S}(\mathbf{r}_s)$ vanishes. The other is that $\mathbf{S}(\mathbf{r}_s)$ leads to a series of spin waves and equation (8.59) is hard to solve. The following is to find the first order non-vanished terms for $\mathbf{S}(\mathbf{r}_s)$.

The operator $\mathbf{S}(\mathbf{r}_s)$ is small since its statistical average vanishes. This allows an expansion,

$$\frac{1}{1-\tilde{\chi}^{-1}\mathbf{S}(\mathbf{r}_s)}=\sum_{n=0}^{\infty}\left[\tilde{\chi}^{-1}\mathbf{S}(\mathbf{r}_s)\right]^n. \tag{8.61}$$

Note that

$$\left\langle\left[\tilde{\chi}^{-1}\mathbf{S}(\mathbf{r}_s)\right]^n\right\rangle=0 \text{ if } n \text{ is odd.} \tag{8.62}$$

Based on this statistical property, an approximation can be made

$$\frac{1}{1-\tilde{\chi}^{-1}\mathbf{S}(\mathbf{r}_s)}\approx\sum_{n=0}^{\infty}\left[\tilde{\chi}^{-1}\mathbf{S}(\mathbf{r}_s)\right]^{2n}=\frac{1}{1-\left[\tilde{\chi}^{-1}\mathbf{S}(\mathbf{r}_s)\right]^2}. \tag{8.63}$$

Namely

$$1-\tilde{\chi}^{-1}\mathbf{S}(\mathbf{r}_s)\approx 1-\left[\tilde{\chi}^{-1}\mathbf{S}(\mathbf{r}_s)\right]^2. \tag{8.64}$$

One insert this equation into Eq.(8.59) and obtains

$$q_s(\mathbf{r}_s)\left[\tilde{\chi}-\mathbf{S}(\mathbf{r}_s)\tilde{\chi}^{-1}\mathbf{S}(\mathbf{r}_s)\right]q_s(r_s)\mathbf{m}\approx q_s(r_s)\mathbf{h}_p. \tag{8.65}$$

Apply the statistical average and one obtains

$$q_s(\mathbf{r}_s)\left[\tilde{\chi}-\left\langle\mathbf{S}(\mathbf{r}_s)\tilde{\chi}^{-1}\mathbf{S}(\mathbf{r}_s)\right\rangle\right]q_s(r_s)\mathbf{m}\approx q_s(r_s)\mathbf{h}_p. \tag{8.66}$$

Compare Eqs. (8.59) and (8.66), the operator $\mathbf{S}(\mathbf{r}_s)$ is simply replaced by $\left\langle\mathbf{S}(\mathbf{r}_s)\tilde{\chi}^{-1}\mathbf{S}(\mathbf{r}_s)\right\rangle$. In the previous literature, the scattering sources might be represented by a non-statistical $\mathbf{S}(\mathbf{r}_s)$. For the uniform spin wave mode, equation (8.66) is still correct, as shown in Chapter 3.

As Vrehen (1970) and Hoeppe (2004) proposed, the static field is perturbed by the dipole field of the voids and causes the spin wave manifold shifts. This effect was

included in the parameter of Ω_H that is proportional to the local static effective field. From the derivations of spin wave bands in Chapter 7, Ω_H causes the bulk manifold shifts. The statistical average in $\left\langle \mathbf{S}(\mathbf{r}_s)\tilde{\boldsymbol{\chi}}^{-1}\mathbf{S}(\mathbf{r}_s)\right\rangle$ also causes such kind of shifts. These shifts can cause two-magnon scattering. Similar to the above derivation, equation (8.66) can be modified,

$$q_s(\mathbf{r}_s)\left[\left\langle\tilde{\chi}\right\rangle + i\boldsymbol{\Gamma}_1 + i\boldsymbol{\Gamma}_2\right]q_s(r_s)\mathbf{m} = q_s(r_s)\mathbf{h}_p. \tag{8.67}$$

Where

$$\boldsymbol{\Gamma}_1 = i\left\langle\left(\Omega_H - \left\langle\Omega_H\right\rangle\right)\tilde{\boldsymbol{\chi}}^{-1}\left(\Omega_H - \left\langle\Omega_H\right\rangle\right)\right\rangle. \tag{8.68}$$

and

$$\boldsymbol{\Gamma}_2 = i\left\langle\mathbf{S}(\mathbf{r}_s)\tilde{\boldsymbol{\chi}}^{-1}\mathbf{S}(\mathbf{r}_s)\right\rangle. \tag{8.69}$$

The porosity scattering originated in part from $\boldsymbol{\Gamma}_1$ that corresponds to the contributions due to non-uniform static fields. The two-magnon term $\left\langle \mathbf{S}(\mathbf{r}_s)\tilde{\boldsymbol{\chi}}^{-1}\mathbf{S}(\mathbf{r}_s)\right\rangle$ is just the first order non-vanishing term. In Eq. (8.63), the odd terms are neglected. The further considerations of these odd terms result in three-magnon scattering, four-magnon scattering, and so on. It's typically assumed that the higher order scattering processes affect little on the linewidth calculations compared with the two-magnon processes.

The two-magnon term $\left\langle \mathbf{S}(\mathbf{r}_s)\tilde{\boldsymbol{\chi}}^{-1}\mathbf{S}(\mathbf{r}_s)\right\rangle$ may be big especially in the manifold region. The secondary scattering processes should hereby be mentioned here. From Eq. (8.65), the spin wave manifold is modified by $\left\langle \mathbf{S}(\mathbf{r}_s)\tilde{\boldsymbol{\chi}}^{-1}\mathbf{S}(\mathbf{r}_s)\right\rangle$. The derivation of this term implies that $\tilde{\chi}$ may be the non-vanishing part of $\tilde{\chi} - \mathbf{S}(\mathbf{r}_s)$. This means that the

equation (8.65) should be modified

$$q_s(\mathbf{r}_s)\left[\langle\tilde{\chi}\rangle + i\boldsymbol{\Gamma}\right]q_s(r_s)\mathbf{m} = q_s(r_s)\mathbf{h}_p . \tag{8.70}$$

where

$$\boldsymbol{\Gamma} = i\left\langle\left(\Omega_H - \langle\Omega_H\rangle + \mathbf{S}(\mathbf{r}_s)\right)\frac{1}{\tilde{\chi} + i\boldsymbol{\Gamma}_1 + i\boldsymbol{\Gamma}_2}\left(\Omega_H - \langle\Omega_H\rangle + \mathbf{S}(\mathbf{r}_s)\right)\right\rangle . \tag{8.71}$$

The operator $\tilde{\Gamma}$ can further modify the spin wave manifold. It can be treated as the higher order effects and not discussed here because the loss rate for dense YIG is always small. In the previous treatment, Schlömann (1969) used an iteration way to make it consistent so as to account for the higher order secondary scattering processes.

The physical meanings of $\boldsymbol{\Gamma}$ are clear. $\boldsymbol{\Gamma}$ is complex. The real part of $\boldsymbol{\Gamma}$ acting on a normal mode represents the relaxation frequency in the unit of ω_M. The imaginary part causes the frequency shift of the normal mode resonance. One of important properties of $\boldsymbol{\Gamma}$ is that $\boldsymbol{\Gamma}$ is a linear derivative operator dependent on ∇_s but not $\mathbf{r}_s$. $\boldsymbol{\Gamma}_1$ and $\boldsymbol{\Gamma}_2$ also have this property. The scattering sources mentioned in this chapter are isotropic. This implies that $\boldsymbol{\Gamma}$ is only a function of ∇_s^2 that is a scalar derivative operator. In the previous two-magnon analyses, the relaxation is a scalar related to the sample geometry and the field configuration. It's not easy to find out the effective term(s) for two-magnon scattering in the linearized torque equation for general sample geometry.

It's interesting that the two-magnon scattering operator $\boldsymbol{\Gamma}$ is independent on the boundary condition related to the sample surfaces. This means that the operator formulation can be used to replace the phenomenological damping models and directly

use the torque equation with physical relaxation,

$$\left(\langle\tilde{\chi}\rangle + i\boldsymbol{\Gamma}\right)\mathbf{m} = \mathbf{h}_p . \tag{8.72}$$

This equation is applicable for any of the sample shape and size. This opens a new way to construct physical damping models for replacement of phenomenological damping models. The only disadvantage is that equation (8.72) is just for the linear response of magnetization. The boundary conditions can also be worked out from this linear differential equation. For the large magnetization precession, the damped torque equation can also be found based on the operator theory, but will not be discussed in this thesis.

8.3.2. Anisotropy Scattering

An example is presented in this section for the understanding of the relaxation operator $\boldsymbol{\Gamma}$. This example is the same as that of Schlömann (1969) based on the assumptions (1) that the magnetostatic approximation is made,

$$\tilde{\mathbf{N}} \approx \frac{1}{2}\sin^2\tilde{\theta}(1+\boldsymbol{\sigma}_y e^{\sigma_y \tilde{\phi}_k}), \tag{8.73}$$

(2) that $\mathbf{m}$ has only the uniform mode

$$\mathbf{m}(t) = \mathbf{m}(\omega)e^{i\omega t}, \tag{8.74}$$

(3) that the secondary scattering processes are neglected, and (4) that only the anisotropy scattering is considered.

Based on the fourth assumption, only the scattering operator related with a_0 and a_z is contained in $\mathbf{S}$, namely,

$$\mathbf{S}(\mathbf{r}_s) \approx a_0(\mathbf{r}_s) + a_z(\mathbf{r}_s)\mathbf{T}\boldsymbol{\sigma}_z\mathbf{T}^{-1}, \tag{8.75}$$

where

$$\mathbf{T} \approx e^{-\boldsymbol{\sigma}_y\varphi_g}. \tag{8.76}$$

The relation for the correlation function, Eq. (6.11), is applicable to the component of $\mathbf{S}(\mathbf{r}_s)$. Based on the above four assumption, one obtains

$$\boldsymbol{\Gamma} \approx i\int\frac{d\mathbf{k}'}{8\pi^3}\left\langle \mathbf{S}^*(\mathbf{k}')\tilde{\boldsymbol{\chi}}^{-1}(\mathbf{k}')\mathbf{S}(\mathbf{k}')\right\rangle. \tag{8.77}$$

where

$$\tilde{\boldsymbol{\chi}}(\mathbf{k}') = \left(\boldsymbol{\sigma}_y + \alpha\right)i\Omega + \Omega_H + D_0k'^2 + \frac{1}{2}\sin^2\theta_k'(1+\boldsymbol{\sigma}_z e^{-2\boldsymbol{\sigma}_y\phi_k'}) \tag{8.78}$$

Here, the operator ∇_s is proportional to the square root of the scalar operator ∇_s^2 that is replaced by 0 because ∇_s^2 acting on the uniform mode approximately vanishes.

Schlömann (1970) and McMichael *et al* (2004) developed the correlations functions for anisotropy. If the components of $\mathbf{S}(\mathbf{k}')$ is written in the form

$$\mathbf{S}(\mathbf{k}') = \begin{pmatrix} S_{11} & S_{12} \\ S_{21} & S_{22} \end{pmatrix}, \tag{8.79}$$

According to McMichael *et al* (2004),

$$\left\langle S_{11}^* S_{11}\right\rangle = \left\langle S_{22}^* S_{22}\right\rangle = \frac{116}{105}A(k'), \tag{8.80}$$

$$\left\langle S_{12}^* S_{21}\right\rangle = \frac{36}{105}A(k'), \tag{8.81}$$

$$\left\langle S_{11}^{*} S_{22} \right\rangle = \frac{44}{105} A(k'), \tag{8.82}$$

and other correlation functions are zero. Here,

$$A(k') = \left(\frac{|\mathbf{H}_A|}{M_0} \right)^2 \frac{8\pi b^3}{\left(1 + k'^2 b^2\right)^2}, \tag{8.83}$$

where b is the average grain size.

It's convenient for the operator calculations to rewrite $\mathbf{S}(\mathbf{k}')$ in a quaternion,

$$\mathbf{S}(\mathbf{k}') = S_u + S_x \boldsymbol{\sigma}_x + S_z \boldsymbol{\sigma}_z . \tag{8.84}$$

The correlation functions in Eqs. (8.80)-(8.82) become

$$\left\langle S_u^{*} S_u \right\rangle = \frac{80}{105} A(k'), \ \left\langle S_x^{*} S_x \right\rangle = \left\langle S_z^{*} S_z \right\rangle = \frac{36}{105} A(k') . \tag{8.85}$$

The other correlation functions are zero. This implies that the components in $\mathbf{S}(\mathbf{k}')$ are orthogonal for the quaternion form.

The trivial derivation gives

$$\boldsymbol{\Gamma} \approx i \int d\mathbf{k}' \frac{A(k')}{105\pi^3} \frac{19\Omega_{\mathbf{k}'} - i\boldsymbol{\sigma}_y \Omega}{\Omega_{\mathbf{k}'}^2 - \Omega^2} . \tag{8.86}$$

where

$$\Omega_{\mathbf{k}'} = \sqrt{\left(i\alpha\Omega + \Omega_H + D_0 k'^2\right)\left(i\alpha\Omega + \Omega_H + D_0 k'^2 + \sin^2\theta_k'\right)} . \tag{8.87}$$

The operator $e^{-2\sigma_y \varphi_k'}$ vanishes because the correlation functions are independent on ϕ_k' and

$$\int_0^{2\pi} d\phi_k' e^{-n\sigma_y \phi_k'} = 0 \text{ for n=1,2,....} \qquad .(8.88)$$

It can be generalized that for polycrystalline samples, the relaxation operator $\mathbf{\Gamma}$ is only dependent on $\boldsymbol{\sigma}_y$ but not on $\boldsymbol{\sigma}_x$ and $\boldsymbol{\sigma}_z$.

The integral of Eq. (8.86) can be evaluated using the residue theorem. For comparison with the results of Schlömann (1969), take the limit of $\alpha \to 0$ and use the residue theorem. The effective Gilbert damping constant α for anisotropy scattering can be found,

$$\alpha \to \lim_{\alpha \to 0} \int d\mathbf{k}' \frac{A(k')\left(19\Omega_{\mathbf{k}'} - i\boldsymbol{\sigma}_y \Omega\right)}{310\pi^2} \delta(\Omega_{\mathbf{k}'} - \Omega). \qquad (8.89)$$

This implies that this effective damping parameter is independent on sample geometry. It is generally inappropriate to use an α scalar number to represent two-magnon scattering. It's interesting that the uniform mode relaxation is only related to $\boldsymbol{\sigma}_y$.

According to Eq. (8.89), the general damping parameter can be a quaternion as

$$\alpha \to \begin{pmatrix} \alpha_1(\omega) & i\alpha_2(\omega) \\ -i\alpha_2(\omega) & \alpha_1(\omega) \end{pmatrix}. \qquad (8.90)$$

The imaginary number originates from temporal Fourier transformation. To take account for the two-magnon relaxation, the Gilbert constant should be replaced by the above tensor. This physical tensor-form relaxation operator is different from Safanov's tensor-form phenomenological damping model (2002). This implies that Safanov's model cannot represent the anisotropy scattering.

For a spherical sample, the magnetic excitation is the uniform mode Larmor circular

precession of the magnetization. The tensor $-i\sigma_y$ can be replaced by 1 in Eq. (8.89). Such result of Eq. (8.89) is consistent with the probability results of Schlömann (1969). The magnetostatic spin wave band is determined by the equation

$$\Omega=\Omega_{k'}. \tag{8.91}$$

Therefore, the delta function in Eq. (8.89) means that only the degenerate spin wave modes contribute to the relaxation. This is also consistent with the magnon energy conservation in the processes of two-magnon scattering. The other sample shape makes the relaxation rate dependent on the spin wave polarization.

8.3.3. Grain Boundary Scattering

According to the discussions in Chapter 6, the generally larger low field effective (LFE) linewidth values relative to the high field effective (HFE) linewidth were qualitatively explained by the high k spin waves that are not present at high field (Patton, 1969, 1970). However, the quantitative formulation of the high k scattering was never done previously. This section provides a preliminary evaluation of the high k scattering due to grain boundaries, called grain boundary scattering.

The scattering operators related to boundaries are $\mathbf{S}_0$ and $\mathbf{S}_3$. But $\mathbf{S}_0$ isn't affected by the grain surface anisotropy. This section only takes account for $\mathbf{S}_3$ that characterizes the grain surface condition while $\mathbf{S}_0$ will be considered in the future experimental investigations on grain size dependence of the LHE linewidth.

Note that $\mathbf{S}_3$ is a scalar operator. For uniform mode, equation (8.77) is still valid and can be written as

$$\Gamma = i\int \frac{d\mathbf{k}}{8\pi^3}\left\langle \mathbf{S}_3^*(\mathbf{k})\mathbf{S}_3(\mathbf{k})\right\rangle \chi(\mathbf{k}). \tag{8.92}$$

For discussions of the correlation function $\left\langle \mathbf{S}_3^*(\mathbf{k})\mathbf{S}_3(\mathbf{k})\right\rangle$, it is convenient to reproduce the expression of $\mathbf{S}_3$,

$$\mathbf{S}_3(\mathbf{r}_s) \approx D_0\xi_0(\hat{\mathbf{z}}_s\cdot\hat{\mathbf{n}}_g)^2\left[\hat{\mathbf{n}}_g\cdot\nabla_s q(\mathbf{r}_s)\right]. \tag{8.93}$$

The vector $\nabla_s q(\mathbf{r}_s)$ is just a delta function at grain surfaces and parallel to $\hat{\mathbf{n}}_g$. In Fourier transformation, one can obtains

$$\hat{\mathbf{n}}_g\cdot\nabla_s q(\mathbf{r}_s) \rightarrow -ik\cdot q(\mathbf{k}). \tag{8.94}$$

This implies that $\hat{\mathbf{n}}_g\cdot\nabla_s q(\mathbf{r}_s)$ doesn't depend on the normal directions of grain surfaces. On the other hand, the operator factor $(\hat{\mathbf{z}}_s\cdot\hat{\mathbf{n}}_g)^2$ is purely dependent on the normal directions of grain surfaces. Therefore, these two factors can be separated.

For quick calculations, one can do the statistical average of $(\hat{\mathbf{z}}_s\cdot\hat{\mathbf{n}}_g)^2$ in the real $\mathbf{r}_s$ space and do that of $\hat{\mathbf{n}}_g\cdot\nabla_s q(\mathbf{r}_s)$ in the $\mathbf{k}$ phase space. For $(\hat{\mathbf{z}}_s\cdot\hat{\mathbf{n}}_g)^2$, the angle between $\hat{\mathbf{z}}_s$ and $\hat{\mathbf{n}}_g$ can be assumed to be uniformly distributed in a range from 0 to π. For this case, it can be obtained,

$$\left\langle(\hat{\mathbf{z}}_s\cdot\hat{\mathbf{n}}_g)^4\right\rangle = \frac{3}{4}. \tag{8.95}$$

Based on Eqs. (8.94) and (8.95), equation (8.92) becomes

$$\Gamma = i\int \frac{d\mathbf{k}}{8\pi^3}\frac{3}{4}\left(D_0\xi_0\right)^2 k^2\left\langle q^*(\mathbf{k})q(\mathbf{k})\right\rangle \chi(\mathbf{k}). \tag{8.96}$$

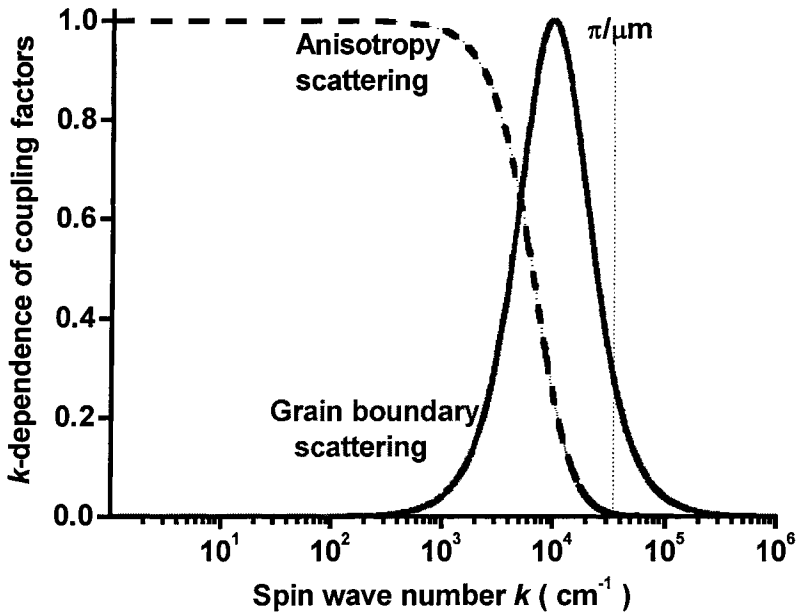

FIG. 8.3. Coupling factors for grain boundary scattering as a function of wave number k. The solid curve shows that for grain boundary scattering and the dashed curve for anisotropy scattering for comparison. These two curves are computed using Eqs. (3.21) and (8.99), respectively. The grain size is 1 μm. The vertical dotted lines show π over this size in the horizontal coordinate, as indicated.

The function $\langle q^*(\mathbf{k})q(\mathbf{k})\rangle$ is the correlation function related to the grain size distribution that is typically a Gaussian distribution. To avoid an inclusion of complicated mathematical calculations, one can simply take Schlömann's (1969, 1970) approximate expression,

$$\langle q^*(\mathbf{k})q(\mathbf{k})\rangle = \frac{8\pi b^3}{\left(1+k^2b^2\right)^2}. \tag{8.97}$$

This is invalid for porous materials. Insert this result into Eq. (8.96) and one obtains

$$\Gamma = i\int \frac{d\mathbf{k}}{8\pi^3} \frac{6\pi b^3 \left(D_0\xi_0\right)^2 k^2}{\left(1+k^2b^2\right)^2} \chi(\mathbf{k}). \tag{8.98}$$

Based on the susceptibility, one can find out that the damping model for GBS also follows the same form as in (8.90).

This result is similar to quantum theory of two-magnon scattering due to the random surface anisotropy in ultra thin films (Arias and Mills, 1999). The two-magnon relaxation is proportional to the square of surface anisotropy. This is because the parameter ξ_0 is proportional to surface anisotropy according to Eq. (7.32) if the surface anisotropy field is constant.

Based on Eq. (8.98), the coupling factor for the grain boundary scattering can be written as

$$C(\mathbf{k}) = \frac{6\pi k^2 b^3 \left(D_0 \xi_0\right)^2}{\left(1+k^2 b^2\right)^2}. \tag{8.99}$$

This factor as a function of wave number is shown in Fig. 8.3, as indicated by the solid curve. For comparison, the coupling factor for anisotropy scattering is also plotted and indicated by the dashed curve. These two curves are evaluated from Eqs. (3.21) and (8.99) with a grain size $b = 1\ \mu\text{m}$. The dotted vertical line shows a reference k value at $k = \pi / b$.

Figure 8.3 shows that the GBS coupling factor, unlike the anisotropy scattering, doesn't vanish even for the k values on the order of the inverse grain size, namely 10^5 cm^{-1}. This factor reaches a maximum at $k = b^{-1}$ and decreases very fast when k is off b^{-1}. The k value for the dipole-exchange spin wave (DE-SW) at low field is on the order of 10^5 cm^{-1} due to exchange interactions. According to Fig. 8.3, the coupling factor at low field should be very small.

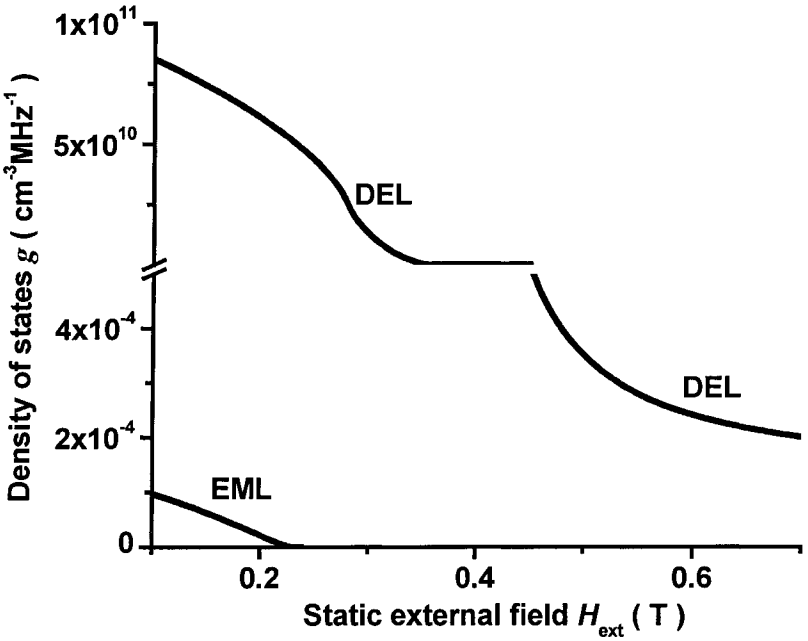

FIG. 8.4. Density of degenerate states for the dipole-exchange Larmor (DEL) and electromagnetic Larmor (EML) spin waves as a function of static external field at the operating point frequency of 10 GHz. The corresponding spin wave bands for the solid curves are indicated by DEL and EML.

However, this doesn't mean that the high k scattering is negligible because the two-magnon scattering also depends on the density of degenerate spin wave states (DOS). For further discussions, it's necessary to show the field dependence of DOS. Based on Chapter 3, the DOS value for each spin wave band can be calculated separately. Fig. 8.4 shows the calculated DOS for the dipole-exchange Larmor (DEL) and electromagnetic Larmor (EML) bands as a function of static external field. The parameters for the DOS evaluation are the same as in Fig. 6.3. For DEL, the DOS is from very high to very low. The part above break shows high DOS at low field and the part below break does low DOS at high field. For EML, the DOS is nonzero at low fields and the top field limit is indicated by $H_X \sim 0.23$ T.

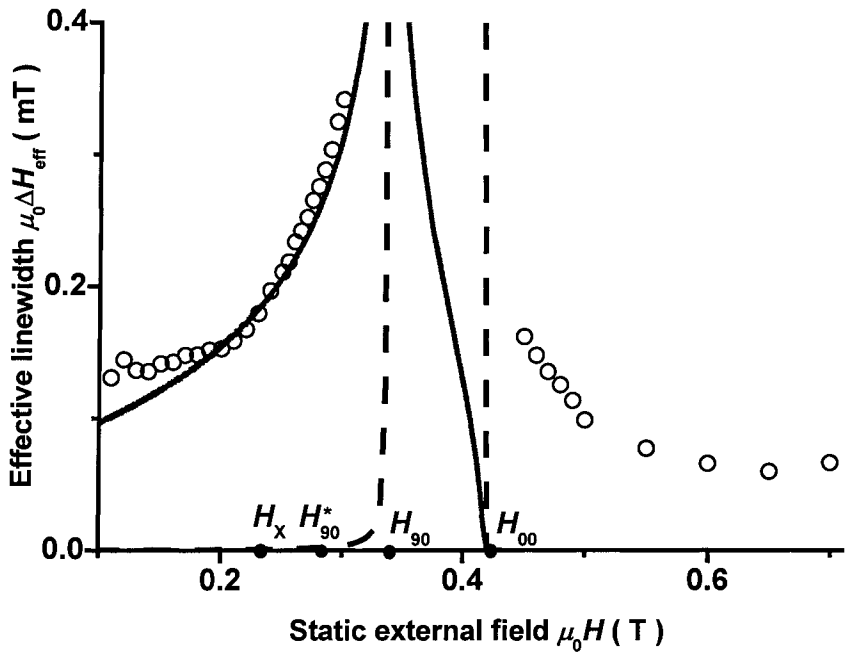

FIG. 8.5. Effective linewidth due to grain boundary scattering (GBS) for the hipped YIG material as a function static external field. The solid and dashed curves show the GBS and anisotropy scattering calculations done with parameters listed in the text. The open circles indicate the measured hipped YIG data. The indicated fields H_X, H^*_{90}, H_{90} and H_{00} are the same as in Fig. 6.6.

Figure 8.4 shows the DOS features of the DEL and EML bands. For DEL, the DOS is very high at low fields as a result of the very high wave number. The part for the in-manifold region is also fairly large since not only low k but also high k spin waves are available. For EML, the DOS is small in the low field region and gradually increases as field decreases. The vanishing field is the same as that of the EML dispersion curves in Fig. 6.3 (see Chapter 6).

Figure 8.5 shows the calculated effective linewidth due to the GBS. The calculations indicated by the solid curve are based on Eq. (8.98) with an effective thickness of surface layer for YIG, $D_0\xi_0 = 9.5$ nm, which is typically on the order of 10

nm for YIG (Yu *et al*, 1975), and an average grain size for the hipped YIG material (see Chapter 6), $b = 8\ \mu m$. The other parameters are the same as in Fig. 6.3. For comparison, the data measured on hipped YIG spheres are also shown. The dashed curve is the contribution due to the anisotropy scattering calculated with the same parameters.

Figure 8.5 shows three points. First, for fields between H_X and H_{90}, the GBS theory is in good agreement with the data. Second, the data show a departure from the GBS theory below H_X. This is due to the low k EML modes that are not considered in the GBS theory. The departure shows up at round 0.23 T, where the DOS for EML modes shows an abrupt change as shown in Fig. 8.4. Finally, the GBS loss is also non-zero and only vanishes at high field.

The intrinsic loss is not included in the solid curve in Fig. 8.5. The inclusion may result in a discrepancy between theory and data. For clarification, more investigations are needed on the experiments (especially grain size dependence) and new theoretical models for grain size distribution and grain boundary condition.

9. SUMMARY

New experimental investigations have been made on the effective linewidth for the polycrystalline yttrium iron garnet (YIG) bulk materials. The objective of this study is to resolve long-standing problems especially in the high field and low field effective linewidths. The efforts are made through (1) the enhancements of the effective linewidth technique, (2) the high precision measurements of effective linewidth for dense YIG and the quasi-qualitative analyses based on the full spin wave dispersion and scattering, and (3) the development of the classical full spin wave dispersion theory and the quantitative classical scattering theory.

9.1. Enhancements of Effective Linewidth Technique

In the effective linewidth technique, the effective linewidth is determined from the measurements of the cavity center frequencies and quality factors as a function of static external magnetic field. In order to improve the measurement accuracy that is of critical importance for the measurements in the high field and low field regions, the dominant errors due to the time and temperature drifts are compensated using the ABA method and the other treatments in the construction of the effective linewidth spectrometer are also made to optimize the measurement performance of spectrometer system, for example, the distortions due to the cables and the waveguide components are minimized. The cavity

measurement accuracy is improved more than ten fold relative to the previous accuracy (Patton, 1972). The ABA method also helps avoid the procedure for accurate temperature stabilization and corrections.

The previous results of gyromagnetic ratio (McKinstry, 1991) showed an abnormal field dependence that is inconsistent with the ferromagnetic resonance (FMR) measurements. In this thesis, the gyromagnetic ratio is tuned up to optimize the linear fitting for the cavity geometry factor and non-magnetic cavity center frequency. The tuned gyromagnetic ratio is found to be consistent with the value of gyromagnetic ratio obtained from the standard FMR measurements.

For the in-manifold effective linewidth measurements, the cavity-overloading problem is typically overcome by the change of the cavity and sample sizes. However, this is very hard for dense YIG, especially the high isostatic pressed (hipped) YIG, which has an extremely high FMR peak and the sample should be too tiny to be manufactured. A rotation technique is developed to make it feasible that the full field effective linewidth can be properly measured using one sample and one cavity. The rotation decouples the microwave field and the external static field, and the cavity losses due to the inserted sample can be decreased significantly. For a sample with a reasonable size, the rotation can make the cavity not overloaded at any field.

9.2. Experimental Results of Effective Linewidth

The high field effective (HFE) linewidth at 10 GHz is accurately measured on the hipped YIG spheres with nearly no porosity and the conventionally sintered (CS) spheres with a moderate porosity. The results show that the HFE linewidth is field dependent and

the infinite field extrapolated effective linewidth is comparable to the intrinsic single crystal YIG linewidth. This solves the longstanding problem that the HFE linewidth should theoretically match up with the intrinsic loss limit as proposed by Kohane and Schlömann (1968).

It's found in this thesis that the origins of the HFE linewidth are understandable under the theoretical frame of the full spin wave bands. Chapter 7 shows how to solve these spin wave bands based on the Gilbert equation, the full Maxwell equations, and quaternion analysis. Four spin wave bands are derived and there are, in the high field region, the electromagnetic spin wave (EM-SW) modes with wave number on the order of electromagnetic wave number. The density of the degenerate magnon states (DOS) for EM-SW modes is found to correlate with the field dependence of the HFE linewidth results. It is known that the two-magnon relaxation is generally proportional to the DOS for low wave number spin waves. One can conclude that qualitatively the field dependence of the HFE linewidth originates from two-magnon scattering due to the EM-SW modes.

The HFE linewidth data of the CS sample shows a distinct departure from the DOS curve for the external static field below around 0.53 T. This is consistent with the effect related to the pseudo manifold shifts due the non-uniform pore-demagnetizing field, as proposed by Vrehen (1970). The CS sample has some residue porosity on the order of 0.01. The pores generate an effective demagnetizing field in a wide range. This demagnetizing field causes the shifts of the manifold by –0.06 to 0.12 T for YIG. The regular dipole exchange spin waves hereby contribute significantly to the HFE linewidth below 0.53 T, namely the abrupt rise of the HFE linewidth data. The Vrehen effect

vanishes in the data of the hipped sample since the porosity can be neglected.

The measured results of the low field effective (LHE) linewidth show an elbow at an external static field of around 0.23 T for the hipped and CS samples. The elbow matches up with the abrupt emergence of the electromagnetic Larmor spin waves. The successful connections of the LHE linewidth with the EM-SW modes further support the important role of the EM-SW modes in the HFE linewidth. In the low field region, the two-magnon processes are also related to the high wave number dipole-exchange spin waves due to grain boundaries.

The effective linewidth in the manifold region has been measured using the cavity rotation technique. The manifold data for the hipped sphere show that the anisotropy scattering dominates since the porosity scattering can be neglected. This proves that the hipping processes can eliminate all the pores. The data also show several peaks that are found to be artificial effects because in the effective linewidth analyses the higher order Walker mode resonances are not considered.

9.3. Effective Linewidth Theory

The spin wave dispersion relationship for general anisotropic materials is derived based on the full Maxwell equations and the linearized Gilbert equation where the Gilbert damping constant can represent the intrinsic losses. The spin wave modes in the unbounded materials are categorized into the dipole-exchange Larmor (DEL) band, the electromagnetic Larmor (EML), the dipole-exchange Anti-Larmor (DEA) band, and the electromagnetic Anti-Larmor (EMA) band. The DEL and EML bands show the EM-SW modes at high fields and low fields, respectively. The dispersion relationship provides

the theoretical frame for two-magnon scattering. The excited magnon (or spin wave) may be scattered into all the magnon in the four spin wave bands.

For extrinsic losses, the two-magnon processes are assumed to be dominant. The scattering sources in the concerning polycrystalline YIG materials are voids, random anisotropy, and grain boundaries. These sources are described by the random unit functions. Based on the grain properties and boundary conditions, the dipole field and the Gilbert equation are modified with the scattering operators. The grain boundary conditions as well as the sample boundary conditions are also described by unit functions.

Based on the operator theory, the random operators on the first order are converted into the self correlation functions that become a linear derivative operator. This first order operator corresponds to the two-magnon processes and is called "relaxation operator". It has been shown how the relaxation operator includes the secondary scattering processes and the manifold shifts due to the effective dipole fields of voids. The relaxation operator provides the physical loss term in the magnetic torque equation. An example for the anisotropy scattering is used to show the consistence with the previous quantum two-magnon theory. This theory is also used to evaluate the high wave number grain boundary scattering. The theoretical results are found quantitatively in good agreement with the LHE linewidth data.

9.4. Perspectives

This thesis provides a start for modern study on the microwave effective linewidth of magnetic materials. (a) The high precision effective linewidth technique can be further applied to the magnetic metals and may resolve the relaxation structures due to free

electrons. (b) The relaxation operator can be worked out to replace the phenomenological damping terms. (c) The operator theory for two-magnon scattering can be applied to a general type of scattering source.

REFERENCE

1. Abdel-Khalek, K., "Quaternion analysis", and references therein, http://arxiv.org/PS_cache/hep-th/pdf/9607/9607152.pdf.
2. Arias, R., and D. L. Mills, "Extrinsic Contributions to the Ferromagnetic Resonance Response of Ultrathin Films", Phys. Rev. B **60**, 7395 (1999).
3. Bich, W., Cox, M.G., and Harris, P.M., "Uncertainty modelling in mass comparisons", Metrologia **30**, 495 (1993/4)
4. Bloembergen, N., and R. V. Pound, "Radiation Damping in Magnetic Resonance Experiments", Phys. Rev. **95**, 8 (1954).
5. Bloembergen, N., "Magnetic Resonance in Ferrites", Proc. ire **44**, 1259 (1956).
6. Celinski, Z., and B. Heinrich, "Ferromagnetic Resonance Linewidth of Fe Ultrathin Films Grown on a bcc Cu Substrate", J. Appl. Phys. **70**, 5935 (1991).
7. Cochran, J. F., B. Heinrich, and G. Dewar, "Ferromagnetic-Resonance Absorption Supermalloy at 9, 24, and 38 GHz", Can. J. Phys. **55**, 787 (1977).
8. R. Codrington, S., J. D. Olds, and H. C. Torrey, "Paramagnetic Resonance in Organic Free Radicals at Low Fields", Phys. Rev. **95**, 607 (1954).
9. Damon, R. W., and J. R. Eshbach, "Magnetostatic Modes of a Ferromagnet Slab" J. Phys. Chem. Solids **19**, 308 (1961).
10. Dillon, J. F., "Ferrimagnetic Resonance in Rare-Earth-Doped Yttrium Iron Garnet. III. Linewidth", Phys. Rev. **127**, 1495 (1962).
11. Dobin, A. Yu., and R. H. Victora, "Surface Roughness Induced Extrinsic Damping in Thin Magnetic Films", Phys. Rev. Lett. **92**, 257204-1 (2004).
12. Gennes, P. G. De, C. Kittel, and A. M. Portis, "Theory of Ferromagnetic Resonance in Rare Earth Garnets II. Line Widths", Phys. Rev. **116**, 323 (1959).
13. Gilbert, T. A., Armour Research Report No. 11 (January 1955).

14. Green J. J., and T. Kohane, "Testing of Ferrite Material in Microwave Application," SCP and Solid State Technology, 46 (1964).
15. Hamilton W. R., "On a New Species of Imaginary Quantities Connected with a Theory of Quaternions", Preceedings of the Royal Irish Academy 2, 424 (1843).
16. Harte, K. J., "Theory of Magnetization Ripple in Ferromagnetic Films", J. Appl. Phys. **39**, 1503(1968).
17. Heinrich, B., R. Urban, and G. Woltersdorf, "Magnetic Relaxation in Metallic films: Single and Multiplayer Structures", J. Appl. Phys. **91**, 7523 (2002).
18. Herring, C. and C. Kittel, "On the Theory of Spin Waves in Ferromagnetic Media", Phys. Rev. **81,** 869 (1951).
19. Hoeppe, U., "Off Resonance Relaxation of Uniform Precession Mode in Microwave Ferrites", International Conference on Ferrites ICF9, San Francisco, August 2004.
20. Hurben, M. J, "Two Magnon Scattering and Relaxation in Thin Ferrite Films", Ph. D. Thesis, Colorado State University, 1996.
21. Hurben, M. J., and C. E. Patton, "Theory of Two Magnon Scattering Microwave Relaxation and Ferromagnetic Resonance Linewidth in Magnetic Thin Films", J. Appl. Phys. **83**, 4344 (1998).
22. Jackson, J. D., *Classical Electrodynamics* (Jhhn Wiley & Sons, Inc. 1998).
23. Kabos, P. and C. E. Patton, "Influence of Microwave Dielectric Properties on the Effective Linewidth in Ferrites", Adv. Ceramics **16**, 67-70 (1985).
24. Kalinikos B. A., and A. N. Slavin, "Theory of Dipole-exchange Spin Wave Spectrum for Ferromagnetic Films with Mixed Exchange Boundary Conditions", J. Phys. C: Solid State Phys. **19**, 7013 (1986).
25. Kalinikos, B. A., M. P. Kostylev, N. V. Kozhus, and A. N. Slavin, "The Dipole-exchange Spin Wave Spectrum for Anisotropic Ferromagnetic Films with Mixed Exchange Boundary Conditions", J. Phys. Condens. Matter **2**, 9861 (2004).
26. Kittel, C., "On the Theory of Ferromagnetic Resonance Bsorption", Phys. Rev. **73**, 155 (1948).
27. Kohane, T., and E. Schlomann, "Linewidth and Off Resonance Loss in Polycrystalline Ferrites at Microwave Frequency," J. Appl. Phys. **39**, 720 (1968).

28. Lax, B. and K. J. Button, *Microwave Ferrites and Ferrimagnetics* (McGraw Hill Book Co., New York, 1962).
29. Landau, L. D. and E. M. Lifshitz, "On the Theory of the Dispersion of Magnetic Permeability in Ferromagnetic Bodies", Physik. Z. Sowjetunion **8**, 153 (1935).
30. McKinstry, K. D., C. E. Patton, M. A. Wittenauer, M. Sankaraman, J. Nyenhuis, F. J. Friedlaender, H. Sato, and A. Schindler, "Off Resonance Loss Measurements in Ferrites at 35 GHz", IEEE Trans. Mag. **25**, 3482 (1989).
31. McKinstry, K. D., Ph. D. Thesis, Colorado State University, 1991.
32. McMichael, R. D., C. G. Lee, M. D. Stiles, F. G. Serpa, P. J. Chen, and W. F. Egelhoff, Jr., "Exchange Bias Relaxation in CoO-biasesd Films", J. Appl. Phys. **87**, 6406 (2000).
33. McMichael, R. D., D. J. Twisselmann, and A. Kunz, "Localized Ferromagnetic Resonance in Inhomogeneous Thin Films", Phys. Rev. Lett. **90**, 227601 (2003).
34. McMichael, R. D., and P. Krivosik, "Classical Model of Extrinsic Ferromagnetic Resonance Linewidth in Ultrathin films", Magnetics, IEEE trans. **40**, 2 (2004).
35. Mills, D. L., "Ferromagnetic Resonance Relaxation in Ultrathin Metal Films: The Role of the Conduction Electrons", Phys. Rev. B **68**, 014419 (2003).
36. Mo, N., Y. Song, and C. E. Patton, "High-field Microwave Effective Linewidth in Polycrystalline Ferrites: Physical Origins and Intrinsic limits", J. Appl. Phys. **97**, 093901 (2005).
37. Moosmuller, H., K. D. McKinstry, and C. E. Patton, "Microwave Effective Linewidth in Thin Metal Films", J. Appl. Phys. **67**, 5521 (1990).
38. Motizuki, K., and M. Sparks, "Theory of Ferromagnetic Resonance Line Shape outside the Spin-wave Manifold", Phys. Rev., **140**, A972 (1965).
39. Nazarov, A, V., D Menard, J. J. Green, C. E. Patton, G. M. Arge, H, J, Van Hook, "Near Theoretical Microwave Loss in Hot Isostatic Pressed (hipped) Polycrystalline Yttrium Iron Garnet", J. Appl. Phys. **94**, 7227 (2003).
40. Osborn, J. A., "Demagnetizing Factors of the General Ellipsoid", Phys. Rev. **67**, 351 (1945).
41. Patton, C. E., "Effective Linewidth due to Porosity and Anisotropy in Polycrystalline Yittrium Iron Garnet and Ca-V-substituted Yittrium Iron Garnet at

10GHz", Phys. Rev. **179**, 352 (1969).

42. Patton, C. E., "Microwave Properties of Fine Grain Polycrystalline Yttrium Iron Garnet", J. Appl. Phys. **41**, 1355 (1970).
43. C. E. Patton, C. H. Wilts, and F. B. Humphrey, "Relaxation Processes for Ferromagnetic Resonance in Thin Films", J. Appl. Phys. **38**, 1358-1359 (1967).
44. Patton, C. E., "Microwave Relaxation and Phenomenological Damping in Thin Films", Czech. J. Phys. **B21**, 490 (1971).
45. Patton, C. E., "A Review of Microwave Relaxation in Polycrystalline Ferrite", Intermag conference, Japan, 433 (1972).
46. Patton, C. E., and T. Kohane, "Ultrasensitive Technique for Microwave Susceptibility Determination Down to 10^{-5}", Rev. Sci. Instr. **43**, 76 (1972).
47. Patton, C. E., "Microwave Resonance and Relaxation", Chapter 10, *Magnetic oxides*, (John Wiley, London, 1975).
48. Patton, C. E., "Classical Theory of Spin Wave Dispersion for ferromagnetic metals", Czech. J. Phys. **B 26**, 925(1976).
49. Pincus, P., M. Sparks, and R. C. LeCraw, "Ferromagnetic Relaxation. II. The Role of Four-Magnon Processes in Relaxing the Magnetization in Ferromagnetic Insulators", Phys. Rev. **124**, 1015 (1961).
50. Platow, W., A. N. Anisimov, G. L. Dunifer, M. Farle, and K. Baberschke, "Correlations between Ferromagnetic-resonance Lnewidths and Sample Quality in the Study of Metallic Ultrathin Films", Phys. Rev. B **58**, 5611 (1998).
51. Rupke, H. D., "Magnetodynamic Modes in Ferrite Spheres for Microwave Filter Application", IEEE Trans. Mag. **1**, 80 (1970).
52. Safonov, V. L., and H. N. Bertram, "Linear Stochastic Magnetization Dynamics and Microscopic Relaxation Mechanisms", J. Appl. Phys. **94**, 529 (2003).
53. Safonov, V. L., "Tensor Form of Magnetization Damping", J. Appl. Phys. **91**, 8653 (2002).
54. Schlömann, E., "FMR in Polycrystalline Ferrites with Large Anisotropy", J. Phys. Chem. Solids **6**, 257 (1958).
55. Schlömann, E., "Spin Wave Analysis of FMR in Polycrystalline Ferrites", J. Phys. Chem. Sol. **6**, 242 (1968).

56. Schlömann, E., "Inhomogeneous Broadening of Ferromagnetic Resonance Lines", Phys. Rev. **182**, 632 (1969).
57. Schlömann, E., "Anisotropy Correlation Function and Grain-Size Distribution in Polycrystalline Magnetic Materials", IEEE Trans. Mag. **1**, 75 (1970).
58. Schlömann, E., and R. I. Joseph, "Surface-Roughness-Induced Demagnetizing Fields in Thin Films and Their Influence Upon the Approach to Saturation", J. Appl. Phys. **41**, 1336 (1970).
59. Schneider, M. L., A. B. Kos, and T. J. Silva, "Dynamic Anisotropy of Thin Permalloy Films Measured by Use of Finite Angle-resolved Inductive Microwave Magnetometry", Appl. Phys. Lett. **86**, 202503 (2005).
60. Scotter, D. G., "Effect of Nonmagnetic Inclusions on the Spin-wave Linewidth in Polycrystalline YIG", J. Appl. Phys. **42**, 4088 (1972).
61. Seiden, P. E. and M. Sparks, "Frequency Dependence of the Two-magnon Ferromagnetic Resonance Linewidth", Phys. Rev. **137**, A1278 (1965).
62. Sparks, M., R. Loudon, and C. Kittel, "Ferromagnetic relaxation. I. Theory of the Relaxation of the Uniform Precession and the Degenerate Spectrum in Insulators at Low Temperatures", Phys. Rev. **122**, 791 (1961).
63. Sparks, M., *Ferromagnetic-Relaxation Theory*, (McGraw Hill Book Co., New York, 1964).
64. Sparks, M., "Ferromagnetic Resonance in Thin Films. II. Theory of Linewidths", Phys. Rev. **1**, 3856 (1970). Sparks, M., "Ferromagnetic Resonance in thin films. III. Theory of mode intensities", Phys. Rev. **1**, 3869 (1970).
65. Soohoo, R. F., *Theory and Applications of Ferrites* (Prentice-Hall, New Jersey, 1960).
66. Taylor, B. N. and Chris E. Kuyatt, "Guidelines for Evaluating and Expressing the Uncertainty of NIST Measurement Results", NIST Technical Note 1297, 1994 Edition.
67. Needham, T., *Visual Complex Analysis*, (Oxford University Press Press, Oxford, 1997);
68. Truedson, J. R., K. D. McKinstry, R. Karim, and C. E. Patton, "Effective Linewidth due to Conductivity Losses in Barium Ferrite at 10GHz", IEEE Trans. Mag. **28**,

3309 (1992). Truedson, J. R., K. D. Mckinstry, and C. E. Patton, "Comparison of Effective Linewidth and FMR Linewidth at 10 GHz in Ho Substituted YIG", IEEE Trans. Mag. **28**, 3312 (1992).

69. Truedson, J. R., K. D. Mckinstry, P. Kabos, and C. E. Patton, "High-field Effective Linewidth and Eddy Current Losses in Moderate Conductivity Single-crystal M-type Barium Hexagonal Ferrite Disks at 10-60 GHz", J. Appl. Phys. **74**, 2705 (1993).
70. Truedson, J. R., P. Kabos, K. D. McKinstry, and C. E. Patton, "High Field Effective Linewidth Eddy Current Losses in Moderate Conductivity Single Crystal Zn-Y Hexagonal Ferrite at 10-35 GHz", J. Appl. Phys. **76**, 432 (1994).
71. Van Hook, H. J. and F. Euler, "Anisotropy Linebroadening in Polycrystalline V-In Substituted YIG", J. Appl. Phys. **40**, 4001 (1969).
72. Vrehen, Q. H. F., "Absorption and Dispersion in Porous and Anisotropic Polycrystalline Ferrites at Microwave Frequencies", J. Appl. Phys. **40**, 1849 (1969).
73. Vrehen, Q. H. F., A. B Van Groenou, and J. G. M. deLau, "Relaxation of Ferromagnetic Precession by Excitation of Spin Waves in a Polycrystalline Nickel-Cobalt Ferrite", Phys. Rev. B **1**, 2332 (1970).
74. Walker, L. R., "Magnetostatic Modes in Ferromagnetic Resonance", Phys. Rev. **105**, 390 (1957).
75. Wilber, W. D., and L. M. Silber, "Effective Linewidth Measurements at 36 GHz in Hexagonal and Cubic Ferrites", J. Appl. Phys. **63**, 3353 (1988).
76. Wigen, P. E., "Dipole-Narrowed Inhomogeneously Broadened Line in Ferromagnetic Thin Films", Phys. Rev. **133**, A1557 (1964).
77. Wolfram, T., and R. E. De Wames, "Magnetoexchange Branches and Spin-Wave Resonance in Conducting and Insulating Films: Perpendicular Resonance", Phys. Rev. B **4**, 3125 (1971).
78. Woltersdorf, G., and B. Heinrich, "Two-magnon Scattering in a Self-assembled Nanoscale Network of Misfit Dislocation", Phys. Rev. B **69**, 184417 (2004).
79. Yu, J. T., R. A. Turk, and P. E. Wigen, "Exchange-dominated Surface Spin Waves in Thin Yttrium Iron Garnet Films", Phys. Rev. B **11**, 420 (1975).